JOURNAL OF THE AERONAUTICAL SCIENCES

VOLUME 23 JUNE, 1956 NUMBER 6

ST. LOUIS JUN 18 1956 PUB

CONTENTS

Analysis of a Rolling Pull-Out Maneuver.... W. J. OAKES, JR., AND P. T. HOLLIDAY 517

The Design and Testing of Supersonic Flutter Models..... JOHN F. MCCARTHY, JR., AND ROBERT L. HALFMAN 530

Free-Flight Measurements of Skin Friction of Turbulent Boundary Layers with High Rates of Heat Transfer at High Supersonic Speeds..... SIMON C. SOMMER AND BARBARA J. SHORT 536

An Approximate Method of Calculating Three-Dimensional Compressible Flow in Axial Turbomachines.....COMDR. CARL O. HOLMQUIST AND W. DUNCAN RANNIE 543

Solution of Complex Nonlinear Plastic Structures by the Method of Tearing..... GABRIEL KRON 557

Elasto-Plastic Bending of Beams on Elastic Foundations .....PAUL SEIDE 563

Some Recent Aerodynamic Techniques in Design of Fin-Stabilized Free-Flight Missiles for Minimum Dispersion....M. W. HUNTER, A. SHEF, AND D. V. BLACK 571

A First-Order Formulation of the Unsteady Supersonic Flow Problem for Finite Wings.....JOHN W. MILES 578

On Strong Transverse Waves Without Shocks in a Circular Cylinder..... STEPHEN H. MASLEN AND FRANKLIN K. MOORE 583

Influence of the Leading-Edge Shock Wave on the Laminar Boundary Layer at Hypersonic Speeds.....LESTER LEES 594

Readers' Forum.....601–612

Published by

INSTITUTE OF THE AERONAUTICAL SCIENCES, INC.

JOURNAL OF THE AERONAUTICAL SCIENCES

Editor: W. R. SEARS
Director, Graduate School of Aeronautical Engineering, Cornell University

Associate Editor: ROBERT R. DEXTER *Managing Editor:* RITA J. TURINO
Editorial Assistant: CAROLINE TAYLOR

Editorial Committee

Aerodynamics and Fluid Mechanics

Holt Ashley
H. Julian Allen
Dean R. Chapman
Francis H. Clauser
Hugh L. Dryden
John C. Evvard
Antonio Ferri
Alexander Flax
Wallace D. Hayes
R. T. Jones
Carl Kaplan
H. W. Liepmann
C. C. Lin
H. F. Ludloff
Harold Luskin
Clark B. Millikan
C. D. Perkins
H. J. E. Reid
George S. Schairer
G. B. Schubauer
John Stack
Theodore Theodorsen
Arthur N. Tifford
Th. von Karman

Flight Testing

R. R. Gilruth
Melvin N. Gough
W. L. Howland
W. F. Milliken, Jr.

Rotating Wing Aircraft

F. B. Gustafson
K. H. Hohenemser
Bartram Kelley
R. B. Maloy
Ralph McClarren
R. H. Miller
R. H. Prewitt
Igor I. Sikorsky

Structures

John E. Duberg
N. J. Hoff
Samuel Levy
J. F. McBrearty
W. Ramberg
E. E. Sechler
F. R. Shanley
C. R. Strang
S. Timoshenko

Meteorology

C. F. Brooks
D. M. Little
F. W. Reichelderfer
K. C. Spengler

Vibration and Flutter

Lee Arnold
M. A. Biot
R. L. Bisplinghoff
Harold A. Cheilek
I. E. Garrick
Martin Goland

Aircraft Design

W. E. Beall
E. H. Heinemann
Hall L. Hibbard
Richard Hutton
C. L. Johnson
A. A. Kartveli
E. G. Stout
F. K. Teichmann
Robert J. Woods

Electronics

Welcome W. Bender
K. C. Black
M. V. Kiebert, Jr.
David S. Little
S. B. Rogers
Paul Rosenberg
L. M. Sherer

Physiologic Problems

H. G. Armstrong
Louis H. Bauer
Robert J. Benford
W. Randolph Lovelace, II
Ross A. MacFarland

Flight Propulsion

William Bollay
George W. Brady
R. P. Kroon
Frank E. Marble
Abe Silverstein
Martin Summerfield
E. S. Taylor

Instruments

Alan G. Binnie
Charles H. Colvin
Frank R. Cook
C. S. Draper
S. G. Eskin
C. F. Savage
R. C. Sylvander

SUBSCRIPTION RATES

JOURNAL OF THE AERONAUTICAL SCIENCES, Published Monthly.—United States and Possessions: 1 Year, $15.00; Single Copies, $1.50. Foreign Countries Including Canada (American Currency Rates): 1 Year, $16.00; Single Copies, $1.50.

AERONAUTICAL ENGINEERING REVIEW, Published Monthly.—United States and Possessions: 1 Year, $3.00; Single Copies, $0.50. Foreign Countries Including Canada (American Currency Rates): 1 Year, $3.50; Single Copies, $0.50.

Notices of change of address should be sent to the Institute at least 30 days prior to actual change of address.

Manuscripts for publication, proofs, and all correspondence should be addressed to the Editorial Office of the JOURNAL.

Correspondence regarding subscriptions may be addressed to the Editorial Office of the JOURNAL OF THE AERONAUTICAL SCIENCES, 2 East 64th Street, New York 21, N.Y., or to the Publication Office, 20th and Northampton Sts., Easton, Pa.

© *Copyright, 1956, by the Institute of the Aeronautical Sciences, Inc.*

Entered as Second Class Matter at the Post Office, Easton, Pa., May 1, 1937. Acceptance for mailing at a special rate of Postage provided for in the Act of August 24, 1912. Authorized April 29, 1937.

JOURNAL OF THE AERONAUTICAL SCIENCES

VOLUME 23 JUNE, 1956 NUMBER 6

Analysis of a Rolling Pull-Out Maneuver

W. J. OAKES, JR.,* AND P. T. HOLLIDAY†

Northrop Aircraft, Inc.

SUMMARY

Four methods for determining the maximum first peak vertical tail load during a rolling pull-out maneuver are examined. The familiar Kelley method and an approximation that $\beta = \alpha$ are compared with a linearized solution of the equations of motion and a constant angle of attack solution of the equations of motion, both derived herein. Time history solutions of the airplane velocities are given for the linearized and constant angle of attack solutions. The resulting vertical tail load factors are compared with the Kelley method and the $\beta = \alpha$ approximation for three current aircraft configurations—straight-, swept-, and delta-wing.

A time history solution of the constant angle of attack equations of motion is shown to be the only consistent method among those examined herein for determining the maximum vertical tail load design condition during a rolling pull-out maneuver. A large order of error is also shown to exist for each of the other three solutions. One source of error is the inability of the linearized method to predict the proper damping in the oscillatory mode. In the transonic speed range stable oscillations as computed by the linearized method are actually shown to be unstable by the constant angle of attack method of calculation.

The rolling pull-out maneuver used in this analysis is shown to be a reasonable maneuver in that the side load factors and control surface trim deflections obtained are small enough to be tolerable.

SYMBOLS

b = wing span
c_t = wing tip chord
c_r = wing root chord
C = mean aerodynamic chord
C_L = lift coefficient = lift/$q_d S$
C_{L_α} = slope of lift curve = $\partial C_L/\partial\alpha$

Stability Derivatives

$$C_{l_p} = \frac{1}{q_d Sb}\frac{\partial L_A}{\partial\left(\frac{Pb}{2U_0}\right)} \qquad C_{n_p} = \frac{1}{q_d Sb}\frac{\partial N_A}{\partial\left(\frac{Pb}{2U_0}\right)}$$

$$C_{l_r} = \frac{1}{q_d Sb}\frac{\partial L_A}{\partial\left(\frac{Rb}{2U_0}\right)} \qquad C_{n_r} = \frac{1}{q_d Sb}\frac{\partial N_A}{\partial\left(\frac{Rb}{2U_0}\right)}$$

$$C_{l_\beta} = \frac{1}{q_d Sb}\frac{\partial L_A}{\partial\beta} \qquad C_{n_\beta} = \frac{1}{q_d Sb}\frac{\partial N_A}{\partial\beta}$$

$$C_{l_{\delta_A}} = \frac{1}{q_d Sb}\frac{\partial L_A}{\partial\delta_A} \qquad C_{n_{\delta_A}} = \frac{1}{q_d Sb}\frac{\partial N_A}{\partial\delta_A}$$

$$C_{Y_p} = \frac{1}{q_d S}\frac{\partial Y_A}{\partial\left(\frac{Pb}{2U_0}\right)} \qquad C_{Y_\beta} = \frac{1}{q_d S}\frac{\partial Y_A}{\partial\beta}$$

$$C_{Y_r} = \frac{1}{q_d S}\frac{\partial Y_A}{\partial\left(\frac{Rb}{2U_0}\right)}$$

$C.P.$ = center of pressure
F_{VT} = vertical tail load
g = gravity acceleration—32.2 ft/sec.²
I_x = moment of inertia about x axis
I_y = moment of inertia about y axis
I_z = moment of inertia about z axis
I_{xz} = product of inertia in the xz plane
l_x = horizontal distance along x axis from $C.G.$ to $C.P.$ of vertical tail
l_z = vertical distance along z axis from $C.G.$ to $C.P.$ of vertical tail
L = rolling moments about x axis
M = pitching moments about y axis
m = mass = weight/g
N = yawing moments about z axis
n = load factor
P = rate of roll about x axis
Q = rate of pitch about y axis
R = rate of yaw about z axis
p = perturbation from an initial value of P
q = perturbation from an initial value of Q
r = perturbation from an initial value of R
q_d = dynamic pressure = $(\rho/2)\,U_0^2$
S_w = wing area
S_t = vertical tail area
T = thrust
t = time
U = velocity of $C.G.$ in direction of x axis
V = velocity of $C.G.$ in direction of y axis
W = velocity of $C.G.$ in direction of z axis
$Wt.$ = airplane weight
v = perturbation from an initial value of V
X = forces along x axis
Y = forces along y axis
Z = forces along z axis

Received April 1, 1955.
* Structures Engineer.
† Research Engineer.

x, y, z = right-handed coordinate system attached to aircraft C.G. and moving with it (see Fig. A-1)

x', y', z' = coordinate system fixed with respect to initial space

α = angle of attack

α_V = angle of attack of vertical tail

β = sideslip angle

$\dot{\Gamma}_0$ = initial time rate of change of the Eulerian pitch angle

δ_A = aileron angle

δ_e = elevator angle

ϵ = moment arm of thrust about C.G.

$\dot{\psi}_0$ = initial time rate of change of the Eulerian yaw angle

Φ_0 = initial bank angle of moving axis system

η = vertical tail efficiency, assumed = 1.0

γ = Eulerian pitch angle

ψ = Eulerian yaw angle

ϕ = Eulerian roll angle

Subscripts

0 = initial condition

W = weight force

max = maximum

A = thrust and aerodynamic forces

V = vertical tail

A dot above a symbol indicates that it is a partial derivative of the symbol with respect to time, $\dot{(\ )} = \partial(\ )/\partial t$

Introduction

During World War II considerable trouble was experienced with the vertical tails on military aircraft. No conditions had been considered which would design the vertical tail for the maneuvering loads that these relatively high-speed aircraft were attaining. Hence, the design condition of a steady 5° yaw angle at limit dive speed was prescribed in 1946 as a solution to this problem.[1] Until lately this has been the critical design condition.

As the limit dive speed radically increased after World War II, it became evident that this yaw angle criteria was not realistic. A perusal of the situation was made with the result that both the Air Force and the Navy discarded the arbitrary yaw criteria and placed more emphasis upon design conditions for the vertical tail which are indicative of the actual attitude of the airplane. One of these design conditions, the rolling pull-out maneuver (any maneuver in which rolling occurs during high load factor flight conditions) has been a design criteria since 1942. Due to the difficulty which many current aircraft configurations have in executing this maneuver, the rolling pull-out has achieved a prominent place in the latest (1953) structural design criteria of both the Navy[2] and the Air Force.[3] This maneuver is now recognized as one of the most critical design conditions for the vertical tail as well as for the whole aft fuselage and the horizontal tail.

In 1944 Gilruth[4] presented an analysis of the sideslip angles that might be expected in a rolling pull-out maneuver. The value of β that he obtained is the steady-state yaw angle due to the steady rolling moment produced by the aileron. This analysis was subsequently found to give half the sideslip angle that White, Lomax, and Turner[5] obtained from their less simplified analysis. Their expression is based on the three linearized lateral equations of motion in which the product-of-inertia terms have been omitted.

The same results were obtained by Kelley[6] in 1948. He extended the analysis of reference 4 to account for the dynamic overshoot due to the abrupt manner in which the rolling moment is applied. Since no damping was considered in the yaw direction, the value of β obtained in reference 6 is twice that derived by Gilruth. Kelley's report is perhaps the most well known and was instrumental in having a rolling pull-out condition inserted in the Air Force vertical tail design criteria.

It has become more apparent in recent years that the simplified expressions used in the past are no longer applicable to current aircraft configurations. An analysis, including some of the nonlinear terms, was made by Stone.[7] In this analysis serious differences were found in comparison with the more simplified expressions. A solution of the equations linearized about accelerated flight condition is presented by Etkin and Collette[8] which also shows considerable difference from the simplified method.

An approximation for the sideslip angle that has been proposed recently is that the sideslip angle be assumed equal to the angle of attack. This approximation is expected to be particularly valid for aircraft whose inertia is concentrated along the fuselage longitudinal axis and for the first 90–180° of high velocity rolls initiated from high angle of attack conditions.

Four methods of predicting the vertical tail angle of attack and corresponding load are compared in this paper. The methods are:

(1) The simplified equation for the vertical tail load presented by Kelley.

(2) The assumption that $\beta = \alpha$.

(3) A solution of the equations of motion in which the angle of attack is held constant.

(4) A linearized solution of the equations of motion.

Numerical solutions of these methods for three airplane configurations form the basis for this comparison. The configurations are those currently most popular—straight-wing, swept-wing, and delta-wing. Since each of these airplanes has a different design criteria, load factor, etc., comparisons regarding rolling pull-out characteristics cannot be made between the three configurations used. Only the differences arising out of the methods of calculation—which are common to all configurations—are of concern here.

In general, it may be said that this paper attempts to define more precisely the attitudes of the airplane in the rolling pull-out maneuver. The more precisely this is done, the more accurate are the loads determined from these attitudes. It is felt that in this approach more realistic and rational design loads will be obtained.

Analysis

The maneuver considered in this paper is an uncoordinated rolling pull-out at $^2/_3$ of the design limit

TABLE 1
Airplane Configuration Characteristics

Aircraft Configuration	Quarter Chord Sweep Degrees	Aspect Ratio	Taper Ratio c_t/c_r	Vertical Tail Area Ratio S_v/S_w	Wing Loading $Wt./S_w$ lbs./ft.^{2}
Straight	0	4.50	0.50	0.073	64
Swept	45	5.50	0.60	0.138	107
Delta	37	3.75	0	0.110	57

load factor. This maneuver is initiated from a banking turn of the proper load factor by application of abrupt opposite aileron to maximum deflection except as limited by maximum available hinge moment or the aileron stops. The load factor is maintained at a constant value by fore-and-aft manipulation of the stick. The rudder is held fixed in the undeflected position.

Four different methods for the determination of the sideslip angle, the vertical tail angle of attack, and the vertical tail load during a rolling pull-out maneuver are presented here. The vertical tail load is assumed to consist entirely of the air load acting on the total vertical tail area without any inertia relief.

Three airplane configurations are considered in this paper. These configurations are typical of the present day state of the art and consist of a straight-wing, a swept-wing, and a delta-wing type. Pertinent geometrical characteristics are given in Table 1. The aerodynamic characteristics for each of the configurations were obtained from wind-tunnel tests and theoretical calculations using acceptable methods. All methods used the same aerodynamic characteristics for each airplane configuration. Since the aerodynamic parameters used are representative of those aircraft types considered, they are not included in this report.

It is reiterated that, since each of these configurations is designed to a different design limit load factor, no comparisons can be made between the various configurations. The use of these different types is to determine the difference, if any, that the various configurations have upon the methods used to determine the vertical tail load.

(1) *Simplified Equation for Vertical Tail Load*

Kelley[6] gives two expressions for the vertical tail load. These loads are computed using a single degree of freedom—the linearized, uncoupled, yawing moment equation. The equation which is of interest here is the rolling pull-out vertical tail load derived in reference 4 and modified in reference 5. The vertical tail load is due to the yaw produced by the aileron deflection and is determined by

$$F_{VT} = q_d S_v \eta C_{L\alpha} \beta_{max} = \frac{n}{4} \frac{Wt.}{S_w} \frac{(Pb)}{(2U_0)} S_v \eta \frac{(C_{L\alpha})_v}{(C_{n\beta})} \tag{1}$$

The corresponding maximum sideslip angle is

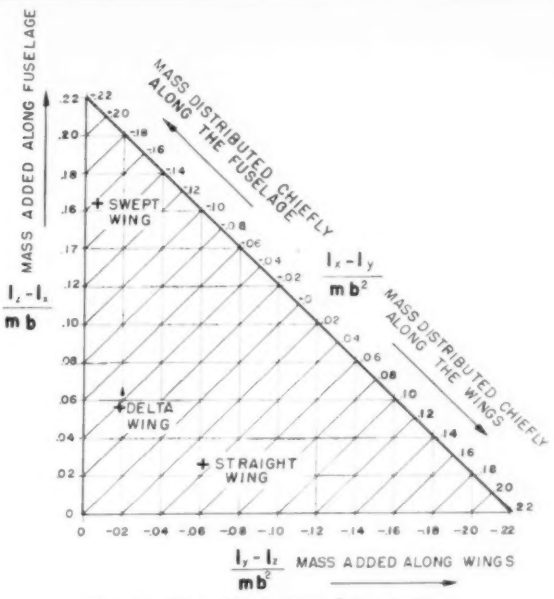

FIG. 1. Mass distribution of the airplane.

$$\beta_{max} = \frac{C_L}{4} \frac{(Pb)}{(2U_0)} \frac{1}{C_{n\beta}} = \frac{C_L}{4} \frac{C_{l\delta A} \cdot \delta_A}{C_{n\beta} C_{lp}} \tag{2}$$

and this value is assumed equal to the vertical tail angle of attack.

(2) *The Assumption that $\beta = \alpha$*

In recent years it has become more apparent that the mass distribution of modern high-speed airplanes has an important effect on the maximum sideslip angles attained in rolling pull-outs. It is obvious that an airplane which has the major portion of its mass in the fuselage will tend to rotate about the longitudinal body axis when the ailerons are deflected. If the airplane is at an angle of attack when the ailerons are deflected, the assumption is made that the initial angle of attack is translated into a sideslip angle at a roll angle of 90°. This sideslip angle at 90° roll is assumed to be the maximum sideslip angle that occurs in the maneuver. Based upon this approximation, the vertical tail load is

$$F_{VT} = (C_{L\alpha})_v q_d S_v \alpha_a \tag{3}$$

Neihouse[9] presented a convenient way of determining to what extent the particular airplane configuration under study has its mass distributed along the fuselage. Fig. 1 reproduces this chart with the three aircraft analyzed in this report shown on it. According to this assumption, the swept-wing airplane considered in this paper should have a sideslip angle approximately equal to the airplane initial angle of attack. This approximation is not expected to be as true of the other two aircraft considered, since they are further down on the chart. It is noted that the placement on Fig. 1 of the three configurations analyzed here does not imply that all airplanes of that general plan form plot in the same region.

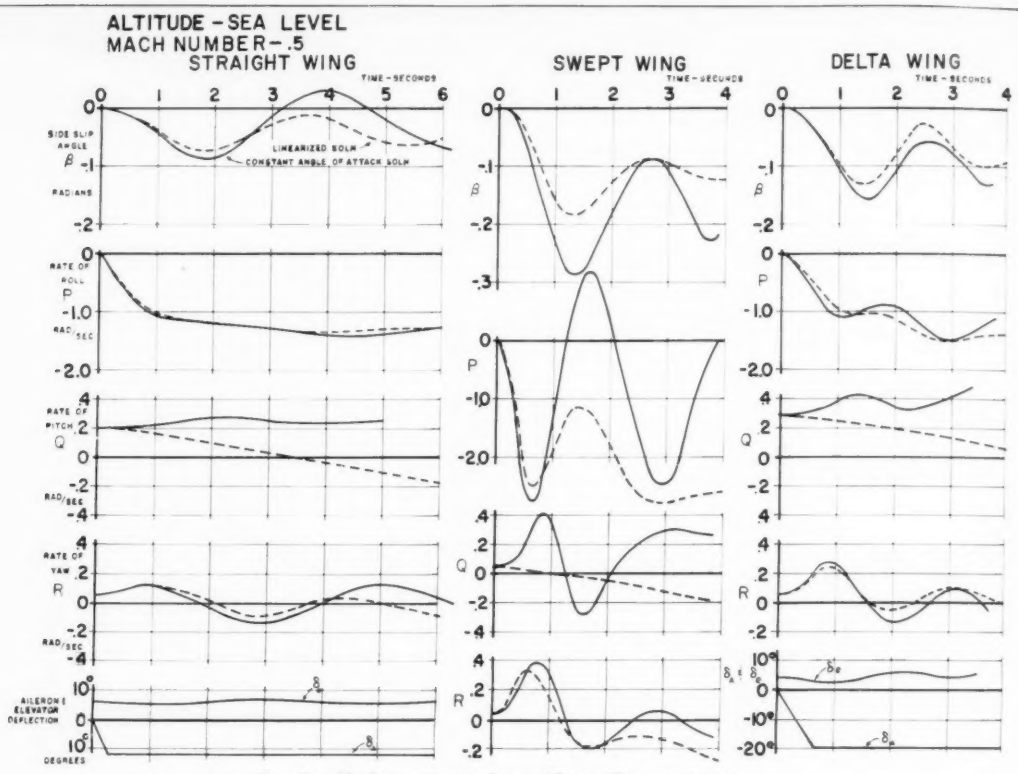

FIG. 2. Airplane response in a rolling pull-out maneuver.

(3) *Constant Angle of Attack Solution*

The constant angle of attack solution prepared in this paper is based upon the exact Eulerian equations of motion which may be found in any standard reference.[10, 11] It is felt that several assumptions may be made without impairing the accuracy of the solution. The assumptions and conditions of this analysis are

(1) The forward velocity is assumed constant.

(2) A constant angle of attack is maintained which is assumed to result in a constant load factor throughout the maneuver.

(3) The drag forces are assumed in balance by the proper thrust variation.

(4) The pitching moments are assumed in balance by the necessary variation in elevator angle.

(5) The aerodynamic forces are assumed to be expressible in terms of constant stability derivatives.

(6) Aeroelastic corrections are applied to the stability derivatives.

In Appendix A the Eulerian equations of motion are subjected to the above six conditions and assumptions. This results in six first-order, nonlinear, differential equations. It is noted that this solution, as shown in the appendix, provides an exact relationship between the Eulerian angular velocities and the rotational velocities of the airplane regardless of the size of the angles involved. The solution of these equations is obtained by a numerical integration performed on digital computing machines. The time increment of integration was varied so that an extrapolation to the correct solution ($\Delta t = 0$) could be made.

The results obtained from the numerical integration are in the form of time histories of the variables P, Q, and R, which define the change of airplane attitude. These quantities are plotted in Fig. 2 together with the sideslip angle β and the elevator angle necessary to maintain the constant angle of attack.

The vertical tail load is computed from the response of the airplane in the rolling pull-out maneuver. The load on the vertical tail is

$$F_{VT} = S_v \eta \, q_d \, (C_{L\alpha})_v \, \alpha_v \tag{4}$$

where $$\alpha_v = -\beta + (R \, l_x / U_0) - (P \, l_z / U_0) \tag{5}$$

The major contribution to the vertical tail angle of attack is the sideslip angle, β.

It should be noted that the rolling velocity contribution is of significant importance—so much so that it cannot be excluded from the analysis. Due to this contribution, the peak tail load may not occur at β_{max} and thus a time history of F_{VT} is necessary in order to determine the peak load.

(4) *Linearized Solution*

Linearization of the Eulerian equations of motion is given in Appendix B. The method of small perturbations from a steady condition is used to linearize the equations. The initial condition of a steady banking turn at $^2/_3$ of the design limit load factor is used

VERTICAL TAIL ANGLE OF ATTACK-DEGREES

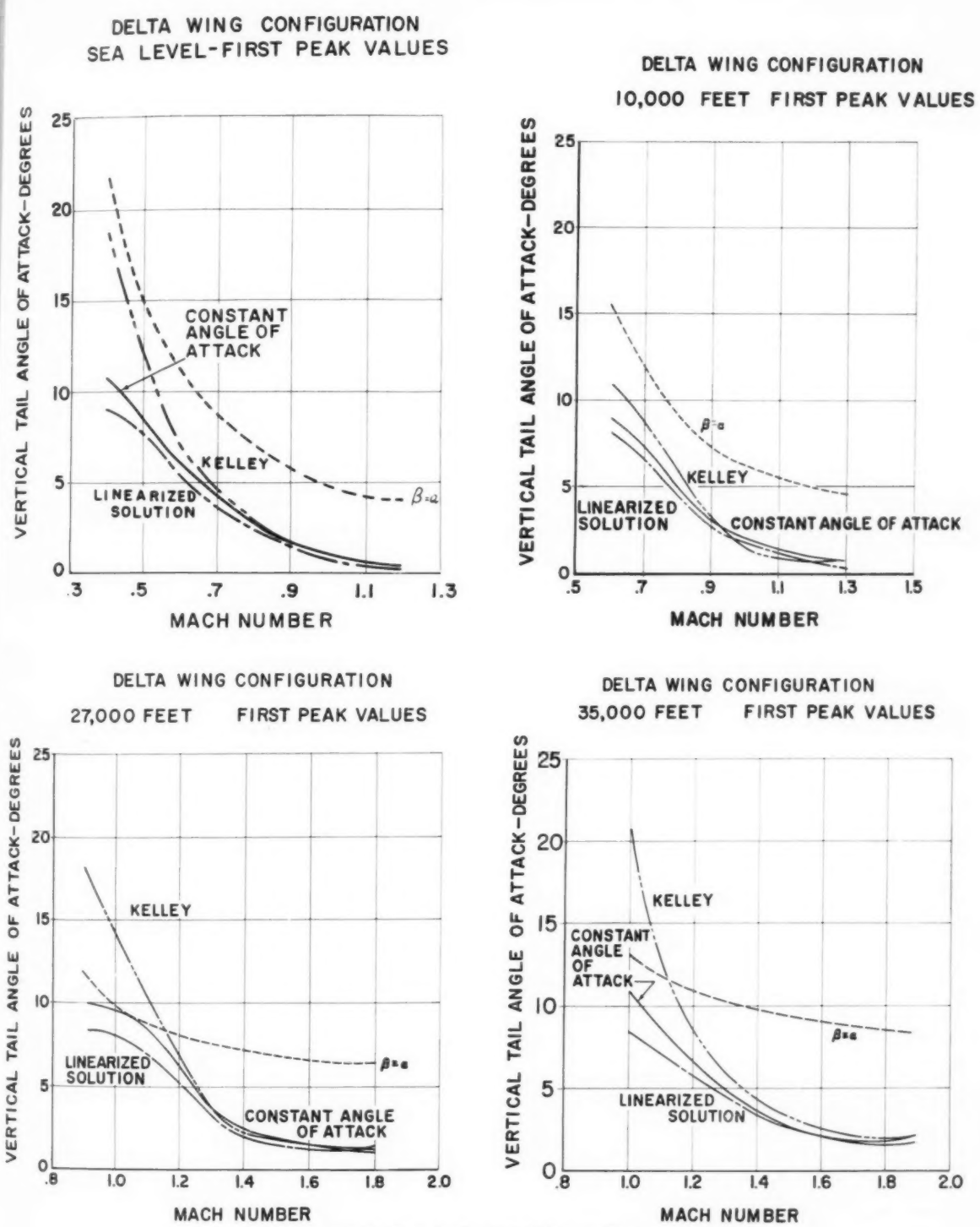

FIG. 3. Maximum vertical tail angle of attack during a rolling pull-out maneuver.

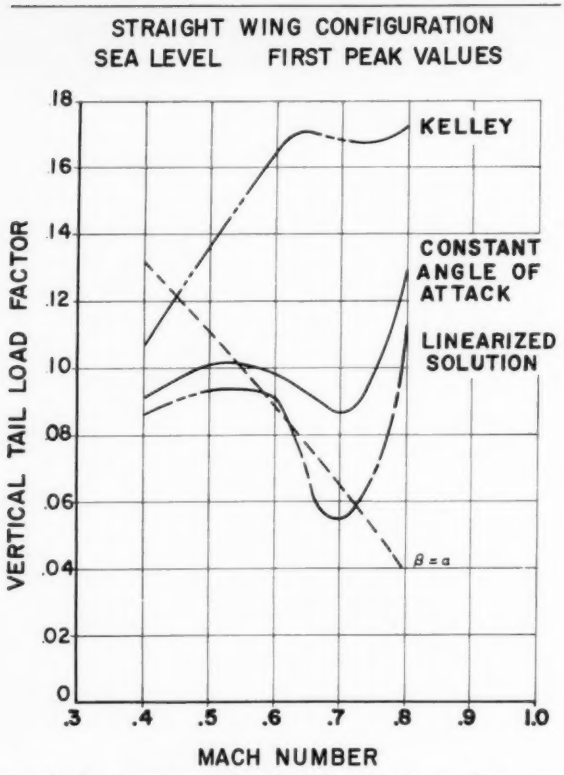

FIG. 4. Maximum vertical tail load factor during a rolling pull-out maneuver.

as the steady condition about which the equations are linearized. It should be mentioned that this procedure results in additional terms due to the steady accelerations which do not occur in the linearized equations for level flight. It is also noted that, unlike the constant angle of attack solution, this solution, since it is linear, will inherently not give a correct solution when the angles involved are as large as these obtained in this analysis.

The conditions and assumptions used for the exact analysis are also pertinent to the linearized analysis. After application of the conditions and assumptions (see Appendix B) three second-order linear differential equations result. An exact solution to these equations is easily obtained on an electronic differential analyzer. The solution is again presented as a time variation of the aircraft velocities, P, Q, R, and the side-slip angle β.

The vertical tail load is computed in the same manner as for the constant angle of attack solution of Section (3)—according to Eq. (4).

Comparison

Time history solutions for the airplane velocities are available only for the constant angle of attack solution and the linearized solution. A typical case for each of the three aircraft configurations considered is given in Fig. 2. The results of both of these analyses are shown. The elevator angle has not been computed for the linearized case. It is obvious that the linearized solution, while retaining some of the essentials of the constant angle of attack solution, does not provide so accurate a solution to the attitude of the airplane. The order of error depends upon the dynamic stability of the airplane, but in general is about 25 per cent. In some cases investigated, the linearized solution predicted a dynamically stable aircraft during the maneuver, while the more exact constant angle of attack solution showed that the airplane was actually extremely unstable or divergent.

Since both other simplified methods—Kelley and $\beta = \alpha$—give values of the maximum sideslip angle during the maneuver which are the first cycle peak values, these first cycle peak values are used throughout the comparison. It is felt that the pilot will not carry the rolling pull-out maneuver much beyond the first peak values, and certainly not so far as the second peak values. Air Force criteria specify that the maneuver be considered only until a roll angle of twice the steady-state initial bank angle is attained, and Navy criteria specify a roll angle of not more than 60°, or until constant rolling velocity is attained, whichever is later. In all cases calculated for all three airplanes, the second peak of β occurred after the maximum roll angle specified in either criteria had been attained.

As the delta configuration is a recent innovation, a more extensive analysis for this type was undertaken. Of particular interest is the comparison of the four methods considered herein for this plan form. The final output of the mathematical analysis in each of

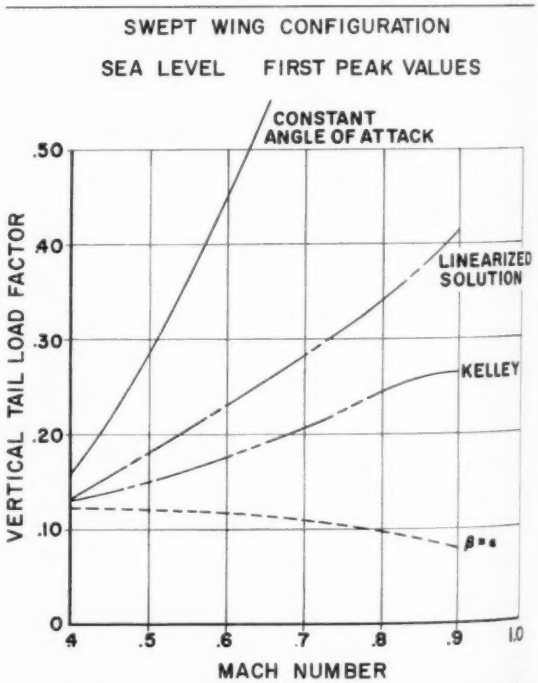

FIG. 5. Maximum vertical tail load factor during a rolling pull-out maneuver.

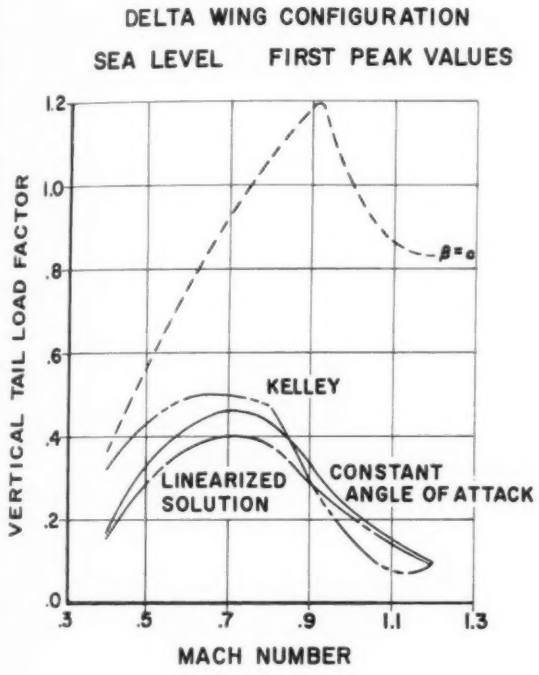

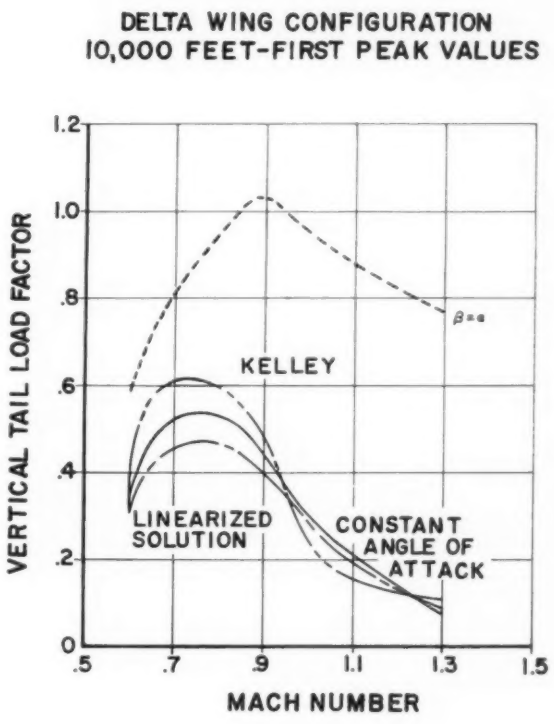

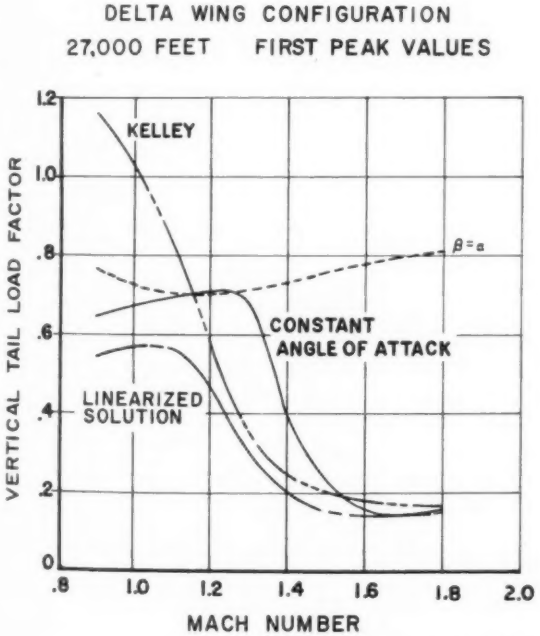

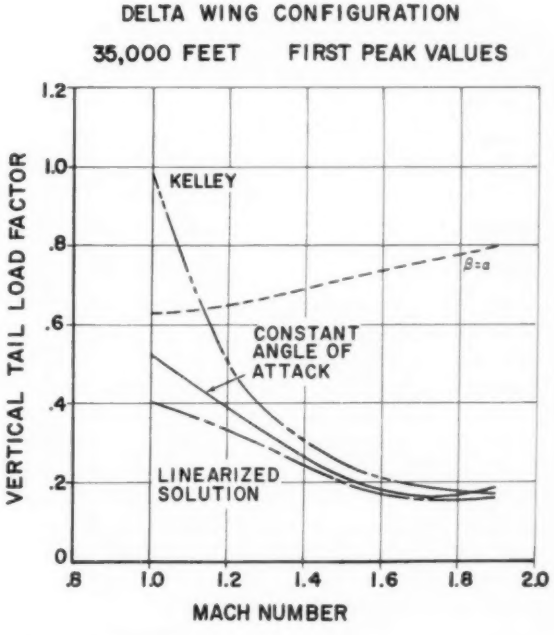

FIG. 6. Maximum vertical tail load factor during a rolling pull-out maneuver.

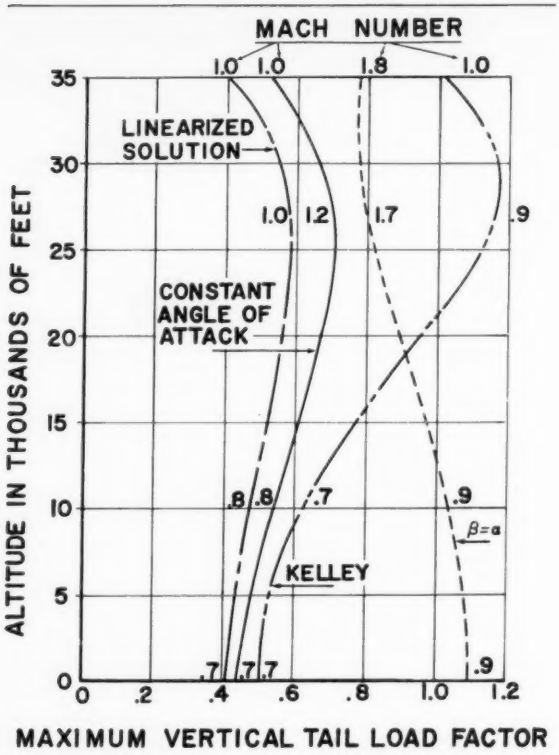

FIG. 7. Maximum vertical tail load factor during a rolling pull-out maneuver as a function of altitude for the delta-wing configuration.

the cases considered is the vertical tail angle of attack. The two simplified methods assume this is the same as the sideslip angle of the airplane, whereas the vertical tail angle of attack is actually calculated in the linearized and the constant angle of attack solutions. Fig. 3 presents this maximum vertical tail angle of attack during a rolling pull-out maneuver for the delta-wing configuration at sea level, 10,000, 27,000, and 35,000 ft. These curves are for a typical case and are representative of both the straight- and swept-wing configurations. For comparative purposes, the maximum (first peak) vertical tail load factors obtained by each of the four methods are plotted in Figs. 4, 5, and 6. From these comparisons, it may be seen that the $\beta = \alpha$ method is not universally applicable to all aircraft configurations. The swept-wing configuration, for which the best agreement was expected, has, instead, the greatest deviation from the constant load factor solution, while the straight-wing configuration shows the closest agreement with the constant load factor solution. The failure of this method to predict the vertical tail load for any aircraft may be attributed to two causes: the dynamic instability of some of these airplanes and the inherently high angle of attack characteristics of other configurations. The dynamic instability causes very large sideslip angles which were not expected in the simplified theory from which the $\beta = \alpha$ approximation was derived. On the other hand, certain configurations, such as the delta, have such inherently large angles of attack that the resulting sideslip angles are too large when compared to those obtained from the constant angle of attack solution.

The Kelley method is an improvement over the $\beta = \alpha$ method although it also suffers when the airplane has low stability or is unstable. The agreement between the Kelley method and the constant angle of attack method is better at sea level than at altitude for the delta-wing configuration since the stability decreases as the altitude increases. A plot showing the vertical tail load factor for the delta wing as a function of altitude is given in Fig. 7. The Kelley method gives a reasonable solution at sea level, but the agreement rapidly declines as the altitude increases. For the critical vertical tail design condition at 27,000 ft., the tail load from the Kelley method exceeds by 57 per cent that obtained from the constant angle of attack analysis. The critical condition also changes from a subsonic one for the Kelley method to a supersonic Mach Number for the constant angle of attack solution.

As might be expected, the linearized method of analysis is a marked improvement over the more simplified methods. However, the linearized method does not, in some cases, accurately predict the damping in the dynamic mode of oscillation. For the cases in which the damping does not become violently unstable, the linearized method may be used within an accuracy of 20 per cent.

It is felt that the constant angle of attack method of solution provides a reasonably precise representation of the airplane attitude and therefore, of the four methods presented, the most exact value of the vertical tail load. The results of this analysis indicate that the critical vertical tail load condition has no relation to any particular point on the load factor-velocity diagram.

The dynamic stability, as measured by the damping in the "Dutch roll" mode, is affected by the method of calculation. Fig. 8 shows the comparison of the time to damp to one half amplitude as computed by the constant angle of attack and the linearized method of analysis for each of the three configurations. In the transonic Mach Number region the constant angle of attack solution predicted instability, while the linearized method indicated a stable motion. Unstable motions are not plotted on the curve; however, the degree of instability increases as the altitude increases. Since damping values are difficult to measure, Fig. 8 should be regarded as an indication of the trend rather than a measure of precise values.

DISCUSSION

The accuracy of the maneuver described in this paper in simulating an actual flight maneuver is dependent on several of the assumptions made in the analysis. An implied assumption is that the pilot will continue the maneuver regardless of the accelerations developed. The side load factor experienced by the pilot is a good measure of the feasibility of using this

maneuver as a design load criteria. If the side loads are excessive, the pilot will tend to relieve the loading by reducing the aileron deflection by attempting to coordinate the rudder to reduce the sideslip, or by reducing the vertical load factor. As shown in Fig. 9, the peak side load factor of the airplane *C.G.* for all three configurations is a reasonable magnitude—when computed using the constant angle of attack solution.

The assumption most open to question is that one which assumes a constant angle of attack rather than constant elevator deflection. In the event that large elevator deflections are necessary to maintain the constant load factor, it is felt that the pilot will tend to keep the elevator fixed. In Fig. 10, the elevator time histories for several Mach Numbers for the straight- and delta-wing configurations at sea level are plotted. As can be seen from that figure, fairly large elevator deflections are required at the lower dynamic pressures. However, the change in elevator angle up to the time at which β is a maximum (first peak) is small. The effect of keeping the elevator at a constant angle will be to change the value of the pitching velocity, Q. As can be seen from the comparison of the linearized and the constant angle of attack methods, a large variation in Q does not make a very large change in the sideslip angle, β. It may be that, for configurations which have very high rates of roll, Q may appreciably affect the sideslip angle.

An important effect of maintaining constant elevator deflection which has not been investigated is its effect on the dynamic stability of the airplane. By keeping the elevator fixed, the damping and spring forces of the longitudinal degree of freedom will affect the stability of the directional degrees of freedom through the nonlinear inertial coupling. Whether the effect will be stabilizing or destabilizing is not known at this time.

An insight into one of the reasons for the failure of the more simplified methods to predict the proper tail loads may be obtained from a consideration of the dynamic stability of the airplane in question. The airplane may be likened to a simple oscillating system to which a sharp input is applied. The damping present in the system will determine the peak magnitude of the response. The abrupt manner in which the aileron deflection is applied forces the dynamic response of the airplane. The damping in the oscillating or "Dutch roll" mode will determine, to a large degree, the peak magnitude of the sideslip angle as well as the other dynamic responses of the airplane. The exact magnitude of both the steady-state and the dynamic overshoot, or peak, value of the sideslip angle will vary with the aircraft configuration being investigated.

The point to be noted here is that the linearized methods of analysis do not predict the correct value of damping in the oscillatory mode. This is evident from the observation of Figs. 2 and 8. It is seen that the inclusion of the nonlinear inertial forces reduces the damping and may, in some cases, cause instability.

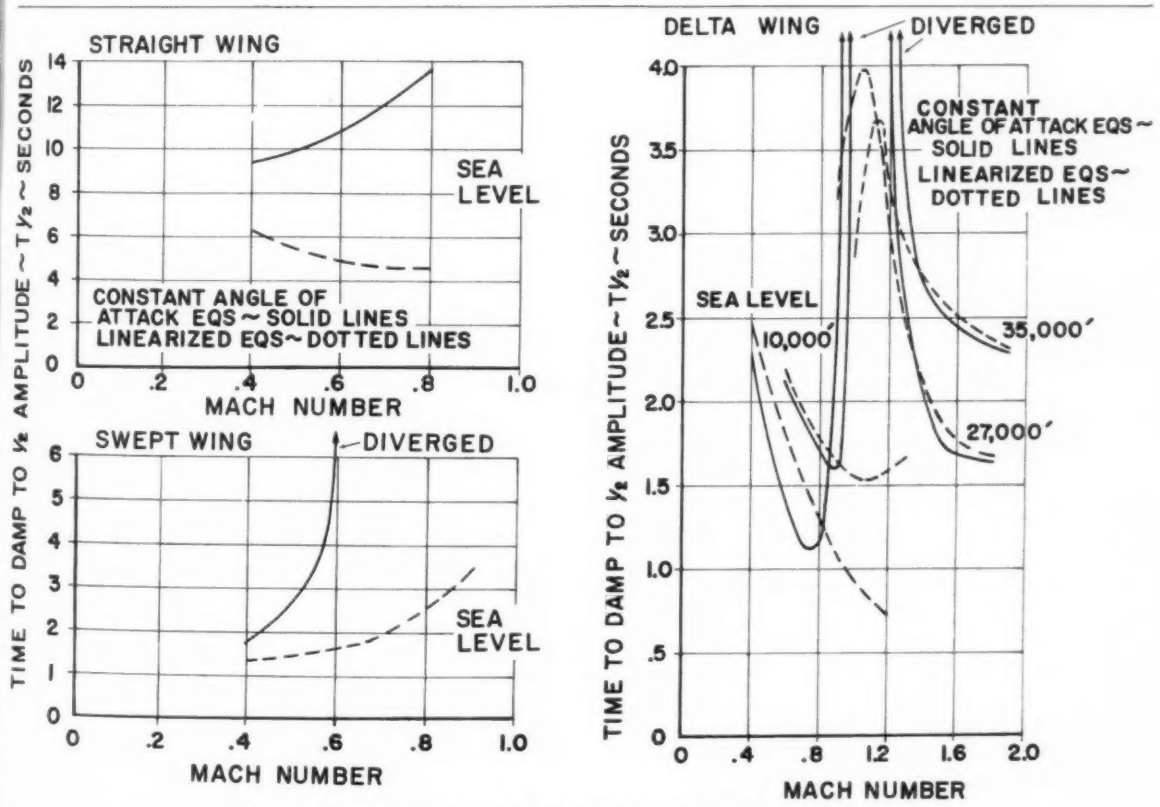

FIG. 8. Dynamic directional stability during a rolling pull-out maneuver.

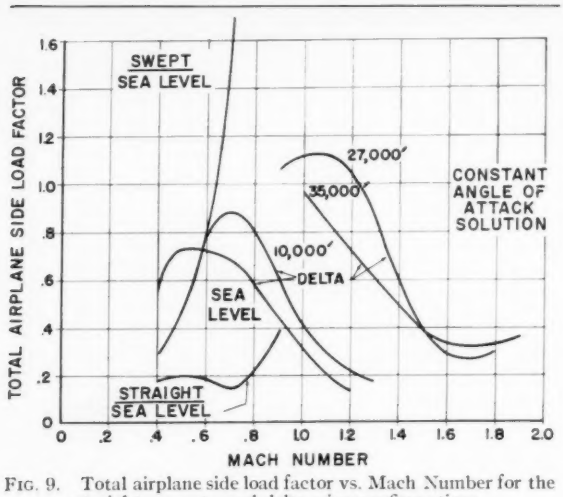

FIG. 9. Total airplane side load factor vs. Mach Number for the straight-, swept-, and delta-wing configurations.

The decrease in damping is also seen to be more severe at high altitudes. The reason for this is because the nonlinear inertial forces are not a function of altitude while the aerodynamic forces decrease with altitude. Therefore, the effects of the nonlinear inertial forces become more predominant at high altitudes.

The region in which rolling pull-out loads are usually considered critical is the subsonic speed range at low altitude. The loss of damping at altitude mentioned above makes the investigation of rolling pull-out loads necessary at high altitudes and Mach Numbers.

Recent accidents have indicated that some consideration should be given to the reduction and sometimes loss of stability in rolling pull-out maneuvers at high Mach Numbers and high altitudes. It may be that the pilot, trying to correct for this decreased stability, actually has such a reaction time lag in his movements that he is aiding the instability by his stick movements, rather than increasing the stability.

CONCLUSIONS

The significant aspects of this analysis may be generalized as follows:

(1) The simplified methods of analysis, when compared with the more precise solutions, do not provide a reliable measure of the vertical tail angle of attack, and consequently, the vertical tail load.

(2) The linearized equations do not provide a consistently accurate solution. They fail to indicate the loss in directional dynamic stability at transonic Mach Numbers and high altitudes due to the nonlinear inertial forces. Although the critical tail load may not occur in this Mach Number and altitude region, the failure of the linearized equations to provide an accurate solution precludes their use in a thorough investigation of vertical tail loads.

(3) The accuracy of the vertical tail loads obtained from the constant angle of attack analysis is felt to be comparable to the current structural design practice. This solution shows that the loss in directional dynamic stability while rolling may lead to high sideslip angles in the unstable region. This instability is caused by the nonlinear inertial forces combining with the unstable tendency of the aerodynamic derivatives in the transonic Mach Number region. Thus, critical vertical tail loads may be expected in this region due to the loss of stability.

(4) The maneuver analyzed herein does not exactly simulate an actual maneuver, in that the pilot, instead of holding constant angle of attack, may tend to keep a constant elevator deflection. It is felt that the first peak sideslip angles, if based upon a constant elevator deflection solution, would not be altered to any great extent from the values calculated herein.

Extension of this study should be made to include (1) refinements of the assumptions and conditions of the analysis, (2) further analysis of specific configurations, and (3) comparison with measured flight-test data.

REFERENCES

[1] U.S. Air Force Specification, *Stress Analysis Criteria*, R-1803-6B, April 2, 1946.

[2] U.S. Navy Specification, *Airplane Strength and Rigidity*, BuAer MIL-A-8629 (AER), August 28, 1953.

[3] U.S. Air Force Specification, *Structural Criteria, Piloted Airplanes, Basic Flight Criteria*, MIL-S-5702, December 14, 1954.

[4] Gilruth, R. R., *Analysis of Vertical Tail Loads in Rolling Pull-Out Maneuvers*, NACA Confidential Bulletin No. L4H14, August, 1944.

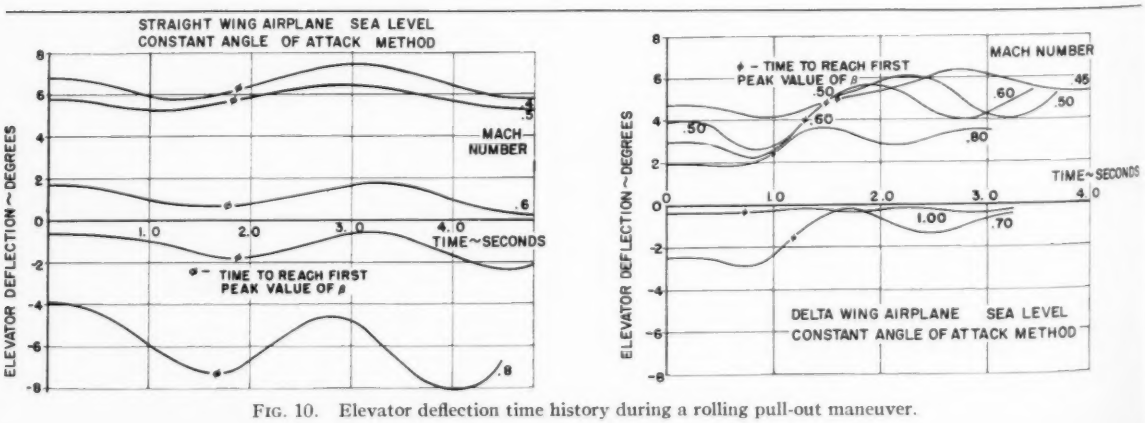

FIG. 10. Elevator deflection time history during a rolling pull-out maneuver.

[8] White, M. D., Lomax, H., and Turner, H. L., *Sideslip Angles and Vertical Tail Loads in Rolling Pull-Out Maneuvers*, NACA Technical Note 1122, April, 1947.

[9] Kelley, J., *Vertical Tail Loads*, U.S.A.F. A.M.C. Memo. Report MCREXA8-4515-12-3, April 7, 1948.

[7] Stone, R. W., *Estimation of the Maximum Angle of Sideslip for Determination of Vertical-Tail Loads in Rolling Maneuvers*, NACA Tech. Report 1136, 1953.

[8] Etkin, B., and Collette, J. G. R., *Vertical-Tail Loads in the Rolling Pull-Out Maneuvers*, Inst. of Aerophysics, U. Toronto, UTIA Report No. 28, January 1, 1954.

[9] Neihouse, A. I., *Effect of Current Design Trends on Airplane Spins and Recoveries*, NACA Research Memo. L52A09, January, 28, 1952.

[10] Perkins, C. D., and Hage, R. E., *Airplane Performance Stability and Control*, First Ed.; John Wiley & Sons, Inc., 1949.

[11] *Dynamics of the Airframe*, BuAer Report AE-61-411, September, 1952.

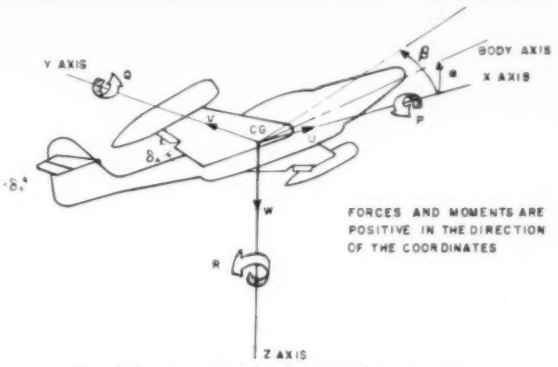

FIG. A-1. Standard NACA coordinate system.

APPENDIX A

Equations of Motion for the Constant Angle of Attack Solution

The Eulerian equations of motion for an airplane with symmetry about the xz plane are (the standard NACA coordinate system is used, Fig. A-1):

$$\left.\begin{aligned} X &= m\,(\dot{U} + QW - RV) \\ Y &= m\,(\dot{V} + RU - PW) \\ Z &= m\,(\dot{W} + PV - QU) \\ L &= I_x\dot{P} - I_{xz}\dot{R} + (I_z - I_y)\,QR - I_{xz}\,PQ \\ M &= I_y\dot{Q} + I_{xz}\,(P^2 - R^2) + (I_x - I_z)\,RP \\ N &= I_z\dot{R} - I_{xz}\dot{P} + I_{xz}QR + (I_y - I_x)\,PQ \end{aligned}\right\} \quad (1a)$$

These equations define the instantaneous angular and linear velocities of the *C.G.* with respect to a coordinate system attached to the airplane and moving with it.

The angular relationship that exists between the moving coordinate system at any time and a fixed reference in space, without regard to the distance the moving system has moved from the reference, is given by means of the Eulerian angles. They are, in order of their application,

ψ = yaw of the airplane—positive nose right
γ = pitch of the airplane—positive nose up
φ = roll of the airplane—positive left wing up

The coordinate transformation that expresses the angular relationship between the moving and fixed coordinate system is as follows:

$$\begin{bmatrix} x \\ y \\ z \end{bmatrix} = \begin{bmatrix} \cos\psi\cos\gamma & \cos\gamma\sin\psi & -\sin\gamma \\ \begin{matrix}-\cos\varphi\sin\psi \\ +\sin\varphi\sin\gamma\cos\psi\end{matrix} & \begin{matrix}\cos\psi\cos\varphi \\ +\sin\varphi\sin\gamma\sin\psi\end{matrix} & \sin\varphi\cos\gamma \\ \begin{matrix}\sin\varphi\sin\psi \\ +\cos\varphi\cos\psi\sin\gamma\end{matrix} & \begin{matrix}-\sin\varphi\cos\psi \\ +\cos\varphi\sin\gamma\sin\psi\end{matrix} & \cos\varphi\cos\gamma \end{bmatrix} \begin{bmatrix} x' \\ y' \\ z' \end{bmatrix} = T_1 \begin{bmatrix} x' \\ y' \\ z' \end{bmatrix} \quad (2a)$$

The time rates of change of the Eulerian angles, which are not orthogonal, are

$$\begin{bmatrix} \dot{\psi} \\ \dot{\gamma} \\ \dot{\varphi} \end{bmatrix} = \begin{bmatrix} 0 & \dfrac{\sin\varphi}{\cos\gamma} & \dfrac{\cos\varphi}{\cos\gamma} \\ 0 & \cos\varphi & -\sin\varphi \\ 1 & \tan\gamma\sin\varphi & \tan\gamma\ \cos\varphi \end{bmatrix} \begin{bmatrix} P \\ Q \\ R \end{bmatrix} \quad (3a)$$

Applying the assumptions and conditions set forth in the analysis, the first and fifth Eulerian equations—the drag and pitching moment equations—are set aside. The condition of constant load factor allows $W = \dot{W} = 0$. The Eulerian Eqs. (1a) then become

$$\left.\begin{aligned} Y &= m\,(\dot{V} + RU) \\ Z &= m\,(PV - QU) \\ L &= I_x\dot{P} - I_{xz}\dot{R} + (I_z - I_y)\,QR - I_{xz}\,PQ \\ N &= I_z\dot{R} - I_{xz}P + I_{xz}\,QR + (I_y - I_x)\,PQ \end{aligned}\right\} \quad (4a)$$

The external forces and moments—Y, Z, L, and N—are composed of thrust, aerodynamic, and weight forces. The aerodynamic and thrust forces may be defined in terms of the velocities measured with respect to the coordinate system moving with the airplane. The principal aerodynamic and thrust forces considered in this analysis are

$$\left.\begin{aligned} Y_A &= q_d S\left[C_{y\beta}\beta + C_{yr}\frac{Rb}{2U_0} + C_{yP}\frac{Pb}{2U_0}\right] \\ Z_A &= n\,m\,g \\ L_A &= q_d Sb\left[C_{l\beta}\beta + C_{lr}\frac{Rb}{2U_0} + C_{lP}\frac{Pb}{2U_0} + C_{l\delta_A}\delta_A\right] \\ N_A &= q_d Sb\left[C_{n\beta}\beta + C_{nr}\frac{Rb}{2U_0} + C_{np}\frac{Pb}{2U_0} + C_{n\delta_A}\delta_A\right] \end{aligned}\right\} \quad (5a)$$

The weight forces must be referred to the fixed coordinate system so that the proper direction of the gravity vector is maintained. The original position ($t = 0$) of the moving coordinated system is coincident

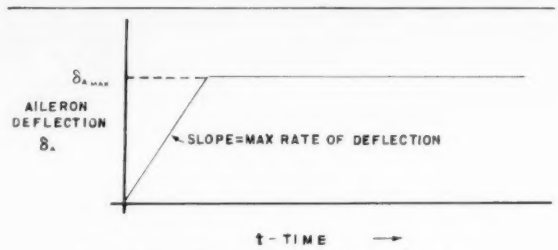

FIG. A-2. Aileron deflection forcing function.

with the fixed reference system which is in a banked position. This initial condition is such that the x axis is level and the y and z axes are rotated from the horizontal and vertical by an angle Φ_0. The components of the weight force in this position are

$$\left.\begin{aligned} X_w &= 0 \\ Y_w &= mg \sin \Phi_0 \\ Z_w &= mg \cos \Phi_0 \end{aligned}\right\} \tag{6a}$$

The weight force components at any subsequent time are transformed by the same transformation as the coordinates.

$$\begin{bmatrix} X_w \\ Y_w \\ Z_w \end{bmatrix} = T_1 \begin{bmatrix} 0 \\ mg \sin \Phi_0 \\ mg \cos \Phi_0 \end{bmatrix} \tag{7a}$$

After inserting the external forces and solving for the first derivatives, the Eulerian Eqs. (4a) become

$$\left.\begin{aligned} \frac{\dot\beta}{\cos^2 \beta} &= -R + \frac{q_d S}{mU_0}\left[C_{y\beta}\beta + C_{yr}\frac{Rb}{2U_0} + C_{yp}\frac{Pb}{2U_0}\right] + \frac{g}{U_0} \\ &\quad [(\cos\varphi\cos\psi + \sin\varphi\sin\gamma\sin\psi)\sin\Phi_0 + \sin\varphi\cos\gamma\cos\Phi_0] \\ Q &= P\tan\beta + \frac{ng}{U_0} - \frac{g}{U_0}[\cos\varphi\cos\gamma\cos\Phi_0 - (\sin\varphi\cos\psi - \cos\varphi\sin\gamma\sin\psi)\sin\Phi_0] \\ \dot P &= (I_z I_y - I_z^2 - I_{xz}^2)\frac{RQ}{I} + \left[(I_z + I_x - I_y)\frac{I_{xz}}{I}\right]PQ + \frac{q_d Sb}{I}\left[(I_z C_{lp} + I_{xz}C_{np})\frac{Pb}{2U_0} + \right. \\ &\quad \left. (I_z C_{lr} + I_{xz}C_{nr})\frac{Rb}{2U_0} + (I_z C_{l\beta} + I_{xz}C_{n\beta})\beta + (I_z C_{l\delta_A} + I_{xz}C_{n\delta_A})\delta_A\right] \\ \dot R &= \left[(I_y - I_z - I_x)\frac{I_{xz}}{I}\right]RQ + (I_{xz}^2 + I_z^2 - I_z I_y)\frac{PQ}{I} + \frac{q_d Sb}{I}\left[(I_{xz}C_{lp} + I_z C_{np})\frac{Pb}{2U_0} + \right. \\ &\quad \left. (I_{xz}C_{lr} + I_z C_{nr})\frac{Rb}{2U_0} + (I_{xz}C_{l\beta} + I_z C_{n\beta})\beta + (I_{xz}C_{l\delta_A} + I_z C_{n\delta_A})\delta_A\right] \end{aligned}\right\} \tag{8a}$$

where $\beta = \tan^{-1} V/U_0$ and $I = I_z I_x - I_{xz}^2$

Together with the Eq. (3a), the above equations form six first-order, nonlinear, differential equations. The independent variables are β, P, R, ψ, γ, and φ.

The rolling pull-out maneuver is initiated from a coordinated banked turn. The initial conditions for the set of Eqs. (8a) and (3a) are those prevailing in a banked turn.

$$\left.\begin{aligned} \Phi_0 &= \cos^{-1}(1/n) \\ R &= (g/U_0)\sin\Phi_0 \\ Q &= (ng/U_0) - (g/U_0)\cos\Phi_0 \end{aligned}\right\} \tag{9a}$$

In addition, $P = \dot P = \beta = \dot\beta = 0$. The initial values of the Eulerian angles are zero, $\psi_0 = \gamma_0 = \varphi_0 = 0$. Constant aerodynamic trim forces are put into the equations so that the initial conditions $\dot P = \dot R = \beta = 0$ are satisfied. The aileron deflection serves as the forcing function and is of the form shown in Fig. A-2.

A simple numerical method of integration was used to solve the equations. The first two terms of a Taylor's expansion of the independent variables was used to give the variables at time $= (k + 1)\,\Delta t$ in terms of the variables and their derivatives at time $= k\Delta t$. For example,

$$\beta_{t=(k+1)\Delta t} = \beta_{t=k\Delta t} + \Delta t \cdot \dot\beta_{t=k\Delta t}$$

The derivatives at time $= k\Delta t$ may be computed from Eqs. (8a) and (3a) starting with the initial conditions, Eq. (9a).

APPENDIX B

Linearized Equations of Motion

The method of small perturbations is used to linearize the Eulerian equations of motion. Since the initial condition for the maneuver considered in this paper is an accelerated flight condition the equations are linearized about the initial conditions. The initial values of the variables in a banked turn are given in Eqs. (9a). The variables are

$$\left.\begin{aligned} U &= U_0 \\ V &= v \approx U_0\beta \\ W &= O \\ P &= p \\ Q &= Q_0 + q \\ R &= R_0 + r \end{aligned}\right\} \tag{1b}$$

After substitution, the Eulerian equations become

$$\left.\begin{aligned} X &= m(R_0 + r)U_0\beta \\ Y &= m(\dot\beta + R_0 + r)U_0 \\ Z &= m(p\beta - Q_0 - q)U_0 \\ L &= I_x\dot p - I_{xz}\dot r + (I_z - I_y)(Q_0r + R_0q + Q_0R_0 + rq) - I_{xz}(pQ_0 + pq) \\ M &= I_y\dot q + I_{xz}[p^2 - (R_0 + r)^2] + (I_x - I_z)(R_0p + pr) \\ N &= I_z\dot r - I_{xz}\dot p + I_{xz}(Q_0R_0 + Q_0r + R_0q + rq) + (I_y - I_x)(Q_0p + qp) \end{aligned}\right\} \tag{2b}$$

Assuming the perturbations are small, the product of perturbations may be neglected. Since the motion is restricted to small deviations from the initial conditions, the Eulerian angles are also assumed to be small so that sines are equal to the angles and cosines are equal to one. The relationships between the time rate of change of the Eulerian angles and P, Q, and R, are simplified, due to the above considerations, to the following equations:

$$\left.\begin{aligned} p &= \dot\varphi \\ Q_0 + q &= \dot\Gamma_0 + \dot\gamma \\ R_0 + r &= \Psi_0 + \dot\psi \end{aligned}\right\} \tag{3b}$$

Setting aside the drag and pitching moment equations according to the assumptions and conditions of the analysis, the Eulerian equations become

$$\left.\begin{aligned} &mU_0(\dot\beta + \Psi_0 + \dot\psi) = q_dS\{C_{y\beta}\beta + C_{y_r}[(\Psi_0 + \dot\psi)b/2U_0] + C_{y_p}(\dot\varphi b/2U_0)\} + mg(\sin\Phi_0 + \varphi\cos\Phi_0) \\ &-mU_0(\dot\Gamma_0 + \dot\gamma) = -n\,mg + mg(\cos\Phi_0 - \varphi\sin\Phi_0) \\ &I_x\ddot\varphi - I_{xz}\ddot\psi + (I_z - I_y)(\Gamma_0\dot\psi + \Psi_0\dot\gamma) - I_{xz}\dot\Gamma_0\dot\varphi + (I_z - I_y)\dot\Gamma_0\Psi_0 = \\ &\qquad q_dSb\{C_{l\beta}\beta + C_{l_p}(\dot\varphi b/2U_0) + C_{l_r}[(\Psi_0 + \dot\psi)b/2U_0] + C_{l\delta_A}\delta_A\} \\ &I_z\ddot\psi - I_{xz}\ddot\varphi + I_{xz}(\dot\Gamma_0\dot\psi + \Psi_0\dot\gamma + \dot\Gamma_0\dot\Psi_0) + (I_y - I_x)\Gamma_0\dot\varphi = q_dSb\{C_{n\beta}\beta + C_{n_p}(\dot\varphi b/2U_0) + \\ &\qquad C_{n_r}[(\Psi_0 + \dot\psi)b/2U_0] + C_{n\delta_A}\delta_A\} \end{aligned}\right\} \tag{4b}$$

At $t = 0$ the initial values of Φ_0, $\dot\Gamma_0$, and Ψ_0 are

$$\left.\begin{aligned} \Phi_0 &= \cos^{-1}1/n \\ \dot\Gamma_0 &= (ng/U_0) - (g/U_0)\cos\Phi_0 \\ \Psi_0 &= (g/U_0)\sin\Phi_0 \end{aligned}\right\} \tag{5b}$$

The initial values of the forces and moments in the banked turn are in balance so the initial forces and moments do not appear in the equations. The small aileron and rudder trim forces necessary to maintain this balance are not indicated. The equations expressing the change from the initial conditions are

$$\left.\begin{aligned} &mU_0(\dot\beta + \dot\psi) = q_dS[C_{y\beta}\beta + C_{y_r}(\dot\psi b/2U_0) + C_{y_p}(\dot\varphi b/2U_0)] + mg\,\varphi\sin\Phi_0 \\ &mU_0\dot\gamma = mg\,\varphi\sin\Phi_0 \\ &I_x\ddot\varphi - I_{xz}\ddot\psi + (I_z - I_y)(\Gamma_0\dot\psi + \Psi_0\dot\gamma) - I_{xz}\Gamma_0\dot\varphi = q_dSb[C_{l\beta}\beta + C_{l_r}(\dot\psi b/2U_0) + C_{l_p}(\dot\varphi b/2U_0) + C_{l\delta_A}\delta_A] \\ &I_z\ddot\psi - I_{xz}\ddot\varphi + I_{xz}(\dot\Gamma_0\dot\psi + \Psi_0\dot\gamma) + (I_y - I_x)\dot\Gamma_0\dot\varphi = q_dSb[C_{n\beta}\beta + C_{n_r}(\dot\psi b/2U_0) + C_{n_p}(\dot\varphi b/2U_0) + C_{n\delta_A}\delta_A] \end{aligned}\right\} \tag{6b}$$

These equations consist of two second-order and one first-order differential linear equations which may be solved on an electronic differential analyzer. The aileron deflection is the forcing function, and its shape is shown in Fig. A-2.

The Design and Testing of Supersonic Flutter Models*

JOHN F. McCARTHY, JR.,† AND ROBERT L. HALFMAN‡
Massachusetts Institute of Technology

SUMMARY

The basic problems of flutter testing in the low supersonic speed range (Mach Number 1.2–2.1) are outlined. The requirements for models which simulate full-scale airplanes when Mach Number is included as a parameter are reviewed and are compared with those where velocity is scaled so that flutter occurs in the range of a low-speed wind tunnel.

A particular type of construction for supersonic flutter models is described in detail. Methods of vibration testing, static testing, and flutter testing are discussed. Particular emphasis is placed on the technique of varying flow parameters rather than model parameters to precipitate flutter. The tool for varying flow parameters is the variable Mach Number supersonic test section of the Massachusetts Institute of Technology Blowdown Wind Tunnel. The aerodynamic features of the supersonic test section are presented.

SYMBOLS

b	=	semichord of wing
c	=	wing chord
c.g.	=	chordwise center of gravity location as fraction of chord
e.a.	=	chordwise elastic axis location as fraction of chord
EI	=	bending stiffness
GJ	=	torsional rigidity
I_α	=	moment of inertia in pitch per unit span
J	=	torsion constant
k	=	reduced frequency, $\omega b/V$
L	=	length
m	=	mass of wing per unit span
M	=	Mach Number
P_r	=	Prandtl Number
r_α	=	dimensionless radius of gyration in pitch, $\sqrt{I\alpha/mb^2}$
RN	=	Reynolds Number
t	=	time
t	=	maximum thickness of airfoil
T	=	absolute temperature
V	=	velocity
γ	=	ratio of specific heats
μ	=	mass ratio $m/\rho b^2$
ρ	=	air density
ω	=	flutter frequency
ω_α	=	torsional frequency

Subscripts

A	=	airplane
M	=	model
0	=	wing root

Presented at the Aeroelasticity Session, Twenty-Third Annual Meeting, IAS, New York, January 24–27, 1955.

* The paper presents some of the research performed at the Aeroelastic and Structures Research Laboratory, Massachusetts Institute of Technology, under sponsorship of the Dynamics Branch, Aircraft Laboratory, WADC, USAF, under Contract No. AF33(038)-22955.

† Formerly, Senior Engineer, Aeroelastic and Structures Research Laboratory. Now, Operations Analyst, Headquarters, Strategic Air Command.

‡ Associate Professor, Department of Aeronautical Engineering.

INTRODUCTION

THE PHENOMENON OF FLUTTER, the self-excited oscillation of an elastic structure in an air stream, appeared early in the development of aircraft. At first, designers could apply only crude corrective measures, and it was not until the early 1930's that aeronautical scientists were able to fashion promising theoretical approaches to the problem of flutter. Although experimental work lagged behind the theoretical attack, the flutter problem in incompressible flow had become quite tractable by the end of the second World War. Both the theoretical and experimental approaches were well developed and understood. Until the advent of transonic and supersonic aircraft, these techniques were adequate for the airplane designer.

Unfortunately, the trend towards higher speeds, increased structural flexibility, and lower aspect ratio lifting surfaces as well as the growing use of large external stores so aggravate the flutter problem that is it now often a primary design consideration rather than an occurrence that can be remedied fairly easily. Because of the questionable reliability of existing methods of flutter analysis in the high-speed range, the airplane designer calls on the experimentalist to provide data that are immediately useful and that can be used to confirm theory. Much has already been done in the transonic range using rockets, bombs, sleds, and wind tunnels. It is the purpose of this paper to review the problems associated with flutter testing in the supersonic speed range and to present some of the solutions which have proved useful.

MODEL THEORY

The dimensionless answers which one hopes to obtain from a model test are the values of M, k, and ω/ω_α at flutter and the flutter mode shape. In order to achieve these answers, the flutter model must simulate the aerodynamic shape and the distributions of mass and stiffness of the full-scale airplane. For bare wings of reasonably large aspect ratio, this simulation can be expressed in terms of certain dimensionless parameters at every spanwise station of the model. These dimensionless parameters, which can be derived from basic flutter theory,[1, 4] are as follows:

b/b_0; m/m_0, c.g., r_α; $EI/(EI)_0$, $GJ/(GJ)_0$, e.a.

Although airfoil shape is easily simulated, it is probably of secondary importance in the flutter problem. For wings where chordwise deformations are appreciable, the chordwise as well as the spanwise distributions of mass and stiffness must be simulated. If the distributions of mass and stiffness are properly matched according to model theory, it follows that the natural frequencies and mode shapes are also matched. For the structural damping coefficients, the model designer can hope only to obtain the correct order of magnitude in his final product through his choice of structural materials.

The dimensionless parameters related to the flow are μ and M. The additional parameters, RN, P_r, and γ, are probably of secondary importance and, except for γ, cannot usually be simulated. The designer achieves the highest Reynolds Number possible by using as large a scale model and as high a fluid density as practical. He has little or no control over the Prandtl Number.

Once the dimensionless parameters of the problem have been fixed, the designer turns to model theory to obtain dimensional design quantities for the model. Corresponding to the three primary scale factors, length, mass, and time, the designer can choose to satisfy only three independent design limitations. The length scale factor is usually determined by the size of the wind tunnel or by the available space for installation if the tests are to be conducted in the atmosphere. The density of the gas in which the model must be tested determines the mass scale factor between airplane and model since μ must be simulated. The speed range of the wind tunnel—or, for high-speed testing, duplication of Mach Number at a reasonable gas temperature—determines the time scale. From these primary scale factors the designer can calculate the scale factors and thus the model values for running mass, bending stiffness, etc.

At this point, the primary difference between high-speed and low-speed flutter models becomes apparent. For low-speed flutter models, the time scale between model and airplane is determined by the length and velocity ratios

$$t_M/t_A = (L_M/L_A)(V_A/V_M)$$

Both these ratios are determined by properties of the low-speed wind tunnel and are of the same order of magtude. For example, a velocity ratio of 1/10 could be used for a 1/10-scale model which simulates a fighter whose maximum speed is 500 m.p.h. and which is to be tested in a wind tunnel with a maximum speed of 90 m.p.h. Therefore, the frequencies of the model are of the same order of magnitude as the frequencies of the airplane. The resulting model is very flexible in order to obtain the low natural frequencies required. Most of the model's weight is concentrated in nonstructural elements which the designer concentrates on making light so that there is enough disposable mass to obtain the necessary mass and inertial properties.

For high-speed flutter models, duplication of Mach Number between model and airplane necessitates a different order of magnitude for the time ratio,

$$t_M/t_A = (L_M/L_A)\sqrt{T_M/T_A}$$

The temperature ratio is usually approximately one so that the frequencies of the model are larger than the frequencies of the airplane by a factor almost equal to the length ratio. Thus high-speed flutter models must be stiff in order to obtain the very high natural frequencies required. Space limitations, caused by very thin wings, further aggravate the designer's problems.

Another problem associated with high-speed flutter testing has been the difficulty in saving models. It has already been shown that the time scale for the high-speed case is much higher than for the low-speed case so that there is much less time to save the model from damage. It can also be shown that the stress level from airplane to model is decreased for the low-speed case and is increased for the high-speed case.

Model Design

A simple construction of balsa, aluminum, and lead (Fig. 1) has proved useful for supersonic flutter tests at M.I.T. The balsa gives the desired aerodynamic shape. The airloads are transmitted by the balsa to the aluminum spar, whose dimensions, b and h, can be varied to control the torsional rigidity and the bending stiffness of the model, and whose chordwise location, d, determines the elastic axis position. 75ST aluminum alloy was selected for the spar because it is light and strong. Also its yield strength is close to its ultimate strength, and thus a maximum linear range is available. The rectangular cross section allows for ease of computation during the design and ease of fabrication in the shop. Two pairs of strain gages are mounted on the spar for use in the vibration and flutter tests; one pair along the elastic axis to pick up bending, and the other at 45° to the elastic axis to pick up torsion. Lead weights, fore and aft of the spar, are designed so as to give the desired mass and inertial properties at each spanwise station. The lead is slit before gluing so that its contribution to the model's stiffness is negligible.

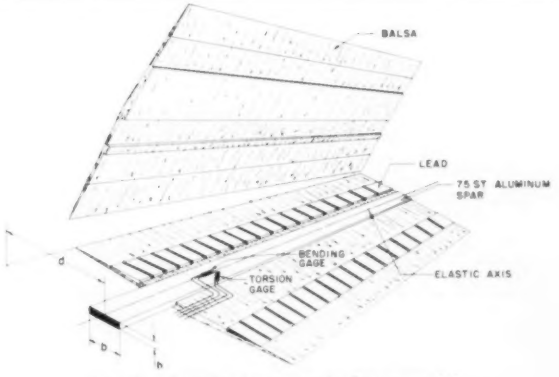

Fig. 1. A typical supersonic flutter model.

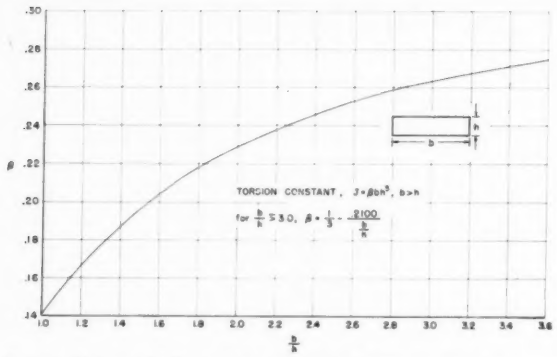

FIG. 2. Values of β for torsion constant of solid rectangular cross section.

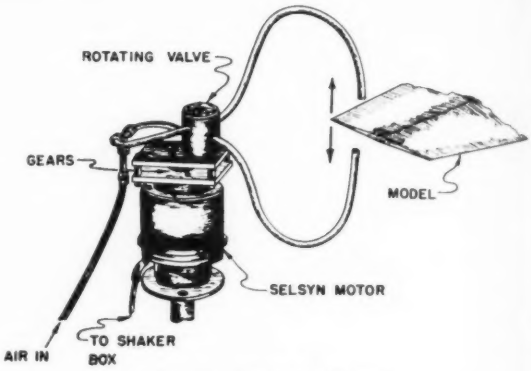

FIG. 5. Air jet shaker unit.

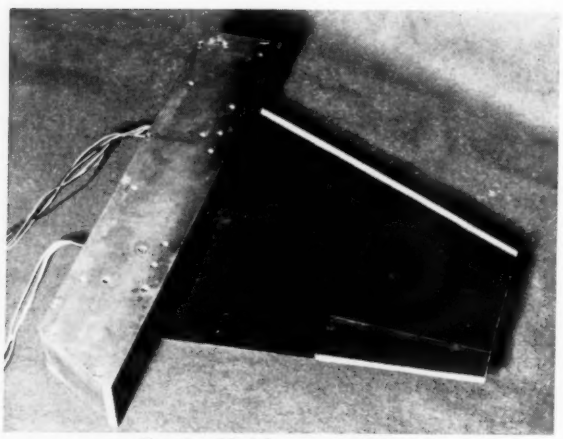

FIG. 3. Model mounted in box.

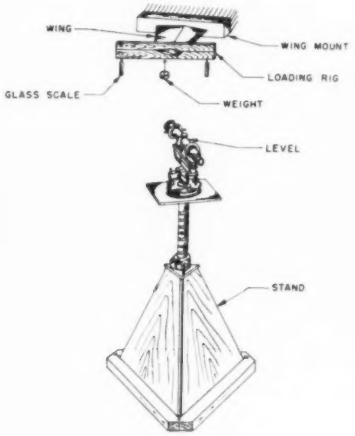

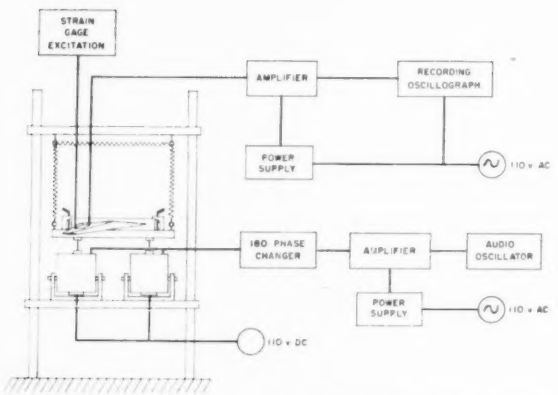

FIG. 4. Setup for vibration test using electromagnetic shaker.

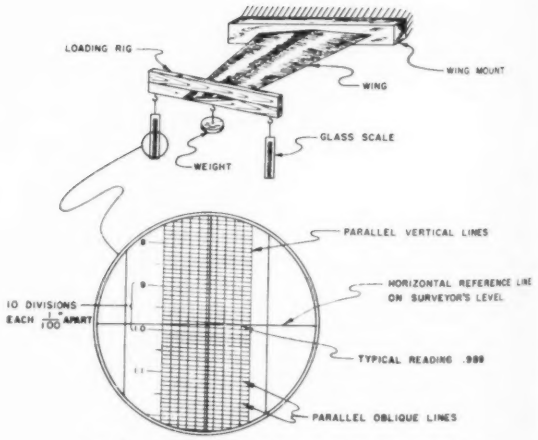

FIG. 6. Setup for static test using glass scales.

In this design, most of the model's stiffness is concentrated in the spar. It has been found that the bending stiffness of the model can be obtained adequately by summing that of the spar and the balsa cross sections. The torsional rigidity is about 5 per cent above that obtained by summing the contributions of the balsa and the aluminum. This increase is probably due to the glue. In computing the sectional properties, the torsion constant of the spar is obtained from Fig. 2.[5] The formula

$$J = (1/6)ct^3$$

can be used to obtain the torsion constant of the balsa since $t \ll c$. In the computations it is convenient to treat the airfoil section as made up entirely of balsa and to take account of the balsa cutouts by using fictitious values for the properties of aluminum and lead. The moduli of elasticity and rigidity of the aluminum are decreased by those of the balsa, and the density of the lead is decreased by that of the balsa.

The model is constructed so that the aluminum spar extends beyond the wind root chord (Fig. 1). Hardwood blocks are glued to the balsa and lead sections of the wing root chord, and the entire assembly is mounted at zero angle of attack in a rectangular steel box which is open on one side. In order to insure a good cantilever mount, the box is then filled with Cerrobend, a metal with a low melting point (158°F.), which expands on setting because of its antimony content (Fig. 3). The box with the model is held in the aluminum model-mount by a series of set screws (Fig. 9). Since the steel boxes are easily built, each wing to be tested can be installed in a box before the tests begin, and rapid change-over is possible during the testing period.

Vibration Tests

The heavy model-mount also aids in the vibration tests in which the method of support and the means of excitation must not affect the natural frequencies of the wing. The model and mounting block are mounted on very soft springs (Fig. 4) so that the frequency of the model with its support is far below any natural frequency of the wing. The massive mounting block thus simulates a cantilever root condition for the model. It is excited by two electromagnetic shakers which can be driven either in phase or out of phase, whose frequency is controlled by an audio oscillator, and whose force is controlled by the gain of an amplifier. The signals from the strain gages, which are fed into a recording oscillograph, are used to detect resonance visually since they increase greatly when the frequency of excitation passes through a natural frequency of the wing. Quantitative measurements of frequency and structural damping are obtained by suddenly cutting the excitation and studying the decay of the strain-gage signals on oscillograph records (see p. 103 ff., reference 4). Structural damping coefficients on the order of 0.02 are achieved for the model design described above.

At the lower frequencies it is sometimes inconvenient to apply shaking forces through a softly supported root mass, and other means of excitation must be used. Alternating air jets (Fig. 5), whose frequency is controlled by a selsyn motor and whose exciting force is controlled by the air pressure, have proved satisfactory up to 200 cycles per sec.[6]

Static Tests

In the static tests, which provide a check on stiffness simulation, the measuring devices must not exert disturbing forces on the wing. A useful optical deflection-measuring arrangement, which gives accuracies of ± 0.001 in., consists of a surveyors' level sighted on glass scales attached to the wing or to the loading rig (Fig. 6). When greater accuracy is needed, an electromagnetic scheme is used to record deflections. Schaevitz coils (linear variable differential transformers) are attached to the wing by flexures at the measuring points (Fig. 7). The voltage output of the measuring coil is matched to that of a master coil by a null-balancing servo drive. The master coil is attached to a dial gage so that deflections are indicated directly if the sensitivities of the measuring and master coils are equal. When several measuring coils are used simultaneously, a switch box can be employed for rapid reading. With this system, deflections can be measured to an accuracy of ± 0.0002 in

Flutter Tests

Apart from the basic design of the models, the chief difference between low-speed flutter models and those to be tested at supersonic speeds in the wind tunnel lies in the aerodynamic problems involved. In incompressible testing, the model flutters when the flow velocity is raised to the flutter velocity. In supersonic flow the Mach Number in the test section is a function only of the geometry of the nozzle, and the velocity is a function only of stagnation temperature. A variable geometry nozzle is required to produce significant changes in flow properties. If a nozzle of fixed geometry were used for flutter testing, the Mach Number in the test section would be fixed, and the model would either remain stable or flutter violently when it was inserted into the air stream. Practically no information would result about the location of the neutrally stable flutter condition. In either event, a series of modification to the model would normally have to be tried in order to bracket closely the desired flutter condition. On the other hand, a nozzle of variable geometry would permit a gradual changing of flow conditions until flutter is encountered and thus produce a maximum amount of useful information with a minimum number of expensive models.

In order that flutter could be approached from a stable flow condition as in the subsonic case, a variable Mach Number supersonic test section was constructed. This test section was designed to be interchangeable with a transonic one in the M.I.T. Blowdown Wind Tunnel. The nozzle is of the asymmetric sliding-block

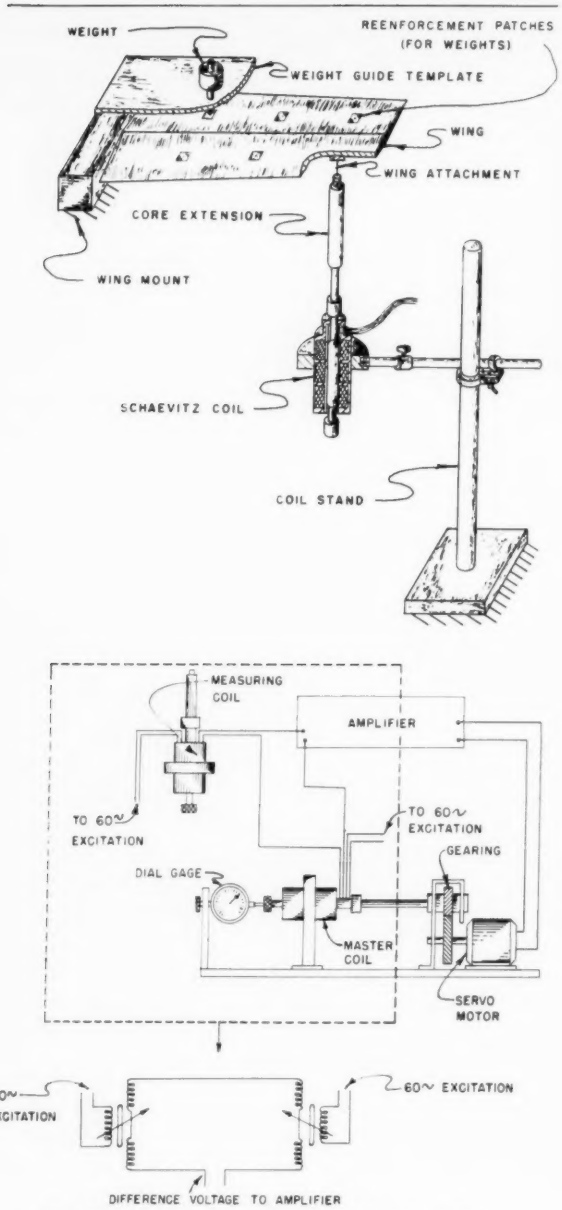

FIG. 7. Setup for static test using Schaevitz coils.

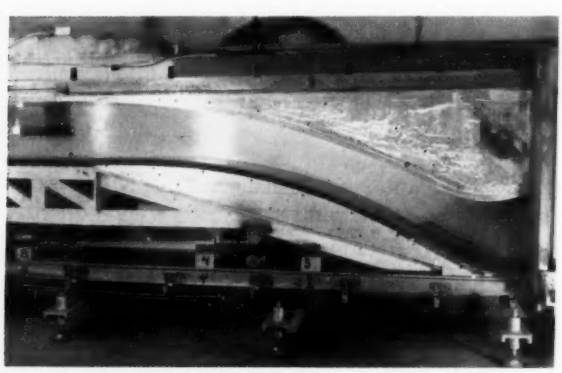

FIG. 8. Variable Mach Number supersonic nozzle.

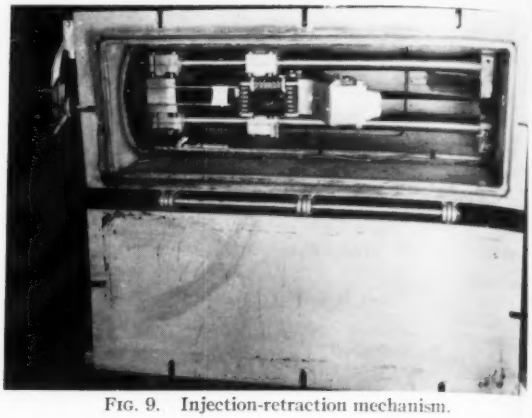

FIG. 9. Injection-retraction mechanism.

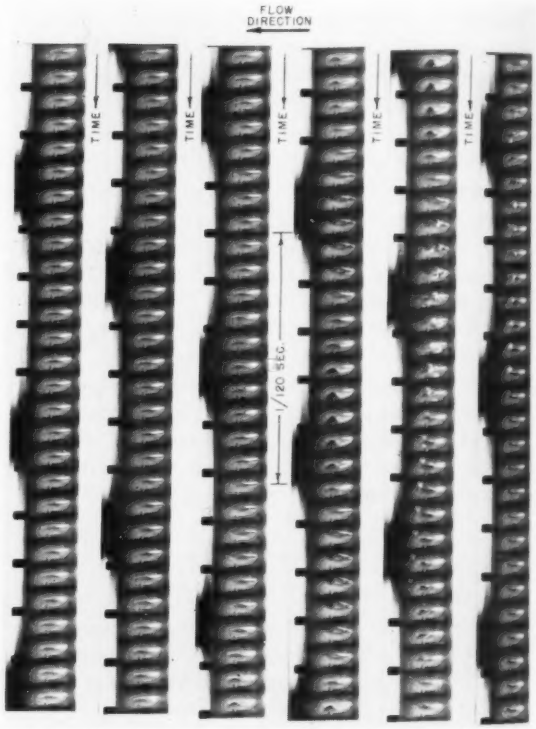

FIG. 10. Some high-speed movies at supersonic flutter.

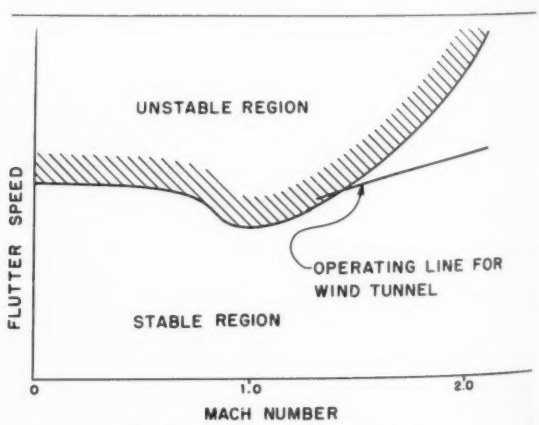

FIG. 11. Possible flutter boundary.

type (Fig. 8), and the Mach Number can be varied through the complete range of the tunnel (1.25–2.10) during a run by moving the sliding block through its travel of 17 in., without any change in the dimensions of the test section (14 by 25 in.). A running time of approximately 35 sec. is available with a 40,000-cubic-ft. reservoir at an initial pressure of 30 lbs. per sq.in. gage. The Reynolds Numbers are on the order of nine million per ft. of reference length. Flow surveys indicate that the flow is very nearly two-dimensional throughout the entire Mach Number range.

The fairly rapid rate of change of Mach Number possible (more than $0.15M$ per sec.) may raise the question of unsteady aerodynamic effects. But if one considers the number of chord lengths of flow, which is a criterion for such unsteady effects, it can readily be seen why there is no problem in this regard. For example, in terms of chord lengths of flow, a running time of 35 sec. at a Mach Number of 1.7 in this test section is equivalent to about 10 min. of running time at 60 m.p.h. Alternatively, at least 100 chord lengths of flow pass over an average semispan wing for each 0.01 change in Mach Number.

Another problem associated with flutter testing in the supersonic speed range is the starting shock which originates in the nozzle throat and moves downstream past the test section. If a flexible model were subjected to the starting shock, it would be destroyed. Therefore, the model is injected into the air stream after supersonic flow is established. This condition is detected by a static cone located aft of the test section. Static pressure rather than total pressure is used because the former is much more sensitive to supersonic flow than the latter.

Injection and retraction of the model is accomplished by a pneumatic cylinder installed in a steel enclosure (Fig. 9). The present mechanism is capable of injection times of 1/2 sec. or less and retraction times of 3/4 sec. or less for the complete travel of 20 in. Little is known about the flow characteristics during injection or about the turbulence caused by the gap in the tunnel wall while the model is retracted. No difficulty arises from these factors, however, since the model can be successfully injected into a stable region (Fig. 11).

A valuable aid in supersonic flutter testing has been

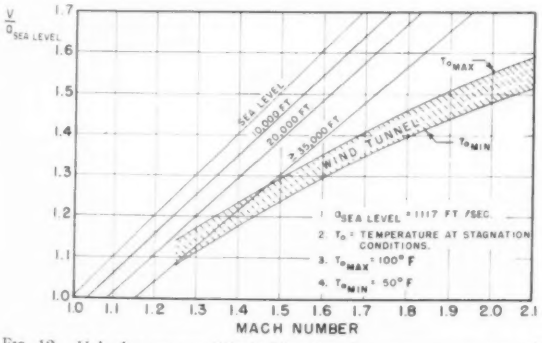

FIG. 12. Velocity versus Mach Number for extreme ranges of atmospheric and wind-tunnel conditions.

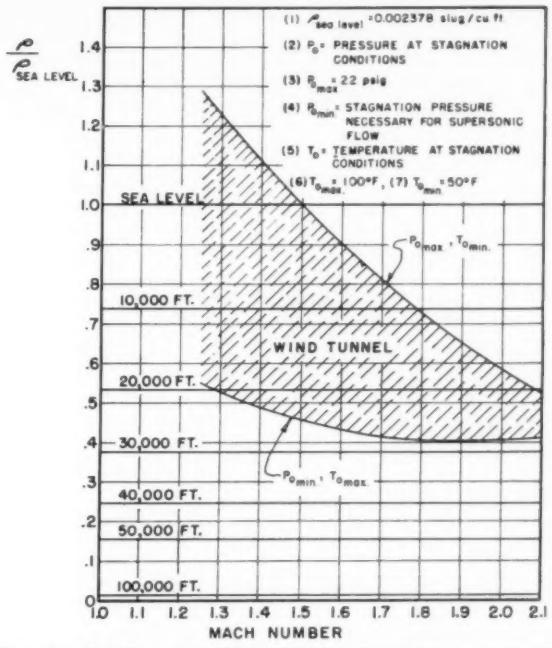

FIG. 13. Density versus Mach Number for extreme ranges of atmospheric and wind-tunnel conditions.

high-speed photography (Fig. 10). Besides giving evidence of model damage, the high-speed movies exhibit clearly the exact nature of the flutter mode shape. The starting of the high-speed camera is recorded on the oscillograph records, and timing pips appear on the edge of the film (Fig. 10). Therefore, timewise coordination between the oscillograph records and the high-speed movies is possible so that the condition of the model is known at every instant of time. The onset of flutter and the flutter frequency can be determined from the signals of the strain gages in the model or independently from the high-speed movies. The time history of the flow in the test section is obtained by recording the stagnation temperature, the stagnation pressure, and the block position. The position of the starting shock relative to the test section can be determined from the static-pressure trace, and the beginning and end of the injection and retraction of the model is recorded by a set of microswitches located at the extreme ends of the travel.

Successful flutter tests have been conducted on straight, swept, and delta wings with and without ailerons. Straight and swept wings with tip tanks have been tested for both the cantilever and free-to-roll root conditions. It is interesting to note that, during a flutter test, it may be necessary to inject the model at high Mach Number and decrease the Mach Number in the test section in order to approach the neutrally stable flutter condition (see Fig. 11 and references 7 and 8). Also, test section temperatures are generally lower than those encountered in the atmosphere, and model heating is not a problem (Fig. 12). Because of the high air densities obtainable with a blowdown wind tunnel, the prob-

(*Continued on page 577*)

Free-Flight Measurements of Skin Friction of Turbulent Boundary Layers with High Rates of Heat Transfer at High Supersonic Speeds

SIMON C. SOMMER* AND BARBARA J. SHORT*

Ames Aeronautical Laboratory, NACA

SUMMARY

The average skin friction of a turbulent boundary layer in the presence of severe aerodynamic heating has been measured in the Ames supersonic free-flight wind tunnel on free-flying hollow-cylinder models at Mach Numbers of 2.8, 3.8, 5.6, and 7.0. The skin friction measured under these conditions is appreciably higher than the skin friction measured in wind tunnels with zero heat transfer, experimentally confirming the trend of theoretical estimates of the effect of heat transfer on skin friction.

The T' method of Rubesin and Johnson was slightly modified to fit experimental data for turbulent boundary layers. Predicted values of skin-friction ratio resulting from use of this method were found to be in excellent agreement with the high-heat-transfer skin-friction data of the present investigation at Mach Numbers up to 7, with the zero-heat-transfer skin-friction data obtained in previous wind-tunnel investigations at Mach Numbers up to 4.5 and with the skin-friction data for heated pipe flow at subsonic speeds.

SYMBOLS

C_F = average skin-friction coefficient
c_f = local skin-friction coefficient
M = Mach Number
R = Reynolds Number
R_b = Reynolds Number based on length from effective turbulent origin to base of tare model
R_c = Reynolds Number based on length from effective turbulent origin to base of test model
R_D = Reynolds Number based on pipe diameter, subsonic pipe flow
St = Stanton Number
T = absolute temperature
x = axial distance
μ = coefficient of viscosity
ρ = density of air

Subscripts

0 = free-stream conditions
1 = conditions at the outer edge of boundary layer
w = conditions at wall
i = incompressible flow

Superscript

$'$ = conditions at which incompressible flow relations must be evaluated in order to represent compressible flow

INTRODUCTION

THE PRESENT STATE of knowledge of the skin friction of turbulent boundary layers at supersonic speeds is primarily guided by the experimental data that exist. These data are fairly complete for conditions close to zero heat transfer at Mach Numbers up to 4.5.[1,2] Unfortunately, there has been little experimental investigation of the effects of heat transfer and further increases in Mach Number on skin friction. Theoretical estimates generally agree that skin friction increases with increasing heat transfer from the boundary layer to the wall and decreases with increasing Mach Number,[3-7] but they are not generally in agreement quantitatively. Since heat-transfer rates will probably be large under conditions of free flight, and since flight speeds of interest extend well beyond a Mach Number of 4.5, a program was initiated in the Ames supersonic free-flight wind tunnel to measure skin friction of the turbulent boundary layer under conditions of large heat transfer and to extend the Mach Number range for which skin-friction data are available. The results of this investigation are reported herein. A more detailed presentation of this material is given in reference 8.

EQUIPMENT AND TEST CONDITIONS

Skin friction was obtained from measurements of the total drag of spin-stabilized hollow-cylinder models of the type shown in Fig. 1. Test and tare models, identical except for length, were gun-launched under the same conditions, and total-drag coefficients were computed from deceleration data. Deceleration of a model was computed from its time-distance history which was

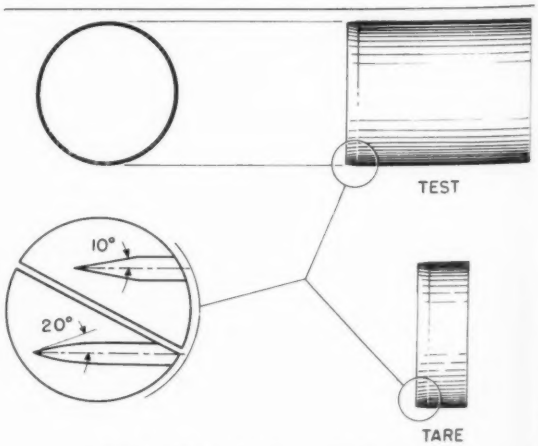

FIG. 1. Typical hollow-cylinder models.

Presented at the Aerodynamics—I Session, Twenty-Third Annual Meeting, IAS, New York, January 24-27, 1955.

* Aeronautical Research Scientist.

recorded by a chronograph and shadowgraphs.[9] The difference between the total drag of a test model and the total drag of a tare model is, except for small corrections, a measure of the average skin-friction drag of the added length of the test model.

Models were made of 75 S-T aluminum, with 1.4 in. outer diameter and 0.030-in.-thick walls. The test models were 2.0 and 2.5 in. long, and the tare models were 0.5 in. long. Two nose contours were used for the primary data, a double wedge with a half-angle of 10° and a circular-arc nose profile with a tangent half-angle at the tip of 20°. The model surfaces were polished both inside and out with successively finer polishing papers and finished with a 4/0 polishing paper. The finish of some typical models observed with a surface interferometer showed the maximum magnitude of the peak to valley roughness to be approximately 20 microinches which is of the order of 1/5 of the laminar sublayer thickness just behind the transition point.

The models were launched from a standard 37-mm. rifled aircraft gun, with the twist of the rifling equal to one turn in 3 ft. A typical test model assembly is illustrated in Fig. 2. The model is protected from the rifling by a plastic film wrapper which breaks away from the model as the assembly leaves the gun. The rifled aluminum disc imparts spin to the model and the Neoprene seal protects the model from powder-gas leakage.

Tests were conducted at nominal Mach Numbers of 2.8 and 3.9 by firing through still air at one atmosphere pressure where the free-stream static temperature was equal to ambient temperature. A nominal Mach Number of 7.2 was obtained by firing upstream through a Mach Number 2 air stream where the free-stream static temperature was about 56 per cent of the ambient temperature. The free-stream Reynolds Number range for the tests was from 3×10^6 to 9×10^6. The Mach Numbers and Reynolds Numbers at the outer edge of the boundary layer were a little lower than the free-stream values due to the flow over the nose profiles. The boundary-layer-edge conditions were calculated by two-dimensional shock-expansion theory. Due to the short flight time of the model, about 0.01 sec., the model wall-temperature rise was calculated[10] to be only about 15° to 45° above its initial value of ambient room temperature of about 530°R.; whereas, recovery

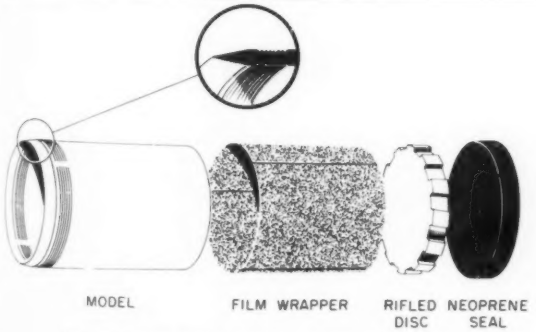

FIG. 2. Test model and sabot, exploded view.

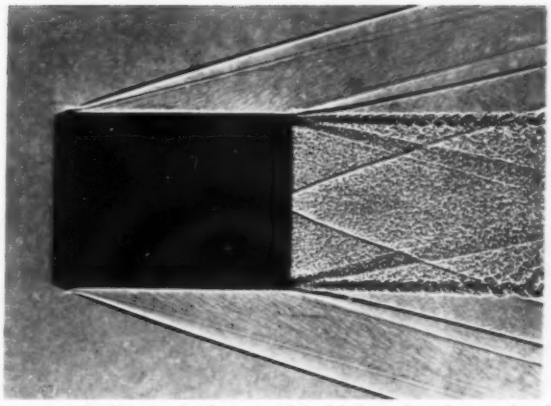

FIG. 3. Shadowgraph of test model with boundary-layer trip of 0.003-in.-deep threads at $M_0 = 3.9$.

temperatures were calculated to be about 1,300° to 3,200°R. The high rates of heat transfer from the boundary layer to the wall are indicated in the large differences between the recovery temperatures and the wall temperatures. The ratio of wall temperature to boundary-layer-edge temperature, T_w/T_1, ranged from 1.03 to 1.75.

Boundary-layer trips were used throughout the program to induce a turbulent boundary layer on the surfaces of the models. A typical boundary-layer trip which consisted of threads cut into the outer and inner surfaces is illustrated in Fig. 2. The trip strength for each test condition was varied until the least disturbance which consistently caused transition to occur on or near the trailing edge of the roughened region was found—that is, until no laminar flow was observed in the shadowgraphs behind the trailing edge of the trip. For illustration, Fig. 3 shows a shadowgraph of a test model with 0.003-in.-deep threads used as a boundary-layer trip at a Mach Number of 3.9. In the original negative, Mach waves produced by the turbulent boundary layer can be seen as far forward as the shock wave from the trip, and eddies in the turbulent boundary layer are visible at the model edge. This detail may be lost in reproduction and may not appear in Fig. 3. When a weaker trip was used at this Mach Number—0.001-in.-deep threads for example—the boundary layer was laminar. Fig. 4 shows a comparison between the type of flow observed when a trip of 0.003-in.-deep threads and 0.001-in.-deep threads are used at a Mach Number of 3.9. Neither Mach waves nor eddies were visible when 0.001-in.-deep threads were used as a boundary-layer trip. The boundary layer is laminar, and turbulence probably started in the annular wake. At a Mach number of 7, 0.003-in.-deep threads, the type which produced turbulent flow at a Mach Number of 3.9, left the boundary layer completely laminar. In order to induce transition in the vicinity of the trip, two wedge-shaped annular rings 0.008 in. high were used. It was also found that 0.006-in.-deep threads cut on the circular-arc nose profile consistently produced turbulent boundary layers at a Mach Number of 7. (The flow over the circular-arc nose profile

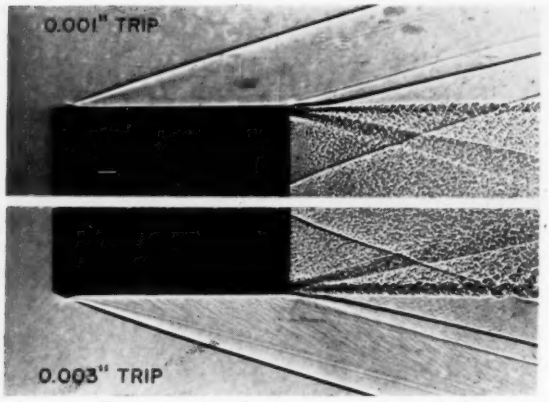

FIG. 4. Shadowgraphs showing comparison of flow over models with boundary-layer trips of 0.001-in. and 0.003-in.-deep threads at $M_0 = 3.9$.

lowered the Mach Number from 7 to 5.6 at the outer edge of the boundary layer.)

The more than 300 shadowgraphs of the data models showed turbulent flow over the external surfaces almost as far forward as the boundary-layer trips with no intermittently turbulent and laminar boundary layers. While the boundary layers on the inner surfaces of the cylinders could not be examined, it is unlikely that they would be different from those on the outer surfaces.

DATA REDUCTION

Skin-friction drag was obtained by subtracting the total drag of a tare model from the total drag of a test model. The measured total drags were adjusted because of small variations in model geometry and test conditions between test and tare models. These adjustments to total drags were made by determining the differences in individual drag components of a test-tare combination by use of available theoretical and experimental information. Adjustments were also made to account for differences in base drag. These differences in base drag were caused by differences in boundary-layer thicknesses just ahead of the trailing edge due to the difference in length between test and tare models. An additional small correction was made for drag due to lift, since the models did not fly at zero angle of attack. The maximum angle of attack, however, was less than 1°, and no visible differences in boundary-layer thickness around the model were ever observed in the shadowgraphs. Differences in drag due to variations in boundary-layer trips could not be ascertained quantitatively; therefore, it was assumed that the drag due to the trip on a tare model was equal to the drag of a trip on a test model, and no corrections were applied to the total drag. The effect of making all these adjstments to the total-drag data changed the skin-friction results by only 5 per cent and noticeably decreased the spread of the total-drag data.

In order to determine the Reynolds Numbers associated with experimental skin friction and to calculate the corresponding incompressible skin-friction coefficient so that, for convenience, the data could be presented in ratio form, the effective point of origin of the turbulent boundary layer was calculated. When the boundary-layer trips were small, the calculation was made by assuming the momentum thickness of the turbulent boundary layer equal to that of the laminar boundary layer at the transition point which was taken to be at the midlength of the trip. The momentum thickness of the laminar boundary layer was obtained theoretically.[11] Knowledge of the position of the effective turbulent origin was applied to determine the Reynolds Numbers required in computing the incompressible skin-friction coefficient from the von Kármán-Schoenherr equation.[12] The assumption of equal laminar and turbulent momentum thickness at the transition point is unjustified in the presence of large boundary-layer trips. The effects of large boundary-layer trips on the final skin-friction results were investigated and will be discussed later.

RESULTS AND DISCUSSION

The experimentally determined values of skin-friction coefficient were compared to the corresponding values of incompressible skin-friction coefficient at the same Reynolds Numbers and are plotted in the form C_F/C_{F_i}, hereafter called skin-friction ratio, as a function of Mach Number in Fig. 5. Values of skin-friction coefficient shown in the figure are mean values of many measurements at each condition. The root-mean-square deviation from the mean value at Mach Numbers of 2.8 and 3.8 was from 1 to 3 per cent; whereas, at Mach Numbers of 5.6, 6.9, and 7.0, where relatively large boundary-layer trips were used, the root-mean-square deviation from the mean value was from 8 to 10 per cent. These data are uncorrected for thickening of the turbulent boundary layer due to the boundary-layer trip and therefore can be considered as lower limits. Any initial thickness of the boundary layer would mean a higher effective Reynolds Number, therefore a lower value of incompressible skin-friction coefficient, and, consequently, a higher value of skin-friction ratio.

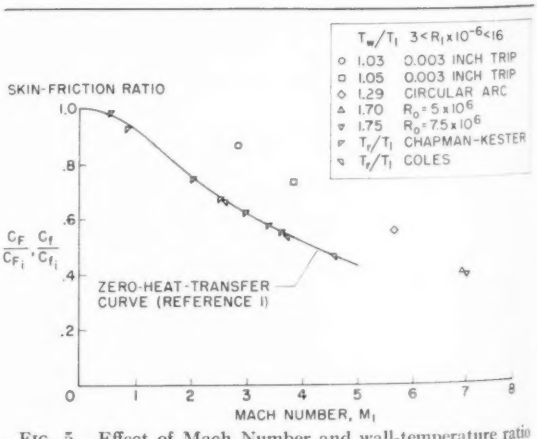

FIG. 5. Effect of Mach Number and wall-temperature ratio on skin-friction ratio with present data uncorrected for boundary-layer thickening at the trip.

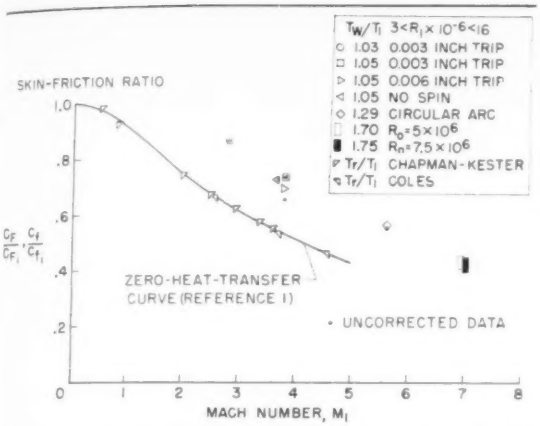

FIG. 6. Effect of Mach Number and wall-temperature ratio on skin-friction ratio with present data corrected for boundary-layer thickening at the trip.

For comparison, the force data of Chapman and Kester[1] and Coles[2] at zero-heat-transfer conditions are also included in the figure. A comparison of the zero-heat-transfer skin-friction data and the uncorrected data of the present investigation indicate a strong dependence of skin-friction ratio on wall-temperature ratio, T_w/T_1, at a given Mach Number.

Since it was found that boundary-layer trips with measurable drag were necessary at Mach Numbers of 5.6, 6.9, and 7.0 to promote turbulent flow over the surfaces of the models, it was required that the effect of these large trips on both skin friction and the corresponding incompressible skin friction be investigated. This was done experimentally by measuring skin friction on a model with a boundary-layer trip of 0.006-in.-deep threads and comparing the results to data obtained from a model with 0.003-in.-deep threads at a Mach Number of 3.8, where small boundary-layer trips produced turbulent flow. It was found that skin friction was 10 per cent lower on the 0.006-in. threaded model than on the 0.003-in. threaded model. The low value of skin friction was not particularly surprising since the boundary layer on the 0.006-in. threaded model, as determined from the shadowgraphs, was measurably thicker than on the 0.003-in. threaded model at corresponding stations along the cylinder. It appeared that there would be a relationship between the thickening of the boundary layer and the drag due to the trip. The thickening of the boundary layer signifies an increase of the momentum thickness. This increased momentum thickness is related to the trip drag since the trip drag must result in momentum being removed from the air flowing around the model. Part of this momentum will be removed from the boundary-layer air and increase the momentum thickness of the turbulent boundary layer. The maximum effect of the trip on incompressible skin friction was determined by calculating the length of run of turbulent flow necessary to produce the momentum thickness which would result if all of the momentum change due to the trip drag were confined to the boundary layer. This effect on skin-friction ratio is shown in Fig. 6. The data uncorrected for boundary-layer thickening are also shown in the figure. It can be seen that when only the incompressible skin-friction coefficient is modified, the results of the 0.003-in. and 0.006-in.-threaded models are in reasonable agreement (within the scatter of the experimental results for the 0.006-in. threaded model). When this correction procedure was used at a Mach Number of 5.6, the effect was small; however, the data at Mach Numbers of 6.9 and 7.0 were raised by about 10 per cent. These data are shown as a range of possible values, depending upon the amount of momentum change due to the drag of the trip being confined to the boundary layer. (All of the corrected data from the present investigation shown in Fig. 6 are tabulated in Table 1.) The agreement in skin-friction ratio between the 0.003-in. and 0.006-in. threaded models, when the turbulent origins were determined assuming normal "fully developed" turbulent boundary layers, suggests that the characteristics of the turbulent boundary layer over the portion of the model for which skin friction was measured were not significantly affected by the presence of the boundary-layer trips.

Also shown in Fig. 6 are the zero-heat-transfer skin-friction data replotted from Fig. 5. At Mach Numbers of 2.8 and 3.8 the present skin-friction ratios are approximately 35 per cent higher than the zero-heat-transfer skin-friction data. Although no measurements of skin friction have been made at zero-heat-transfer conditions at very high Mach Numbers, any reasonable extrapolation of the zero-heat-transfer curve would indicate that the same trend of increasing skin-friction ratio with decreasing wall-temperature ratio will persist to a Mach Number of 7.

Because the data of Fig. 6 show an appreciable effect of wall-temperature ratio on skin-friction ratio, and since the models of the present investigation were spin stabilized, it was essential to determine to what extent these results had been influenced by model spin. It was felt that one test condition would suffice to demonstrate the effect of spin on the present results. An aerodynamically stable model was tested at a Mach Number of 3.8 where experimental scatter was least and the boundary-layer trip was small. The result of this investigation is shown in Fig. 6. It can be concluded that for the spin rates used, the effect of spin on the present results is small, probably within the scatter of the data.

TABLE 1
Final Results

M_i	T_w/T_i	R_1/x $\times 10^{-6}$	R_b $\times 10^{-6}$	R_x $\times 10^{-6}$	C_F	C_F/C_{F_i}	Symbol
2.81	1.03	1.58	0.63	3.00	0.00284	0.867	○
3.82	1.05	2.13	0.88	4.07	0.00227	0.730	□
5.63	1.29	1.83	1.05	4.71	0.00170	0.562	◇
6.90	1.70	2.08	1.03	4.06	0.00125	0.404	
			to	to		to	▯
			2.97	6.09		0.451	
7.00	1.75	3.14	1.35	6.06	0.00115	0.395	
			to	to		to	▮
			5.21	9.92		0.446	
3.78	1.05	2.13	1.75	4.94	0.00204	0.694	▷
3.67	1.05	1.99	0.20	3.78	0.00240	0.724	◁

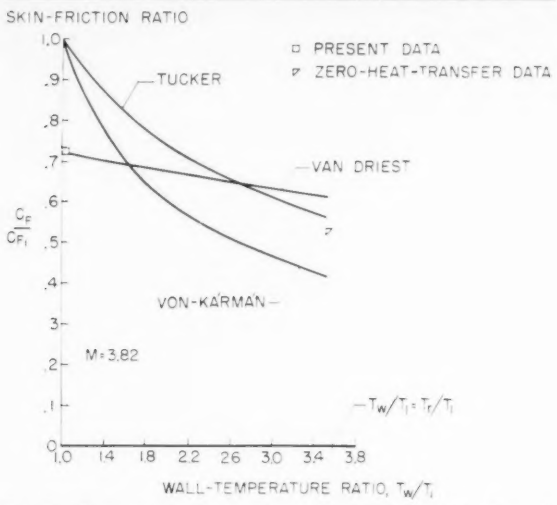

FIG. 7. Comparison of experimental and theoretical effect of wall-temperature ratio on skin-friction ratio at $M_1 = 3.82$.

The results of Fig. 6 confirm qualitatively the conclusions of many analyses, namely those of von Kármán,[3] Monaghan,[4] Tucker,[5] Van Driest,[6] and Clemmow,[7] among many, that skin-friction ratio increases with decreasing wall-temperature ratio at a given Mach Number and Reynolds Number. The results of these analyses differ widely in the magnitude of this increase, as is shown in Fig. 7, where skin-friction ratio is plotted as a function of wall-temperature ratio. Values of skin-friction ratio from these analyses were calculated with μ assumed to be proportional to $(T)^{0.76}$ at a Reynolds Number of 10^7. For clarity of presentation, the results of only three analyses are illustrated at only one Mach Number, $M_1 = 3.82$. An experimental data point from the present investigation and one point from the zero-heat-transfer curve are included in the figure for comparison. The results of the theory of Van Driest agree well with experimental data at wall-temperature ratios near unity. As wall temperature approaches recovery temperature, this theory overestimates the skin-friction ratio by about 20 per cent. Although the method of Tucker and the theory of von Kármán were devised for application at zero-heat-transfer conditions, it is interesting to evaluate skin-friction ratio at conditions of large heat transfer and to compare these results with experimental data. At a wall-temperature ratio of unity, these analyses predict a skin-friction ratio of unity, which greatly overestimates skin-friction ratio. At recovery temperature, Tucker's method predicts skin-friction ratio reasonably well; whereas, the theory of von Kármán considerably underestimates skin-friction ratio.

T′ Method for Evaluating Skin Friction

Since no one of the many theories considered so far adequately predicts the effects of both wall-temperature ratio and Mach Number on skin-friction ratio, the present authors investigated the possibility of applying a laminar-flow method to turbulent flow. Young and Janssen,[13] in 1952, applied the laminar flow T' method of Rubesin and Johnson[14] to evaluate skin-friction ratio for turbulent flow and compared the results with some zero-heat-transfer skin-friction data over the limited Mach Number range from 1.5 to 2.5. The agreement was good. The Rubesin and Johnson T' method consists of finding a reference temperature, T', at which the density and viscosity for compressible flow must be evaluated if incompressible flow relations for zero heat transfer are to apply. The theoretical results of Crocco-Conforto for laminar flow on a flat plate were used to find the following expression:

$$T'/T_1 = 1 + 0.032\,M_1^2 + 0.58[(T_w/T_1) - 1] \quad (1)$$

With the more complete data now available at zero-heat-transfer conditions and with the results of the present investigation at large rates of heat transfer, it is the purpose of the remainder of the paper to further evaluate the reliability of the T' method in predicting the effect of heat transfer as well as Mach Number on skin-friction ratio for turbulent flow. Eq. (1) was used in conjunction with the von Kármán-Schoenherr incompressible skin-friction equation for turbulent flow. Fig. 8 shows the results of the T' method compared to the zero-heat-transfer skin-friction data and data of the present investigation at wall-temperature ratios near unity. Eq. (1) predicts a large effect of heat transfer on skin-friction ratio and, in fact, predicts an effect which agrees very well with the experimental data. Although Eq. (1) underestimates skin-friction ratio at zero heat transfer above a Mach Number of 2.5, the shape of the zero-heat-transfer curve is remarkably similar to the trend of the experimental data. Because of the encouraging results, it was felt that the agreement would be better, particularly at the high Mach Numbers, if the coefficients of Eq. (1) were modified to fit the experimental data. The coefficients were slightly modified to fit the data at a Mach Number of 3.82 from the present experiment and from the zero-heat-transfer curve. The following expression was obtained:

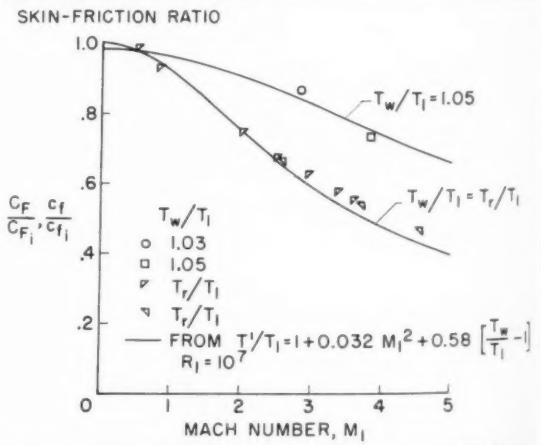

FIG. 8. Comparison of skin-friction ratio as determined by use of the laminar flow T' expression with experimental values.

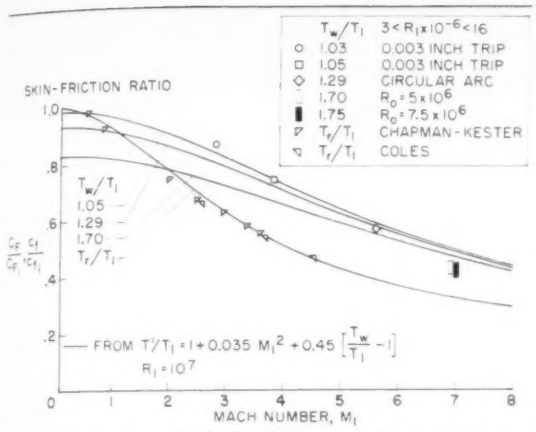

FIG. 9. Comparison of skin-friction ratio as determined by use of the modified T' expression with experimental values.

$$T'/T_1 = 1 + 0.035\ M_1^2 + 0.45[(T_w/T_1) - 1] \quad (2)$$

Curves of skin-friction ratio as a function of Mach Number were obtained from Eq. (2) and are compared to the data of the present investigation and the zero-heat-transfer skin-friction data in Fig. 9. Agreement between the predicted values and the experimentally determined values of skin-friction ratio is excellent over the entire range of Mach Numbers and wall-temperature ratios.

Because the curves of Fig. 9 show appreciable changes in skin-friction ratio with changes in wall-temperature ratio at the low Mach Numbers, particularly at subsonic speeds, it was deemed desirable to compare the results of the T' method with experimental data at subsonic Mach Numbers. Because of the lack of experimental data on flat plates with sufficiently high rates of heat transfer, the predictions of the T' method were compared with pipe flow data. Since experimental skin-friction results at large rates of heat transfer were very meager, heat-transfer data were also used in the form Stanton Number ratios. It has been demonstrated by Colburn[15] for this speed range that Stanton Number is proportional to skin friction or that Stanton Number ratio is equivalent to skin-friction ratio. In Fig. 10, skin-friction ratio as predicted by the T' method is compared to experimental and theoretical results at subsonic speeds in smooth pipes as a function of wall-temperature ratio. The predictions of the T' method differ very slightly from the theoretical results of von Kármán-Nikuradse,[16] and Drew, Koo, and McAdams[15] which were devised for subsonic pipe flow. The T' prediction agrees well with the experimental skin-friction results of reference 16 and was slightly higher when compared to the heat-transfer results of references 16 and 17. It seems that the modified T' method can be used to predict skin-friction ratios at subsonic speeds as well as at supersonic speeds.

Fig. 11 summarizes the comparison between experiment and the modified T' method. The 45° line is the line of perfect agreement. The experimental skin-friction data shown in the figure were obtained over a wide range of test conditions, from subsonic speeds to a Mach Number of 7 and with a variety of wall-temperature ratios. The correlation is excellent and demonstrates the wide range of usefulness of the T' method in predicting skin-friction ratio.

The procedure for applying the T' method to evaluate skin-friction ratio, C_F/C_{F_i}, for any Mach Number, M_1, any wall-temperature ratio, T_w/T_1, and any Reynolds Number, R_1, by use of Eq. (2) and the von Kármán-Schoenherr incompressible flow equation, is as follows:

(a) Evaluate T'/T_1 from Eq. (2).

(b) Evaluate R' from the relationship

$$R'/R_1 = (\rho'/\rho_1)\ (\mu_1/\mu')$$

but if we assume constant pressure through the boundary layer, $(\rho'/\rho_1) = (T_1/T')$, and therefore,

$$\frac{R'}{R_1} = \frac{1}{(T'/T_1)\ (\mu'/\mu_1)} \quad (3)$$

The ratio (μ'/μ_1) can be determined from the Sutherland equation

$$\mu'/\mu_1 = (T'/T_1)^{1.5}\ [(T_1 + 216)/(T' + 216)] \quad (4)$$

(c) Evaluate C_F' at the Reynolds Number, R', from the von Kármán-Schoenherr equation,

$$0.242/\sqrt{C_F} = \log_{10}(C_F R) \quad (5)$$

(d) Evaluate C_F from the relationship

$$C_F'/C_F = \rho_1/\rho' = T'/T_1 \quad (6)$$

(e) Evaluate C_{F_i} from Eq. (5) for a Reynolds Number R_1.

It should be pointed out that the evaluation of skin-friction ratio by use of Eq. (2) can be simplified if the Prandtl-Schlichting relationship

$$C_F = 0.46/(\log_{10} R)^{2.6} \quad (7)$$

for incompressible flow is used instead of the von Kármán-Schoenherr equation.

When Eq. (7) is combined with Eq. (2), the resulting

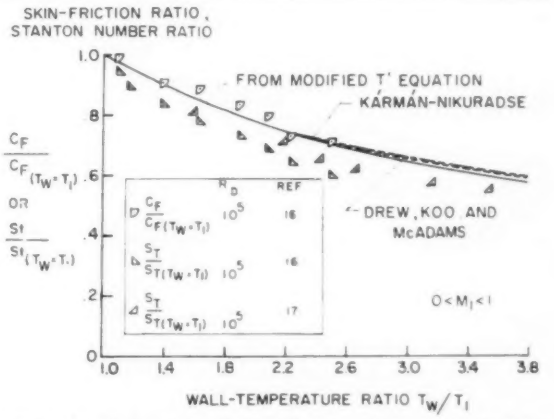

FIG. 10. Comparison of skin-friction ratio as determined by use of the modified T' expression with experimental and theoretical results at subsonic speeds.

equation for the evaluation of C_F/C_{F_i} is in closed form.

$$\frac{C_F}{C_{F_i}} = \left[\frac{\log_{10} R_1}{\log_{10} \dfrac{R_1}{(T'/T_1)\ (\mu'/\mu_1)}}\right]^{2.6} \frac{1}{T'/T_1} \qquad (8)$$

Conclusions

The results of the experimental measurements of skin friction of the turbulent boundary layer which have been made on free-flying models at high supersonic speeds, and the results of the investigation of the T' method can be summarized as follows:

(1) The effect of wall-temperature ratio on skin-friction ratio is large, an increase of the order of 35 per cent at Mach Numbers of 2.8 and 3.8, when free-flight data of this experiment are compared to zero-heat-transfer skin-friction data.

(2) Although skin-friction measurements at conditions of zero heat transfer are not available at Mach Numbers as high as 7, the results of this investigation indicate that the same trend of increasing skin-friction ratio with decreasing wall-temperature ratio will persist at very high Mach Numbers.

(3) The T' method of Rubesin and Johnson for laminar boundary layers, with the defining equation for T' slightly modified, has been found to predict skin-friction ratios which agree well with measured values over a wide range of Mach Numbers and wall-temperature ratios.

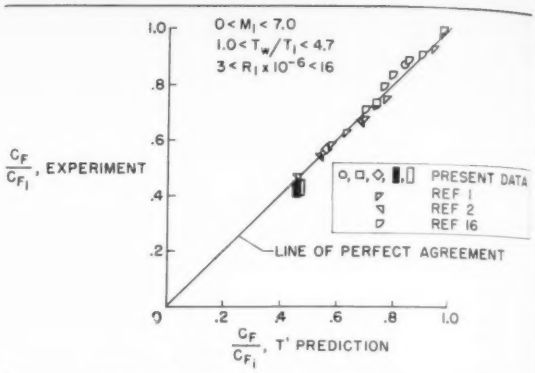

FIG. 11. Correlation between skin-friction ratio determined experimentally and predicted by the modified T' method.

References

[1] Chapman, Dean R., and Kester, Robert H., *Turbulent Boundary-Layer and Skin-Friction Measurements in Axial Flow Along Cylinders at Mach Numbers Between 0.5 and 3.6*, NACA TN 3097, 1954.

[2] Coles, D., *Measurements in the Boundary Layer on a Smooth Flat Plate in Supersonic Flow*, Ph.D. Thesis, Calif. Inst. Tech., 1953.

[3] von Kármán, Th., *The Problems of Resistance in Compressible Fluids*, GALCIT Pub. No. 75, 1936 (From R. Accad. D'Italia, 1936).

[4] Monaghan, R. J., *A Review and Assessment of Various Formulae for Turbulent Skin Friction in Compressible Flow*, British RAE TN No. Aero. 2182, 1952.

[5] Tucker, Maurice, *Approximate Calculation of Turbulent Boundary-Layer Development in Compressible Flow*, NACA TN 2337, 1951.

[6] Van Driest, E. R., *Turbulent Boundary Layer Flow in Compressible Fluids*, Journal of the Aeronautical Sciences, Vol. 18, No. 3, p. 145, March, 1951.

[7] Clemmow, D. M., *The Turbulent Boundary Layer Flow of a Compressible Fluid Along a Flat Plate*, British Rep. No. 50/6, Dir. of Guided Weapons Res. and Dev., August, 1950.

[8] Sommer, Simon C., and Short, Barbara, J., *Free-Flight Measurements of Turbulent-Boundary-Layer Skin Friction in the Presence of Severe Aerodynamic Heating at Mach Numbers From 2.8 to 7.0*, NACA TN 3391, 1955.

[9] Seiff, Alvin, James, Carlton S., Canning, Thomas N., and Boissevain, Alfred G., *The Ames Supersonic Free-Flight Wind Tunnel*, NACA RM A52A24, 1952.

[10] Carslaw, H. S., and Jaeger, J. C., Conduction of Heat in Solids, pp. 93–102, 377; Oxford Univ. Press, 1948.

[11] Van Driest, E. R., *Investigation of the Laminar Boundary Layer in Compressible Fluids Using the Crocco Method*, NACA TN 2597, 1952.

[12] Schoenherr, Karl E., *Resistance of Flat Surfaces Moving Through a Fluid*, Soc. of Naval Arch. and Marine Engrs. Trans., Vol. 40, pp. 279–313, 1932.

[13] Young, George B. W., and Janssen, Earl, *The Compressible Boundary Layer*, Journal of the Aeronautical Sciences, Vol. 19, No. 4, pp. 229–236, April, 1952.

[14] Rubesin, M. W., and Johnson, H. A., *A Critical Review of Skin-Friction and Heat-Transfer Solutions of the Laminar Boundary Layer of a Flat Plate*, ASME Trans., Vol. 71, No. 4, p. 383, May, 1949.

[15] Colburn, Allan P., *A Method of Correlating Forced Convection Heat Transfer Data and a Comparison with Fluid Friction*, American Inst. of Chem. Engrs. Trans., Vol. XXIX, pp. 174–210, 1933.

[16] Lowdermilk, Warren H., and Grele, Milton D., *Heat Transfer from High-Temperature Surfaces to Fluids. II—Correlation of Heat-Transfer and Friction Data for Air Flowing in Inconel Tube with Rounded Entrance*, NACA RM E8L03, 1949.

[17] Desmon, L. G., and Sams, E. W., *Correlation of Forced-Convection Heat-Transfer Data for Air Flowing in Smooth Platinum Tube with Long-Approach Entrance at High Surface and Inlet-Air Temperatures*, NACA RM E50H23, 1950.

An Approximate Method of Calculating Three-Dimensional Compressible Flow in Axial Turbomachines

COMDR. CARL O. HOLMQUIST* AND W. DUNCAN RANNIE†

Naval Air Test Center and California Institute of Technology

ABSTRACT

The two principal existing methods of calculating axially-symmetric compressible flow in turbomachines are: (1) a simplified one-dimensional analysis and (2) numerical methods using the complete or linearized flow equations. The first is not satisfactory for multistage turbines with appreciable wall divergence; the second is very tedious and time consuming. The purpose of this investigation is to extend the approximate methods, successfully used in calculating incompressible flow in compressors with constant blade height, to the analysis of compressible flow in turbomachines with variable blade height. Assuming that the blades can be completely defined by the exit flow angle and neglecting the influence of downstream blades, the analysis is made considering the flow between successive blade rows only. With these restrictions, subsonic and isentropic supersonic flow patterns can be determined for compressor or turbine arbitrary boundary shapes as long as separation does not occur. Average losses can be accounted for by the use of a polytropic law, and the effect of radial variations in stagnation temperature can be included without difficulty. Examples are given illustrating the flexibility and practical value of the iteration method which has been developed and the rapid convergence of successive solutions.‡

SYMBOLS

β_2	=	stator spouting angle measured from the plane perpendicular to the axis
β_3	=	rotor spouting angle measured relative to the rotating wheel
c	=	axial distance between stations, ft.
C_1	=	constant obtained from axial velocity integral
C_2	=	constant obtained from radial momentum integral
C_p	=	specific heat at constant pressure
Δ	=	used to denote incremental changes of a quantity in the radial direction
$F(\xi_2)$	=	cotangent of stator spouting angle β_2 as a function of radius, $F(\xi_2) = \lambda_2/\phi_2$
$G(\xi_3)$	=	cotangent of rotor relative spouting angle β_3 as a function of radius, $G(\xi_3) = (\lambda_3 + \xi_3)/\phi_3$
γ	=	ratio of specific heats
g	=	acceleration of gravity
$H(\xi_3)$	=	dimensionless work output of rotor as a function of radius, $H(\xi_3) = \xi_2\lambda_2 + \xi_3\lambda_3$
m	=	dimensionless mass flow, $m = W\omega/(2\pi g p_t R_0)$
M	=	Mach Number based on total velocity, $M = \Phi/\sqrt{\gamma\tau}$
M_g	=	"governing" Mach Number as defined on p. 87 of reference 1, $M_g = \sqrt{(\phi^2 + \theta^2)/\gamma\tau}$
n	=	polytropic exponent
η	=	polytropic efficiency $[\gamma/(\gamma - 1)]\eta = n/(n - 1)$
ω	=	angular velocity of rotor, radians per sec.
p	=	pressure, lbs. per sq.ft.
P	=	dimensionless pressure, $P = p/p_t$
ρ	=	density, lb. sec.^{2}/ft.^{4}
Q	=	dimensionless density, $Q = (\omega^2 R_0^2\rho)/p_t$
R	=	gas constant
R_0	=	reference radius, ft.
r	=	radius from the axis, ft.
ξ	=	dimensionless radius, $\xi = r/R_0$
T	=	absolute temperature, °R.
τ	=	dimensionless temperature, $\tau = [R/(\omega^2 R_0^2)]T$
u	=	radial component of absolute velocity, ft. per sec.
θ	=	dimensionless radial component of absolute velocity, $\theta = u/(\omega R_0)$
v	=	tangential component of absolute velocity, ft. per sec.
λ	=	dimensionless tangential component of absolute velocity, $\lambda = v/(\omega R_0)$
w	=	axial component of absolute velocity, ft. per sec.
ϕ	=	dimensionless axial component of absolute velocity, $\phi = w/(\omega R_0)$
Φ	=	dimensionless total absolute velocity, $\Phi = \sqrt{\phi^2 + \lambda^2 + \theta^2}$
W	=	mass flow, lb. per sec.
z	=	axial distance along axis of rotor from reference point, ft.
ζ	=	dimensionless axial distance, $\zeta = z/R_0$
$(\ )_1$	=	subscript to denote station immediately upstream of stator
$(\ )_2$	=	subscript to denote station immediately downstream of stator and immediately upstream of rotor
$(\ )_3$	=	subscript to denote station immediately after rotor
$(\ )_i$	=	subscript to denote inner boundary of channel
$(\ )_o$	=	subscript to denote outer boundary of channel
$(\ )_t$	=	subscript to denote total conditions
$\partial f/\partial\zeta$	=	slope of streamline
$\partial^2 f/\partial\zeta^2$	=	rate of change of slope of streamline

Presented at the Aerodynamics Session, Twenty-Third Annual Meeting, IAS, New York, Jan. 24–27, 1955.

* Senior Engineer, Carrier Branch, Flight Test Division.

† Associate Professor, Mechanical Engineering Department.

‡ The opinions expressed herein are those of the authors and do not necessarily reflect the views of the Navy Department.

(1) INTRODUCTION

IN THE MODERN AIRCRAFT gas turbine, the flow is necessarily in the transonic range for two reasons: (1) to keep the weight and size of the machine at a minimum and (2) to fit the mass flow and pressure ratio of the compressor. Earlier turbojet engines had single-stage transonic turbines, but present engines employ multistage turbines with rapid channel divergence in order to use effectively the increased pressure ratios and keep the axial velocities compatible with the blade speed. In these types of machines, the flow at the mean blade height is mainly axial, and the aspect ratio of the blades is usually above unity for weight-saving considerations.

One of the principal methods available to the design engineer for the analysis of axially-symmetric, compressible flow in turbomachines is a simplified one-dimensional analysis. This method is used extensively in preliminary design considerations and is simple and straightforward. Since only the exit flow angles from the blade rows at the mean blade height are considered, the radial distributions of velocity and energy are not determined. Although this analysis gives reasonably accurate results for a single-stage turbine with a fairly high hub ratio and small channel divergence, the one-dimensional method is inadequate for large channel divergence where the radial distribution of velocities becomes significant. It is particularly inadequate for the design of multistage turbines with channel wall divergence since it is difficult to get the proper balance of work on the individual stages. This work balance is strongly affected by the radial distribution of the axial and radial velocities. Since the one-dimensional analysis is done at the mean blade height, it gives no information as to the radial distribution of velocities.

The second principal method of analysis of axially-symmetric compressible flow in turbomachines is by numerical methods using the complete or linearized flow equations to solve for the complete velocity and energy field through the machine. Since the determination of the entire flow field involves six unknowns at each point in the flow (three components of velocity, pressure, temperature, and density), the analysis using these numerical methods is necessarily lengthy and extremely complicated and cannot be considered suitable from the point of view of the design engineer. Monroe[1] formulated the idealized problem in terms of a stream function for the velocities in the meridional plane and solved the resulting nonlinear differential equation by a simultaneous application of the relaxation technique of Southwell and an iteration process. Wu[2] has utilized various relaxation methods, matrix systems, and finite difference schemes to solve the complete hydrodynamical equations for the entire flow field in many types of problems. Vavra,[3] Reissner,[4] Goldstein,[5] Wislicenus,[6] and many others have employed various techniques to solve the complete, or nearly complete, equations by some numerical method. Although these numerical methods are not considered suitable for practical design purposes, they are general and can be used for centrifugal, mixed flow, or axial flow machines with blades of any aspect ratio.

In an effort to simplify the problem of solving the complete flow field, linearized analyses have been provided by Marble[7, 8] and Fabri.[9] The linearization procedure given by Marble[7] was based on the assumption that disturbances in the radial and axial velocities are small compared with the mean axial velocity, and the results are sufficiently accurate if the vorticity effects are not large. A second-order linearization was introduced[8] to handle problems with greater vorticity effects. However the computation required to find the three-dimensional flow in any particular case is rather lengthy using the linearized solutions and involves some type of numerical integration.

The analysis of flow in turbomachinery where channel boundaries are purely cylindrical, or vary only slightly from a cylindrical shape, has been extensively investigated by Rannie,[10] Traupel,[11] Sinnette,[12, 13] and others. In these analyses, the radial momentum equation used in the treatment is of the form,

$$(1/\rho)\,(\partial p/\partial r) = v^2/r \qquad (1)$$

where the radial force and other momentum terms have been neglected. The distribution of axial velocity is approximated by assuming axial symmetry, and since the centrifugal force within the rotating fluid body is balanced only by the radial pressure gradient, the resulting flow calculated in this manner is in reality that which must exist far downstream of the blades where radial velocities and accelerations have vanished. No information is provided by these analyses on how rapidly the change in velocity pattern takes place as the fluid passes through the blade row.

The purpose of this paper is to present an approximate method for the analysis of compressible flow in modern axial turbomachines which gives sufficiently accurate information for design purposes and yet retains the simplicity necessary to be of practical value to the design engineer. This is the logical step forward from the one-dimensional method to the analysis of compressible flow in axial turbomachines. Methods that have been successfully employed in the incompressible case[10] have been modified and extended to the analysis of compressible flow in arbitrarily shaped axially-symmetric channels. It is obvious that little simplification over the so-called "numerical" methods can be obtained if the complete flow and energy fields are to be determined in the analysis. In this paper, the flow is analyzed at the station immediately downstream of the blade row by a consideration of the upstream conditions, channel configuration, and blade shapes. The blade trailing-edge angle only is considered, and the complete flow field through the blade row is not determined.

The method of analysis presented is extremely flexible and has been used to solve the direct and inverse problems, subsonic and supersonic, for arbitrary axial boundary configurations. In the solution of the direct problem as defined by Marble,[7] the choice of blade speed, blade spouting angle, boundary configuration, and upstream conditions can be arbitrary, and the three-dimensional velocity field, blade loading, and distribution of energy in the field are determined. In the inverse problem, for a given blade loading, blade speed, boundary configuration, and fluid state ahead of all blades, the blade spouting angle, velocity field and energy distribution can be determined. By a simple change of sign in the equations used, the method can be applied equally well to an axial compressor as to an axial turbine. Although this method is not as general as those used by Wu,[2] for example, it is more flexible and practical for blading of aspect ratio greater than

unity and is sufficiently accurate in view of the assumptions used in the treatment.

The analysis is carried out on the basis of steady, axially-symmetric flow with infinitely many blades. The fluid is assumed to be compressible, but all other real fluid effects are neglected except as they may be approximated by a "polytropic efficiency" and the use of the polytropic exponent "n." As a result of this assumption, the possibility of separation of flow at the channel walls or along the blades is excluded. Boundary-layer effects are not considered in the analysis. In the supersonic solution, the occurrence of shock waves is excluded. Radial or nearly radial blades are presupposed so that the radial force can be neglected, and the radial momentum equation used in the treatment has the form,

$$(1/\rho)(\partial p/\partial r) = (v^2/r) - [u(\partial u/\partial r)] - [w(\partial u/\partial z)] \quad (2)$$

This assumption seems justified in view of the investigations of Karlsson[14] who, by a two-dimensional analysis of incompressible flow with an infinite number of blades, showed that the effect of the radial force resulting from normal blade twist is of negligible magnitude.

The effect of downstream blades on conditions upstream is neglected, and the blade shape is specified by the trailing edge angle only. Simply stated, a blade row is assumed whose only effect on the flow is to turn it through a specified angle distribution which is a function of radius across the channel. An assumption similar to this has been used successfully in the analysis of flow through a compressor[10] and should be even more applicable to turbines where the blade solidity is high. The equations are particularly suited to the analysis of flows with a prescribed radial total enthalpy distribution.

Subject to the above assumptions, the resulting "exact" equations are solved by an approximate method using a simple iteration procedure. An integral for the axial velocity is derived in terms of known upstream conditions and the downstream pressure. The pressure distribution is found by integrating the radial momentum equation and applying the energy equation at a boundary. The mass flow equation is used to solve for the constant obtained from the axial velocity integral. The iteration is started by assuming an axial velocity distribution and continued until the solution is reached—i.e., until the velocity distribution produced by an iteration is the same as that assumed for that particular iteration.

(2) Fundamental Equations

(2.1) *Basic Differential Equations in Nondimensional Form*

A stream annulus of small radial extent in the diverging channel of a turbine stator and rotor section is shown in Fig. 1, and absolute velocity components are

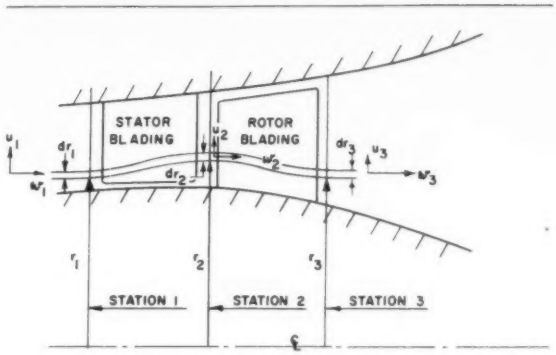

FIG. 1 CHANNEL AND STREAM ANNULUS

considered at stations 1, 2, and 3. Generally, there will be a shift in the stream surface in passing through either stator or rotor blading, and three components of velocity will be present at each station.

With the basic assumptions enumerated in the preceding section, the continuity equation is written in differential form as:

$$\rho_1 w_1 r_1 dr_1 = \rho_2 w_2 r_2 dr_2 = \rho_3 w_3 r_3 dr_3 \quad (3)$$

For a row of stator blades, the energy equation must hold along a stream surface, and for a row of rotor blades, the energy equation must hold along a relative stream surface. Hence, in terms of absolute velocities at stations 1, 2, and 3, the energy relations become:

$$C_p T_{1t} = [\gamma/(\gamma-1)](p_1/\rho_1) + (1/2)(u_1^2 + v_1^2 + w_1^2) = [\gamma/(\gamma-1)](p_2/\rho_2) + (1/2)(u_2^2 + v_2^2 + w_2^2) = C_p T_{1t} \quad (4)$$

$$[\gamma/(\gamma-1)](p_2/\rho_2) + (1/2)(u_2^2 + v_2^2 + w_2^2 - 2\omega r_2 v_2) = [\gamma/(\gamma-1)](p_3/\rho_3) + (1/2)(u_3^2 + v_3^2 + w_3^2 + 2\omega r_3 v_3) \quad (5)$$

Neglecting the radial force, the radial momentum equation, Eq. (2), must hold at all stations. If the flow is considered to be isentropic along a relative stream surface, the following relations must hold along this surface:

$$\rho_2/\rho_1 = (p_2/p_1)^{1/\gamma} = (T_2/T_1)^{1/(\gamma-1)} \quad (6)$$

$$\rho_3/\rho_2 = (p_3/p_2)^{1/\gamma} = (T_3/T_2)^{1/(\gamma-1)} \quad (7)$$

If a polytropic flow is considered, γ will be replaced by n in Eqs. (6) and (7). The above equations are fundamental in the solution of the direct and inverse problems.

For ease in handling the equations and to avoid the use of large numbers in calculation, the analysis is completed in nondimensional form. The notation used for dimensionless quantities is given in the section on Symbols. Axial and radial coordinates are made nondimensional by referring them to a standard radial dimension R_0. Velocities are made dimensionless by referring them to a standard blade speed ωR_0. With this procedure, the perfect gas equation is $P = Q\tau$ and

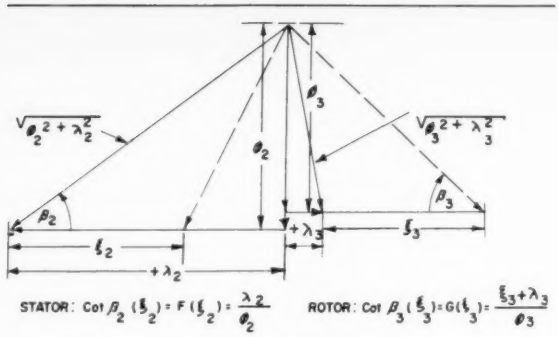

FIG. 2 TYPICAL TURBINE VELOCITY DIAGRAM SHOWING SIGN CONVENTION

Eqs. (3), (4), (5), (2), (6), and (7) become, respectively:

$$Q_1\phi_1\xi_1 d\xi_1 = Q_2\phi_2\xi_2 d\xi_2 = Q_3\phi_3\xi_3 d\xi_3 \tag{8}$$

$$[\gamma/(\gamma-1)]\tau_{1t} = [\gamma/(\gamma-1)]\,(P_1/Q_1) + (1/2)\times(\theta_1^2+\lambda_1^2+\phi_1^2) = [\gamma/(\gamma-1)]\,(P_2/Q_2) + (1/2)\,(\theta_2^2+\lambda_2^2+\phi_2^2) = [\gamma/(\gamma-1)]\tau_{2t} \tag{9}$$

$$[\gamma/(\gamma-1)]\,(P_2/Q_2) + (1/2)\,(\theta_2^2+\lambda_2^2+\phi_2^2-2\xi_2\lambda_2) = [\gamma/(\gamma-1)]\,(P_3/Q_3) + (1/2)\,(\theta_3^2+\lambda_3^2+\phi_3^2+2\xi_3\lambda_3) \tag{10}$$

$$(1/Q)\,(\partial P/\partial\xi) = (\lambda^2/\xi) - [\theta(\partial\theta/\partial\xi)] - [\phi(\partial\theta/\partial\zeta)] \tag{11}$$

$$Q_2/Q_1 = (P_2/P_1)^{1/\gamma} = (\tau_2/\tau_1)^{1/(\gamma-1)} \tag{12}$$

$$Q_3/Q_2 = (P_3/P_2)^{1/\gamma} = (\tau_3/\tau_2)^{1/(\gamma-1)} \tag{13}$$

(2.2) *Equations for the Direct Problem for Isentropic Flow*

The basic equations are derived for a rotor with infinitely many blades on the basis of isentropic, nonviscous, compressible, axially-symmetric, steady flow. Radial or nearly radial blades are assumed so that the radial force can be neglected. The channel shape, blade shape, mass flow, and upstream conditions are assumed specified for the direct problem.

The derivation of the basic integral for the axial velocity follows the general procedure given by Rannie[10] for the incompressible case. The dimensionless total temperature at station 2 immediately upstream of the rotor blading,

$$[\gamma/(\gamma-1)]\tau_{2t} = [\gamma/(\gamma-1)]\tau_2 + (1/2)\,(\theta_2^2+\lambda_2^2+\phi_2^2) \tag{14}$$

is introduced into Eq. (10), and the resulting equation is differentiated in respect to the radius ξ_2 on the left side and ξ_3 on the right side.

$$\left[\frac{\gamma}{\gamma-1}\frac{d\tau_{2t}}{d\xi_2} - \frac{d(\xi_2\lambda_2)}{d\xi_2}\right]d\xi_2 = \left[\frac{\gamma}{\gamma-1}\frac{d}{d\xi_3}\left(\frac{P_3}{Q_3}\right) + \frac{1}{2}\frac{d}{d\xi_3}\,(\theta_3^2+\lambda_3^2+\phi_3^2) + \frac{d(\xi_3\lambda_3)}{d\xi_3}\right]d\xi_3 \tag{15}$$

With Eqs. (8) and (13), differentiation of the first term of the right side of the above equation results in:

$$\frac{\gamma}{\gamma-1}\frac{d}{d\xi_3}\left(\frac{P_2}{Q_2}\right) = \frac{P_2^{1/\gamma}}{Q_2P_3^{1/\gamma}}\frac{dP_2}{d\xi_3} + \frac{\gamma}{\gamma-1}P_3^{(\gamma-1)/\gamma}\frac{d}{d\xi_3}\left(\frac{P_2^{1/\gamma}}{Q_2}\right)$$

$$\frac{\gamma}{\gamma-1}\frac{d}{d\xi_3}\left(\frac{P_3}{Q_3}\right) = \frac{1}{Q_3}\frac{dP_3}{d\xi_3} + \frac{\gamma}{\gamma-1}\frac{P_3}{P_2^{1/\gamma}}\frac{d}{d\xi_2}\left(\frac{P_2^{1/\gamma}}{Q_2}\right)\frac{\phi_3\xi_3}{\phi_2\xi_2} \tag{16}$$

Using the radial momentum equation at station 3 immediately downstream of the rotor blading,

$$(1/Q_3)\,(\partial P_3/\partial\xi_3) = (\lambda_3^2/\xi_3) - [\theta_3(\partial\theta_3/\partial\xi_3)] - [\phi_3(\partial\theta_3/\partial\zeta_3)] \tag{11}$$

substituting Eqs. (11) and (16) into (15), and using the differential form of the mass flow relation, Eq. (8), for the ratio $d\xi_2/d\xi_3$, the following differential equation is obtained.

$$\frac{\lambda_3^2}{\xi_3} + \frac{1}{2}\frac{\partial}{\partial\xi_3}\,(\lambda_3^2+\phi_3^2) + \frac{\partial(\xi_3\lambda_3)}{\partial\xi_3} = \left(\frac{P_3}{P_2}\right)^{1/\gamma}\frac{\phi_3\xi_3}{\phi_2\xi_2}\left[\frac{\gamma}{\gamma-1}\frac{\partial\tau_{2t}}{\partial\xi_2} - \frac{\partial(\xi_2\lambda_2)}{\partial\xi_2} - \frac{\gamma}{\gamma-1}\tau_2\left(\frac{P_3}{P_2}\right)^{(\gamma-1)/\gamma}\frac{\partial}{\partial\xi_2}\left(\ln\frac{P_2^{1/\gamma}}{Q_2}\right)\right] + \phi_3\frac{\partial\theta_3}{\partial\zeta_3} \tag{17}$$

For a cascade with an infinite number of blades, the exit flow is parallel to the tangent of the camber line at the trailing edge, and its direction is independent of the direction of flow approaching the cascade. For most practical applications, the direction of flow leaving the cascade is very nearly constant and independent of the inlet direction throughout the design operating range. With this assumption for the rotor, it is therefore assumed that the rotor spouting angle β_3 is a known function of radius at station 3. Using the turbine sign convention shown in Fig. 2, it is therefore possible to describe the relation between λ_3 and ϕ_3 along the radius at station 3 with a function $G(\xi_3)$ such that:

$$\lambda_3 = G(\xi_3)\phi_3 - \xi_3 \tag{18}$$

Eliminating λ_3 from Eq. (17) with the above relation, the following differential equation is obtained:

$$\frac{\partial\phi_3}{\partial\xi_3} + \phi_3\left[\frac{G^2}{\xi_3\,(1+G^2)} + \frac{1}{2(1+G^2)}\frac{\partial(1+G^2)}{\partial\xi_3}\right] = \frac{1}{1+G^2}\left\{\left(\frac{P_3}{P_2}\right)^{1/\gamma}\frac{\xi_3}{\phi_2\xi_2}\left[\frac{\gamma}{\gamma-1}\frac{\partial\tau_{2t}}{\partial\xi_2} - \frac{\partial(\xi_2\lambda_2)}{\partial\xi_2} - \frac{\gamma}{\gamma-1}\tau_2\left(\frac{P_3}{P_2}\right)^{(\gamma-1)/\gamma}\frac{\partial}{\partial\xi_2}\left(\ln\frac{P_2^{1/\gamma}}{Q_2}\right)\right] + \frac{\partial\theta_3}{\partial\zeta_3} + 2G\right\} \tag{19}$$

If P_3, ξ_3, $\partial\theta_3/\partial\zeta_3$, and the known quantities at station 2 are considered to be functions of ξ_3 (to be determined in the iteration process), the integral for the dimension-

less axial velocity ϕ_3 can be immediately written down as:

$$\phi_3 = \frac{e^{+\int_{\xi_i}^{\xi_3} \frac{d\xi_3}{\xi_3(1+G^2)}}}{\xi_2\sqrt{1+G^2}}\left(\int_{\xi_i}^{\xi_3} e^{-\int_{\xi_i}^{\xi_3}\frac{d\xi_3}{\xi_3(1+G^2)}}\left\{\frac{1}{\sqrt{1+G^2}}\left(\frac{P_3}{P_2}\right)^{1/\gamma}\frac{\xi_3}{\phi_2\xi_2}\left[\frac{\gamma}{\gamma-1}\frac{d\tau_{2t}}{d\xi_2} - \frac{d(\xi_2\lambda_2)}{d\xi_2} - \frac{\gamma}{\gamma-1}\tau_2\left(\frac{P_3}{P_2}\right)^{(\gamma-1)/\gamma}\frac{d}{d\xi_2}\left(\ln\frac{P_2^{1/\gamma}}{Q_2}\right)\right] + \frac{1}{\sqrt{1+G^2}}\left(2G + \frac{d\theta_3}{d\zeta_3}\right)\right\}\xi_3 d\xi_3 + C_1\right) \quad (20)$$

It is noted that no linearization has been performed in arriving at the above integral. The expression for ϕ_3 is complicated, but its numerical evaluation by a simple iteration process to be described later is straightforward. Once a set of streamlines have been assumed, all factors involving the upstream conditions become known functions of ξ_3. In the solution of the direct problem, it is assumed that $G(\xi_3)$ is a given function of ξ_3. Thus in the integrand, P_3 and $d\theta_3/d\zeta_3$ are the unknowns that must be determined in the iteration process in order to evaluate the integral.

An alternate form for the square bracket in the integrand can be obtained by using the energy and radial momentum equations at station 2:

$$\left\{\frac{\lambda_2^2}{\xi_2} - \phi_2\frac{d\theta_2}{d\zeta_2} + \frac{1}{2}\frac{d}{d\xi_2}(\lambda_2^2 + \phi_2^2) - \frac{d(\xi_2\lambda_2)}{d\xi_2} - \frac{\gamma}{\gamma-1}\tau_2\left[\left(\frac{P_3}{P_2}\right)^{(\gamma-1)/\gamma} - 1\right]\frac{d}{d\xi_2}\left(\ln\frac{P_2^{1/\gamma}}{Q_2}\right)\right\} \quad (21)$$

In the case that $P_{2t} = 1$ (isentropic expansion to station 2 from stagnation conditions), the bracketed term in the integrand of Eq. (20) may be further simplified to:

$$\left[\frac{\gamma}{\gamma-1}\frac{d\tau_{2t}}{d\xi_2}(1 - P_3^{(\gamma-1)/\gamma}) - \frac{d}{d\xi_2}(\xi_2\lambda_2)\right] \quad (22)$$

The constant of integration C_1 is determined by integrating Eq. (8). The integrated form of this relation equates the total flow rate upstream to that at station 3:

$$m = \int_{\xi_i}^{\xi_3} Q_2\left(\frac{P_3}{P_2}\right)^{1/\gamma}\phi_3\xi_3 d\xi_3 \quad (23)$$

Using Eq. (13) in Eq. (11), the integral form of the radial momentum equation becomes:

$$P_3 = \left[\frac{\gamma-1}{\gamma}\left(\frac{Q_2}{P_2^{1/\gamma}}\right)\int_{\xi_i}^{\xi_3}\left(\frac{\lambda_3^2}{\xi_3} - \theta_3\frac{d\theta_3}{d\xi_3} - \phi_3\frac{d\theta_3}{d\zeta_3}\right)d\xi_3 + C_2\right]^{\gamma/(\gamma-1)} \quad (24)$$

The constant of integration C_2 is obtained by applying the energy relation [Eq. (10)] at a boundary.

Having assumed a set of stream surfaces for a particular boundary configuration, the value of $d\theta_3/d\zeta_3$ can be approximated from the values of the slope and rate of change of slope of these stream surfaces at station 3. At each point on a streamline at station 3, the following relation must hold:

$$\theta_3 = \phi_3(df/d\zeta)_3 \quad (25)$$

where $(df/d\zeta)_3$ is the slope of the streamline in question. Thus the value of $d\theta_3/d\zeta_3$ becomes:

$$d\theta_3/d\zeta_3 = (d\phi_3/d\zeta_3) + (df/d\zeta)_3\,[\phi_3(d^2f/d\zeta^2)_3] \quad (26)$$

In order to approximate the value of $d\theta_3/d\zeta_3$ at points across the channel, it is therefore necessary to estimate the slope and curvature of the assumed streamlines at each point.

For the isentropic solution of the direct problem for the rotor with an arbitrary channel shape, Eqs. (10), (13), (18), (20), (23), (24), and (26) are applicable.

The derivation of the integral for the axial velocity in the case of the stator is carried out in a similar fashion using the form of the energy relation given as Eq. (9). With the sign convention of Fig. (2), Eq. (18) for the stator (stations 1 to 2) becomes:

$$\lambda_2 = F(\xi_2)\phi_2 \quad (27)$$

The integral for ϕ_2 obviously takes the same form as Eq. (20), and is given here only for completeness:

$$\phi_2 = \frac{e^{+\int_{\xi_i}^{\xi_2}\frac{d\xi_2}{\xi_2(1+F^2)}}}{\xi_2\sqrt{1+F^2}}\left(\int_{\xi_i}^{\xi_2} e^{-\int_{\xi_i}^{\xi_2}\frac{d\xi_2}{\xi_2(1+F^2)}}\left\{\frac{1}{\sqrt{1+F^2}}\left(\frac{P_2}{P_1}\right)^{1/\gamma}\frac{\xi_2}{\phi_1\xi_1}\left[\frac{\gamma}{\gamma-1}\frac{d\tau_{1t}}{d\xi_1} - \frac{\gamma}{\gamma-1}\tau_1\left(\frac{P_2}{P_1}\right)^{(\gamma-1)/\gamma}\frac{d}{d\xi_1}\left(\ln\frac{P_1^{(1/\gamma)}}{Q_1}\right)\right] + \frac{1}{\sqrt{1+F^2}}\frac{d\theta_2}{d\zeta_2}\right\}\xi_2 d\xi_2 + C_1\right) \quad (28)$$

For the isentropic solution of the direct problem for the stator with an arbitrary channel shape, Eqs. (9), (12), (23), (24), (26), (27), and (28) (with appropriate subscripts) are applicable.

(2.3) *Equations for the Direct Problem for Polytropic Flow*

The equations for a polytropic process through a rotor are derived with the same assumptions as used in the preceding section with the exception that the isentropic relation (13) is now replaced by:

$$Q_3/Q_2 = (P_3/P_2)^{1/n} = (\tau_3/\tau_2)^{1/(n-1)} \quad (29)$$

where n is related to the so-called polytropic efficiency η for an expansion ($n < \gamma$) by: (reference 15, p. 449)

$$[n/(n-1)]\eta = \gamma/(\gamma-1) \quad (30)$$

The continuity equation, Eq. (8), the energy equation, Eq. (10), the radial momentum equation, Eq. (11) and the blade angle relation, Eq. (18), remain the same in differential form. The resulting integral for the axial velocity for the polytropic case can be derived in the same general form as Eq. (20) with an additional

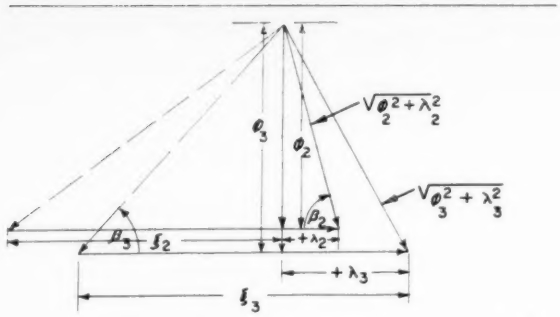

Stator: $\cot \beta_2(\xi_2) = F(\xi_2) = \dfrac{\lambda_2}{\phi_2}$ Rotor: $\cot \beta_3(\xi_3) = G(\xi_3) = \dfrac{\xi_3 - \lambda_3}{\phi_3}$

FIG. 3 TYPICAL COMPRESSOR - VELOCITY DIAGRAM SHOWING SIGN CONVENTION

term in the integrand as follows:

$$\phi_3 = \frac{e^{+\int_{\xi_i}^{\xi_3} \frac{d\xi_3}{\xi_3(1+G^2)}}}{\xi_3\sqrt{1+G^2}}\left(\int_{\xi_i}^{\xi_3} e^{-\int_{\xi_i}^{\xi_3} \frac{d\xi_3}{\xi_3(1+G^2)}} \left\{\frac{1}{\sqrt{1+G^2}}\left(\frac{P_3}{P_2}\right)^{1/n}\frac{\xi_2}{\phi_2\xi_2}\left[\frac{\gamma}{\gamma-1}\frac{d\tau_{2l}}{d\xi_2} - \frac{d(\xi_2\lambda_2)}{d\xi_2} - \frac{\gamma}{\gamma-1}P_3^{(n-1)/n}\frac{d}{d\xi_2}\left(\frac{P_2^{1/n}}{Q_2}\right)\right] + \frac{1}{\sqrt{1+G^2}}\left[2G + \frac{d\theta_3}{d\zeta_3} + \frac{1}{\phi_3}\frac{(\gamma-n)}{(\gamma-1)(n-1)}\left(\frac{P_2^{1/n}}{Q_2}\right)\frac{dP_3^{(n-1)/n}}{d\xi_3}\right]\right\} \times \xi_3 d\xi_3 + C_1\right) \quad (31)$$

The integrated form of the mass flow equation is

$$m = \int_{\xi_i}^{\xi_3} Q_2\left(\frac{P_3}{P_2}\right)^{1/n}\phi_3\xi_3 d\xi_3 \quad (32)$$

and the integral form of the radial momentum equation is:

$$P_3 = \left[\frac{n-1}{n}\left(\frac{Q_2}{P_2^{1/n}}\right)\int_{\xi_i}^{\xi_3}\left(\frac{\lambda_3^2}{\xi_3} - \theta_3\frac{d\theta_3}{d\xi_3} - \phi_3\frac{d\theta_3}{d\zeta_3}\right)d\xi_3 + C_2\right]^{n/(n-1)} \quad (33)$$

Eqs. (10), (18), (26), (29), (31), (32), and (33) are used in the solution of the polytropic direct problem for the rotor.

In the case of the stator for polytropic flow, Eq. (27) is used in place of Eq. (18), and the resulting integral for the axial velocity is similar to Eq. (31) with G replaced by F and the terms $(d/d\xi_2)(\xi_2\lambda_2)$ and $2G$ omitted. Eqs. (9), (26), (29), (32), and (33) are applicable (with appropriate subscripts).

(2.4) *Equations for the Inverse Problem for Isentropic Flow*

In the inverse problem for the rotor, the boundary configuration, blade speed, blade loading, and fluid state ahead of the rotor section are assumed known, and the blade spouting angle, velocity field, and energy distribution behind the rotor are to be determined. Thus the same basic assumptions and differential equations are used as in the isentropic direct problem with the exception that now the blade relation, Eq. (18), is replaced by the following given function which describes the work output of the rotor as a function of the radius at station 3:

$$H(\xi_3) = \xi_2\lambda_2 + \xi_3\lambda_3 \quad (34)$$

The function $H(\xi_3)$ gives the dimensionless rate of change of angular momentum per unit mass flow at the particular radius and represents the energy taken out of the stream. By multiplying this function by suitable constants it can readily be converted to B.t.u. per pound of mass flow.

For the isentropic inverse problem, the derivation remains the same up to and including Eq. (17). Using Eq. (34) to eliminate λ_3, the integral for the axial velocity is found to be:

$$\phi_3 = \int_{\xi_i}^{\xi_3}\left\{\left(\frac{P_3}{P_2}\right)^{1/\gamma}\frac{\xi_3}{\phi_2\xi_2}\left[\frac{\gamma}{\gamma-1}\frac{d\tau_{2l}}{d\xi_2} - \frac{\gamma}{\gamma-1}\times P_3^{(\gamma-1)/\gamma}\frac{d}{d\xi_2}\left(\frac{P_2^{1/\gamma}}{Q_2}\right) + \frac{(H-\xi_2\lambda_2)}{\xi_3^2}\frac{d}{d\xi_2}(\xi_2\lambda_2)\right] + \frac{d\theta_3}{d\zeta_3} - \frac{1}{\phi_3}\left(1 + \frac{H-\xi_2\lambda_2}{\xi_3^2}\right)\frac{dH}{d\xi_3}\right\}d\xi_3 + C_1 \quad (35)$$

Again the numerical evaluation of this integral by the iteration process to be described later is straightforward once a set of streamlines has been assumed. The unknowns P_3 and $d\theta_3/d\zeta_3$ appear in the integrand as in the direct problem. Because of the nature of the differential equation, however, the axial velocity ϕ_3 also appears in the integrand.

Since the mass flow and radial momentum integrals remain unchanged, Eqs. (10), (13), (23), (24), (26), (34), and (35) are applicable to the solution of the isentropic inverse problem.

If the inverse problem could be conceivably applied to a stator, it would consist of prescribing values of λ_2 as a function of ξ_2 and solving for the resulting velocity field, distribution of energy, and blade shape (as described by the blade trailing-edge angle). In this case, the integral for the axial velocity simplifies to:

$$\phi_2 = \int_{\xi_i}^{\xi_2}\left\{\left(\frac{P_2}{P_1}\right)^{1/\gamma}\frac{\xi_2}{\phi_1\xi_1}\left[\frac{\gamma}{\gamma-1}\frac{d\tau_{1l}}{d\xi_1} - \frac{\gamma}{\gamma-1}P_2^{(\gamma-1)/\gamma}\frac{d}{d\xi_1}\left(\frac{P_1^{1/\gamma}}{Q_1}\right)\right] + \frac{d\theta_2}{d\zeta_2} - \frac{\lambda_2}{\phi_2\xi_2}\frac{d}{d\xi_2}(\xi_2\lambda_2)\right\}d\xi_2 + C_1 \quad (36)$$

where $\lambda_2(\xi_2)$ is a prescribed function of the radius at station 2. Eqs. (9), (12), (23), (24), (26), and (36) (with appropriate subscripts) would be applicable.

(2.5) *Equations for the Inverse Problem for Polytropic Flow*

The resulting integral for the axial velocity at station 3 for polytropic flow is similar to Eq. (35) of the preceding section with the addition of a correction term:

$$\phi_3 = \int_{\xi_t}^{\xi_3} \left\{ \left(\frac{P_3}{P_2}\right)^{1/n} \frac{\xi_3}{\phi_2 \xi_2} \left[\frac{\gamma}{\gamma - 1} \frac{d\tau_{2t}}{d\xi_2} - \frac{\gamma}{\gamma - 1} \times P_3^{(n-1)/n} \frac{d}{d\xi_2} \left(\frac{P_2^{1/n}}{Q_2} \right) + \frac{(H - \xi_2\lambda_2)}{\xi_3^2} \frac{d}{d\xi_2} (\xi_2\lambda_2) \right] + \frac{d\theta_3}{d\xi_3} + \frac{1}{\phi_3} \left[\frac{(\gamma - n)}{(\gamma - 1)(n - 1)} \left(\frac{P_2^{1/n}}{Q_2} \right) \frac{dP_3^{(n-1)/n}}{d\xi_2} - \left(1 + \frac{H - \xi_2\lambda_2}{\xi_3^2} \right) \frac{dH}{d\xi_3} \right] \right\} d\xi_3 + C_1 \quad (37)$$

Eqs. (10), (26), (29), (32), (33), (34), and (37) are used in the solution of the polytropic inverse problem for the rotor.

(2.6) *Changes in Equations for the Compressor Solution*

In the development of the equations in the preceding sections, the turbine sign convention given in Fig. 2 has been adopted. If the equations are to be used for compressor design, Eq. (18) for the direct rotor problem becomes, in accordance with Fig. 3:

$$\lambda_3 = \xi_3 - G(\xi_3)\phi_3 \quad (38)$$

and the energy relation, Eq. (10), is changed to:

$$[\gamma/(\gamma - 1)](P_2/Q_2) + (1/2)(\theta_2^2 + \lambda_2^2 + \phi_2^2 - 2\xi_2\lambda_2) = [\gamma/(\gamma - 1)](P_3/Q_3) + (1/2)(\theta_3^2 + \lambda_3^2 + \phi_3^2 - 2\xi_3\lambda_3) \quad (39)$$

Using these equations, the derivation is carried out in exactly the same manner as set forth in the preceding sections for the turbine.

For the inverse problem for the compressor, the work output function [Eq. (34)] becomes:

$$H(\xi_3) = \xi_2\lambda_2 - \xi_3\lambda_3 \quad (40)$$

Using Eqs. (39) and (40) in place of Eqs. (10) and (34), the relations for the inverse compressor problem are derived in the same manner as for the turbine.

(3) Iteration Procedure

(3.1) *Procedure for the Direct Problem*

The general scheme of iteration is exactly the same for the direct and inverse problems, subsonic or supersonic, isentropic or polytropic. In Example 2 of the Appendix, one complete iteration is given for a typical rotor solution for the isentropic direct problem. In the examples presented, the blade trailing edge angle functions $F(\xi_2)$ and $G(\xi_3)$ have been assumed to be constant and independent of radius in order to simplify the axial velocity integral and the computation. This assumption is by no means necessary. For arbitrary given functions $F(\xi_2)$ and $G(\xi_3)$, the exponential integrals of Eq. (20) should be evaluated at various stations

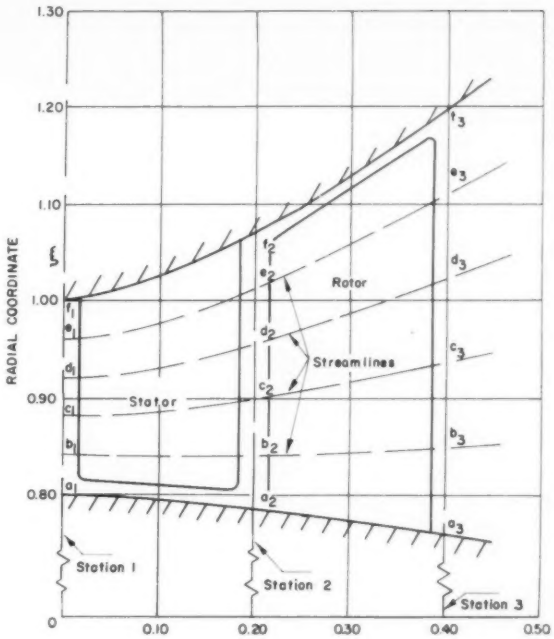

FIG. 4 CHANNEL CONFIGURATION AND COORDINATES FOR EXAMPLES 1 AND 2

across the channel by plotting the integrand and determining the value of the integral graphically.

In the solution of the direct problem, it is assumed that the boundary configuration, blade speed, blade trailing edge angle, and upstream conditions are prescribed. It is further assumed that the mass flow rate is fixed and is compatible with the given upstream conditions.

Once the problem has been set up, the first step is to assume a set of stream surfaces as shown in Fig. 4. For most applications, these stream surfaces should be chosen on the basis of equal annular areas in a plane perpendicular to the axis of the machine. The accuracy of the solution can be improved by increasing the number of stations across the channel. However, it is believed that for most purposes, six or seven steps will give sufficient accuracy for design work.

Having assumed a reasonable set of streamlines, the second step is to estimate the axial velocity distribution at the downstream station. Taking average or middle-channel values for the prescribed upstream conditions, the mass flow relation and the energy equation for the rotor can be combined into one equation in terms of ϕ_3. Using average values in Eqs. (10) and (23), the relation is obtained as follows:

$$\bar{\tau}_3 = \bar{\tau}_{2t} - [(\gamma - 1)/2\gamma][\bar{\theta}_3^2 + \bar{\lambda}_3^2 + \bar{\phi}_3^2 + 2(\overline{\xi_2\lambda_2} + \overline{\xi_3\lambda_3})] \quad (41)$$

$$m = \bar{Q}_2(\bar{\tau}_3/\bar{\tau}_2)^{1/(\gamma-1)}\,\bar{\phi}_3\,[(\xi_0^2 - \xi_t^2)]/2 \quad (42)$$

Substituting Eq. (41) into Eq. (42) gives:

$$m = \bar{Q}_2 \left\{ \frac{\bar{\tau}_{2t} - [(\gamma - 1)/2\gamma][\bar{\theta}_3^2 + \bar{\lambda}_3^2\bar{\phi}_3^2 + 2(\bar{\xi}_2\bar{\lambda}_2 + \bar{\xi}_3\bar{\lambda}_3)]}{\bar{\tau}_2} \right\}^{1/(\gamma-1)} \bar{\phi}_3 \left(\frac{\xi_0^2 - \xi_i^2}{2} \right) \tag{43}$$

Using Eq. (18) to eliminate $\bar{\lambda}_3$ and Eq. (25) to eliminate $\bar{\theta}_3$, Eq. (43) becomes a relation involving only one unknown, $\bar{\phi}_3$. The solution must be found by trial and error. In general, there will be two values of $\bar{\phi}_3$ for a given mass flow which satisfy this equation and correspond to average subsonic and supersonic solutions as is illustrated in Fig. 5. If no value of $\bar{\phi}_3$ satisfies Eq. (43), the prescribed mass flow cannot be forced through the channel because of choking, and the boundary configuration or upstream conditions must be altered accordingly.

Having determined the average value of the axial velocity at station 3, an estimate of the distribution of this velocity across the channel can be made considering the total temperature gradient, the blade shape, and the pressure distribution expected at the downstream station.

For an arbitrary channel shape, seven equations are used in the solution. For the direct isentropic rotor problem, these relations are Eqs. (10), (13), (18), (20), (23), (24), and (26). Using the estimated radial distribution of the axial velocity obtained from a consideration of average values, Eq. (24) is iterated across the channel to determine the pressure gradient. The tangential velocity distribution is found from Eq. (18), the radial velocity from Eq. (25), and the value of $d\theta_3/d\zeta_3$ from Eq. (26). In order to evaluate θ_3, $d\theta_3/d\xi_3$, and $d\theta_3/d\zeta_3$ at various points across the channel, it is necessary to estimate as accurately as possible the slope and curvature of each streamline at the station in question. Knowing the complete channel configuration, slopes, and curvatures at points across the channel can be easily estimated using a simple linear distribution scheme, or a large scale drawing can be constructed and the values of slope and curvature taken graphically from this. The value of $d\phi_3/d\zeta_3$ in Eq. (26) can be taken as the average value between stations along the axis. However, it is to be noted that even a relatively large error in the estimation of the above quantities will have little effect upon the pressure gradient obtained because of the nature of the integrated form of Eq. (24). The actual pressure distribution across the channel is found by applying the energy equation at a boundary to determine the constant C_2.

With these values of P_3 and $d\theta_3/d\zeta_3$, the axial velocity integral can now be iterated across the channel for values of ϕ_3 in terms of the constant C_1. If the curvature of the channel is not large, the value of $d\theta_3/d\zeta_3$ is very small compared to the other factors in the integrand ($2G$, for example), and hence a relatively large error in estimating $d\theta_3/d\zeta_3$ has a small effect on the resulting value of ϕ_3. The constant C_1 is obtained by iterating the mass flow relation (23) across the channel, and a new axial velocity distribution is obtained.

The above described process is the procedure for one complete iteration of the given equations. Normally in the subsonic case, the distribution of ϕ_2 thus obtained is used in the next iteration, and the process is repeated until the axial velocity distribution produced by an iteration is the same as that assumed for that particular iteration. This is the solution. Values of τ_2 and Q_2 are then found by use of Eq. (13).

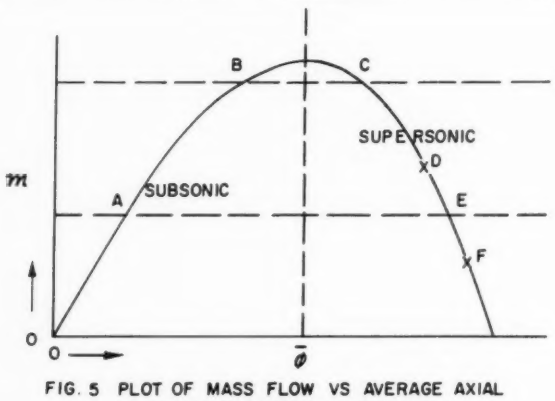

FIG. 5 PLOT OF MASS FLOW VS AVERAGE AXIAL VELOCITY FOR CHANNEL FLOW

(3.2) *Procedure for the Inverse Problem*

Generally, the same procedure of iteration, as described above for the direct problem, is used in the solution of the inverse problem. Eqs. (10), (13), (23), (24), (26), (34), and (35) are applicable for the isentropic inverse rotor solution.

It is noted that the integrand of Eq. (35) contains a term involving $1/\phi_3$. Since in any practical solution the axial velocity at any point across the channel will not be zero, this term does not cause any real difficulty in the iteration procedure. However, if the original estimate of the axial velocity profile at the downstream station differs greatly from the actual solution, it has been found that successive iterations will "oscillate" about the real solution but will eventually converge as in the direct problem.

It is obvious that the work output function $H(\xi_3)$, given as Eq. (34), must be prescribed reasonably. For any given channel shape, blade speed, upstream conditions, and mass flow, there is a limited range of blade angles which can be used before the smooth flow over the blades is destroyed by separation effects. The limitation thus imposed by the maximum turning angle through the blade row also limits not only the amount of work that can be extracted, but also the distribution of this work across the channel.

(3.3) *Convergence of Subsonic and Supersonic Solutions*

Fig. 5 indicates that, for any given setup, there is normally a supersonic as well as a subsonic solution for the direct and inverse problems. Experience in work-

ing various types of examples has shown that if the flow is in the low subsonic range, point A of Fig. 5, for example, the iteration process converges very rapidly, and only two or three iterations are necessary to obtain an accuracy of four significant figures in the solution. However as the flow becomes highly subsonic, as at point B, the convergence becomes less rapid, and more iterations are necessary to obtain the solution. It is interesting to note that, in the subsonic range, the process will converge from any reasonable assumed distribution of the axial velocity. It is even possible to obtain a solution in which the flow is supersonic in one part of the channel and subsonic in the remainder (Example 1).

It has been found, however, that if the flow is completely supersonic (point E of Fig. 5, for example), the iteration process diverges rapidly away from the solution. Thus if an axial velocity distribution is assumed whose average value is represented by point D, successive iterations will result in decreasing values of ϕ_3, and eventually the subsonic solution at point A will be reached. If an axial velocity distribution corresponding to point F is assumed, successive iterations will rapidly increase ϕ_3 toward infinity. It is the realization of this phenomenon which makes it possible to obtain the isentropic supersonic solution in a given problem. Having made two successive iterations at each of the points D and F and having noted the relative change in the constant C_1 in these iterations, a simple interpolation will give the values of ϕ_3 corresponding to the solution at point E once the solution has been "straddled."

It is important to point out the basic reason why the proposed iteration process is successful. For either the direct or inverse problems, six unknowns must be solved for at the downstream station. These are the three components of velocity, the pressure, the density, and the temperature. Using the isentropic (or polytropic) relation along stream surfaces, two of these (Q_3 and τ_3) can be eliminated. The remaining four unknowns are made functions of the axial velocity ϕ_3 and the boundary and streamline configuration. The radial velocity is eliminated in terms of ϕ_3 by Eq. (25), the tangential velocity λ_3 by Eq. (18) or Eq. (34), and the pressure P_3 by the integral, Eq. (24). Thus, effectively, only one unknown remains, the axial velocity ϕ_3, and for any assumed distribution of ϕ_3, all other unknowns are determined. An iteration process must be used to determine ϕ_3 because of the complexity of the equations involved.

(3.4) *Correction for the Displacement of Streamlines*

Having assumed a set of stream surfaces for any particular example and having found the corresponding solution by the proposed iteration procedure, it is possible to make a correction to determine more accurately the actual position of the stream surfaces and thus refine the solution. The mass flow functions $m(\xi_2)$ and $m(\xi_3)$ are plotted against radius for conditions at stations 2 and 3 as is shown in Fig. 6 for Example 2 of the Appendix. Using this diagram and fixing the radial coordinates at station 3, it is possible to estimate new corresponding upstream coordinates. With these corrected upstream radial coordinates and the upstream conditions corresponding to them, the problem is reworked and a new solution found. It is to be emphasized that this is a small correction and that the new solution will not vary more than one or two per cent from the solution based on the original stream surfaces. An illustration of this method is given in Example 2 of the Appendix.

(4) Additional Corrections and Simplifications

(4.1) *Corrections to the Basic Solution*

If it is desired to solve for the flow pattern and distribution of energy in the field at any axial station in the blade row itself, this can be done approximately by multiplying the axial velocity by a function that accounts for the blade thickness and thus reduces the effective area of the channel. Assuming a blade thickness function $t(\zeta)$ and a blade spacing s, the increased axial velocity at any point within the blade row would be:

$$(\phi)_\zeta = \phi \left\{ s / [s - t(\zeta)] \right\} \tag{44}$$

where s and $t(\zeta)$ are assumed to be known functions at any radial position across the channel. The assumptions used in the direct problem, including that of axial

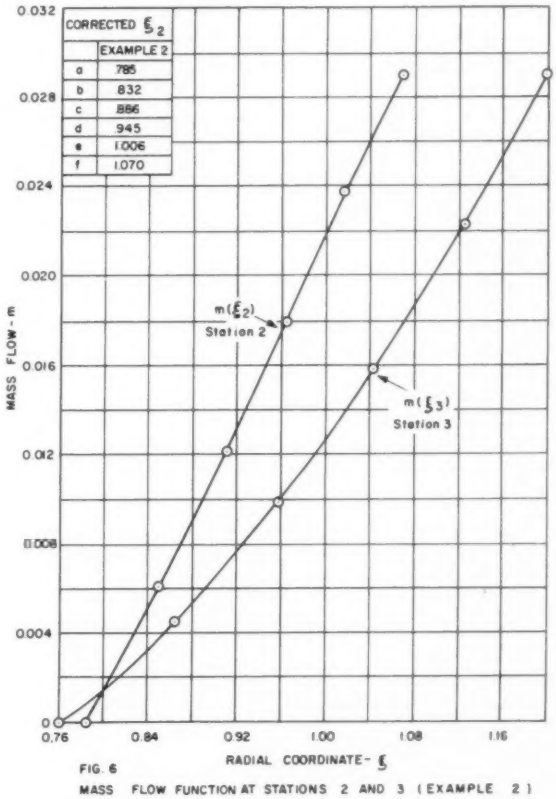

FIG. 6
MASS FLOW FUNCTION AT STATIONS 2 AND 3 (EXAMPLE 2)

symmetry, remain unchanged, except that the blade spouting angle now becomes the mean camber line at the point in question. The fundamental equations and iteration procedure remain unchanged except for the use of the above indicated expression for the axial velocity.

One of the basic assumptions used in the derivation of the fundamental equations given in Section (2) is that the effects of the vorticity of the flow downstream on upstream conditions are negligible. A correction to the upstream conditions due to vorticity effects downstream could be made using the approximate theory suggested by Marble[7] for the three-dimensional case. If the hub ratio is large, the simpler two-dimensional approximation given by Rannie[10] can be used. Once the upstream conditions have been changed using this higher order correction, the corresponding new solution can then be found by the same procedure previously outlined.

(4.2) *Simplification of Flow Patterns*

An investigation has been made to determine whether or not there are any special cases in which the equations, used in this analysis of three-dimensional, compressible flow, reduce to a simple expression for the axial velocity. Consider the integrated radial momentum relation given as Eq. (24). Since the value of P_3 appears in the integrated mass flow relation, Eq. (23), to the power $1/\gamma$, it is clear that, generally, no simplification can be made for a channel of arbitrary shape where the values of $\theta_3(d\theta_3/d\xi_3)$ and $\phi_3(d\theta_3/d\zeta_3)$ cannot be expressed in terms of constants and the radius ξ_3.

However, one simplification does occur in the example of a rotor section in a cylindrical channel. In this case, if the velocity after the rotor is purely axial, Eq. (24) reduces to $P_3 = {C_2}^{\gamma/(\gamma-1)}$. If, in addition, the total temperature and pressure are constant across the channel at station 2 and if $\lambda_2 = \alpha/\xi_2$ (vortex flow), Eq. (17) for a straight channel reduces to $\phi_3 = C_1$. The constant C_2 is evaluated by applying the energy equation at a boundary, and the mass flow integral becomes:

$$m = \int_{\xi_i}^{\xi_0} \frac{1}{\tau_{2t}} \left(1 - \frac{\gamma - 1}{2\gamma} \frac{C_1^2}{\tau_{2t}}\right)^{1/(\gamma-1)} C_1 \xi_1 d\xi_1 \quad (45)$$

or, since τ_{2t} is constant,

$$m = \frac{C_1}{\tau_{2t}} \left(1 - \frac{\gamma - 1}{2\gamma} \frac{C_1^2}{\tau_{2t}}\right)^{1/(\gamma-1)} \frac{{\xi_0}^2 - {\xi_i}^2}{2} \quad (46)$$

Even in this simplified case, Eq. (46) must be solved by trial and error for the constant C_1. This particular example gives a constant mass flow per unit area, and the work is taken out uniformly across the channel.

With the exception of the above case, it can be generally stated that there are no special conditions or flow patterns in three-dimensional compressible flow through turbomachinery using this method which result in a simple closed-form solution for the downstream axial velocity.

(4.3) *Proposed Optimum Turbine Design Condition*

In the design of a turbine, the condition that normally controls the amount of heat that can be released in the combustion chamber is the limiting temperature that the first stage rotor blade root can safely withstand in continuous operation. Since the blade stresses decrease from root to tip, the allowable temperature is higher at the tip than at the root. This fact allows the possibility of increasing the amount of heat released in the combustion chamber, and hence the energy in the jet exhaust, for a fixed amount of work taken out of a turbine.

In formulating the optimum turbine design condition, reference will be made to a one-stage turbine with an arbitrary, but fixed, boundary configuration, such as is shown in Fig. 4. It is assumed that the total pressure in the combustion chamber, the blade speed, mass flow, and total amount of work to be extracted by the turbine are fixed by conditions in the compressor. It is further assumed that the distribution of the maximum allowable total temperature across the channel at station 2 upstream of the rotor, based on limiting blade temperatures, is known. Since the total enthalpy is conserved through the stator row, the limiting total temperature profile at station 1 is therefore known.

In order that the maximum energy be left in the exhaust gases at station 3, the condition is imposed that the velocity shall be axial after the turbine ($\lambda_3 = 0$) and that the total enthalpy shall be constant across the channel at this station ($d\tau_{3t}/d\xi_3 = 0$).

To simplify the formulation of the proposed optimum turbine design condition, it is assumed that the known limiting total temperature profile at station 1 is linear and that the combustion chamber can be constructed so as to give this desired total temperature variation across the channel.

The design problem can then be formulated as follows: Given a one-stage turbine with fixed boundary configuration, combustion chamber total pressure, blade speed, mass flow, and linear total temperature profile at station 1, what are the blade spouting angles of stator and rotor so that a given amount of work can be extracted by the rotor and yet leave the total temperature constant and the velocity axial at station 3?

With the above assumptions and conditions, Eq. (34) can be written:

$$H(\xi_3) = \xi_2 \lambda_2 \quad (47)$$

and Eq. (10) in terms of total temperatures becomes:

$$[\gamma/(\gamma - 1)]\tau_{2t} - \xi_2\lambda_2 = [\gamma/(\gamma - 1)]\tau_{3t} \quad (48)$$

If τ_{3t} is to be constant at station 3, then the work must be taken out across the channel in such a way that:

$$\Delta\xi_2\lambda_2 = \Delta[\gamma/(\gamma - 1)]\tau_{2t} \quad (49)$$

Since the linear change in total temperature at station 2 is assumed known, the distribution of work across the channel is determined by Eq. (49) and by the total amount of work to be extracted.

In view of the discussion given previously on limiting blade angles, it will obviously not always be possible to obtain the above proposed optimum condition, particularly if the upstream total temperature gradient is large. Furthermore, the above considerations could not reasonably apply to a multistage turbine since boundary-layer effects and mixing would soon destroy the original total temperature profile. However, the designer should not overlook the possibility of increasing the gross thrust of a turbine by the use of a total enthalpy gradient based on blade limiting temperatures.

(5) Other Results and Conclusions

Once the boundary configuration and other necessary conditions have been assumed for any particular problem, experience in working various examples by the proposed iteration process has shown that a basic solution for the direct problem accurate to four significant figures can be obtained for a stator in approximately four hours and can be obtained for a rotor in approximately six hours. The calculations for the inverse problem are somewhat simpler and less time is normally required for this solution.

Solutions to various types of problems in three-dimensional, compressible turbine flow have been obtained by the method proposed in this paper, and some of the results are of special significance. For example, both the subsonic and supersonic solutions have been calculated for a turbine rotor section similar to that shown in Fig. 4. The mass flow functions at stations 2 and 3 were then plotted against the radial co-ordinate, and the position of the displaced streamlines was estimated for the subsonic and supersonic case. A plot of the streamline shift for this example is given in Fig. 7 and clearly indicates that the shift is in one direction when the "governing" Mach Number is subsonic and in the opposite direction when the "governing" Mach Number is supersonic. The "governing" Mach Number has been defined by Monroe[1] as the Mach Number based on the meridional velocity instead of the total velocity. The results given in Fig. 7 agree with the Mach Number area rule and Monroe's observation that the deflection of the "meridional Mach surfaces" is in different directions for subsonic and supersonic "governing" Mach Numbers.

Examples have been worked out for a turbine section which show the effect of a decrease in "polytropic efficiency" on the three-dimensional velocity field and distribution of energy in the flow. For a given channel configuration, blade speed, blade spouting angle distribution, and mass flow, the results of the calculations show that when the efficiency has dropped to 94.5 per cent, the average axial velocity at station 3 has increased 2.7 per cent, the average total pressure has decreased 2.5 per cent, and the work absorbed has increased 4.7 per cent when compared with the isentropic solution. When the "polytropic efficiency" has dropped to 86.8 per cent, results show that the average axial velocity at station 3 has increased 8.2 per cent, the average total pressure has decreased 8.0 per cent, and the work output has increased 17.0 per cent when compared with the isentropic solution.

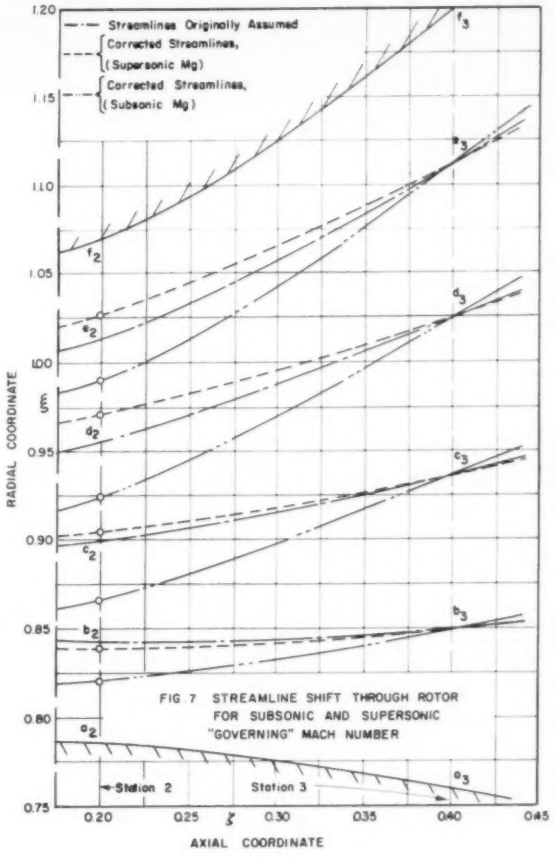

FIG. 7 STREAMLINE SHIFT THROUGH ROTOR FOR SUBSONIC AND SUPERSONIC "GOVERNING" MACH NUMBER

The results of these examples show the reason for the "loading up" of the first stages of a multistage turbine as the efficiency drops. As the efficiency decreases, more work is taken out in the initial stage, and less total pressure is left for the remaining turbine stages. Thus, the last stage of a multistage turbine may well act as a compressor if the efficiency of the system has dropped sufficiently. In view of this, it is apparent that the design engineer should design his machine for the expected efficiency in the operating range, and not on the basis of isentropic flow.

An example has been constructed to illustrate the increase in gross thrust obtainable by the use of a radial total temperature gradient. Assuming a one-stage turbine configuration similar to that shown in Fig. 4 and keeping the mass flow, combustion chamber total pressure, blade speed, and work extracted constant in each case, the gross thrust of the turbine was calculated for: (a) a constant radial total temperature of 1,450°F. and (b) a linear total temperature gradient of 400°F. with the same root total temperature of 1,450°F. The results show that an increase in gross thrust of 918 lbs., or 7.7 per cent, was obtained by the use of the radial total temperature gradient indicated.

(6) Appendix

The following data are used for Examples 1 and 2:

ω = 734 radians per sec. $\quad p_{1t}$ = 16,300 lbs. per sq.ft. $\quad R_0$ = 1.25 ft.
γ = 1.33 $\quad \omega R_0$ = 917.5 ft. per sec. $\quad c$ = 0.25 ft.
R = 1,719 sq.ft. per sec.^{2}°F. $\quad \omega^2 R_0^2$ = 0.8418 × 10^6 sq.ft. per sec.^{2} $\quad W$ = 164 lbs. per sec.

Coordinates, slopes, and curvatures for Fig. 4:

ξ_1	ξ_2	ξ_3	$(\partial f/\partial\zeta)_1$	$(\partial f/\partial\zeta)_2$	$(\partial f/\partial\zeta)_3$	$(\partial^2 f/\partial\zeta^2)_1$	$(\partial^2 f/\partial\zeta^2)_2$	$(\partial^2 f/\partial\zeta^2)_3$
0.8000	0.7850	0.7600	−0.0500	−0.1000	−0.1500	−0.2500	−0.2500	−0.2500
0.8438	0.8496	0.8661	0.0047	0.0360	0.0791	0.1332	0.1467	0.1720
0.8854	0.9098	0.9605	0.0567	0.1627	0.2829	0.4972	0.5163	0.5474
0.9252	0.9661	1.046	0.1065	0.2813	0.4684	0.8455	0.8620	0.8891
0.9633	1.019	1.126	0.1541	0.3935	0.6398	1.179	1.189	1.205
1.000	1.070	1.200	0.2000	0.5000	0.8000	1.500	1.500	1.500

Example 1

Solution for the stator of Fig. 4 with a radial total temperature gradient of 400°F. and radial coordinates based on equal areas in the plane perpendicular to the axis. This is an isentropic, subsonic solution for the direct problem for a stator [$F(\xi_2)$ given]. Eqs. (12), (14), (23), (24), (26), (27) (with appropriate subscripts for stations 1 and 2) and the following equation are applicable for F constant and $P_{1t} = 1$:

$$\phi_2 = \frac{1}{\xi_2^{F^2/(1+F^2)}\,(1+F^2)}\left(\int_{\xi_i}^{\xi_2}\left\{\left(\frac{P_2}{P_1}\right)^{1/\gamma}\frac{\xi_2}{\phi\,\xi_1}\left[\frac{\gamma}{\gamma-1}\,\frac{d\tau_{1t}}{d\xi_1}\,(1-P_2^{(\gamma-1)/\gamma})\right]+\frac{d\theta_2}{d\zeta_2}\right\}\xi_2^{F^2/(1+F^2)}d\xi_2\right)+\frac{C_1}{\xi_2^{F^2/(1+F^2)}} \qquad (50)$$

Conditions at station 1: (given)

	ξ_1	τ_{1t}	τ_1	ϕ_1	θ_1
a_1	0.8000	3.798	3.740	0.6829	−0.0341
b_1	0.8438	3.978	3.917	0.7012	0.0033
c_1	0.8854	4.147	4.084	0.7115	0.0403
d_1	0.9252	4.309	4.243	0.7254	0.0773
e_1	0.9633	4.466	4.398	0.7317	0.1128
f_1	1.000	4.615	4.545	0.7366	0.1473

$\lambda_1 = 0$, $P_{1t} = 1$, $P_1 = 0.940$, $F = 2.75$, $\beta_2 = 19°59'$, $m = 0.02920$, $\Delta T = +400$°F., $d\tau_{1t}/d\xi_1 = +16.458$.

Solution at station 2:

	ξ_2	ϕ_2	θ_2	λ_2	P_2	τ_2	M
a_2	0.7850	0.7423	−0.0742	2.041	0.5093	3.213	1.04
b_2	0.8496	0.7080	0.0255	1.947	0.5615	3.447	0.968
c_2	0.9098	0.6832	0.1112	1.879	0.6000	3.653	0.909
d_2	0.9661	0.6646	0.1870	1.828	0.6290	3.841	0.963
e_2	1.019	0.6507	0.2560	1.789	0.6523	4.017	0.831
f_2	1.070	0.6402	0.3200	1.761	0.6700	4.179	0.805

$C_1 = 0.5994$, $C_2 = 0.8459$, $P_{1t} = P_{2t}$, $Q_{1t} = Q_{2t}$, $\tau_{1t} = \tau_{2t}$.

Example 2

Solution for the rotor of Fig. 4 with a radial total temperature gradient of 400°F. and radial coordinates based on equal areas in a plane perpendicular to the axis. This is an isentropic, subsonic solution for the direct problem for a rotor [$G(\xi_3)$ given]. One complete iteration is given for this example to show the method used. Eqs. (10), (11), (13), (18), (23), (24), and the following equations are applicable for G constant and $P_{2t} = 1$:

$$\phi_3 = \frac{1}{\xi_3^{G^2/(1+G^2)}\,(1+G^2)}\left(\int_{\xi_i}^{\xi_3}\left\{\left(\frac{P_3}{P_2}\right)^{1/\gamma}\frac{\xi_3}{\phi_2\xi_2}\left[\frac{\gamma}{\gamma-1}\,\frac{d\tau_{2t}}{d\xi_2}\,(1-P_3^{(\gamma-1)/\gamma})-\frac{d}{d\xi_2}\,(\xi_2\lambda_2)\right]+2G+\frac{d\theta_3}{d\zeta_3}\right\}\xi_3^{G^2/(1+G^2)}\,d\xi_3\right)+$$

$$\frac{C_1}{\xi_3^{G^2/(1+G^2)}} \qquad (51)$$

Conditions at station 2 are assumed to be the same as after the stator of Example 1. Data used in the iteration, in addition to the coordinates, slopes, and curvatures previously given, are:

$G = 1.96$ $\quad 2G = 3.920$
$[\gamma/(\gamma-1)]\,(d\tau_{2t}/d\xi_2) = 11.550$ $\quad m = 0.02920$
$\beta_3 = 27°02'$ $\quad G^2/(1+G^2) = 0.7935$

	ξ_3	$\Delta\xi_3$	Factor	$\overline{\left(\frac{\xi_3}{(\phi_2\xi_2)}\right)}$	$\frac{-d(\xi\lambda_z)}{d\xi_c}$	$\frac{1}{\xi_2^{0.7935}}$	$\overline{Q_2}\frac{(\xi_t^2-\xi_{t-1}^2)}{2}$	$\frac{(\gamma-1)(\xi_t-\xi_{t-1})}{\gamma\tau_{2i}}$
a_3	0.7600					1.243		
		0.1061	0.02083	1.372	−0.8050		0.01386	0.006773
b_3	0.8661					1.121		
		0.0944	0.01874	1.492	−0.9302		0.01411	0.005767
c_3	0.9605					1.032		
		0.0859	0.01716	1.587	−0.9948		0.01413	0.005042
d_3	1.046					0.9646		
		0.0794	0.01593	1.663	−1.088		0.01406	0.004491
e_3	1.126					0.9102		
		0.0742	0.01495	1.724	−1.186		0.01391	0.004055
f_3	1.200					0.8653		

"Factor" above $= 1/\xi_3^{G^2/(1+G^2)}(1+G^2)\int_{\xi_{i-1}}^{\xi_i}\xi_3^{G^2/(1+G^2)}\,d\xi_3$

Try $C_1 = 0.1926$.

	ϕ_3	$G\phi_3$	λ_3	θ_3	λ_3^2/ξ_3	$\overline{\lambda_3^2/\xi_3}$	$\theta_3^2/2$
a_3	0.2395	0.4694	−0.2906	−0.0359	0.1111		0.0006
						0.0944	
b_3	0.3095	0.6066	−0.2595	0.0245	0.0777		0.0003
						0.0689	
c_3	0.3675	0.7203	−0.2402	0.1040	0.0601		0.0054
						0.0536	
d_3	0.4205	0.8242	−0.2222	0.1970	0.0472		0.0194
						0.0418	
e_3	0.4709	0.9230	−0.2028	0.3013	0.0365		0.0454
						0.0315	
f_3	0.5212	1.022	−0.1784	0.4170	0.0265		0.0869

	$-\frac{\partial(\theta_3^2/2)}{\partial\xi_3}$	$\frac{\partial\phi_3}{\partial\zeta_3}\left(\frac{\partial f}{\partial\zeta}\right)_3$	$\phi_3\left(\frac{\partial^2 f}{\partial\zeta^2}\right)_3$	$\frac{\partial\theta_3}{\partial\zeta_3}$	$-\phi_3\frac{\partial\theta_3}{\partial\zeta_3}$	$-\phi_3\overline{\frac{\partial\theta_3}{\partial\zeta_3}}$	$\Delta P_3^{(\gamma-1)/\gamma}$
a_3		+0.3771	−0.0599	+0.3172	−0.0760		
	+0.0028					−0.0219	+0.00051
b_3		−0.1576	+0.0532	−0.1044	+0.0323		
	−0.0540					+0.0612	+0.00044
c_3		−0.4464	+0.2012	−0.2452	+0.0901		
	−0.1630					+0.0865	−0.00012
d_3		−0.5714	+0.3739	−0.1975	+0.0830		
	−0.3274					+0.0433	−0.00109
e_3		−0.5752	+0.5674	−0.0078	+0.0037		
	−0.5593					−0.0779	−0.00246
f_3		−0.4760	+0.7818	+0.3058	−0.1594		

The constant C_2 is found by applying Eq. (10) at the inner channel boundary:

$\tau_3 = 3.798 - 0.1240\,[0.0574 + 0.0844 + 0.0013 + 2(1.602 - 0.2209)] = 3.438$

$P_3 = 0.5094\,(1.070)^{4.03} = 0.6692 \qquad C_2 = (0.6692)^{0.2481} = 0.9052$

	$P_3^{(\gamma-1)/\gamma}$	P_3	$(P_3/P_2)^{1/\gamma}$	Average	$(1-P_3^{(\gamma-1)/\gamma})$	Average
a_3	0.9052	0.6692	1.228		0.0948	
				1.185		0.0945
b_3	0.9057	0.6710	1.143		0.0943	
				1.116		0.0941
c_3	0.9061	0.6720	1.089		0.0939	
				1.070		0.0939
d_3	0.9060	0.6718	1.051		0.0940	
				1.034		0.0945
e_3	0.9049	0.6680	1.018		0.0951	
				1.004		0.0963
f_3	0.9025	0.6615	0.9904		0.0975	

The axial velocity integral [Eq. (51)] is iterated in steps across the channel as follows:

	$\Delta\phi_3$	ϕ_3	Average
$0.02083\ [1.626\ (1.091 - 0.8050) + 3.92 + 0.1064]$	0.0936	0.0936	0.0468
$0.01874\ [1.665\ (1.087 - 0.9302) + 3.92 - 0.1748]$	0.0751	0.1686	0.1311
$0.01716\ [1.698\ (1.085 - 0.9948) + 3.92 - 0.2213]$	0.0661	0.2347	0.2016
$0.01593\ [1.720\ (1.091 - 1.088) + 3.92 - 0.1026]$	0.0609	0.2956	0.2651
$0.01495\ [1.731\ (1.112 - 1.186) + 3.92 + 0.1490]$	0.0592	0.3545	0.3250

The mass flow relation [Eq. (23)] is iterated to solve for C_1 as follows:

$$0.02920 = 0.01642\,(0.0468 + 1.182C_1) + 0.01575\,(0.1311 + 1.077C_1) + 0.01512\,(0.2016 + 0.9985C_1) + 0.01454\,(0.2651 + 0.9374C_1) + 0.01397\,(0.3250 + 0.8877C_1)$$

$$C_1 = 0.01493/0.07750 = 0.1926$$

Solution at station 3:

	ξ_3	ϕ_3	θ_3	λ_3	P_3	τ_3	τ_{3t}	M
a_3	0.7600	0.2395	−0.0359	−0.2906	0.6692	3.438	3.455	0.177
b_3	0.8661	0.3095	0.0245	−0.2595	0.6710	3.603	3.623	0.185
c_3	0.9605	0.3675	0.1040	−0.2402	0.6720	3.758	3.780	0.201
d_3	1.046	0.4205	0.1970	−0.2222	0.6718	3.904	3.928	0.226
e_3	1.126	0.4709	0.3013	−0.2028	0.6680	4.041	4.070	0.256
f_3	1.200	0.5212	0.4170	−0.1784	0.6615	4.165	4.201	0.294

Correction of the solution for the displacement of streamlines:

$$m(\xi_2) = \int_{\xi_i}^{\xi_2} Q_2\phi_2\xi_2 d\xi_2$$

$$m(\xi_3) = \int_{\xi_i}^{\xi_3} Q_3\phi_3\xi_3 d\xi_3$$

	ξ_2	$m(\xi_2)$		ξ_3	$m(\xi_3)$
a_2	0.7850	0	a_3	0.7600	0
b_2	0.8496	0.00616	b_3	0.8661	0.00450
c_2	0.9098	0.01218	c_3	0.9605	0.00982
d_2	0.9661	0.01802	d_3	1.046	0.01578
e_2	1.019	0.02369	e_3	1.126	0.02227
f_2	1.070	0.02920	f_3	1.200	0.02920

The mass flow functions given above are plotted against radius on Fig. 6 and a corrected ξ_2 is obtained and, hence, new conditions at station 2. Corresponding to these new conditions upstream, the corrected solution is found to be:

	ξ_3	ϕ_3	θ_3	λ_3	P_3	τ_3	τ_{3t}	M
a_3	0.7600	0.2339	−0.0351	−0.3016	0.6692	3.438	3.457	0.179
b_3	0.8661	0.3029	0.0240	−0.2724	0.6710	3.559	3.580	0.187
c_3	0.9605	0.3631	0.1027	−0.2488	0.6725	3.698	3.720	0.204
d_3	1.046	0.4173	0.1955	−0.2285	0.6723	3.850	3.874	0.228
e_3	1.126	0.4682	0.2996	−0.2081	0.6692	4.007	4.036	0.257
f_3	1.200	0.5192	0.4154	−0.1824	0.6620	4.166	4.202	0.294

$C_1 = 0.1881$ $C_2 = 0.9052$

References

[1] Monroe, G. M., *A Study of Compressible Fluid Motion in Turbomachines with Infinitely Many Blades*, Ph.D. Thesis, California Institute of Technology, 1951.

[2] Wu, Chung-Hua, NACA TN 1795, 2214, 2302, 2407, 2455, 2492, 2604, 2702, 2750, 2961.

[3] Vavra, M. H., *Steady Flow of Nonviscous Elastic Fluids in Axially Symmetric Channels*, Journal of the Aeronautical Sciences, Vol. 17, No. 3, pp. 149–156, 172, March, 1950.

[4] Reissner, H., *Blade Systems of Circular Arrangement in Steady, Compressible Flow*, Courant Anniversary Volume—Studies and Essays, Interscience Publishers, Inc., 1948

[5] Goldstein, A. W., *Axisymmetric Supersonic Flow in Rotating Impellers*, NACA TN 2388, 1951.

[6] Traugott, S. C., Smith, L. H., Jr., and Wislicenus, G. F., *A Practical Solution of a Three-Dimensional Flow Problem of Axial-Flow Turbomachinery*, Department of Mechanical Engineering, Johns Hopkins University, 1952.

[7] Marble, F. E., *The Flow of a Perfect Fluid Through an Axial Turbomachine with Prescribed Blade Loading*, Journal of the Aeronautical Sciences, Vol. 15, No. 8, pp. 473–485, August, 1948.

(*Continued on page 582*)

Solution of Complex Nonlinear Plastic Structures by the Method of Tearing

GABRIEL KRON*

General Electric Company

SUMMARY

A tensorial method is developed to solve in easy stages the stresses and deformations in complex statically indeterminate trusses, when stressed beyond the proportional limit. The method consists of tearing the plastic structure apart into smaller structures, or into its component bars, setting up the nonlinear deformation-versus-stress equations of each small structure separately, then interconnecting the component nonlinear equations by tensorial methods. The unknown redundant forces are found by one inversion and by a successive multiplication of vectors with matrices. Detailed numerical example of a truss with ten nonlinear bars is also worked out and checked against another method.

INTRODUCTION

The Problem

THE PURPOSE OF THE PRESENT PAPER is to extend the piece-wise numerical solution of complex elastic structures[6] to *nonlinear* problems also. As a first step in that direction a statically indeterminate truss is assumed to be stressed beyond the proportional limit, and the effect of the plastic stress range is investigated. The structure will be made statically determinate, as is customary, by cutting the redundant members and applying along their axis unknown forces.

The structure will be torn apart into its ultimate components, the individual beams. Each beam will be assumed to follow a *nonlinear* stress-strain relation, Displacement $= f$ (Force). The nonlinear beam equations $\bar{D} = f(\bar{F})$ will be interconnected by special laws of transformation, and the unknown redundant forces will be solved by successive approximation.

It is possible to interconnect the individual beams first into several subdivisions and then only to interconnect the latter into the final structure. In order not to make the paper too lengthy, these intermediate interconnections are not considered. For the linear case such steps have already been covered in references 3 and 6.

PREVIOUS WORKS

The tensorial analysis of pin-jointed *linear* airplane structures has been pioneered by Langefors.[1, 2] He also pioneered the solution of such structures by the method of tearing.[2] The *nonlinear* plastic deformation study in the present pages follows the basic formulas of Wilder[4] and Hoff.[5] Their methods require, however, the simultaneous establishment of all the nonlinear equations describing the entire system (Method of Complementary Energy). On the other hand the present paper establishes and solves the nonlinear equations in easy stages by standard tensorial and tearing methods, starting with the isolated individual beam equations.

It is emphasized that the present paper should not be considered as a matric reformulation of the scalar equations of Wilder. Rather the paper replaces the energy relations of Wilder by the topological concept of "connection tensor" $\bar{C}$. This latter in turn enables a systematic tearing apart and piecewise solution of complex structures, linear or nonlinear. Such a partitioning of the physical system is not practicable by the use of the energy method.

TEARING APART NONLINEAR SYSTEMS

It is believed by the author that if a small-scale nonlinear system with a *few variables* can be solved by some approximate or exact method, the same nonlinear system on a larger scale, *with a very large number of variables*, can usually be solved piecemeal by the method of tearing. A limitation is that across the points of tear a known relation, such as $\bar{x} = \bar{C}\bar{x}'$, must exist between the pre-tearing variables $\bar{x}'$ and after-tearing variables $\bar{x}$. ($\bar{C}$ itself may be a function of $\bar{x}$ or $\bar{x}'$.)

It should also be emphasized that the method of tearing merely *speeds up* and enlarges the scope of whatever conventional method is available to solve a nonlinear problem. If the physics of the nonlinear problem is such that the method of approximation to be used does not converge, or oscillates, the mere fact of tearing the physical system into smaller parts will not make the problem convergent. However, a judicious way of tearing may produce convergence. Due to the very fact that the method of tearing employs the physical system itself or its model, *many opportunities arise to make appropriate changes in the model itself (besides tearing) to force a speedier convergence.*

LINEAR ANALYSIS

Given System

Let the statically indeterminate truss of Fig. 1 be considered. It has eight applied forces as shown. If four of the redundant bars are cut and unknown forces acting along their axes are assumed [Fig. 2(a)], the structure becomes statically determinate. It will be assumed first that no plastic deformations arise and the structure is linear.

Received December 19, 1954. Revised and received June 3, 1955.

* Consulting Engineer, G-E, Schenectady, N.Y.

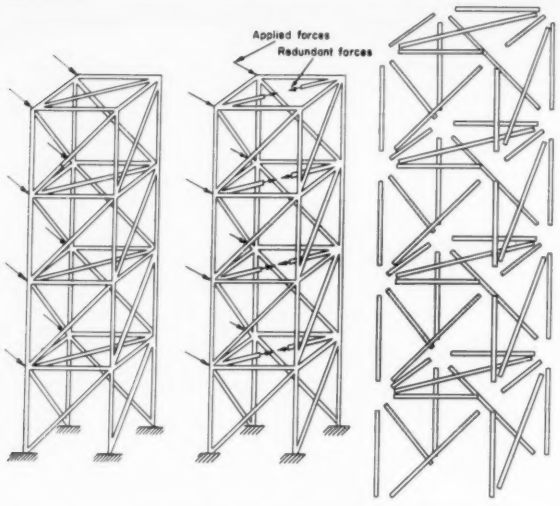

FIG. 1 (*left*). Given statically indeterminate structure. FIG. 2. Statically determinate structure: (a) *center*, "interconnected" system; (b) *right*, "primitive" system.

"Primitive" System

If all bars (including the redundants) are isolated, the "primitive" system of Fig. 2(b) is established. Its "equation of solutions" may be written by mere inspection as

$$\bar{D} = \bar{Z}\bar{F} \tag{1}$$

where $\bar{F}$ are the applied forces and $\bar{D}$ are the displacements. The flexibility matrix $\bar{Z}$ is diagonal, and each of its element has the form (when plasticity is ignored)

$$Z = L/(EA) \tag{2}$$

Connection Tensor

If a unit force is impressed at any junction-point of Fig. 1, the internal stress appearing in every bar can be calculated outright by statical methods given in textbooks on structures. (A small numerical example is worked out later.) *The internal stresses due to one of the unit applied forces form one column of the connection tensor* $\bar{C}$. If all the internal stresses are calculated in succession for each unit applied force $\bar{F}^a$ and for each unit redundant force $\bar{F}^r$, all the columns of $\bar{C}$ are thereby established. They represent by $\bar{F} = \bar{C}\bar{F}'$ the relations between all internal stresses $\bar{F}$ and all external forces $\bar{F}' = \bar{F}^e$.

Since the external forces $\bar{F}'$ consist of the sum of applied and redundant forces

$$\bar{F}' = \bar{F}^e = \bar{F}^a + \bar{F}^r \tag{3}$$

the connection tensor $\bar{C}$ can be split into two sets of columns as

$$\bar{C} = i\left[\overset{a}{\bar{C}_a} \middle| \overset{r}{\bar{C}_r}\right] \tag{4}$$

and $\bar{F} = \bar{C}\bar{F}'$ may be written as

$$\bar{F} = \bar{C}\bar{F}' = \bar{C}\bar{F}^e = \bar{C}_a\bar{F}^a + \bar{C}_r\bar{F}^r \tag{5}$$

Interconnected System

Knowing the flexibility matrix $\bar{Z}$ of all isolated bars and their interconnection $\bar{C}$, the flexibility matrix $\bar{Z}'$ of the interconnected system is by $\bar{Z}' = \bar{C}_i\bar{Z}\bar{C}$

$$\bar{Z}' = \begin{matrix} a \\ r \end{matrix}\begin{bmatrix} \overset{a}{\bar{C}_a{}_i\bar{Z}\bar{C}_a} & \overset{r}{\bar{C}_a{}_i\bar{Z}\bar{C}_r} \\ \bar{C}_r{}_i\bar{Z}\bar{C}_a & \bar{C}_r{}_i\bar{Z}\bar{C}_r \end{bmatrix} = \begin{matrix} a \\ r \end{matrix}\begin{bmatrix} \overset{a}{\bar{Z}_1} & \overset{r}{\bar{Z}_2} \\ \bar{Z}_3 & \bar{Z}_4 \end{bmatrix} \tag{6}$$

The equation of the system is thus

$$\begin{bmatrix} \bar{D}_a \\ \bar{0} \end{bmatrix} = \begin{bmatrix} [\bar{F}^a & \bar{F}^r] \\ \bar{Z}_1 & \bar{Z}_2 \\ \bar{Z}_3 & \bar{Z}_4 \end{bmatrix} \begin{matrix} \bar{D}_a = \bar{Z}_1\bar{F}^a + \bar{Z}_2\bar{F}^r & (7a) \\ \bar{0} = \bar{Z}_3\bar{F}^a + \bar{Z}_4\bar{F}^r & (7b) \end{matrix}$$

The displacements $\bar{D}_r$ due to the redundant beams are assumed to be zero. The values of the redundant forces $\bar{F}^r$ are unknown.

Calculation of Redundant Stresses

Let the second equation be solved for $\bar{F}^r$

$$\bar{F}^r = -(\bar{Z}_4)^{-1}\bar{Z}_3\bar{F}^a = -\bar{Y}^4\bar{Z}_3\bar{F}^a = \bar{B}\bar{F}^a \tag{8}$$

The matrix $\bar{Z}_4$, whose inverse has to be calculated, has as many rows and columns as there are redundant forces.

Often there exist a large number of redundant bars (as in airplane structures) so that the inverse of $\bar{Z}_4$ cannot be found in one step on the available digital computer. In such cases the resultant structure is torn apart into several subdivisions first and then only into the individual bars, as has been shown by Langefors in reference 3. He shows that the process of tearing reduces the number of redundant variables, as well as leading to great savings in the inverse calculation of the remaining redundants.

Calculation of Other Quantities

If $\bar{F}^r$ has been found, the displacements due to the applied $\bar{F}^a$ are found by substituting $\bar{F}^r$ into Eq. (7a)

$$\left.\begin{aligned} \bar{D}_a &= \bar{Z}_1\bar{F}^a + \bar{Z}_2\bar{F}^r \\ \bar{D}_a &= (\bar{Z}_1 - \bar{Z}_2\bar{Y}^4\bar{Z}_3)\,\bar{F}^a \\ &= \bar{Z}_1'\bar{F}^a \end{aligned}\right\} \tag{9}$$

The stresses in the individual bars $\bar{F}$ are found by Eq. (5)

$$\bar{F} = \bar{C}_a\bar{F}^a + \bar{C}_r\bar{F}^r = \bar{C}\bar{F}^e \tag{10}$$

The amount of stretching of each bar is found by Eq. (1).

$$\bar{D} = \bar{Z}\bar{F} \tag{11}$$

PLASTIC CREEP

Nonlinear Stress-Strain Relation

Let it be assumed now that for each isolated bar of Fig. 2a the relation between the axial stress F and strain D is no longer linear but is nonlinear

$$D = ZF + Z_p f(F) \tag{12}$$

where $f(F)$ is an *arbitrary function* of F. For steady creep $f(F)$ is independent of time.

Wilder in reference 4 assumes the following nonlinear stress-strain relation in each bar

$$D = \{[L/(AE)]F\} + \{(3/7)[L/(AE)]P_R\}(F/P_R)^n \tag{13}$$

That is, for each isolated bar

$$\left.\begin{array}{l|l} Z = L/(AE) & \text{Alternative definitions:} \\ Z_p = (3/7)[L/(AE)]P_R & Z_p = (3/7)[L/(AE)](P_R)^{1-n} \\ f(F) = (F/P_R)^n & f(F) = F^n \end{array}\right\} \tag{14}$$

The following derivation will be independent of the actual form of $f(F)$.

Primitive System

The nonlinear "equations of solution" of the primitive system of Fig. 2a (all bars isolated) is

$$\bar{D} = \bar{Z}\bar{F} + \bar{Z}_p\bar{f}(\bar{F}) \tag{15}$$

In the present example of isolated bars the symbols describe the following constants:

(1) $\bar{Z}$ (the "elastic" flexibility matrix) is diagonal and contains the bar flexibilities. It is the same that occurs in the linear case, Eq. (1).

(2) $\bar{Z}_p$ (the "plastic" flexibility matrix) is also diagonal and contains the constant coefficients Z_p of the nonlinear terms.

(3) $\bar{f}(\bar{F})$ is a *vector*. Each of its elements is an arbitrary function of its respective stress F. When $\bar{f}(\bar{F})$ is defined as $(F/P_{Rk})^n$, its value is

$$\bar{f}(\bar{F}) = (\bar{F}/P_{Rk})^n = [\overset{1}{(F^1/P_{R1})^n}\overset{2}{(F^2/P_{R2})^n}\ldots \overset{k}{(F^k/P_{Rk})^n}] \tag{16a}$$

Another alternative definition is

$$\bar{f}(\bar{F}) = \bar{F}^n = [\overset{1}{(F^1)^n}\overset{2}{(F^2)^n}\ldots\ldots\overset{k}{(F^k)^n}] \tag{16b}$$

It should be emphasized that Eq. (15) may represent the nonlinear equations of *any set* of small structures, into which the resultant system has been torn apart, and not necessarily only those of isolated bars.

Connection Tensor

The connection tensor $\bar{C}$ of the nonlinear system is identical with that of the linear system. This is due to the fact that the linear relations existing between the stresses *on the two sides of each point of tear* are assumed to remain unchanged. That is, $\bar{F} = \bar{C}\bar{F}'$ is independent of the rest of the system.

Even if it happens that $\bar{F} = \bar{C}\bar{F}'$ assumes a different form for the nonlinear case, the basic derivations in this paper are still valid.

Invariance of Elastic Energy

It should be recalled from reference 7 that if $\bar{F} = \bar{C}\bar{F}'$ is given, the law of transformation of $\bar{D}$ follows from the fact that the stored elastic energy in the primitive system of Fig. 2(b) is the same as in the interconnected system of Fig. 2(a) (if each bar is subjected to the same stress). That is

$$\bar{F}\bar{D} = \bar{F}'\bar{D}' \tag{17}$$

From the above relation follows the law of transformation of $\bar{D}$ as $\bar{D}' = \bar{C}_t\bar{D}$. By making the assumption that the *form* of the stress-strain equation $\bar{D} = \bar{Z}\bar{F}$ remains invariant, the law of transformation of the elastic $\bar{Z}$ follows as $\bar{Z}' = \bar{C}_t\bar{Z}\bar{C}$.

Now *in a steady plastic creep the stored elastic energy is still the same in the primitive system of Fig. 2b and in the interconnected system of Fig. 2(a)* (if the stresses in the individual bars are the same). Hence the law of transformations of the displacement vector remains unchanged.

$$\bar{D}' = \bar{C}_t\bar{D} \tag{18}$$

(Strictly speaking, the law of transformation of $\bar{D}$ [Eq. (18)] follows from topological considerations, and the invariance of elastic energy [Eq. (17)] is only a *consequence* of the underlying topology. However, for engineers, the reverse derivation appears to be more plausible.)

The question still remains: What is the law of transformation of $\bar{Z}$ and $\bar{Z}_p$? Again the invariance of the form of Eq. (15) will be used as a determining factor.

Laws of Transformation of $\bar{Z}$, $\bar{Z}_p$, and $\bar{f}$

The nonlinear equation of the primitive system of Fig. 2(a) is given in Eq. (15) as

$$\bar{D} = \bar{Z}\bar{F} + \bar{Z}_n\bar{f}(\bar{F}) \tag{19}$$

Let $\bar{F}$ be replaced by $\bar{C}\bar{F}'$ where $\bar{F}' = \bar{F}^e$ are the external forces

$$\bar{D} = \bar{Z}\bar{C}\bar{F}' + \bar{Z}_n\bar{f}(\bar{C}\bar{F}')$$

and let the equation be pre-multiplied by $\bar{C}_t$

$$\bar{C}_t\bar{D} = \bar{C}_t\bar{Z}\bar{C}\bar{F}' + \bar{C}_t\bar{Z}_n\bar{f}(\bar{C}\bar{F}') \tag{20}$$

Since it is intended to maintain the form of Eq. (19) invariant for the interconnected system also, the equation of the interconnected system must be

$$\bar{D}' = \bar{Z}'\bar{F}' + \bar{Z}'_n\bar{f}'(\bar{F}') \tag{21}$$

It follows that the laws of transformation are [comparing Eq. (20) with Eqs. (21) and (18)]:

$$(1) \qquad \bar{Z}' = \bar{C}_t\bar{Z}\bar{C} \tag{22}$$

$$(2) \qquad \bar{Z}'_p = \bar{C}_t\bar{Z}_p \tag{23}$$

$$(3) \qquad \bar{f}'(\bar{F}') = \bar{f}(\bar{C}\bar{F}') \tag{24}$$

The elastic $\bar{Z}$ transforms the same manner as in the linear case. The plastic $\bar{Z}_p$ transforms as a covariant vector $\bar{D}$, while the nonlinear $\bar{f}$ becomes only rearranged internally as a tensor of valence zero.

Partitioned Equations

Replacing $\bar{C}$, $\bar{F}'$, and $\bar{D}'$ by their partitioned form, the single Eq. (21) becomes

$$\begin{bmatrix} \bar{D}_a \\ \bar{0} \end{bmatrix} = \begin{bmatrix} \bar{F}^a & \bar{F}^r \\ \bar{Z}_1 & \bar{Z}_2 \\ \bar{Z}_3 & \bar{Z}_4 \end{bmatrix} + \begin{bmatrix} \bar{f}(\bar{C}\bar{F}^\epsilon) \\ \bar{Z}_{ap} \\ \bar{Z}_{rp} \end{bmatrix} \tag{25}$$

where $\bar{Z}_{ap} = \bar{C}_a \bar{Z}_p \mid \bar{Z}_{rp} = \bar{C}_r \bar{Z}_p$ (26)

$$\bar{f}(\bar{C}\bar{F}^\epsilon) = \bar{f}(\bar{C}_a\bar{F}^a + \bar{C}_r\bar{F}^r) = (\bar{C}_a\bar{F}^a + \bar{C}_r\bar{F}^r)^n \tag{27}$$

Writing the two nonlinear equations separately

$$\bar{D}_a = \bar{Z}_1\bar{F}^a + \bar{Z}_2\bar{F}^r + \bar{Z}_{ap}\bar{f}(\bar{C}_a\bar{F}^a + \bar{C}_r\bar{F}^r) \tag{28a}$$

$$\bar{0} = \bar{Z}_3\bar{F}^a + \bar{Z}_4\bar{F}^r + \bar{Z}_{rp}\bar{f}(\bar{C}_a\bar{F}^a + \bar{C}_r\bar{F}^r) \tag{28b}$$

The redundant forces $\bar{F}^r$ (also $\bar{D}_a$) are unknown, while $\bar{F}^a$ is known.

If so desired, the above equation of the given structure may be used with similar equations of other structures to build up the nonlinear equations of superstructures.

Final "Equations of Solution"

Let Eq. (28b) be multiplied by the inverse of $\bar{Z}_4$

$$\bar{F}^r = -\bar{Y}^4\bar{Z}_3\bar{F}^a - \bar{Y}^4\bar{Z}_{rp}\bar{f}(\bar{C}_a\bar{F}^a + \bar{C}_r\bar{F}^r)$$

If the following matrix products are introduced

$$\bar{B} = -\bar{Y}^4\bar{Z}_3 \mid \bar{G} = -\bar{Y}^4\bar{Z}_{rp} \tag{29}$$

the nonlinear equation for $\bar{F}^r$ is

$$\bar{F}^r = \bar{B}\bar{F}^a + \bar{G}\bar{f}(\bar{C}_a\bar{F}^a + \bar{C}_r\bar{F}^r) \tag{30}$$

The expression in parentheses represents the internal stresses $\bar{F}$ in the individual bars.

The last equation and Eq. (28a) represent the "equations of solution" of the nonlinear system. The equations are in a final form ready to evaluate numerically the unknown vectors $\bar{F}$, $\bar{F}^r$, and $\bar{D}_a$ for any assumed numerical set of impressed forces $\bar{F}^a$.

The above two equations of the given structure and similar equations of other structures may be interconnected by a $\bar{C}$ to construct the nonlinear equations of superstructures. In other words, the inversion of $\bar{Z}_4$ of the subdivisions of a superstructure may be performed either before or after their interconnection.

Steps to Solve for F^r

The nonlinear equation [Eq. (30)] for $\bar{F}^r$ may be solved for any assumed applied forces $\bar{F}^a$ by successive approximations only. In particular, the following steps may be made:

(1) First assume the plastic effects absent and $\bar{f}(\bar{F}) = \bar{0}$. Then the redundant forces are

$$\bar{F}_0{}^r = \bar{B}\bar{F}^a \tag{31}$$

(2) Substitute $\bar{F}_0{}^r$ into Eq. (30) and find the internal stresses $\bar{F}$ of the individual bars

$$\bar{F} = \bar{C}_a\bar{F}^a + \bar{C}_r\bar{F}_0{}^r = \bar{F}_0{}^a + \bar{F}_0{}^{rr} \tag{32}$$

valid in the absence of plastic deformations.

(3) Knowing $\bar{F}_0$ find $\bar{f}(\bar{F}_0)$ by raising each element of $\bar{F}_0$ into the nth power.

(4) The first improved value of $\bar{F}^r$ is found by

$$\bar{F}_1{}^r = \bar{F}_0{}^r + \bar{G}\bar{f}(\bar{F}_0) \tag{33}$$

Steps (2), (3), and (4) are repeated until the improvement in $\bar{F}^r$ is negligible. That is, the kth improved value of $\bar{F}^r$ is found in three steps:

$$\left.\begin{array}{ll} \text{(a)} & \bar{F}_{k-1} = \bar{F}_0{}^a + \bar{C}_r\bar{F}_{k-2}{}^r \\ \text{(b)} & \bar{f}(\bar{F}_{k-1}) = (\bar{F}_{k-1})^n \\ \text{(c)} & \bar{F}_k{}^r = \bar{F}_0{}^r + \bar{G}\bar{f}(\bar{F}_{k-1}) \end{array}\right\} \tag{34}$$

Successive Approximations

For any assumed value of applied forces $\bar{F}^a$ each approximation consists of adding vectors and multiplying a matrix ($\bar{C}_r$ or $\bar{G}$) by a vector. *No inversion of matrices occurs, nor a multiplication of two matrices.* The vector $\bar{F}_0{}^r$ and $\bar{F}_0{}^a$ are calculated only once for each assumed set of applied forces $\bar{F}^a$.

It may be mentioned that if the inverse of matrix $\bar{Z}_4$ is calculated by tearing apart the entire system into n subdivisions, then the factorized form of $\bar{Y}^4$ contains only a small fraction $(1/\sqrt{n})$ of nonzero elements of that of a conventional inverse. Hence, if $\bar{G}$ of Eq. (29) is left also in a factorized form (as $-\bar{Y}^4\bar{Z}_{rp}$), then the product $\bar{G}\bar{f}$ would also require less multiplications by a factor of $1/\sqrt{n}$ during each successive approximation.

Of course, the convergence of the approximations may be improved by other available methods.

After $\bar{F}^r$ and the internal stresses $\bar{F}$ have been found by successive approximation, the displacements $\bar{D}_a$ due to the applied forces may be found by Eq. (28a).

Numerical Example

Given Structure

Let the example worked out by Wilder in reference 4 be repeated by the tensorial method of the present paper. The statically indeterminate structure of Fig. 3 is considered and is made statically determinate by cutting two of the bars [Fig. 4(a)]. One applied force $\bar{f}^a = 10$ exists.

Constants of the "Primitive" Structure

The "elastic" impedance matrix $\bar{Z}$ of the ten bars of the "primitive" system of Fig. 4(b) is (showing the diagonal elements L/AE of $\bar{Z}$ in a vector form to save space)

$$\begin{array}{rccccccccccc} & a & b & c & d & e & f & g & h & i & j \\ \bar{Z} = & [120 & 250 & 250 & 120 & 200 & 120 & 250 & 250 & 120 & 200] \end{array} \tag{35}$$

The value of plastic force vector P_R for each bar is [needed in $f(F) = (F/P_R)^n$]

$$\begin{array}{rl} P_R = & [10.125 \quad 8.1 \quad -8.1 \quad -10.125 \quad -8.1 \\ & 10.125 \quad 8.1 \quad -8.1 \quad -10.125 \quad 8.1] \end{array} \tag{36}$$

Each diagonal element of the "plastic" flexibility matrix is defined by Wilder as

$$Z_p = (3/7)[L/(AE)]P_R \tag{37}$$

The diagonal elements of $\bar{Z}_p$ are thus (arranged in a vector form)

$$\bar{Z}_p = (3/7)\,[1212 \quad 2025 \quad -2025 \quad -1212 \quad -1620 \quad 1212 \quad 2025 \quad -2025 \quad -1212 \quad 1620] \tag{38}$$

The exponent n (shape parameter) is 6.56.

Connection Tensor

Each applied force $\bar{F}^a$ and unknown redundant force $\bar{F}^r$ is assumed temporarily to be unity. Assuming each unit force to act in succession, the internal stresses in all bars due to them are calculated by any manner. In Figs. 5 to 7 a force polygon at each joint is constructed for that purpose. The internal forces due to each unit force are listed in a vertical column. (Compressions are positive.)

In the present example there exist one applied force and two redundant forces. Hence, there are three columns in $\bar{C}$

$$\bar{C} = \begin{array}{c} \\ a \\ b \\ c \\ d \\ e \\ f \\ g \\ h \\ i \\ j \end{array} \begin{array}{c} \begin{array}{ccc} 0 & 1 & 2 \end{array} \\ \left[\begin{array}{ccc} 0.75 & -0.6 & \\ 1.25 & 1. & \\ & 1. & \\ -1.5 & -0.6 & \\ & -0.8 & -0.8 \\ 0.75 & & -0.6 \\ & & 1. \\ -1.25 & & 1. \\ & & -0.6 \\ 1. & & -0.8 \end{array}\right] \end{array} = [\bar{C}_a|\bar{C}_r] \tag{39}$$

The matrix splits by a vertical line into $\bar{C}_a$ and $\bar{C}_r$.

Flexibility Matrices

The "elastic" flexibility matrix $\bar{Z}'$ is found by $\bar{C}_t\bar{Z}\bar{C}$ [where $\bar{Z}$ is given in Eq. (35)]

$$\bar{Z}' = \left[\begin{array}{cc|c} 1386 & 366.5 & -526.5 \\ 366.5 & 714.4 & 128 \\ \hline -526.5 & 128 & 842.4 \end{array}\right] = \begin{bmatrix} \bar{Z}_1 & \bar{Z}_2 \\ \bar{Z}_3 & \bar{Z}_4 \end{bmatrix} \tag{40}$$

The "plastic" flexibility matrix $\bar{Z}_p'$ is by $\bar{C}_t\bar{Z}_p$ [Eq. (23)]

$$\bar{Z}'_p = \frac{3}{7}\left[\begin{array}{cccc} 909 & 2531 & 1818 & 1818 \\ -729 & 2025 & -2025 & 729 \\ & & & 1296 \\ & 2531 & & 1620 \\ \hline 0 & 0 & 0 & 0 \\ 2025 & -2025 & -729 & -1296 \end{array}\right] = \begin{bmatrix} \bar{Z}_{ap} \\ \bar{Z}_{rp} \end{bmatrix} \tag{41}$$

Final "Equations of Solution"

The inverse of $\bar{Z}_4$ of Eq. (40) is

$$\bar{\Gamma}^1 = \begin{bmatrix} 0.00143895 & -0.00021864 \\ -0.00021864 & 0.00122031 \end{bmatrix} \tag{42}$$

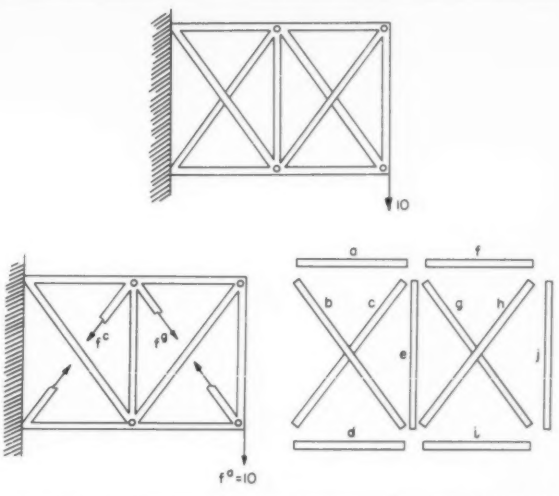

FIG. 3 (*top*). System to be solved numerically. FIG. 4 (*bottom*). System made statically determinate: (a) *left*, "interconnected" system; (b) *right*, "primitive" system.

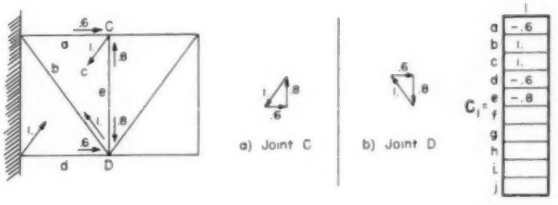

FIG. 5. Internal stresses due to unit applied force: (a) *left*, internal stresses; (b) *center*, force polygons; (c) *right*, connection tensor.

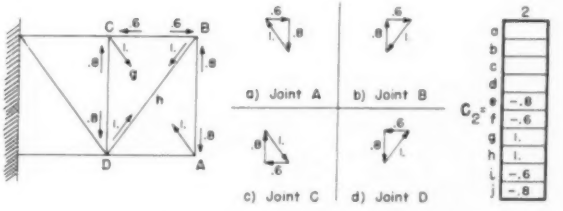

FIG. 6. Internal stresses due to unit redundant force in bar c: (a) *left*, internal stresses; (b) *center*, force polygons; (c) *right*, connection tensor.

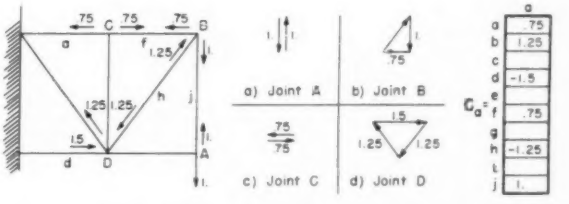

FIG. 7. Internal stresses due to unit redundant force in bar g: (a) *left*, internal stresses; (b) *center*, force polygons; (c) *right*, connection tensor.

The product $\bar{B} = -\bar{Y}^4\bar{Z}_3$ is

$$\bar{B} = \begin{matrix} \\ 1 \\ 2 \end{matrix}\begin{matrix} 0 \\ \left[\begin{matrix} -0.64249 \\ 0.72262 \end{matrix}\right. \end{matrix} \tag{43}$$

The product $\bar{G} = -\bar{Y}^4\bar{Z}_{rp}$ is left this time in a factorized form, since $\bar{Z}_{rp}$ is half empty and $\bar{Y}^4$ is a small matrix. On the other hand $\bar{G}$ would be a full matrix. (Also the unmultiplied form gives a better comparison with the columns of Wilder's example.)

Elastic Case

Wilder assumes the single applied force as $F^a = 10$. The redundant forces in the linear case are

$$\bar{F}_0{}^r = \bar{B}\bar{F}^a = \begin{matrix} \\ 1 \\ 2 \end{matrix}\left[\begin{matrix} -6.4249 \\ 7.2262 \end{matrix}\right] \tag{44}$$

(This vector will be used several times during the successive approximations.)

The *external* forces are thus

$$\bar{F}^r = \bar{F}^e = \begin{matrix} 0 & 1 & 2 \\ [10 & -6.429 & 7.2262] \end{matrix} \tag{45}$$

The *internal* stresses in each bar due to the single applied force $\bar{F}^a = 10$ are

$$\bar{F}_0{}^a = \bar{C}_a\bar{F}^a =$$

$$\begin{matrix} a & b & c & d & e & f & g & h & i & j \\ [7.5 & 12.5 & 0 & -15 & 0 & 7.5 & 0 & -12.5 & 0 & 10] \end{matrix} \tag{46}$$

(This vector will also be used several times during the successive approximations.) The internal stresses due to the redundant forces $\bar{F}_0{}^r$ are

$$\bar{F}_0{}'^r = \bar{C}_r\bar{F}_0{}^r =$$

$$\begin{matrix} [3.8549 & -6.4249 & -6.4249 & 3.8549 & -.6411 \\ -4.3357 & 7.2262 & 7.2262 & -4.3357 & -5.781] \end{matrix} \tag{47}$$

The total internal forces are their sum

$$\bar{F}_0 = \bar{C}\bar{F}^e =$$

$$\begin{matrix} [11.355 & 6.075 & -6.425 & -11.145 & -.6411 \\ 3.164 & 7.226 & -5.274 & -4.335 & 4.219] \end{matrix} \tag{48}$$

Effect of Plastic Deformations

The vector $\bar{f}(\bar{F}) = (\bar{F}/P_{Rk})^n$ is, when the exponent n is 6.56,

$$\bar{f}(\bar{F}) = \begin{matrix} [2.1214 & 0.1515 & 0.2188 & 1.8771 & 0 \\ 0.0005 & 0.4729 & 0.0599 & 0.0038 & 0.0139] \end{matrix} \tag{49}$$

The product $\bar{Z}_{rn}\bar{f}(\bar{F})$ is

$$\bar{Z}_{rn}\bar{f} = \begin{bmatrix} -134.7 \\ 351.8 \end{bmatrix} \tag{50}$$

The effect of plasticity is by $-\bar{Y}^4(\bar{Z}_{rn}\bar{f})$

$$-\bar{Y}^4(\bar{Z}_{rn}\bar{f}) = \bar{G}\bar{F} = \begin{bmatrix} 0.2707 \\ -0.4588 \end{bmatrix} \tag{51}$$

Hence the first corrected values of the redundant forces are by Eq. (34)

$$\bar{F}_1{}^r = \begin{bmatrix} F^1 \\ F^2 \end{bmatrix} = \begin{bmatrix} -6.1542 \\ 6.7674 \end{bmatrix} \tag{52}$$

All results check with those of Wilder.[4]

Calculating now the corrected internal forces $\bar{F}_1$, a new set of redundant forces may be calculated.

References

[1] Langefors, B., *Analysis of Elastic Structures by Matrix Transformation with Special Regard to Semimonocoque Structures*, Journal of the Aeronautical Sciences, Vol. 19, No. 7, pp. 451-458, July, 1952.

[2] Langefors, B., *Structural Analysis of Swept-back Wings by Matrix-Transformation*, Saab Technical Notes 3, Saab Aircraft Company, Linköping, Sweden, 1951.

[3] Langefors, B., *Exact Reduction and Solution by Parts of Equation for Elastic Structures*, Saab Technical Notes 24, Saab Aircraft Company, Linköping, Sweden, 1953.

[4] Wilder, Th. W., III, *An Analysis of Statically Indeterminate Trusses Having Members Stressed Beyond the Proportional Limit*, NACA TN 2886, Langley Aeronautical Laboratory, Langley AFB, Va.

[5] Hoff, N. J., *Approximate Analysis of Structures in the Presence of Large Creep Deformations*, Quarterly of Applied Mathematics, Vol. XII, No. 1, pp. 49–55, April, 1944.

[6] Kron, G., *Solving Highly Complex Elastic Structures in Easy Stages*, Journal of Applied Mechanics, Vol. 22, No. 2, pp. 235-244, June, 1955.

[7] Kron, G., *Tensor Analysis of Networks*, John Wiley and Sons, New York, 1939.

IAS Twenty-Fifth Annual Meeting

Hotel Sheraton-Astor, New York City, January 28-31, 1957

The Meetings Committee plans to schedule sessions on Aerodynamics, Aeroelasticity, Design, Electronics, Flight Propulsion, Instruments, Rotating Wing Aircraft, Safety in Flight, Structures, Air Transportation, etc.

Members or organizations wishing to have papers considered for presentation at this meeting should submit outlines or short abstracts to the Meetings Committee, 2 East 64th St., New York 21, N.Y., no later than August 15, 1956.

Elasto-Plastic Bending of Beams on Elastic Foundations†

PAUL SEIDE‡

Northrop Aircraft, Inc.

ABSTRACT

Two methods for the determination of elasto-plastic deformations of elastically supported beams having a bilinear stress-strain curve are presented and compared. One method involves the numerical solution of the fourth-order nonlinear differential equation associated with the engineering theory of beam bending while the other linearizes the problem by replacing the nonlinear moment-curvature diagram with its linear asymptotes. Results obtained through the two methods are in excellent agreement. The linearized method is recommended for investigation of the initial phases of bending of elastically supported beams in which only a few plastic regions appear. Neither method has any particular advantages when the beam has many plastic regions—i.e., both methods involve a tremendous amount of computation. Computed deflections for finite elastically supported beams are in good agreement with experimental results; differences of five per cent are consistent in the elastic and in most of the plastic regions.

SYMBOLS

b = width of beam at any layer in the cross section; maximum width of beam
E = Young's modulus of beam material
$\bar{E}$ = slope of linear strain hardening portion of stress-strain curve
h = half-depth of beam cross section
I_0 = moment of inertia of beam cross section
k = foundation modulus
L = length of finite beam
M = bending moment at any beam station
M_p = maximum possible bending moment in perfectly plastic beam
M^* = bending moment causing yielding of outermost beam fibers ($M^* = \sigma^* I_0/h$)
P = applied concentrated load
P^* = concentrated load for which yielding begins at outermost beam fibers
$\bar{P}^*$ = $M_p P/M^*$
q = distributed load on beam
$\tilde{q}$ = nondimensional distributed load ($\tilde{q} = q/M^*\lambda^2$)
$\bar{q}$ = nondimensional distributed load ($\bar{q} = q/M_p\bar{\lambda}^2$)
$\tilde{l}$ = nondimensional bending moment ratio ($\tilde{l} = M/M^*$)
$\bar{l}$ = nondimensional bending moment ratio ($\bar{l} = M/M_p$)
V = shear force
w = beam deflection
w^* = beam deflection at point of application of concentrated load when yielding begins
$\bar{w}^*$ = $M_p w^*/M^*$
x = distance along beam
y = distance from neutral axis to any layer in beam cross section
δ = $\chi_m - \chi_p$
ϵ = strain
ϵ^* = yield strain
λ = $(k/4EI_0)^{1/4}$
ρ = beam radius of curvature
σ = stress
σ^* = yield stress
$\tilde{\chi}$ = nondimensional distance along beam ($\tilde{\chi} = \lambda x$)
$\tilde{\chi}_m$ = nondimensional length of finite beam ($\tilde{\chi}_m = \lambda L$)
χ = nondimensional distance along beam ($\chi = \bar{\lambda} x$)
$\tilde{\chi}_p$ = nondimensional length of first plastic region
χ_p = nondimensional length of first plastic region [$\chi_p = (\bar{\lambda}/\lambda)\tilde{\chi}_p$]
ψ = ratio of depths of elastic core and cross section
$sgn\ (\ )$ = +1 if quantity in parentheses is positive, −1 if quantity is negative
$\bar{\lambda}$ = $(k/4\bar{E}I_0)^{1/4}$

Presented at the Structures Session, Twenty-Third Annual Meeting, IAS, New York, January 24–27, 1955.

† The present paper is essentially a condensation of the author's dissertation for the degree of Doctor of Philosophy at Stanford University, prepared under contract N6ONR-251 Task Order 11 (NR-064-240) for the Office of Naval Research.

‡ Research Engineer, Structural Research Group.

INTRODUCTION

IN CONTRAST TO the voluminous literature on elastic beam bending, specific information available on elasto-plastic beam deformations is very meager. This deficiency may be attributed to several factors. First, the solutions for elasto-plastic beams include several parameters that do not enter into elastic problems—i.e., the shape of the stress-strain curve, the shape of the cross section, and the nonlinear dependence of deflection on load, thus substantially increasing the number of calculations necessary to completely define the results for any problem. The nonlinearity of the differential equations for beam bending makes it impossible or exceedingly difficult and tedious to obtain exact or even approximate solutions for most problems. Finally, a knowledge of the ultimate load of a structure is often sufficient for design purposes. This load can be obtained adequately in most cases through the methods of limit design without an investigation of the intermediate stages of elasto-plastic deformation.

The present paper is concerned with the elasto-plastic bending of beams on elastic foundations. This class of problems is not susceptible to the methods of limit analysis since an ultimate load cannot be defined as for other structures. It is intuitively obvious that the beam will offer resistance to further bending so long as the foundation continues to resist additional loading or until the beam material actually fractures. The important analytical question is, then, not what maximum load can be carried but what deflections will be encountered. Hence, for these problems a detailed analysis of beam deformations is necessary and methods for overcoming the difficulties associated with the solution of nonlinear differential equations must be sought.

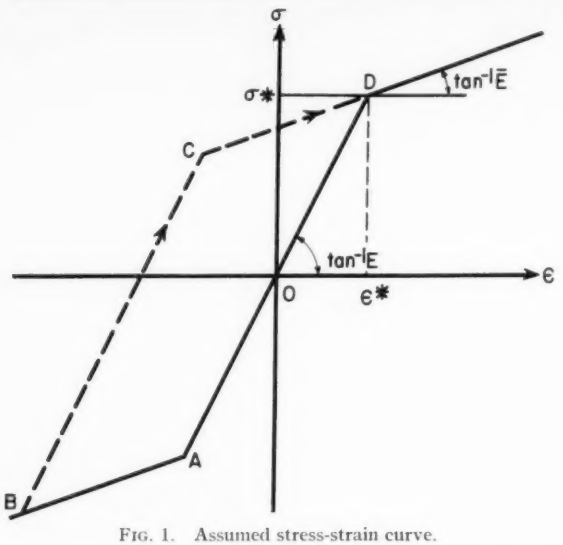

FIG. 1. Assumed stress-strain curve.

The results of such an investigation are reported herein.

ASSUMPTIONS

Most of the assumptions made in the engineering theory of elasto-plastic bending of beams are those made in the corresponding Bernoulli-Euler theory of elastic beams: plane cross sections of the undeformed beam are assumed to remain plane and perpendicular to the neutral axis of the deformed beam, and all stress components except the normal stress in longitudinal beam fibers are neglected. The relationship between fiber stress and strain is, however, assumed to be given by the stress-strain curve for the beam material in tension and compression, which is, of course, nonlinear as compared to the relationship for elastic beams.

In the present investigation, the nonlinear stress-strain curve is assumed to be the same for both tension and compression and is represented by two straight lines, as indicated by the solid curve in Fig. 1. The slope of the elastic portion is given by Young's modulus E of the material, while the slope of the second line, $\bar{E}$, indicates the degree of strain hardening after the yield stress σ^* is reached. If the yield stress has been exceeded in any fiber and the stress is then decreased, the strain decreases along a line parallel to AD—dashed line BC for example. When the stress has decreased an amount $2\sigma^*$ from its original value, further decreases in stress cause the strain to decrease along a line such as CD, the extension of the strain hardening path for initial loading. Thus the beam material can be made to show a Bauschinger effect—that is, a decrease in the compressive yield point for fibers loaded beyond the tensile yield point and vice versa. The two-straight-line representation of a stress-strain curve is a fair approximation for many materials such as mild steel, annealed rail steel, and the aluminum alloys.

A further simplification of the problem under consideration is afforded by restricting the investigation to beams with cross sections having at least a horizontal axis of symmetry and which are restrained to bend about that axis. Thus bending out of the plane of loading and shifting of the location of the neutral axis with applied moment for the general cross section are not considered. The foundation itself is assumed to be of the Winkler type with deflections at any point proportional to the vertical load applied at that point.

DIFFERENTIAL EQUATIONS OF INITIAL ELASTO-PLASTIC BENDING

The moment in a beam restrained to bend about a horizontal axis of symmetry and of a material with identical stress-strain curves for tension and compression is given by

$$M = 2\int_0^h yb(y)\sigma(y)\,dy \tag{1}$$

For initial loading of the beam (monotonic increase of the elasto-plastic cross-sectional moment at every point), the stress-strain relations are given by

$$\sigma = E\epsilon \qquad (|\epsilon| \leq \epsilon^*) \tag{2a}$$

$$\sigma = [E\epsilon^* + \bar{E}(|\epsilon| - \epsilon^*)]sgn\ \epsilon \qquad (|\epsilon| \geq \epsilon^*) \tag{2b}$$

The use of the assumed geometry of deformation yields the usual expression for fiber strain in terms of the distance of the fiber from the neutral axis and the beam curvature

$$\epsilon = y/\rho \tag{3}$$

It is more convenient, however, to replace the beam curvature by the parameter ψ which is the ratio of the height of the elastic region of a cross section to the total height of the beam (see Fig. 2). This is achieved through the relationship

$$\epsilon^* = \sigma^*/E = (\psi h/\rho)sgn\ \rho \tag{4}$$

The substitution of Eqs. (3) and (4) into Eqs. (2) yields

$$\sigma = (\sigma^*/\psi h)y\ sgn\ \rho \qquad (|y| \leq \psi h) \tag{5a}$$

$$\sigma = \sigma^*\{1 + (\bar{E}/E)\,[(|y|/\psi h) - 1]\}sgn(y/\rho) \qquad (|y| \geq \psi h) \tag{5b}$$

Eq. (1) for the bending moment then becomes

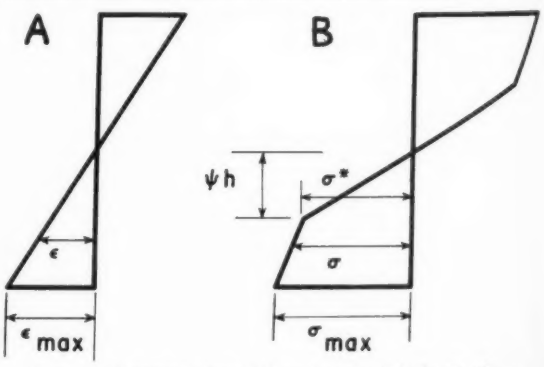

FIG. 2. Assumed stress (A) and strain (B) distributions.

$$M = 2\sigma^* \left\{ \frac{1}{\psi h} \int_0^{\psi h} y^2 b(y)\, dy + \int_{\psi h}^{h} \left[1 + \frac{\bar{E}}{E} \times \left(\frac{|y|}{\psi h} - 1 \right) \right] yb(y)\, dy \right\} sgn\ \rho \quad (6)$$

With the introduction of the positive bending moment required to produce yielding of the extreme fibers of the beam

$$M^* = \frac{\sigma^* I_0}{h} = \left[2\sigma^* \int_0^h y^2 b(y)\, dy \right] \Big/ h \quad (7)$$

and recognition that positive bending moment produces curvature, the final equation for bending moment becomes

$$\frac{M}{M^*} sgn \left(\frac{M}{M^*} \right) = \frac{1}{\psi} + \left(1 - \frac{\bar{E}}{E} \right) \times \frac{\int_{\psi h}^{h} \left(1 - \frac{y}{\psi} \right) yb(y)\, dy}{\int_0^h y^2 b(y) dy} \quad (8)$$

The right side of Eq. (8) is a function of ψ only and can be solved, at least in principle, to yield

$$\psi = \psi(|M/M^*|) \quad (9)$$

from which

$$\frac{1}{\rho} = -\frac{d^2w}{dx^2} = \frac{\sigma^*}{Eh} \frac{sgn\ (M/M^*)}{\psi(|M/M^*|)} \quad (10)$$

A second relationship between deflection and bending moment is obtained from the equations of equilibrium of vertical forces and moments for an element of the elastically supported beam (see Fig. 3).

$$dM/dx = V \quad (11a)$$

$$dV/dx - kw + q = 0 \quad (11b)$$

which may be combined to yield

$$(d^2M/dx^2) - kw + q = 0 \quad (12)$$

The final equations for elasto-plastic bending of elastically supported beams are now obtained by combining Eqs. (10) and (12) and nondimensionalizing the resulting equation to obtain

$$(d^4\bar{l}/d\tilde{\chi}^4) + 4[sgn\ \bar{l}/\psi(|\bar{l}|)] = -(d^2\tilde{q}/d\tilde{\chi}^2) \qquad (|\bar{l}| \leq 1) \quad (13)$$

where $\bar{l} = M/M^*$, $\tilde{\chi} = \lambda x$, $\lambda = (k/4EI_0)^{1/4}$, $\tilde{q} = q/M^*\lambda^2$. Relationships for moments, shears, and deflections in terms of the nondimensional parameter $\bar{l}$ are given by

$$M = M^*\bar{l} \quad (14a)$$

$$V = M^*\lambda(d\bar{l}/d\tilde{\chi}) \quad (14b)$$

$$w = (M^*\lambda^2/k)\ [(d^2\bar{l}/d\tilde{\chi}^2) + \tilde{q}\,] \quad (14c)$$

Eq. (13) applies only to beam cross sections which have been strained beyond the yield strain of the material. For those cross sections which are wholly elastic Eq. (13) is replaced by

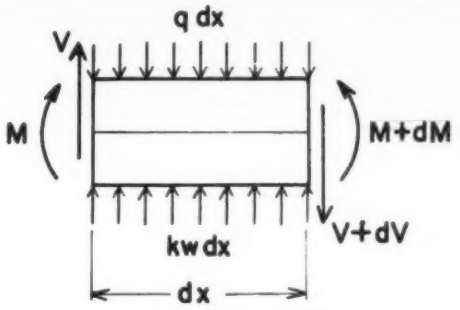

FIG. 3. Element of beam.

$$(d^4\bar{l}/d\tilde{\chi}^4) + 4\bar{l} = -(d^2\tilde{q}/d\tilde{\chi}^2) \qquad (|\bar{l}| \leq 1) \quad (15)$$

LINEARIZED DIFFERENTIAL EQUATIONS

The solution of Eqs. (13) and (15) in conjunction with appropriate boundary conditions is difficult, even numerically, since the curvature parameter ψ is not an explicit function of $\bar{l}$ and has a different nonlinear form for beams having different cross sections (see Appendix A). Fortunately an approximate expression can be obtained that is applicable to any symmetrical cross section and has the further and, by far, more important advantage of being linear.

A series of graphs of the moment parameter M/M_p plotted against the curvature parameter $M^*/M_p\psi$ for beams with I, rectangular, and elliptic cross sections is shown in Fig. 4 for several values of the strain hardening parameter $\bar{E}/E$. The moment M_p is the limiting moment that a perfectly plastic beam cross section will carry and is given by the limit of Eq. (8), with $\bar{E}/E$ equal to zero, as ψ approaches zero.

$$\frac{M_p}{M^*} = \int_0^h yb(y)\, dy \Big/ \int_0^h y^2 b(y)\, dy \quad (16)$$

It can be immediately seen that not only do the curves for different cross-sectional shapes fall very close to one another but they are also closely represented by the asymptotic solid lines

$$M^*/M_p\psi = |M/M_p| \qquad (|M| \leq M_p) \quad (17a)$$

$$M^*/M_p\psi = (E/\bar{E})\ [|M/M_p| - 1 + (\bar{E}/E)] \qquad (|M| \geq M_p) \quad (17b)$$

Eqs. (13) and (15) can thus be approximated by the linear expressions

$$\frac{d^4\bar{l}}{d\tilde{\chi}^4} + 4\bar{l} = 4\left(1 - \frac{\bar{E}}{E} \right) sgn\ \bar{l} - \frac{d^2\tilde{q}}{d\tilde{\chi}^2} \qquad (|\bar{l}| \geq 1) \quad (18a)$$

$$(d^4\bar{l}/d\tilde{\chi}^4) + 4\bar{l} = -(d^2\tilde{q}/d\tilde{\chi}^2)\ (M^*/M_p) \qquad (|\bar{l}| \leq 1) \quad (18b)$$

where $\bar{l} = M/M_p$, $\tilde{\chi} = (k/4\bar{E}I_0)x^{1/4}$, and $\tilde{q} = q/M_p\tilde{\lambda}^2$. Special attention must be paid to the limiting case of a perfectly plastic beam ($\bar{E}/E = 0$) as indicated in Appendix B.

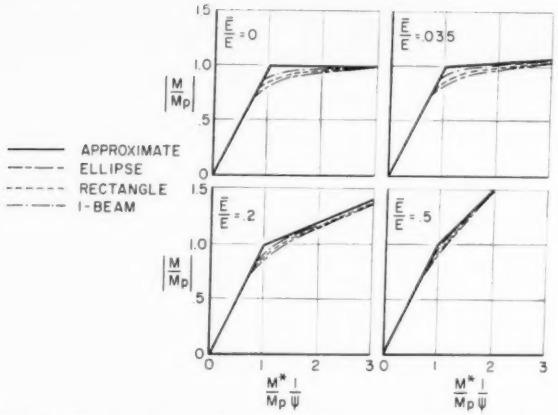

FIG. 4. Exact and approximate moment-curvature relationships.

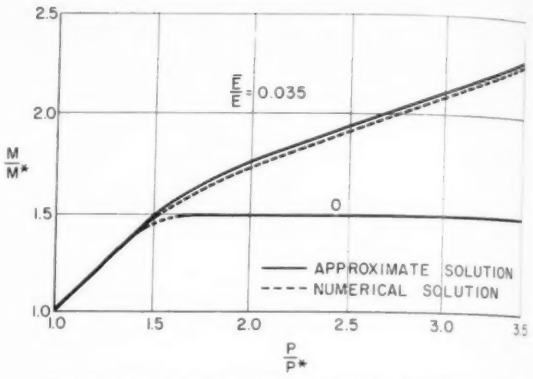

FIG. 7. Exact and approximate maximum moments.

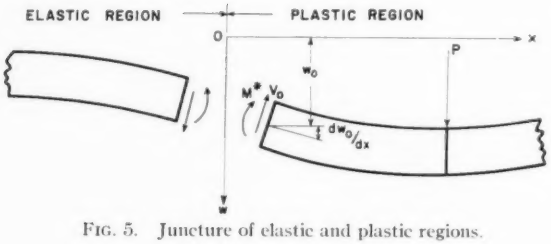

FIG. 5. Juncture of elastic and plastic regions.

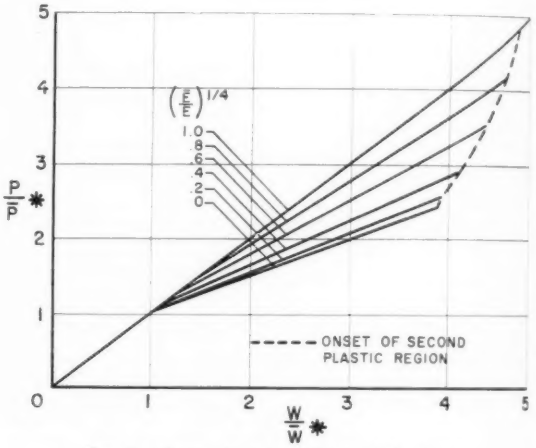

FIG. 8. Approximate maximum deflections.

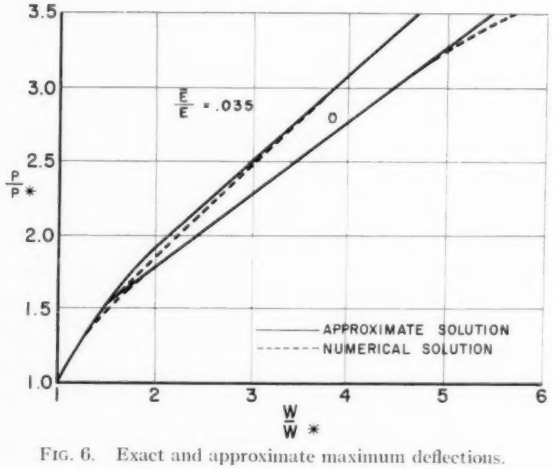

FIG. 6. Exact and approximate maximum deflections.

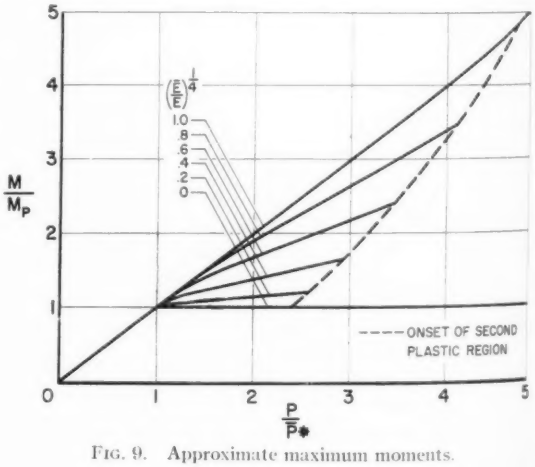

FIG. 9. Approximate maximum moments.

Infinite Elastically Supported Beam Subjected to a Concentrated Load

To test the adequacy of the linearized equations for the determination of the deflections of elastically supported beams, an investigation of an infinite beam subjected to a single concentrated load was made by means of both a numerical solution of Eq. (13) and an analytical solution of Eqs. (18a) and (18b). A detailed derivation of the linearized solution is given in Appendixes B and C. For the numerical solution of Eq. (13) the following approach was used:

When the concentrated load P has exceeded a value P^* ($P^* = 4M^*\lambda$), each half of the beam is divided at first into two regions, a plastic region in the vicinity of the load and an elastic region that extends to infinity (see Fig. 5). The moment at the juncture of the elastic and plastic regions of the beam is equal to M^*. If the shear force at the juncture is assigned some value, the deflection and slope of the elastic region at the juncture are determined. These values of moment, shear, deflection, and slope are then four initial conditions for the fourth-order differential equation defining the plastic region, which can now be solved by numerical integration methods. The process of numerical integration is continued until a point is reached at which the slope of the beam, or the third derivative of the moment [see Eq. (14c)], vanishes. The length of the plastic region is then known, and the value of the first derivative of the moment at that point yields the concentrated load applied to the beam. This procedure can be continued until some other part of the beam becomes plastic or, as was found in the analysis, until some part of the initial plastic region is subject to a decrease in moment. A more detailed description of the numerical analysis and the attendant difficulties is given in reference 1.

Numerical results computed with the linearized theory are compared in Figs. 6 and 7 with the corresponding results of the numerical integration process. Shown are the variation with load of the deflection and bending moment beneath the concentrated load for an infinite rectangular beam of a perfectly plastic material and of a material having a strain hardening parameter equal to 0.035. The deflection w^* is the deflection beneath the load when yielding is first encountered and is given by $2M^*\lambda^2/k$. Maximum deviations between the two sets of results are found in the vicinity of the yield load, as is to be expected since the approximate and "exact" moment-curvature diagrams differ most in this region, but are less than 2 per cent. Over most of the range of load shown, the results of the two methods are practically indistinguishable, thus indicating that the linearized analysis is decidedly adequate.

In Figs. 8 and 9 approximate values of maximum deflection and moment in an infinite beam are given for various values of the strain hardening parameter $\bar{E}/E$. The analytic results indicate that both these quantities for a given load vary almost linearly with the quantity $(\bar{E}/E)^{1/4}$. Thus, accurate determination of the strain hardening slope of the stress-strain curve of a material is important when the slope is small, since only slight variations in the slope have a pronounced effect on deflections and moments. In Figs. 8 and 9 the onset of a second plastic region in the beam is indicated by dashed curves. No further calculations have been made because of the excessive time and labor that would be involved.

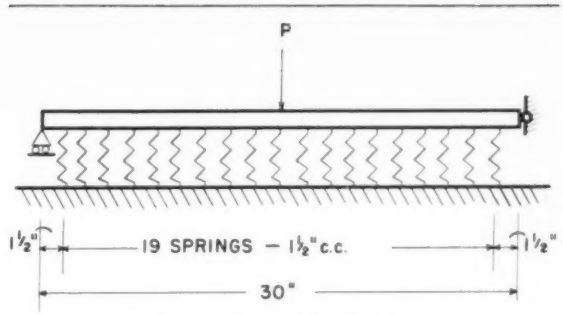

Fig. 10. Schematic test setup.

Comparison of Theory and Experiment

The experimental results reported by Richards in reference 2 provide an opportunity for investigating the validity of the results of the present investigation. Nine simply supported 24ST dural beams of rectangular cross section were subjected to a centrally applied concentrated load. Each beam had a length between supports of 30 in. and was supported on 19 elastic springs at $1^1/_2$ in. spacing. The test setup is shown schematically in Fig. 10.

The cross sections of the beams were of two different sizes, seven being $^1/_2$ in. wide and $^3/_4$ in. deep and two being $^1/_2$ in. wide and 1 in. deep. The spring constant was equal to 197 lbs. per in. and was divided by the spring spacing to yield a foundation modulus k of 131 lbs. per in. per in. The variation with load of deflections at the center of each beam and at four stations on either side were obtained during the tests. The results for all beams of a given size were in very close agreement.

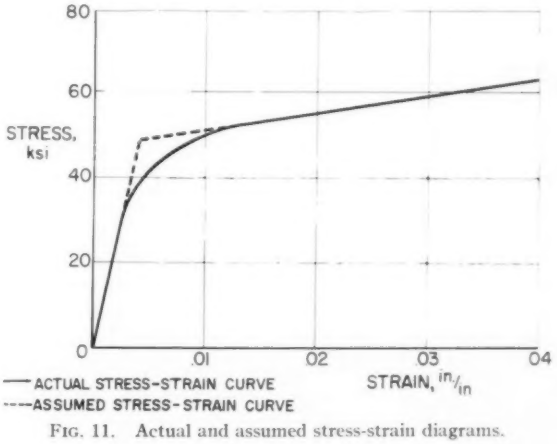

Fig. 11. Actual and assumed stress-strain diagrams.

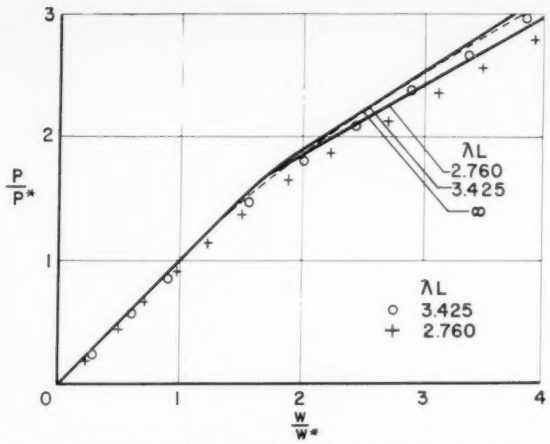

FIG. 12. Comparison of theoretical and experimental maximum deflections.

In comparing the experimental and theoretical results, some allowance has to be made for differences between the stress-strain curve of the beam material and the curve assumed in the theoretical investigation. The stress-strain curve obtained for the beam material is shown by the solid curve in Fig. 11. Young's modulus is 11×10^6 lbs. per sq.in. and the curve slopes gradually beyond a stress of about 30,000 lbs. per sq.in. until it becomes linear with a slope equal to 0.035 times the initial Young's modulus. This stress-strain curve was replaced by the two dashed lines shown in the figure, which gave a value of the ficticious yield stress σ^* equal to 49,400 lbs. per sq.in. Pertinent quantities for each of the two types of beams are given in the following table:

	Beam I		Beam II
h, in.	3/4		1
b, in.		1/2	
L, in.		30	
I_0, in.^{4}	9/512		1/24
E, psi		11×10^6	
k, psi		131	
λ, in.$^{-1}$	0.114		0.092
λL	3.425		2.760
P^*, lbs.	1012		1288
w^*, in.	0.477		0.483

The experimental results, reduced to the nondimensional forms P/P^* and w/w^*, are shown by the circles and crosses in Fig. 12. For comparison, theoretical results obtained from the linearized analyses of Appendixes B and C for finite beams are indicated by the solid curves. While the theoretical results are consistent with experiment, there is a 5 per cent error in both the elastic and upper plastic ranges. In the vicinity of the yield load the error is about 12 per cent, but this is to be expected since the assumed stress-strain curve and the derived bilinear moment-curvature diagram are most in error in this region.

Also shown in Fig. 12 is the approximate load-deflection curve for an infinite beam. This is very close to the curve for a beam with an effective length of 3.425 and leads to the conclusion that the lower limit of effective length for interchangeability of finite and infinite beam results is similar to that indicated by Hetenyi in reference 3 for elastic beams, namely $\lambda L > \pi$. It is recommended, however, that when infinite beam results are used for finite beams the yield load and deflection for the finite beam should be used in calculating the quantities P/P^* and w/w^*.

A striking indication of the validity of the use of infinite beam results for finite beams of relatively long effective length is shown in Fig. 13 by a comparison of deflections computed for the infinite beam by the numerical integration method and those obtained experimentally for the beam with effective length equal to 3.425. The shapes of the theoretical and experimental deflection curves are practically identical over most of the finite beam length, but deviate, of course, near the supports where the infinite beam deflections do not vanish.

Conclusions

Numerical methods of integration of ordinary differential equations have application to the problem of plastic bending of beams on elastic foundations, especially in those cases where there is a definite distinction between elastic and plastic regions for which the use of variational methods has not yet been developed as a practical method. These numerical methods have been applied to the problem of the bending under concentrated load of an infinite rectangular beam on an elastic foundation. The fourth-order nonlinear differential equation involved was obtained by using the assumptions of elementary beam theory for a material with a bilinear stress-strain curve.

Since the time and labor involved in the use of numerical methods is considerable, however, an approximate theory has been developed whereby the differential equation of bending is linearized by replacing the nonlinear moment-curvature diagram by straight lines. Numerical results of this theory are in good agreement with those obtained by the numerical integration procedure and with experiment. They have the advantage

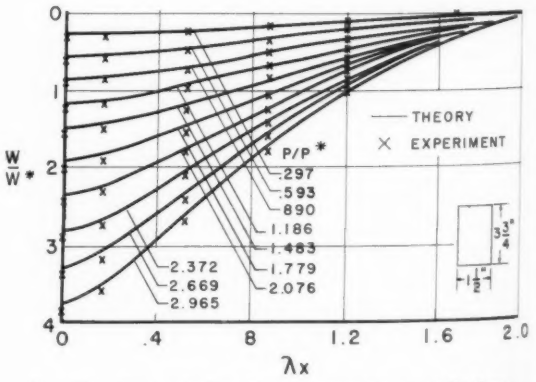

FIG. 13. Theoretical and experimental beam deflections.

of being expressible in a form applicable to beams of other than rectangular cross sections.

The approximate theory yields adequate results in much less time than does numerical integration of the more exact equation so long as only one or two plastic regions have appeared in the beam. With the development of many plastic regions, however, there is little difference between the amount of work involved in the application of either method to specific problems, except, possibly, in the case of the perfectly plastic beam.

References

[1] Seide, Paul, *Elasto-Plastic Bending of Beams on Elastic Foundations*, Tech. Rep. No. 17, Div. Engrg. Mech., Stanford U., September 1, 1953.

[2] Richards, Cedric W., *Experimental Investigation of Plastic Bending of Beams on Elastic Foundations*, Tech. Rep. No. 6, Div. Engrg. Mech., Stanford U., March 1, 1950.

[3] Hetenyi, M., *Beams on Elastic Foundation*, The University of Michigan Press, 1946.

Appendix A

Moment-Curvature Relationships

The relationship between bending moment and curvature for the elasto-plastic regions of a beam is given by Eq. (8). For some cross-sectional shapes this relationship reduces to the following:

$$\text{Rectangle:} \quad |\bar{l}| = \frac{1}{2}\left(1 - \frac{\bar{E}}{E}\right)(3 - \psi^2) + \frac{\bar{E}}{E}\frac{1}{\psi} \tag{A1}$$

$$\text{Ellipse:} \quad |\bar{l}| = \frac{2}{\pi}\left(1 - \frac{\bar{E}}{E}\right)\left[\frac{1}{\psi}\sin^{-1}\psi + \frac{1}{3}(5 - 2\psi^2)(1 - \psi^2)^{1/2}\right] + \frac{\bar{E}}{E}\frac{1}{\psi} \tag{A2}$$

Appendix B

Bending of a Perfectly Plastic Simply Supported Beam Under a Central Concentrated Load

For a perfectly plastic beam the approximate theory indicates a plastic region consisting of a point only—that is, plastic hinges form. Initially a plastic hinge appears at only the center cross section at which the moment remains equal to M_p and the beam slope is discontinuous. The remainder of the beam is elastic and is governed by Eq. (18b) with q equal to zero. The general solution of this equation is

$$\bar{l} = e^{\tilde{x}}(A \sin \tilde{\chi} + B \cos \tilde{\chi}) + e^{-\tilde{x}}(C \sin \tilde{\chi} + D \cos \tilde{\chi}) \tag{B1}$$

subject to the boundary conditions

$$\left.\begin{aligned} \bar{l} &= 1 \\ d\bar{l}/d\tilde{\chi} &= -P/2M_p\lambda \end{aligned}\right\} \tag{B2}$$

at $\tilde{\chi} = 0$, and

$$\bar{l} = d^2\bar{l}/d\tilde{\chi}^2 = 0 \tag{B3}$$

at $\tilde{\chi} = (1/2)\tilde{\chi}_m$. Substitution of Eq. (B1) into Eqs. (B2) and (B3) yields

$$A = \frac{\cos \tilde{\chi}_m - \sin \tilde{\chi}_m + e^{-\tilde{\chi}_m} + (P/2M_p\lambda)(e^{-\tilde{\chi}_m} - \cos \tilde{\chi}_m)}{2(\sinh \tilde{\chi}_m - \sin \tilde{\chi}_m)} \tag{B4a}$$

$$B = \frac{(P/2M_p\lambda)\sin \tilde{\chi}_m - (\cos \tilde{\chi}_m + \sin \tilde{\chi}_m + e^{-\tilde{\chi}_m})}{2(\sinh \tilde{\chi}_m - \sin \tilde{\chi}_m)} \tag{B4b}$$

$$C = \frac{(P/2M_p\lambda)(e^{\tilde{\chi}_m} - \cos \tilde{\chi}_m) - (\cos \tilde{\chi}_m + \sin \tilde{\chi}_m + e^{\tilde{\chi}_m})}{2(\sinh \tilde{\chi}_m - \sin \tilde{\chi}_m)} \tag{B4c}$$

$$D = \frac{\cos \tilde{\chi}_m - \sin \tilde{\chi}_m + e^{\tilde{\chi}_m} - (P/2M_p\lambda)\sin \tilde{\chi}_m}{2(\sinh \tilde{\chi}_m - \sin \tilde{\chi}_m)} \tag{B4d}$$

Of interest is the center deflection which is given by

$$\frac{w}{\bar{w}^*} = \frac{P}{\bar{P}^*} + \left(\frac{P}{\bar{P}^*} - 1\right)\left(\frac{\sinh \tilde{\chi}_m + \sin \tilde{\chi}_m}{\sinh \tilde{\chi}_m - \sin \tilde{\chi}_m}\right)^2 \tag{B5}$$

where

$$\bar{P}^* = 4M_p\lambda[(\cosh \tilde{\chi}_m + \cos \tilde{\chi}_m)/(\sinh \tilde{\chi}_m + \sin \tilde{\chi}_m)] \tag{B6a}$$

$$\bar{w}^* = (2M_p\lambda^2/k)[(\sinh \tilde{\chi}_m - \sin \tilde{\chi}_m) \div (\sinh \tilde{\chi}_m + \sin \tilde{\chi}_m)] \tag{B6b}$$

For the infinite beam, Eqs. (B4) become

$$\left.\begin{aligned} A &= B = 0 \\ C &= -[1 + (P/2M_p\lambda)] \\ D &= 1 \end{aligned}\right\} \tag{B7}$$

and Eqs. (B5) and (B6) reduce to

$$\left.\begin{aligned} w/\bar{w}^* &= 2(P/\bar{P}^*) - 1 \\ \bar{P}^* &= 4M_p\lambda \\ \bar{w}^* &= 2M_p\lambda^2/k \end{aligned}\right\} \tag{B8}$$

Eqs. (B7) and (B8) are valid only for

$$1 \leq P/\bar{P}^* \leq 2.434 \tag{B9}$$

after which other plastic hinges appear in the beam. For the finite beam the upper limit of validity depends on the beam length and is obtained only after lengthy computations.

It should be noted that the discussion of a "paradox" connected with other plastic hinges in a perfectly plastic beam, given on page 122 of reference 1, is incorrect. It can be shown that further beam deflections can be calculated.

Appendix C

Bending of a Strain-Hardening Simply Supported Beam Under a Central Concentrated Load

In investigating the bending of a finite elastically supported beam in which only one plastic region has developed in the vicinity of the concentrated load, the origin of coordinates is taken at the cross section in the right half of the beam common to both the elastic and plastic regions. In the elastic region to the right

of this section, Eq. (18b) is valid, while in the plastic region to the left, Eq. (18a) holds. The boundary conditions to be satisfied are those of continuity of moment, shear, deflection, and slope at the common section, zero moment and deflection at the support, zero slope beneath the load, and the condition that the moment at the common section is equal to M_p. A further condition is the equality of applied load and the shear at the center of the beam. Only one half of the beam is treated because of the symmetry of the problem.

The general solution of Eqs. (18) for the present problem is given by

$$\bar{l} = e^{\bar{\chi}}(A_p \cos \bar{\chi} + B_p \sin \bar{\chi}) + e^{-\bar{\chi}}(C_p \cos \bar{\chi} + D_p \sin \bar{\chi}) + [1 - (\bar{E}/E)]\, sgn\, \bar{l} \qquad (|\bar{l}| \geq 1) \quad \text{(C1a)}$$

$$\bar{l} = e^{\bar{\chi}}(A_e \cos \bar{\chi} + B_e \sin \bar{\chi}) + e^{-\bar{\chi}}(C_e \cos \bar{\chi} + D_e \sin \bar{\chi}) \qquad (|\bar{l}| \leq 1) \quad \text{(C1b)}$$

Substitution of Eqs. (C1) into the first eight boundary conditions then yields

$$A_e = -(\cos \delta + D_e \sin \delta)/(e^{\delta} - \cos \delta) \quad \text{(C2a)}$$

$$B_e = -[\sin \delta - D_e(\cos \delta - e^{-\delta})]/(e^{\delta} - \cos \delta) \quad \text{(C2b)}$$

$$C_e = (e^{\delta} + D_e \sin \delta)/(e^{\delta} - \cos \delta) \quad \text{(C2c)}$$

$$A_p,\ C_p = \pm(1/4)\,(\bar{E}/E)^{1/4}\,[1/(e^{\delta} - \cos \delta)]\,\{2D_e[\sinh \delta - \sin \delta - (\bar{E}/E)^{1/2}(\sinh \delta + \sin \delta)] - [e^{\delta} + \cos \delta + \sin \delta + (\bar{E}/E)^{1/2}(e^{\delta} + \cos \delta - \sin \delta) \mp 2(\bar{E}/E)^{3/4}(e^{\delta} - \cos \delta)]\} \quad \text{(C2d)}$$

$$B_p,\ D_p = (1/4)\,(\bar{E}/E)^{1/4}\,[1/(e^{\delta} - \cos \delta)]\{2D_e\,[\sinh \delta - \sin \delta \mp 2(\bar{E}/E)^{1/4}(\cosh \delta - \cos \delta) + (\bar{E}/E)^{1/2}(\sinh \delta + \sin \delta)] - [e^{\delta} + \cos \delta + \sin \delta \pm 2(\bar{E}/E)^{1/4} \sin \delta - (\bar{E}/E)^{1/2}(e^{\delta} + \cos \delta - \sin \delta)]\} \quad \text{(C2e)}$$

$$D_e = \frac{(e^{\delta} + \cos \delta + \sin \delta)\sinh \frac{1}{2}\bar{\chi}_p \sin \frac{1}{2}\bar{\chi}_p + \left(\frac{\bar{E}}{E}\right)^{1/4} \sin \delta \left(\sinh \frac{1}{2}\bar{\chi}_p \cos \frac{1}{2}\bar{\chi}_p - \cosh \frac{1}{2}\bar{\chi}_p \sin \frac{1}{2}\bar{\chi}_p\right) + \left(\frac{\bar{E}}{E}\right)^{1/2} \times}{(e^{\delta} + \cos \delta - \sin \delta)\cosh \frac{1}{2}\bar{\chi}_p \cos \frac{1}{2}\bar{\chi}_p + \left(\frac{\bar{E}}{E}\right)^{3/4}(e^{\delta} - \cos \delta)\left(\cosh \frac{1}{2}\bar{\chi}_p \sin \frac{1}{2}\bar{\chi}_p + \sinh \frac{1}{2}\bar{\chi}_p \cos \frac{1}{2}\bar{\chi}_p\right)}$$

$$(\sinh \delta - \sin \delta)\sinh \frac{1}{2}\bar{\chi}_p \sin \frac{1}{2}\bar{\chi}_p + \left(\frac{\bar{E}}{E}\right)^{1/4}(\cosh \delta - \cos \delta)\left(\cosh \frac{1}{2}\bar{\chi}_p \sin \frac{1}{2}\bar{\chi}_p - \sinh \frac{1}{2}\bar{\chi}_p \cos \frac{1}{2}\bar{\chi}_p\right) - \left(\frac{\bar{E}}{E}\right)^{1/2}(\sinh \delta + \sin \delta)\cosh \frac{1}{2}\bar{\chi}_p \cos \frac{1}{2}\bar{\chi}_p \quad \text{(C2f)}$$

Eqs. (C1) and (C2) completely define the solution of the problem in terms of the parameter $\bar{\chi}_p$. The load corresponding to a given value of $\bar{\chi}_p$ is determined by the value of the first derivative of $\bar{l}$ at $\bar{\chi} = -(1/2)\bar{\chi}_p$, using Eq. (C1a) and the computed values of A_p, B_p, C_p, and D_p.

The solution can be reduced somewhat for the infinite beam for which $\delta \to \infty$. Then

$$A_e = B_e = 0 \quad \text{(C3a)}$$

$$C_e = 1 \quad \text{(C3b)}$$

$$A_p,\ C_p = \pm\frac{1}{4}\left(\frac{\bar{E}}{E}\right)^{1/4}\left\{\left[1 - \left(\frac{\bar{E}}{E}\right)^{1/2}\right]D_e - \left[1 + \left(\frac{\bar{E}}{E}\right)^{1/2} \mp 2\left(\frac{\bar{E}}{E}\right)^{3/4}\right]\right\} \quad \text{(C3c)}$$

$$B_p,\ D_p = \frac{1}{4}\left(\frac{\bar{E}}{E}\right)^{1/4}\left\{\left[1 \mp \left(\frac{\bar{E}}{E}\right)^{1/4}\right]^2 D_e - \left[1 - \left(\frac{\bar{E}}{E}\right)^{1/2}\right]\right\} \quad \text{(C3d)}$$

$$D_e = -\frac{\tanh \frac{1}{2}\bar{\chi}_p \tan \frac{1}{2}\bar{\chi}_p + \left(\frac{\bar{E}}{E}\right)^{3/4}\left(\tanh \frac{1}{2}\bar{\chi}_p + \tan \frac{1}{2}\bar{\chi}_p\right) + \left(\frac{\bar{E}}{E}\right)^{1/2}}{\left[\left(\frac{E}{\bar{E}}\right)^{1/4} - \tan \frac{1}{2}\bar{\chi}_p\right]\left[\left(\frac{\bar{E}}{E}\right)^{1/4} + \tanh \frac{1}{2}\bar{\chi}_p\right]} \quad \text{(C3e)}$$

Some Recent Aerodynamic Techniques in Design of Fin-Stabilized Free-Flight Missiles for Minimum Dispersion*

M. W. HUNTER,† A. SHEF,‡ AND D. V. BLACK**

Douglas Aircraft Company, Inc.

SUMMARY

In the past, finned rocket design techniques were usually based on an attempt to restrict the flight-path angular deviation during burning by obtaining maximum possible longitudinal stability to decrease the effect of internal rocket disturbances. In recent years, with the increased interest in rocketry and guided missiles design, more sophisticated design techniques have been developed. These permit appreciable reduction in dispersion by considering the conflicting stability requirements from internal and external disturbances. Not only is optimum compromise attempted, but the component errors are attacked individually by fundamental spin programming (other than simple monotonic programs) and by utilization of techniques similar to those used in such fields as feedback theory and noise analysis. It is shown that the use of such combined techniques effectively reduces rocket flight-path angular dispersion.

INTRODUCTION

THE ONCE PROPOUNDED theory of obtaining maximum possible longitudinal stability to restrict the dispersion of fin-stabilized rockets can be shown to be inadequate to meet current accuracy requirements. With the impetus put on rocket and missile design in the last decade, more adroit techniques of dispersion reduction have been developed. Techniques range in complexity from the simple error averaging methods of monotonic spin programming to highly intricate guided missile systems. This paper is concerned with discussion of methods normally allocated to the less costly portion of this complexity spectrum. These methods, however, are applicable to the free-flight boost phase of some guided missile systems as well as to free-flight rocketry.

A complete discussion of the problem of free-flight rocket dispersion for all rocket applications would be an extremely ambitious undertaking and would exceed the intended scope of this paper. Therefore, attention will be directed only to certain significant portions of the rocket dispersion problem.

In flight, trajectory disturbances can be allocated to two groups according to their effects. These are "angular errors"—i.e., error sources that manifest change in rocket flight-path angle—and "speed-change errors"—i.e., errors that manifest change in rocket velocity or flight-path distance at a given time of flight. This paper is limited to discussion of the former error group only. Angular deviation is accrued during flight in both the motor-burning, or thrust, phase and in the period after motor burnout, or glide phase. For most rocket systems the deviation at the target directly traceable to angular-type errors is due almost entirely to the angular error accrued during the thrust phase. This angular error accumulated up to burnout is referred to as latent angular dispersion because its significance lies in its effect on flight-path deviation after motor burnout. It is helpful to consider the thrust phase as comparable to the barrel phase of gun-fired projectiles because each bears the same relation to the remainder of the trajectory. Whereas angular dispersion for a shell is dependent primarily on gun rigidity and, therefore, is usually negligible, rocket latent angular dispersion is dependent on a variety of influences and is usually a substantial factor in the accuracy problem. In attempting to reduce rocket dispersion, the goal is not necessarily the reduction of latent angular dispersion to a level comparable to that of a gun-fired projectile, but rather the reduction of this error to a magnitude commensurate with the other errors in the rocket system.

The dispersion-reduction techniques as discussed in this paper have primary application to ground-launched rockets and missiles, although the basic theories also have some utility in air-launched rocket design.

DISCUSSION

Having once established the latent angular dispersion to be of primary interest in this particular application, it is not difficult to put the kinematics of the burning period on a rational analytical basis in order to observe the buildup of this dispersion. Actually, the foundations of the theory of latent dispersion were established during World War II by several groups working under different auspices including, among others, Follin, Blitzer, and Davis at California Institute of Technology, and Rosser, Newton, and Gross at Allegany Ballistic Laboratory for the Office of Scientific Research and Development, National Defense Research Committee.[1] The body of work described in this paper takes the basic analysis and extends it as a result

Presented at the Aerodynamics—II Session, Twenty-Third Annual Meeting, IAS, New York, January 24–27, 1955.

* The basic work from which information for this paper was taken was supported by the Ordnance Corps, Department of the Army.

† Design Engineer—Missiles.

‡ Design Specialist.

** Aerodynamics Engineer.

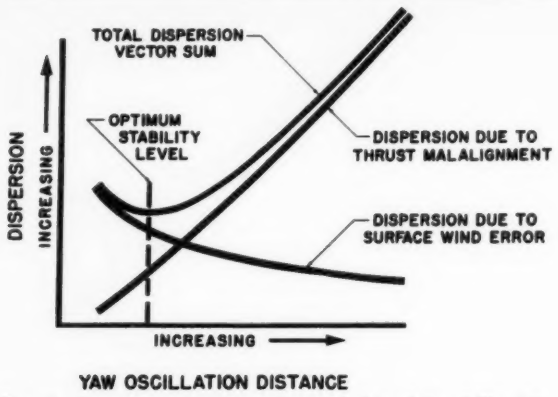

FIG. 1. Latent angular dispersion variation with stability (deflection component).

of obtaining additional empirical dispersion data in recent years from detailed examination of the deviating motion of rockets during burning. The notation used has, in general, followed that of Rosser et al.

As shown in reference 1, the motion of a rocket during burning is unique in that it is usually characterized by approximately constant acceleration (over the region of interest), resulting in a linear increase in velocity with time and a consequent quadratic increase of dynamic pressure, thus rapidly increasing restoring forces on the rocket. In addition, attitude deviations cause the large accelerating force of the rocket to be deflected laterally, producing flight-path deviations the random portion of which results in latent angular dispersion. The equations of motion with time as the independent variable are seen to be linear but with variable coefficients due to the quadratic buildup of aerodynamic forces. In order to solve these equations for the analytical evaluation of latent dispersion, it is necessary to rewrite them considering rocket distance traveled as the independent variable, since the dynamic pressure is directly proportional to this variable. Thus the deviating motion can be evaluated in terms of burning distance rather than burning time, and the distance traveled by the rocket during one period of oscillation becomes the useful measure of stability rather than the rocket natural frequency. This stability index, itself a distance, is utilized as the normalizing parameter for the distance history of the motion. This index is sometimes called "yaw oscillation distance," or "wave length," and is written as

$$\sigma = \frac{V}{f} = 2\pi \sqrt{\frac{I}{(dC_M/d\alpha)\ (\rho/2)\ S\bar{c}}}$$

where

σ = yaw oscillation distance (ft.)
V = rocket instantaneous velocity (ft./sec.)
f = rocket natural frequency (cycles/sec.)
I = rocket moment of inertia in pitch (slug-ft.^{2})
$dC_M/d\alpha$ = slope of pitching moment curve (per rad.)
ρ = air density (slugs/ft.^{3})
S = reference area of rocket (ft.^{2})
$\bar{c}$ = reference length of rocket (ft.)

In many cases, yaw oscillation distance varies slowly enough during burning so that a single value may be taken as being representative of rocket stability; to this degree it differs from the behavior of the continuously varying natural frequency and is consequently extremely useful.

Solution of the equations of motion under the variety of disturbed conditions which produce latent angular dispersion is found to result in a series of closed-form transfer functions, the values of which depend on the number of wave-length units traversed while on the launcher and in free-flight to burnout. The functions relate each type and amount of input disturbance to a corresponding amount of output dispersion.

In considering ground-launched rockets, attention can be focused on two categories of these disturbances, each of which has one dominating component. These two basic groups are (1) "internal errors," whose most representative and probably most important component for current rocket designs is generally thrust malalignment, and (2) "external errors," which are dominatingly influenced by wind. Although wind may be allowed for in prelaunch aiming, a certain amount due to measuring error and due to wind variability in time and space always goes uncompensated. Without recourse to mathematical analysis it is possible through simple logic to determine characteristic effects of these error inputs. It is evident from rocket accuracy considerations that these two error sources introduce conflicting rocket longitudinal stability requirements. Excessive stability, while decreasing thrust malalignment dispersion, causes accelerated rockets to "weathercock" strongly into the wind and to initiate subsequent deviations from the intended flight direction. Low stability, on the other hand, permits excessive flight-path deviation due to thrust malalignment. Therefore, in minimizing flight-path angular dispersion for fixed values of these two types of error input, a stability compromise is necessary. Fig. 1 is presented to illustrate the type of optimizing necessary. This figure shows the effect on latent angular dispersion of a change in rocket longitudinal stability as depicted by change in rocket yaw oscillation distance for a hypothetical rocket design and for typical values of wind error and thrust malalignment. However, even with proper compromise, the optimized dispersion level may be undesirably large. The remainder of this paper will be concerned with discussion of the possible reduction of this optimum by attacking each component individually.

The two basic approaches to this problem are (1) reduce rocket sensitivity to error inputs, and (2) reduce magnitude of error inputs. In the first approach a practical consideration is to attempt to remove one of the two conflicting stability requirements by some auxiliary technique, thereby permitting the reduction of angular dispersion by raising or lowering the rocket

stability level in accord with the minimum dispersion requirements of the remaining error source.

Before considering dispersion-reduction techniques of this type, it is desirable to examine the functional relationship of the several factors affecting rocket dispersion due to the internal and external type of errors considered here. Certain simple approximations can be developed from each of the closed-form transfer functions previously discussed, assuming long thrust-phase distance compared to rocket wave length (which is approximately true for many rocket systems). Thrust malalignment dispersion is thus found to be

$$\theta_T \cong \frac{\sigma L \beta}{8k^2[(2\pi^2/\sigma)\ p + 1]} \text{ (rad.)}$$

where L = thrust malalignment distance defined as the perpendicular distance from the rocket center of gravity to the thrust vector (ft.)

k = radius of gyration in pitch (ft.)

p = launcher guidance length defined as the distance during which the rocket is mechanically constrained by the launcher

β = dispersion reduction factor resulting from use of auxiliary techniques

Similarly, dispersion due to error in wind assessment is written as

$$\theta_W \cong \frac{V_w}{\sqrt{2G\ [p + (\sigma\ \pi^2)]}} \text{ (rad.)}$$

where V_w = wind error due to measuring error and variability in time and space (ft./sec.)

G = rocket longitudinal acceleration (ft./sec.^{2})

Combining these dispersion contributions statistically, since these are random inputs, yields an estimate of latent angular dispersion,

$$\bar{\theta} = \sqrt{\theta_T^2 + \theta_W^2}$$

Since each of the contributions varies in a different fashion with wave length, the optimum wave length for minimum dispersion can be derived. For the case of very short launcher length, there results

$$\sigma_{\text{opt.}} = \left[\frac{4\pi\ k^2\ V_w}{\sqrt{GL\beta}}\right]^{2/3}$$

The value of minimum dispersion at $\sigma_{\text{opt.}}$ can be obtained as

$$\bar{\theta}_{\text{min.}} = \frac{\sqrt{3}}{8}\left[\frac{(4\pi)^2 L\beta V_w^2}{Gk^2}\right]^{1/3}$$

This equation presents several parameter relationships that merit further comment. Obviously, the most effective dispersion reduction can be obtained from direct reduction of the wind measuring error. Lessening the magnitude of L or β has effectiveness equal to increasing rocket longitudinal acceleration or the square of the radius of gyration. Unfortunately, the latter two factors are limited by practical considerations dictated by pay load and motor design. Thus, for reduction of latent angular dispersion of rocket designs commensurate with the assumptions on launcher length and burning distance, the parameters most amenable to exploitation are error input magnitudes, L and V_w, and the internal error reduction factor, β.

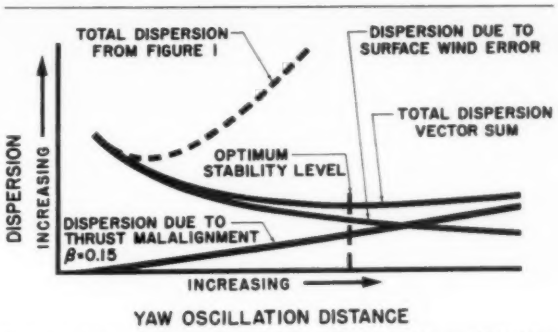

FIG. 2. Latent angular dispersion variation with stability (deflection component).

Before considering methods of reducing these three factors, it is of interest to show the double effect on minimizing dispersion of reductions in magnitudes of L and β—i.e., the direct effect on internal error and the indirect, or feedback, effect on external error. Fig. 2 presents the latent angular dispersion for the hypothetical rocket of Fig. 1 with the same typical wind error inputs but with reduction of 85 per cent in the thrust malalignment error through the reduction of L or β.

As demonstrated in this figure, an 85 per cent reduction in the internal error factor indicates a new optimum wave length four times larger than the previous optimum. This reduced stability in turn produces a rocket less sensitive to the given wind error and subsequently lowers $\bar{\theta}_{\text{min.}}$ to about 60 per cent of the former value.

Reduction of Internal Error Effects

Magnitudes of internal malalignment errors are dependent to some extent on rocket manufacturing techniques. Since thrust malalignment is composed of nozzle mechanical malalignment, lateral offset of rocket center of gravity, and motor gas malalignment, some reduction in malalignment error, L, could probably be obtained by improved manufacturing methods. The extent of this reduction is, of course, dependent partially upon the magnitude and behavior of the gas malalignment component. Because reduction of manufacturing malalignments is a mechanical rather than an aerodynamic design problem, no further attention will be given this feature here. However, in the actual rocket design problem this region for improvement should not be disregarded.

The internal type of error as typified by thrust malalignment is more amenable to suppression by simplified auxiliary devices than is the wind error. In particular, spinning of the rocket about its longitudinal

axis is an established technique of dispersion reduction. Gyroscopic stabilization by extremely high roll rates has been standard practice for many years for shells and finless rockets. Reduction of dispersion by an averaging technique through slow spin which causes malalignment error input to be scattered in all meridional directions, yielding less resultant angular deviation, is a simple but effective device. The simplest spin techniques, and therefore the first to yield to analysis, are the monotonic programs of constant spin acceleration and constant spin velocity. Fig. 3 shows the relation between the important parameters for the case of constant spin acceleration for the hypothetical rocket design and typical error values of Fig. 1. Fig. 3 indicates that the dispersion reduction factor, β, which in this case is the ratio of dispersion for the spun rocket to dispersion for the nonspun rocket and which includes the effect of launcher length, is dependent on rocket spin rates and launcher guidance length. To obtain error reductions on the order of 90 per cent or more, long launchers or high spin rates are necessary. These high spin rates are especially uneconomic, due to the transient nature of the growth of the dispersion. As typified by the curves of Fig. 4, practically all of the thrust malalignment dispersion is established in a fraction of the first wave length of rocket travel. This results from the steadily increasing velocity, producing rapidly increasing dynamic pressure and thus increasing ability to restrain the pitching motion produced by the malalignment. The short time of dispersion growth in the nonspun rocket indicates that any spin action for purposes of dispersion reduction must occur during or immediately after launch. A particular case of constant spin acceleration is also illustrated in Fig. 4, further demonstrating the short action time of spin effectiveness. Except for reducing certain dispersion inputs of secondary importance, the spin which continues to increase or is maintained after this initial wave-length fraction is essentially wasted. What actually occurs in the interaction of simple spin and dispersion is demonstrated in a schematic fashion in Fig. 5. A rocket cross section is shown with vector representation of thrust malalignment error input and flight path error output. The spin is seen first to scatter the input over a variety of directions. The resultant output is building rapidly at first and then slowly and is not permitted to accrue in one direction, thus being made smaller. Its direction is the weighted average of all increments of output in a variety of directions. Consequently, the output has advanced in phase angle, about 45° in many cases. When the input first leads output by half a revolution, a decrease in output actually occurs, but the input is carried rapidly away from this position. After this first opposition, any further coincidence or opposition is insignificant due to the rise in rocket stability "stiffness" brought on by increasing velocity. The steady-state dispersion has been reached.

Theoretical analysis of the equations of motion, as typified by the characteristics in Figs. 4 and 5, leads to the intuitive realization that there may be fundamental techniques other than simple spin which can produce substantial improvements in dispersion reduction. In particular, from the nature of the dispersion growth curve of the nonspun rocket in Fig. 4, it is reasonable to postulate that if an instantaneous 180° rotation of the rocket were inserted into the motion at some proper time during the short growth period of the dispersion, the remaining time would be spent in tending to cancel the flight path error produced before rotation. The result is shown in Fig. 6 in comparison with a wholly nonspun case and a simple spin solution. The dispersion history of the rocket, obtained solely from mathematical considerations, is then merely a set of two nonrotating cases connected by an instant of roll motion so that cancellation may be effected. Such instantaneous rotation cannot be obtained physically, but does offer a model of the cancellation phenomenon and its characteristics. As seen from the figure, the dispersion apparently may be reduced to zero without resorting to spin which is not utilized later in flight.

Achieving a complete cancellation of thrust malalignment dispersion, even for the physically impossible case of instantaneous rotation of π radians, is dependent upon rotating at exactly the correct flight distance after launch. This timing effect is demonstrated in Fig. 7 which shows the amount of dispersion reduction obtained by this technique as a function of distance traveled up to time of rotation. The critical nature of the timing of this event is apparent from this figure.

While instantaneous roll is not physically practical, the substitution of realistic motion would still tend to approximate the phenomenon. The dispersion reduction obtainable with a practical roll program based on dispersion cancellation philosophy can be determined by further study. Additional study is probably warranted since effective dispersion reduction may be attainable by this technique without the penalties imposed by long launcher guidance lengths and high roll rates required in continuous spin programs.

As was indicated previously, the importance and value of spin programming in increasing rocket accuracy is not only in the reduction of one dispersion component —i.e., thrust malalignment—but also in the subsequent significant feedback in minimizing windage dispersion which effectively suppresses wind influence loop gain.

It must be noted that this analysis of the effect of spin on dispersion is predicated on the assumption that internal error malalignments remain fixed in missile coordinates. This assumption is evidently reasonable for the structural malalignments mentioned previously; however, it is not quite so evident that motor-gas malalignment behaves in this fashion. The motor-gas malalignment effect on rocket dispersion could be further investigated by considering gas malalignment as a random input to the rocket system. This would necessitate having a statistical evaluation of the behavior of motor-gas malalignment.

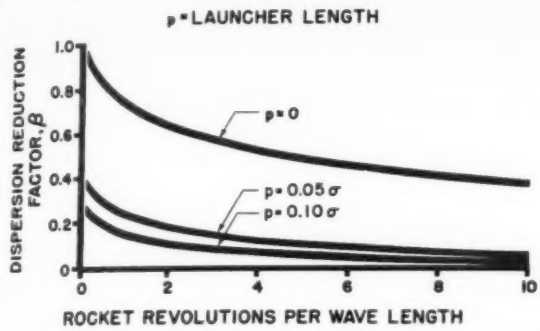

FIG. 3. Thrust malalignment dispersion reduction achieved with a constant acceleration spin.

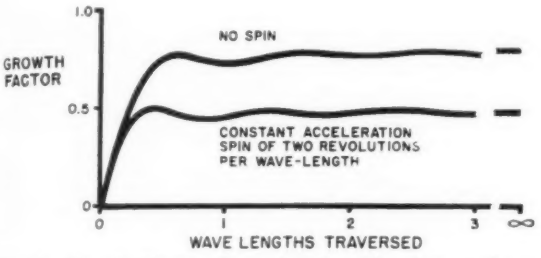

FIG. 4. Growth history of angular dispersion due to thrust malalignment (zero launcher length).

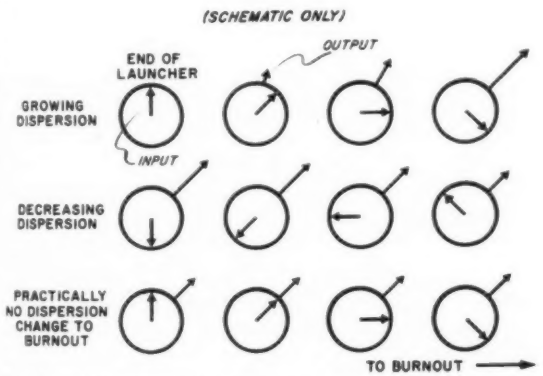

FIG. 5. Dispersion due to thrust malalignment; effect of monotonic spin (schematic only).

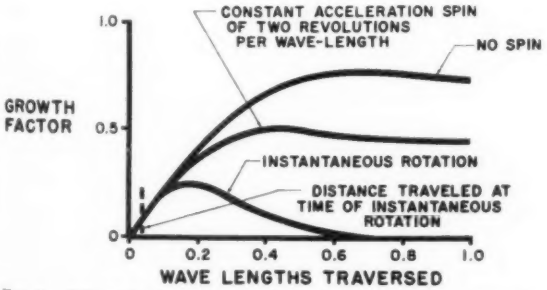

FIG. 6. Effect of spin on dispersion growth history (zero launcher length).

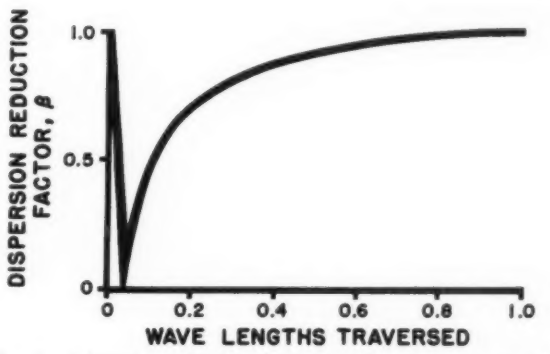

FIG. 7. Dispersion reduction obtained by instantaneous roll of π radians (zero launcher length)

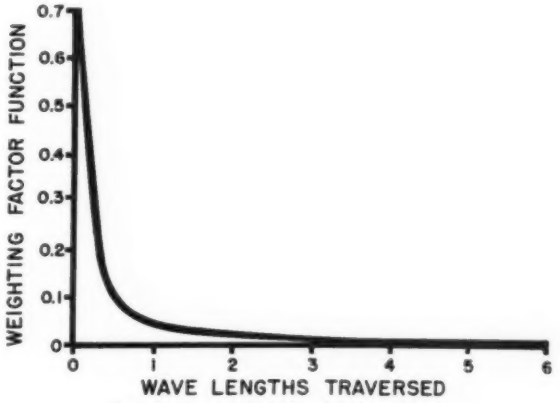

FIG. 8. Surface wind weighting factor.

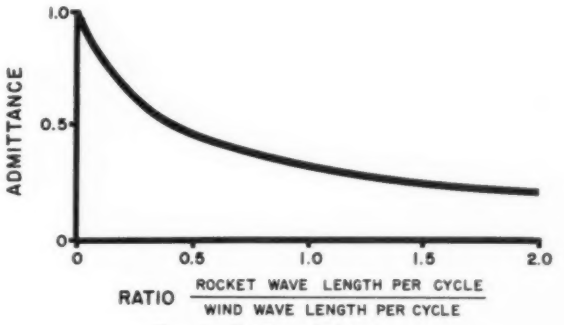

FIG. 9. Rocket admittance.

Reduction of External Error Effects

With the reduction of internal error requirements on stability by proper spin programming, rocket stability can be reduced to a minimum level dictated only by glide phase stability requirements. The effect of this reduced stability on dispersion due to wind for our hypothetical rocket is evident in Fig. 2.

When a reasonable limit is reached on attempts to insulate the rocket from the effect of wind errors, it is expedient for the rocket designer to turn his attention to reduction of the wind error by increasing the accuracy of wind measurement.

Accuracy of wind assessment for prelaunch aiming is dependent upon two criteria. First, it is desired that measurement be made of the same moving air mass that the rocket will sense in flight, since time and space variations in the mean wind velocity may easily introduce appreciable error. (However, exact and complete surveys over such an air mass are almost invariably tactically impractical.) Second, the measuring instrument or instruments, in addition to being accurate, should approximate the dynamic response characteristics of the rocket to the wind as a randomly fluctuating quantity. Attempts to measure the air mass are aided by the fact that, as in the case of the internal error effect, the major portion of rocket dispersion is accrued within the first wave length of flight. Fig. 8 shows the importance of wind measurement along the rocket thrust-phase trajectory path. From this figure it can be seen that about 75 per cent of the wind effect is accrued within the first wave length of travel of the hypothetical rocket, an effect typical of many cases. Therefore, accuracy of wind measurement can be degraded as distance from launcher increases, the limiting case being a single measurement near the end of launch. However, even in this case sufficient rocket accuracy may be obtainable if accurate wind measuring equipment is used and if the time variation error of the mean wind velocity is negligible.

Since rocket accuracy is dependent on assessment of the same air mass the rocket senses in flight, time variations can be fully as important as space variations. Measuring error due to this time variation could be reduced through use of an accurate prediction theory; however, at present, no such theory is available. Reduction in that wind error due to time variation is related to the combined wind measurement and rocket-launching procedure. Reducing the time delay between these two events to zero will also reduce to zero the wind-time variation error. Time variation errors can be effectively reduced either by slaving the launcher to the wind measuring equipment or by launching upon recurrence of a previously measured wind.

Rocket Admittance Theory

In order to determine wind-frequency response characteristics of accelerated free-flight rockets, an analytic theory of missile admittance has been developed in which wind is considered as a random input to the rocket aerodynamic system. The mathematical technique involved with this evaluation, although certainly not new in concept, is of interest because it demonstrates a new application of the established theory of generalized harmonic analysis. This rather lengthy development is presented in detail in reference 2.

Since the measure of rocket stability is a distance, wind eddies relative to rocket yaw wave length are significant rather than time fluctuations of wind. The wind-frequency response characteristics of rockets with high longitudinal acceleration, as developed by this theory, indicate that even wind eddies of wavelength size are relatively unimportant and that the long-steady trends in wind determine rocket flight-path deviations. Fig. 9 presents the frequency response characteristics of a typical rocket design. The ordinate scale is plotted as an admittance ratio—i.e., rocket response for a randomly fluctuating wind normalized by rocket response to a constant wind. The independent variable is the ratio of the rocket wave length to the wind wave length.

The degree of natural damping due to the acceleration of the rocket is apparent in this figure, since importance of wind effect decreases continuously as wind frequency increases—i.e., there are no resonance peaks. This high level of system damping is relatively independent of rocket aerodynamic damping. Other effects on frequency response investigated were those of launcher length and burning distance relative to rocket yaw wave length. For the typical rocket designs investigated, launcher length effect was determined to be relatively unimportant and burning distance effect is unimportant beyond approximately one wave length.

The results of studies of this type are vital in the proper design of wind-sensing instruments for rocket systems since instrument response should be made to match rocket admittance in order that the mean wind velocity reported by the instrument be exactly the same as that which is effective in perturbing the rocket. If, in addition, information concerning the statistical characteristics of the randomly fluctuating wind—i.e., the wind-power spectrum which forces the system via the admittance—were available, further extension of the analysis would be feasible. For example, it might be possible to simplify a large portion of the response-matching problem by neglecting those bandwidths in which little surface wind activity occurs. It would also be possible to combine power spectral density and admittance and thus obtain a value for the apparent noise level of the rocket wind system. Such results would be, in essence, an evaluation of the maximum latent angular accuracy obtainable for a rocket in the presence of its environment in those environmental conditions for which data could be secured.

However, much work needs to be done to obtain sufficient basic information concerning wind-power spectra and the effects of terrain and atmospheric conditions on power spectra before adequate wind analysis

of this type can be made. Most of the information available at present is based on turbulence measurements in the upper air; these data are pertinent to air-launched rockets but not necessarily to ground-fired rockets, since in general, small-scale terrain effects and ground thermal effects strongly influence the nature of the phenomenon.

Despite the lack of specific power spectral information to perform these refinements, the establishment of the admittance characteristics produces a valuable tool in the problem of effective reduction of external error dispersion. For this purpose, the rocket admittance function provides all the information necessary to perform response matching. If the instrumentation can be matched to the rocket overall eddy sizes, lack of precise knowledge of the statistical nature of the randomly fluctuating wind does not degrade dispersion-reduction effectiveness. The lowest value of uncompensated wind present will have been obtained for given system mean wind time and space variations; it will remain, however, to evaluate that quantity from actual firing statistics rather than from analytical considerations.

Conclusion

By combining specialized dispersion-reduction techniques (minimizing separately the effects of rocket internal errors and environmental assessment errors) with techniques of optimizing rocket stability on the basis of conflicting stability requirements, effective reduction can be obtained in rocket flight-path angle dispersion during the thrust phase.

Dispersion due to internal errors, primarily thrust malalignment, can probably be reduced to a negligible amount by proper spin programming. Mathematical analysis of the interaction between spin and thrust malalignment dispersion indicates that fundamental spin programs exist, based on the philosophy of dispersion cancellation and resulting in substantial dispersion-reduction without the penalties imposed by long launcher guidance lengths and high roll rates required in continuous spin programs.

Dispersion due to external errors, as manifest by wind error, can be reduced not only by decreasing longitudinal stability but also by improving design in wind measuring equipment with particular regard to matching rocket and instrument dynamic response characteristics. The matching can be accomplished by utilizing the admittance function derived from rocket motion analysis. If, in addition, wind-power spectral density were available for typical rocket-launching environments, further insight into the problem might be gained.

References

[1] Rosser, J. B., Newton, R. R., and Gross, G. L., *Mathematical Theory of Rocket Flight*, McGraw-Hill Book Company, Inc., New York, 1947.

[2] Robinson, S. M., *Response of Accelerated Free-Flight Rockets to Wind*, Douglas Aircraft Company, Inc., Report SM-18443, January, 1955 (unclassified).

The Design and Testing of Supersonic Flutter Models

(*Continued from page 535*)

lem of obtaining low model mass ratios (μ) is somewhat alleviated. Some variation in μ is possible for a given model by varying the stagnation pressure (Fig. 13).

Conclusions

Model theory shows that, because of physical limitations, the frequencies of flutter models where Mach Number is simulated are an order of magnitude higher than those of models where the velocity is scaled so that flutter occurs within the range of a low-speed wind tunnel. For high-speed flutter models, new techniques of model design, vibration testing, and static testing must be developed to account for the very high frequencies.

In most flutter tests it is more feasible to vary the flow parameters rather than the model parameters to obtain the neutrally stable flutter conditions. For supersonic flutter testing in the wind tunnel, significant changes in the flow parameters can only be achieved with a variable geometry nozzle.

References

[1] Bisplinghoff, R. L., Ashley, H., and Halfman, R. L., *Aeroelasticity*, Addison Wesley Press, Inc., Cambridge, 1955.

[2] McCarthy, J. F., Jr., Halfman, R. L., Prigge, J. S., Jr., and Levey, G. M., *Supersonic Flutter Model Tests—Part I, Model Design and Testing Techniques*, WADC TR 54-113 (to be published).

[3] Halfman, R. L., McCarthy, J. F., Jr., Prigge, J. S., Jr., and Wood, G. A., Jr., *A Variable Mach Number Supersonic Test Section for Flutter Research*, WADC TR 54-114, December, 1954.

[4] Smilg, B., and Wasserman, L. S., *Application of Three-Dimensional Flutter Theory to Aircraft Structures*, AF Technical Report No. 4798, July, 1942.

[5] Timoshenko, S., and Goodier, J. N., *Theory of Elasticity*, 2nd Ed., p. 275–278; McGraw-Hill Book Co., Inc., New York, 1951.

[6] Smith, R. H., *Air Jet Vibrator for Determining Natural Frequencies of Aircraft*, S.M. Thesis, Massachusetts Institute of Technology, October, 1943.

[7] Garrick, I. E., *Some Research on High-Speed Flutter*, Third Anglo-American Aeronautical Conference, 1951.

[8] Garrick, I. E., and Rubinow, S. I., *Flutter and Oscillating Air-Force Calculations for an Airfoil in a Two-Dimensional Supersonic Flow*, NACA TR No. 846, 1946.

A First-Order Formulation of the Unsteady Supersonic Flow Problem for Finite Wings

JOHN W. MILES*

University of California, Los Angeles

SUMMARY

The determination of the pressure distribution over a thin, finite wing in supersonic flow due to a prescribed incidence that varies slowly in time (so that the square of the reduced frequency may be regarded as negligible) is reduced to a pair of steady flow problems. The first of these is the steady flow problem for the given plan form with modified incidence. The second corresponds to a modified steady flow problem in which the wake is neglected and the potential is required to vanish along subsonic trailing edges. In the absence of subsonic trailing edges the solution to the second problem follows directly from the solution to the first problem, and the results then reduce to those previously known.

(1) INTRODUCTION

IT HAS BEEN KNOWN for some time (see references 1 to 3, the last being restricted to two-dimensional flow) that the problem of determining the pressure distribution over a thin wing executing a low frequency motion of small amplitude in supersonic flight may be transformed to a corresponding problem in steady flow, provided that the trailing edge is nowhere subsonic. It is the purpose of the present paper to eliminate the trailing-edge restriction by an appropriate extension of the transformation. This extension was suggested to the writer by a result surmised by Evvard[4] for a particular class of plan forms and proved (by Harmon[5]) for the special case of a linear variation (in time) of angle of attack.

(2) STATEMENT OF PROBLEM

Consider a thin wing that is approximately coincident with the plane $z = 0$ in a flow of supersonic velocity U directed along the positive x axis. The aerodynamic incidence α ($U\alpha$ being defined as the normal velocity, positive *down*, at the surface) over the wing is assumed to exhibit a harmonic time dependence of angular frequency ω and complex amplitude $\bar{\alpha}$—viz.,

$$\alpha(x, y, t) = Rl\{\bar{\alpha}(x, y)e^{i\omega t}\} \tag{2.1}$$

Given $\bar{\alpha}$, it is required to determine $\bar{\gamma}$, the complex amplitude of the pressure jump across the wing, which may be defined in dimensionless form such that

$$p(x, y, 0-, t) - p(x, y, 0+, t) = (1/2)\rho_0 U^2 Rl\{\bar{\gamma}(x, y)e^{i\omega t}\} \tag{2.2}$$

The top and bottom of the lifting surface S, formed by the projection of the wing plan form on the plane $z = 0$, are denoted here by $z = 0+$ and $z = 0-$, respectively.

The assumption of a harmonic time dependence may be regarded as sufficiently general, within the framework of linearized theory, by virtue of Fourier's theorem. The treatment of motions varying so slowly that second derivatives of the aerodynamic forces with respect to time may be neglected—e.g., the dynamic stability problem—is particularly simple in that it suffices to determine the corresponding results for harmonic motion by retaining only terms of first order in frequency. It is this approximation, herein designated as *first order*, that will be posed in Section 4 below, but the problem first will be formulated in Section 3 for arbitrary values of the frequency.

(3) FORMULATION OF BOUNDARY VALUE PROBLEM

The boundary value problem relating $\bar{\gamma}$ to $\bar{\alpha}$ will be formulated in terms of dimensionless variables based on some characteristic length l (usually chosen as the maximum wing chord but arbitrary in the present analysis) and the free-stream velocity U, so that x, y, z are dimensionless with respect to l, and the angular frequency ω is referred to the U/l through the reduced frequency parameter

$$k = \omega(l/U) \tag{3.1}$$

If, in this dimensionless system, the complex velocity potential $\bar{\phi}$ is defined such that the perturbation velocity $\boldsymbol{q}$ is given by

$$\boldsymbol{q}(x, y, z, t) = URl\{\nabla\bar{\phi}(x, y, t)\, e^{i\omega t}\} \tag{3.2}$$

it follows from the equations of motion that the complex pressure amplitude is given by

$$\bar{\gamma}(x, y) = 4[\bar{\phi}_x(x, y, 0+) + ik\,\bar{\phi}(x, y, 0+)] \tag{3.3}$$

The differential equation satisfied by $\bar{\phi}$ may be deduced from the fact that the velocity potential must satisfy the wave equation with respect to a fixed reference frame—i.e., one with respect to which the free-stream flow is at rest. The reference frame to which x is referred is moving with the wing, however, and it is expedient to introduce a modified potential Φ through the well-known transformation

$$\bar{\phi} = e^{-i\kappa x}\,\Phi \tag{3.4}$$

where κ is related to the reduced frequency k and the free-stream Mach number M according to

$$\kappa = kM^2/B^2, \qquad B^2 = M^2 - 1 \tag{3.5}$$

The differential equation satisfied by Φ then is found

Received December 14, 1954.

* Professor, Department of Engineering.

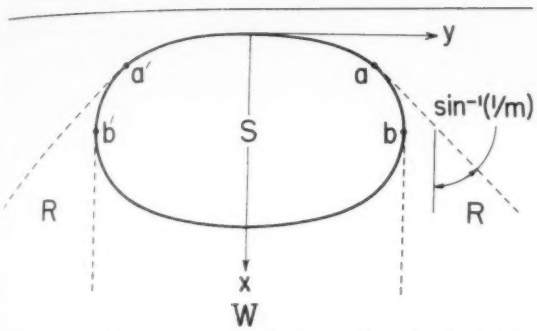

FIG. 1. A typical wing, showing the regions S, W, and R. The leading edge between a and a′ and the Mach waves tangent to the edge at a and a′ form the upstream boundary of the domain of influence of the wing.

to be[1]

$$B^2\Phi_{xx} - \Phi_{yy} - \Phi_{zz} + (kM/B)^2\Phi = 1 \qquad (3.6)$$

The motivation of the transformation Eq. (3.4) is, in the present context, the elimination of the term of order k that would appear in the equation satisfied by $\bar{\phi}$ in a coordinate system moving with the wing. The same end result also could have been achieved by introducing a Lorentz transformation in passing to this coordinate system from the fixed reference frame.[6] While the latter approach offers many aesthetic advantages,* especially in the symmetric form achieved by the simultaneous incorporation of the Prandtl-Glauert scale transformation (cf. reference 6), the transformation of Eq. (3.4) is simpler and more direct for the problem at hand.

The substitution of Eq. (3.4) in Eq. (3.3) relates $\bar{\gamma}$ to Φ according to

$$\bar{\gamma}(x, y) = 4e^{-ikx}\,[\Phi_x(x, y, 0+) - (ik/B^2)\Phi(x, y, 0+)] \qquad (3.7)$$

It is convenient, moreover, to introduce a modified incidence A according to

$$\bar{\alpha}(x, y) = e^{-ikx}\,A(x, y) \qquad (3.8)$$

The boundary conditions to be imposed on Φ follow from the considerations that: (a) the flow must be tangent to both the upper and lower wing surfaces, so that $\bar{\phi}_z = -\bar{\alpha}$ over S; (b) the pressure must be continuous across the wake W, delineated on the plane $z = 0$ by the trailing edge of the wing and the streamlines drawn downstream from the wing tips (b and b′ in Fig. 1); and (c) the potential must be continuous across the remainder of the plane $z = 0$ (R in Fig. 1). The imposition of (a) at both the upper ($z = 0+$) and lower ($z = 0-$) sides of S implies that both $\bar{\phi}$ and $\bar{\gamma}$ must be antisymmetric with respect to $z = 0$, whence (b) and (c) can be satisfied only by requiring the perturbation pressure and potential to vanish over W and R, respectively. It then follows that

$$\Phi_z = -A, \qquad (x, y) \text{ in } S \qquad (3.9a)$$

$$\Phi_x - (ik/B^2)\Phi = 0, \qquad (x, y) \text{ in } W \qquad (3.9b)$$

$$\Phi = 0, \qquad (x, y) \text{ in } R \qquad (3.9c)$$

The regions S, W, and R are depicted in Fig. 1.

To complete the mathematical formulation of the problem it is necessary to pose the *initial* conditions

$$\Phi \equiv 0, \qquad x \le x_0(y, z) \qquad (3.10a)$$

$$\Phi_x = \Phi_y = \Phi_z \equiv 0, \qquad x < x_0(y, z) \qquad (3.10b)$$

where $x = x_0(y, z)$ is the equation of the envelope of those downstream Mach waves that emanate from the leading edge of the wing. It follows as a particular consequence of Eq. (3.10a) that the boundary condition (3.9c) need be applied only on and downstream of the Mach lines that are tangent to the leading edge in the plane of the wing (at the points a and a′ in Fig. 1).

The linearized unsteady flow problem for a supersonic wing now has been described by the differential Eq. (3.6), the boundary conditions (3.9), and the initial conditions (3.10). In the following section these equations will be solved on the assumption that terms of order $(kM/B)^2$ may be neglected, so that Eq. (3.6) reduces to

$$B^2\Phi_{xx} - \Phi_{yy} - \Phi_{zz} = 0 \qquad (3.11)$$

It should be remarked that this approximation implicitly assumes the validity of a perturbation solution of Eq. (3.6) based on an expansion in even powers of (kM/B). It may be verified that such an expansion is possible in virtue of the hyperbolic character of Eq. (3.6) and the consequently finite extent of the domain of dependence of any point in the flow field. In subsonic flow ($B^2 < 1$), on the other hand, Eq. (3.6) would be elliptic (in essence, the Helmholtz equation), and it would be necessary to replace the initial conditions [Eq. (3.10)] by the Sommerfeld *radiation* and *finiteness* conditions at infinity. Unfortunately, the approximation of Eq. (3.11), which then would appear essentially as Laplace's equation, would not be uniformly valid (for fixed k) with respect to distance from the wing, and it would be impossible for any solution thereof to satisfy the radiation condition at infinity.

(4) Reduction to Study Flow Problem

Let $\Phi^{(0)}\{A\}$ denote symbolically the solution to the reduced problem obtained by setting $k = 0$ wherever it occurs *explicitly* in Eqs. (3.6) and (3.9)—viz.,

$$B^2\Phi_{xx}^{(0)} - \Phi_{yy}^{(0)} - \Phi_{zz}^{(0)} = 0 \qquad (4.1)$$

$$\Phi_z^{(0)} = -A, \qquad (x, y) \text{ in } S \qquad (4.2a)$$

$$\Phi_x^{(0)} = 0, \qquad (x, y) \text{ in } W \qquad (4.2b)$$

$$\Phi^{(0)} = 0, \qquad (x, y) \text{ in } R \qquad (4.2c)$$

$$\Phi^{(0)} \equiv 0, \qquad x \le x_0(y, z) \qquad (4.3a)$$

$$\Phi_x^{(0)} = \Phi_y^{(0)} = \Phi_z^{(0)} \equiv 0, \qquad x < x_0(y, z) \qquad (4.3b)$$

The boundary value problem presented by Eqs. (4.1)–

* In particular, the parameter (κ/M) then appears as the reduced frequency in the modified time coordinate.

(4.3) is the steady flow problem for the given plan form, but it should be specifically remarked that A depends *implicitly* on k through the transformation of Eq. (3.8).

A knowledge of $\Phi^{(0)}$ alone would suffice for a first-order (in frequency) approximation to $\bar{\phi}$ if the plan form in question had no subsonic trailing edges, for then the boundary conditions of Eqs. (3.9b) and (4.2b) could have no influence on Φ at any point on the wing. The resulting expression for Φ would contain no terms of first order in k, and it would follow that $\Phi = \Phi^{(0)} + 0(k^2M^2/B^2)$. The presence of subsonic trailing edges, on the other hand, requires that $\Phi^{(0)}$ be supplemented by a term of $0(k/B^2)$ in order to satisfy Eq. (3.9b).

Let $\Phi^{(1)}\{A\}$ denote symbolically the solution to a modified steady flow problem in which the potential is assumed to be continuous across the region W, so that

$$B^2\Phi_{xx}{}^{(1)} - \Phi_{yy}{}^{(1)} - \Phi_{zz}{}^{(1)} = 0 \tag{4.4}$$

$$\Phi_z{}^{(1)} = -A, \qquad (x, y) \text{ in } S \tag{4.5a}$$

$$\Phi^{(1)} = 0, \qquad (x, y) \text{ in } W + R \tag{4.5b}$$

$$\Phi^{(1)} \equiv 0, \qquad x \leq x_0(y, z) \tag{4.6a}$$

$$\Phi_x{}^{(1)} = \Phi_y{}^{(1)} = \Phi_z{}^{(1)} \equiv 0, \qquad x < x_0(y, x) \tag{4.6b}$$

Then it may be shown to be direct substitution that a first-order approximation to Eqs. (3.6), (3.9), and (3.10) is given by

$$\Phi = \Phi^{(0)} + (ik/B^2)\int_{x_0(y,z)}^{x} [\Phi^{(0)} - \Phi^{(1)}]\, dx + 0(k^2M^4/B^4) \tag{4.7}$$

It remains to calculate the dimensionless, complex pressure amplitude $\bar{\gamma}$. Substituting Φ from Eq. (4.7) in Eq. (3.7), neglecting terms of second order in k therein, and noting, from Eq. (3.8), that

$$\Phi^{(0)}\{A\} = \Phi^{(0)}\{e^{ikx}\bar{\alpha}\} \tag{4.8a}$$

$$= \Phi^{(0)}\{[1 + (ikM^2/B^2)x]\bar{\alpha}\} + 0(k^2M^4x^2/B^4) \tag{4.8b}$$

and similarly for $\Phi^{(1)}$, it is found that

$$\bar{\gamma}\{\bar{\alpha}\} = 4[1 - (ikM^2/B^2)x]\Phi_x{}^{(0)}\{[1 + (ikM^2/B^2)x]\bar{\alpha} - 4(ik/B^2)\Phi^{(1)}\{\bar{\alpha}\}\} + 0(k^2M^2/B^4) \tag{4.9}$$

The error term in this last result is based on the assumption $x = 0(1)$, as will be the case for points on the wing.

The solution of the steady flow problem presented by Eqs. (4.1)–(4.3) for a plan form with a subsonic trailing edge usually will lead more directly to $\Phi_x{}^{(0)}$, rather than $\Phi^{(0)}$, and it is convenient to introduce the *quasi-steady solution**

$$\bar{\gamma}^{(0)}\{\bar{\alpha}\} = 4\Phi_x{}^{(0)}\{\bar{\alpha}\} \tag{4.10}$$

where $\Phi_x{}^{(0)}\{\bar{\alpha}\}$ is determined from Eqs. (4.1)–(4.3) after replacing A by $\bar{\alpha}$. Eq. (4.9) then may be rewritten in the form

$$\bar{\gamma}\{\bar{\alpha}\} = \bar{\gamma}^{(0)}\{\bar{\alpha}\} + (ik/B^2)\,[M^2\bar{\gamma}^{(0)}\{x\bar{\alpha}\} - M^2x\bar{\gamma}^{(0)}\{\bar{\alpha}\} - 4\Phi^{(1)}\{\bar{\alpha}\}] + 0(k^2M^4/B^4) \tag{4.11}$$

It should be emphasized that $\bar{\gamma}^{(0)}\{x\bar{\alpha}\}$ denotes the quasi-steady solution for the modified incidence $x\bar{\alpha}$, whereas $x\bar{\gamma}^{(0)}\{\bar{\alpha}\}$ denotes the product of x and the quasi-steady solution for the prescribed incidence $\bar{\alpha}$. It also may be remarked that *if the plan form has no subsonic trailing edges* the auxiliary solution $\Phi^{(1)}$ may be replaced by $\Phi^{(0)}$ on the wing and is related to $\bar{\gamma}^{(0)}$ according to

$$4\Phi^{(1)}\{\bar{\alpha}\} = \int_{x_0(y,0)}^{x} \bar{\gamma}^{(0)}\{\bar{\alpha}\}dx, \qquad (x, y) \text{ in } S \tag{4.12}$$

but this result is not valid within the domain of influence of a subsonic trailing edge.

The prescribed incidence $\bar{\alpha}$ may depend on the reduced frequency k, but, in consistency with the approximations already invoked, only the leading term need be retained in those terms of Eq. (4.11) that appear within the square brackets. Consider, for example, the pitching oscillation of amplitude α_0 about $x = a$, for which

$$\bar{\alpha} = \alpha_0[1 + ik\,(x - a)] \tag{4.13}$$

Both terms in this expression would have to be retained in the first term in Eq. (4.11), but the approximation $\bar{\alpha} = \alpha_0$ would suffice for the remaining terms. In treating the plunging oscillation of amplitude h, for which

$$\bar{\alpha} = ikh \tag{4.14}$$

it generally would not be permissible, on the other hand, to neglect the terms of order k in Eq. (4.11) in consequence of the fact that $\bar{\alpha}$ is homogeneous in k. Thus, in dynamic stability analyses the equations of motion would contain no terms in phase with the displacement h, and the quantity ikh might represent the angle of incidence in body coordinates.

(5) Example: Trapezoidal Wing

Consider the trapezoidal wing shown in Fig. 2, consisting of a supersonic leading edge ($x = 0$, $|y| < b$), two subsonic trailing edges ($\pm y = b + x \cot \Lambda$, $0 < x < 1$, $\Lambda > \pi/2$), and a supersonic trailing edge ($x = 1$, $|y| < b + \cot \Lambda$). It is convenient to introduce the modified sweep parameter

$$m = B \cot \Lambda \tag{5.1}$$

which, for the plan form illustrated, is restricted according to

$$-1 < m \leq 0 \tag{5.2}$$

* The adjective *quasi-steady* is used here to designate the unsteady flow approximation calculated from the prescribed $\bar{\alpha}$ on the hypothesis that the flow at any instant may be regarded as steady. This is to be contrasted with the description *first order in frequency*, which implies that *all* terms of first order in the frequency in the equations of motion have been included, rather than only those present in α.

If m were positive (but less than one) the subsonic trailing edges would be subsonic leading edges, while if m were less than -1 they would become supersonic trailing edges. It also is assumed that

$$Bb > 1 \tag{5.3}$$

so that no point on the wing is influenced by both subsonic edges; but, by superimposing edge effects (cf. reference 4), the results may be applied to a wing satisfying the less severe restriction

$$Bb > (1/2)\,(1 - m) \tag{5.4}$$

The characteristic length implied in the foregoing definitions is the maximum chord, as shown in Fig. 2.

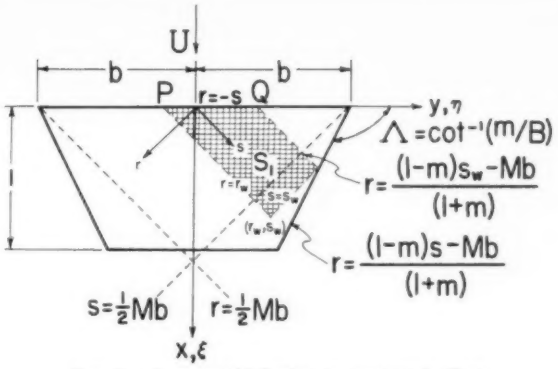

FIG. 2. A trapezoidal wing in supersonic flow.

The plan form shown in Fig. 2 is divided into three regions by the inboard Mach lines from the leading edge corners. The domains of dependence for points between and forward of these Mach lines do not contain the subsonic edges, and the quasi-steady solution is given by the well-known result[7]

$$\Phi^{(0)} = \Phi^{(1)} = \frac{1}{\pi}\int_0^x d\xi \int_{y-[(x-\xi)/B]}^{y+[(x-\xi)/B]} \frac{\bar{\alpha}(\xi, \eta)d\eta}{R}, \quad |y| < b - \frac{x}{B} \tag{5.5}$$

where R denotes the *hyperbolic distance*

$$R = +[(x - \xi)^2 - B^2(y - \eta)^2]^{1/2} \tag{5.6}$$

The quasi-steady solution at a point lying between the starboard subsonic edge and the Mach line emanating from the intersection of this edge with the supersonic leading edge may be calculated by Evvard's method[4] and is given by (cf. Eq. (80a) of reference 4, after appropriate changes of notation)

$$\bar{\gamma}^{(0)}\,|\,\bar{\alpha}_1^1 = \frac{4}{\pi}\int_{S_1}\int R^{-1}\bar{\alpha}_\xi\,(\xi, \eta)d\xi d\eta + \frac{4}{\pi}\int_P^Q \frac{\bar{\alpha}(0, \eta)d\eta}{R|_{\xi=0}} \tag{5.7}$$

The area S_1, as shown in Fig. 2, is bounded by the upstream Mach lines through the point in question, the reflection of the starboard Mach line in the subsonic edge, and the supersonic leading edge; PQ is the arc—a straight line for the wing of Fig. 2—intercepted from the supersonic leading edge by S_1. Evvard's method also yields the solution to Eqs. (4.4)–(4.6) in the form

$$\Phi^{(1)}\,|\,\bar{\alpha}_1^1 = \frac{1}{\pi}\int_{S_1}\int \frac{\bar{\alpha}(\xi, \eta)d\xi d\eta}{R} \tag{5.8}$$

The corresponding results for points adjacent to the port subsonic edge follow from symmetry considerations.

The first-order approximation now may be completed by substituting Eqs. (5.7) and (5.8) in Eq. (4.11) to obtain

$$\bar{\gamma}_1^1\,|\,\bar{\alpha}_1^1 = \frac{4}{\pi}\int_{S_1}\int R^{-1}[\bar{\alpha}_\xi + ik\bar{\alpha} - (ikM^2/B^2)\,(x - \xi)\bar{\alpha}_\xi]d\xi d\eta + \frac{4}{\pi}\,[1 - (ikM^2/B^2)x]\int_P^Q \frac{\bar{\alpha}(0, \eta)d\eta}{R|_{\xi=0}} + 0\,(k^2M^4/B^4) \tag{5.9}$$

The expression of the foregoing results in rather more explicit form is expedited by the introduction of the characteristic coordinates (in the notation of reference 4)

$$r_w = (M/2B)\,(x - By), \qquad s_w = (M/2B)\,(x + By) \tag{5.10a}$$

$$x = (B/M)\,(r_w + s_w), \qquad y = (1/M)\,(-r_w + s_w) \tag{5.10b}$$

$$r = (M/2B)\,(\xi - B\eta), \qquad s = (M/2B)\,(\xi + B\eta) \tag{5.10c}$$

$$\xi = (B/M)\,(r + s), \qquad \eta = (1/M)\,(-r + s) \tag{5.10d}$$

The equations of the various Mach waves and the starboard subsonic edge in these characteristic coordinates are given in Fig. 2, and the result [Eq. (5.9)] goes over to*

* Cf. Eq. (103) of reference 4, which is the result to which reference was made in the last sentence of Section 1 above.

$$\bar{\gamma}\{\bar{\alpha}\} = \frac{4}{M\pi}\int_{[(1-m)s_w - Mb]/(1+m)}^{r_w} (r_w - r)^{-1/2}\, dr \int_{-r}^{s_w} (s_w - s)^{-1/2}\left[\bar{\alpha}_\xi + ik\bar{\alpha} - \left(\frac{ikM}{B}\right)(r_w + s_w - r - s)\bar{\alpha}_\xi\right] ds +$$

$$\frac{4}{B\pi}\left[1 - \left(\frac{ikM}{B}\right)(r_w + s_w)\right]\int_{-r_w}^{[Mb-(1-m)s_w]/(1+m)} (r_w + s)^{-1/2}\,(s_w - s)^{-1/2}\,\bar{\alpha}\left(0, \frac{2s}{M}\right) ds \quad (5.11)$$

where the ξ and η arguments of $\bar{\alpha}$ in the first integral are expressed in terms of r and s according to Eq. (5.10d).

Other wings for which $\bar{\gamma}^{(0)}$ and $\Phi^{(1)}$ may be determined explicitly [and, therefore, to which Eq. (4.11) may be applied advantageously] include all plan forms to which Evvard's method is applicable and those plan forms for which generalized conical flow methods[8, 9] can be used to obtain solutions not only for the prescribed $\bar{\alpha}$ but also $x\,\bar{\alpha}$.

(6) Conclusion

Given $\bar{\alpha}$ (the complex amplitude of the incidence over a thin finite wing in supersonic flow), an approximation to $\bar{\gamma}$ (the resulting complex amplitude of the pressure jump) that is correct through terms of first order in the reduced frequency may be constructed by determining the quasi-steady approximation $\bar{\gamma}^{(0)}\{\bar{\alpha}\}$ due to $\bar{\alpha}$—i.e., the pressure jump calculated on the hypothesis that the instantaneous flow is steady—and by adding $[ikM^2/(M^2-1)]\,[\bar{\gamma}^{(0)}\{x\bar{\alpha}\} - x\,\bar{\gamma}^{(0)}\{\bar{\alpha}\}]$ where $\bar{\gamma}^{(0)}\{x\bar{\alpha}\}$ is the quasi-steady approximation associated with the incidence $x\bar{\alpha}$, and subtracting $[ik/(M^2-1)]\,\Phi^{(1)}$ where $\Phi^{(1)}$ is the quasi-steady potential calculated from the incidence $\bar{\alpha}$ on the hypothesis of no wake (so that $\Phi^{(1)}$ vanishes along subsonic trailing edges, as well as along leading edges).

References

[1] Miles, J. W., *On Harmonic Motion at Supersonic Speeds* Journal of the Aeronautical Sciences, Vol. 16, No. 6, p. 381, June, 1949.

[2] Moskowitz, Barry, and Moeckel, W. E., *First Order Theory for Unsteady Motion of Thin Wings at Supersonic Speeds*, NACA TN 2034, February, 1950.

[3] Sauer, R., *Elementare Theorie des langsam schwingenden Überschallflügels*, Zeitschrift für angewandte Mathematik und Physik, Vol. 1, pp. 248–253, 1950.

[4] Evvard, J. C., *Use of Source Distributions for Evaluating Theoretical Aerodynamics of Thin Finite Wings at Supersonic Speeds*, NACA Rep. 951, 1950.

[5] Harmon, S. M., *Theoretical Relations Between the Stability Derivatives of a Wing in Direct and in Reverse Supersonic Flow*, NACA TN 1943, 1949.

[6] Miles, J. W., *On the Transformation of the Linearized Equations of Supersonic Flow*, Quarterly of Applied Mathematics, Vol. 12, No. 1, pp. 1–12, April, 1954.

[7] Puckett, A. E., *Supersonic Wave Drag of Thin Airfoils*, Journal of the Aeronautical Sciences, Vol. 13, No. 9, pp. 475–484, September, 1946.

[8] Hayes, W. D., Roberts, R. C., and Haaser, N., *Generalized Linearized Conical Flow*, NACA TN 2667, 1952.

[9] Lance, G. N., *The Delta Wing in a Non-Uniform Supersonic Stream*, The Aeronautical Quarterly, Vol. V, No. 3, pp. 55–72, May, 1954.

An Approximate Method of Calculating Three-Dimensional Compressible Flow . . .

(*Continued from page 556*)

[8] Marble, F. E., and Michelson, I., *Analytical Investigation of Some Three-Dimensional Flow Problems in Turbomachines*, NACA TN 2614, 1952.

[9] Fabri, J., and Seistrunck, R., *Ecoulements Tourbillonnaires dans les Machines Axiales*, Office National d'Etudes et de Recherches Aeronautiques, Publication No. 45, 1950.

[10] Bowen, J. T., Sabersky, R. H., and Rannie, W. D., *Theoretical and Experimental Investigations of Axial Flow Compressors*, Report on research conducted under Navy Contract N6-ORI-102, Task Order IV, Mechanical Engineering Laboratory, California Institute of Technology, January, 1949.

[11] Traupel, W., *New General Theory of Multistage Axial Flow Turbomachines*, NavShips 250-445-1, Navy Dept. (Translated by C. W. Smith, General Electric Corporation).

[12] Sinnette, J. T., Costello, G. R., and Cummings, R. L., *Expressions for Measuring the Accuracy of Approximate Solutions to Compressible Flow through Cascades of Blades*, NACA TN 2501, 1951.

[13] Sinnette, J. T., Jr., *Increasing the Range of Axial Flow Compressors by Use of Adjustable Stator Blades*, Journal of the Aeronautical Sciences, Vol. 14, No. 5, pp. 269–282, May, 1947.

[14] Karlsson, T., *On the Influence of Radial Components of Blade Forces in Axial Turbomachines*, M.E. Thesis, California Institute of Technology, 1953.

[15] Wislicensus, G. F., *Fluid Mechanics of Turbomachinery*. McGraw-Hill Book Company, Inc., New York, 1947.

On Strong Transverse Waves Without Shocks in a Circular Cylinder

STEPHEN H. MASLEN* AND FRANKLIN K. MOORE*

Lewis Flight Propulsion Laboratory, NACA

SUMMARY

A study is made of large-amplitude pressure waves transverse to the axis of a circular cylinder—for instance, a rocket or jet engine. It is shown that strong permanently isentropic—i.e., shock-free—waves can occur in transverse modes if viscosity is neglected. This result is in sharp contrast to that for a plane mode where acoustic waves are known to steepen progressively into shocks. The form and frequency of these lateral waves depend on amplitude.

Two effects of viscosity on strong transverse waves are considered: dissipation in the wall boundary layer, and the steady second-order motion ("acoustic streaming") induced by that boundary layer.

The possible isentropy of strong transverse waves suggests that, if energy is suitably supplied—for example, by coupling with burning—extremely violent waves may be more likely in transverse than in longitudinal resonance. A study of boundary-layer dissipation tends to confirm this, especially for short chambers.

SYMBOLS

a_0	= velocity of sound in the absence of the wave
erfc	= complementary error function, Eq. (15)
$f(\alpha)$, $g(\alpha)$, $F_i(\alpha)$	= functions of α defined in Eq. (6) and Appendix A
$J_n(\alpha)$	= Bessel function of the first kind of order n
L	= cylinder length
n	= integer denoting the mode of oscillation [see Eq. (6)]
P	= nondimensional pressure, (P'/P_0)
R	= cylinder wall radius
t	= nondimensional time $(\omega t')$
T	= nondimensional temperature (T'/T_0)
u,v,w	= nondimensional axial, radial, and tangential velocities (cylindrical coordinates) $(u'/a_0$, etc.)
$\underline{u}$	= nondimensional velocity vector $(\underline{u}'/a_0)$
x	= nondimensional axial coordinate $(\omega x'/a_0)$
α	= nondimensional radial coordinate $(\omega r'/a_0)$
β	= nondimensional wall radius $(\omega R/a_0)$
γ	= ratio of specific heats
δ	= viscosity parameter, $2\mu_0\omega/\gamma P_0$
ϵ	= amplitude parameter, Eq. (4)
η	= radial boundary-layer coordinate, $(\beta - \alpha)/\delta$
ζ_2, $\bar{\zeta}_2$	= frequency perturbation, Eqs. (6b), (20)
θ	= angle in cylindrical coordinates
μ	= nondimensional viscosity, μ'/μ_0
μ_T	= $\left.\dfrac{d\mu(T)}{dT}\right\|_{T=1}$
ρ	= nondimensional density, ρ'/ρ_0
σ	= Prandtl Number
φ	= velocity potential such that $\nabla\varphi = \underline{u}$
ω	= frequency
ω_1	= first-order frequency

Subscripts

0	= dimensional flow properties in the absence of a wave
α, θ, t	= partial derivative with respect to α, θ, t

Superscripts

(1), (2), (3), . . .	= order of solution [Eq. (4)]

primes denote derivatives with respect to α, or dimensional quantities

Presented at the Aerodynamics Session, Twenty-Third Annual Meeting, IAS, New York, January 24–27, 1955.

* Aeronautical Research Scientist.

INTRODUCTION

PRESSURE OSCILLATIONS of large, even destructive, amplitude are common in combustion chambers of present-day rocket and jet engines. It has been proposed by several authors[1, 2, 3] that such oscillations can be generated from weak acoustic disturbances by coupling with the heat released by unsteady burning. These analyses depend critically on the assumption that the waves are small so that only the initial problem is solved. The character of the finite wave structure remains unknown. If the acoustic mode is longitudinal (particle movement parallel to the chamber axis) the strong wave resulting from amplification must be a shock, traveling back and forth in the chamber, as in a pulse jet. If, as it sometimes happens, the mode is transverse to the axis of the cylinder—e.g., Fig. 1, where the particles "slosh" between the nodes—the nature of the corresponding strong wave pattern is not so obvious. It is of especial interest to know whether the shape and frequency of strong transverse waves may, for practical purposes, be represented by linear acoustic theory. Further, by considering the viscous dissipation of various wave patterns, some idea of the relative likelihood of the occurrence of various modes may be gained.

In a plane wave, the mechanism by which a pressure pulse steepens into a shock is well known—the high-pressure portion of the pulse has an elevated speed of sound, and hence overtakes the low-pressure portion ahead of it. A pulse moving transversely in a cylinder is also subject to the steepening effect; however, steepening is complicated by the scattering effect of continuous reflection at a curved wall. For example, when plane pulse P (see Fig. 2) passes a place where the wall changes slope, a reflection provides, in addition to the continuing pulse P', a new wave pattern enclosed by the front P''. While the picture is not intended to explain entirely what happens in a cylinder, it does illustrate that resonant wave motion transverse to the cylindrical axis is not as simple as in the plane case.

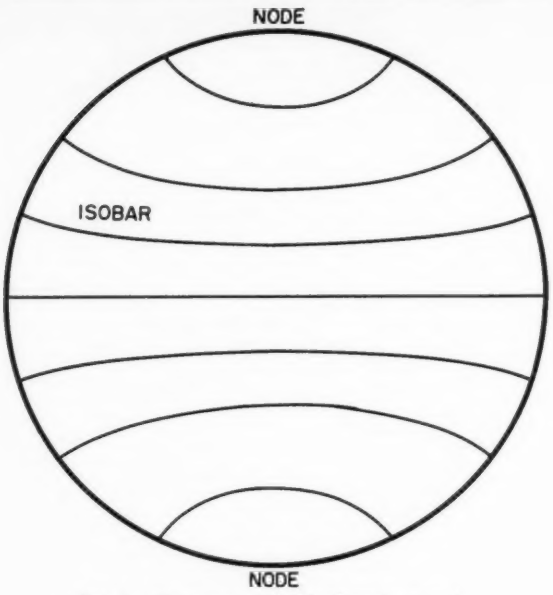

FIG. 1. Transverse "sloshing" mode, $n = 1$.

Therefore, considering fully developed acoustic oscillations in a closed cylinder, a longitudinal mode may be regarded as a train of plane pulses, each subject to steepening—unaffected, of course, by the specular reflections occurring at the ends of cylinder. Shocks may therefore be expected to appear as a result of longitudinal combustion chamber resonance. In contrast, a transverse mode cannot be regarded as a train of separate pulses, owing to the wall scattering. Thus it is not clear that shocks must appear in transverse resonance.

To explore this matter, it is appropriate to consider normal modes of transverse oscillation in a cylinder,

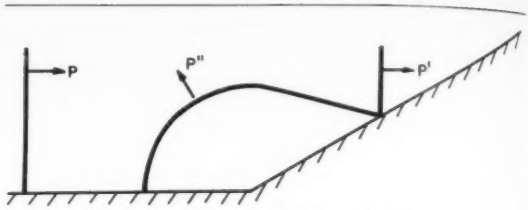

FIG. 2. Scattering of acoustic pulse.

and to investigate the consequences of finite wave strength by finding higher approximations to the wave motion, as done in plane-wave problems by numerous investigators, the first of whom was Rayleigh.[4] The circular-cylindrical chamber appropriate to jet engines is a suitable geometry for the present study. In the absence of oscillation, quiescent air is assumed inside the cylinder with no energy addition or other variations of state. This postulate is equivalent to the assumption of channel flow through the chamber with negligible Mach Number. Although a very strong oscillation probably cannot be maintained in the absence of energy addition—as by burning—to drive it, such addition is neglected herein. If the effect of burning were included at a wall or interface, as some coupling analyses[1, 3, 3] assume, the present work would be changed only in detail, but not in the approach or, perhaps, the qualitative results.

A secondary factor which is considered in the present analysis of strong waves is a wall effect called "streaming." This is a second-order phenomenon arising because of the boundary-layer flow at the chamber wall. The streaming (described by Rayleigh[5] and Schlichting[6] for plane waves) consists of a steady rotational flow which occupies the entire chamber and is explicitly independent of viscosity. In combustion chambers a somewhat different description of streaming is required.

The equations of motion of a viscous compressible fluid can be written in nondimensional form for constant Prandtl Number and specific heats as

$$\left.\begin{aligned}
&\rho_t + \nabla\cdot(\rho\underline{u}) = 0\\
&\rho\frac{D\underline{u}}{Dt} + \frac{1}{\gamma}\nabla P = \frac{\delta^2}{2}\left\{\mu[\nabla^2\underline{u} + \nabla(\nabla\cdot\underline{u})] + \nabla\left[\underline{u}\cdot\nabla\mu - \frac{2}{3}\mu\nabla\cdot\underline{u}\right] + (\nabla\mu\cdot\nabla)\underline{u} - (\underline{u}\cdot\nabla)\nabla\mu\right\}\\
&\rho\frac{DT}{Dt} - \frac{\gamma-1}{\gamma}\frac{DP}{Dt} = \frac{\delta^2}{2\sigma}\nabla\cdot(\mu\nabla T) + \frac{(\gamma-1)}{2}\mu\delta^2\left\{\begin{aligned}&\nabla^2(\underline{u}\cdot\underline{u}) - (\nabla x\underline{u})\cdot(\nabla x\underline{u})\\&-2\underline{u}\cdot(\nabla^2\underline{u}) - (2/3)(\nabla\cdot\underline{u})^2\end{aligned}\right\}\\
&P = \rho T
\end{aligned}\right\} \tag{1}$$

The solution of Eqs. (1) will be considered by first examining the potential flow oscillations in the absence of viscosity, and then finding the viscous contribution.

THE POTENTIAL FLOW

In this case $\delta = 0$ and it may be postulated that a velocity potential, φ, exists such that $\nabla\varphi = \underline{u}$. The energy and state equations yield the isentropic flow relation, $P = \rho^\gamma$. Then Eqs. (1) yield

$$\nabla^2\varphi - \varphi_{tt} = 2\nabla\varphi\cdot\nabla\varphi_t + [(\gamma-1)/2](\nabla\varphi\cdot\nabla\varphi)\nabla^2\varphi + (1/2)\nabla\varphi\cdot\nabla(\nabla\varphi\cdot\nabla\varphi) + (\gamma-1)\varphi_t\nabla^2\varphi \tag{2}$$

while the pressure is related to φ by

$$1 - P^{(\gamma-1)/\gamma} = (\gamma-1)[\varphi_t + (1/2)\nabla\varphi\cdot\nabla\varphi] \tag{3}$$

Lacking a direct solution of these equations it is assumed that P and φ can be expanded in a series in powers of some

amplitude parameter ϵ. Thus,

$$\left.\begin{aligned} \varphi &= \epsilon\varphi^{(1)} + \epsilon^2\varphi^{(2)} + \epsilon^3\varphi^{(3)} + \dots \\ P &= 1 + \epsilon P^{(1)} + \epsilon^2 P^{(2)} + \epsilon^3 P^{(3)} + \dots \end{aligned}\right\} \tag{4}$$

Then Eq. (2) yields

$$\left.\begin{aligned} \nabla^2\varphi^{(1)} - \varphi_{tt}{}^{(1)} &= 0 \\ \nabla^2\varphi^{(2)} - \varphi_{tt}{}^{(2)} &= \left[\nabla\varphi^{(1)}\cdot\nabla\varphi^{(1)} + \frac{\gamma-1}{2}\,\varphi_t{}^{(1)}\varphi_t{}^{(1)}\right]_t \\ \nabla^2\varphi^{(3)} - \varphi_{tt}{}^{(3)} &= \frac{1}{2}\nabla\varphi^{(1)}\cdot\nabla[\nabla\varphi^{(1)}\cdot\nabla\varphi^{(1)}] - \frac{\gamma-1}{2}\nabla\varphi^{(1)}\cdot\nabla\varphi^{(1)}\varphi_{tt}{}^{(1)} + (\gamma-1)^2\varphi_t{}^{(1)}\varphi_t{}^{(1)}\varphi_{tt}{}^{(1)} + \\ &\qquad [2\nabla\varphi^{(1)}\cdot\nabla\varphi^{(2)} + (\gamma-1)\varphi_t{}^{(1)}\varphi_t{}^{(2)} + (\gamma-1)\nabla\varphi^{(1)}\cdot\nabla\varphi^{(1)}\varphi_t{}^{(1)}]_t \end{aligned}\right\} \tag{5}$$

etc.

Solutions of these equations, periodic in time, are desired. If they are solved successively, the first three orders of solution for a transverse wave potential are

$$\left.\begin{aligned} \varphi^{(1)} &= \sin t\cos n\theta J_n(\alpha) && \text{(standing)}^* \\ &= \sin(t+n\theta)\,J_n(\alpha) && \text{(traveling)}^* \\ \varphi^{(2)} &= (1/4)\sin 2t\,\{[J_n{}^2(\alpha) - (\gamma+1)g(\alpha)] + [J_n{}^2(\alpha) - (\gamma+1)f(\alpha)]\cos 2n\theta\} && \text{(standing)} \\ &= (1/2)\sin 2(t+n\theta)\,[J_n{}^2(\alpha) - (\gamma+1)f(\alpha)] && \text{(traveling)} \\ \varphi^{(3)} &= (1/4)\sin 3t\,[F_1(\alpha)\cos 3n\theta + F_2(\alpha)\cos n\theta] + [(\sin t)/4]\,[F_3(\alpha)\cos 3n\theta + F_4(\alpha)\cos n\theta] && \text{(standing)} \\ &= \sin 3(t+n\theta)F_1(\alpha) + \sin(t+n\theta)F_5(\alpha) && \text{(traveling)} \end{aligned}\right\} \tag{6a}$$

where f, g, and F_i are described more fully in Appendix A.

The frequency is found to be dependent upon the amplitude and may be written

$$\omega = \omega_1(1 + \epsilon^2\zeta_2 + \dots) \tag{6b}$$

where ω_1 is such that $J_n'(\beta) = 0$, and $\omega_1 = \beta a_0/R$

and

$$\zeta_2 = \frac{\beta}{\beta^2 - n^2}\frac{1}{J_n(\beta)}\begin{cases}(1/4)F_4'(\beta) & \text{standing wave} \\ F_5'(\beta) & \text{traveling wave}\end{cases} \tag{6c}$$

Values of ζ_2 are given in Appendix B for $n = 1$ and $\gamma = 1.4$.

From these expressions and Eqs. (3) and (4), the pressure can be found and is

$$\left.\begin{aligned} P^{(1)} &= -\gamma\,P_{10}\cos t\cos n\theta && \text{(standing)} \\ &= -\gamma P_{10}\cos(t+n\theta) && \text{(traveling)} \\ P^{(2)} &= -\gamma\cos 2t\,[P_{20}\cos 2n\theta + P_{21}] - \gamma\,[P_{22}\cos 2n\theta + P_{23}] && \text{(standing)} \\ &= -2\gamma\,[P_{20}\cos 2(t+n\theta) + P_{23}] && \text{(traveling)} \\ P^{(3)} &= -\gamma\cos 3t\,[P_{30}\cos 3n\theta + P_{31}\cos n\theta] - \gamma\cos t\,[P_{32}\cos 3n\theta + P_{33}\cos n\theta] && \text{(standing)} \\ &= -4\gamma\,P_{30}\cos 3(t+n\theta) - \gamma\,P_{34}\cos(t+n\theta) && \text{(traveling)} \end{aligned}\right\} \tag{7}$$

where the P_{ij} are functions of α and are given in Appendix C. They are illustrated in Fig. 3 for $n = 1$ and $\gamma = 1.4$. Since the P_{ij} of Eq. (7) are all of unit order, the solution to third order should give a satisfactory description of oscillations that, while having a pressure amplitude moderate compared with average static pressure, have tremendous intensity on an acoustic scale.

Now, referring again to Eq. (5), it can be demonstrated—the proof follows by induction—that, to all orders of approximation, the $\varphi^{(n)}$ are harmonic in time and angle as illustrated in Eq. (6a), provided the frequency is permitted to depend on the wave amplitude [see Eq. (6b)]. This frequency dependence involves only even powers of the amplitude. Furthermore, the pressure is symmetric in both time and angle [for the first three orders, observe Eq. (7)]. On the other hand, the corresponding plane wave problem has no such periodic solution. The first-order plane traveling mode has the shape $\sin(t + x)$, which is analogous to $\varphi^{(1)}$ of Eq. (6a). However the corresponding second-order plane solution varies as $t\sin 2(t + x)$, which is not periodic. This lack of periodicity is generally understood to be associated with the steepening of the longitudinal mode into a shock pattern.

Hence, as opposed to the nonexistence of such a strong permanent isentropic longitudinal mode of oscillation, it appears that there exists a permanent strong potential form for the resonant modes of oscillation transverse to the axis of a circular cylinder. Further, the frequency is near the acoustic. Of course, these results depend on the unproved assumption of convergence of the assumed series [see Eq. (14)]. However, the first three approximations, at least, show no indication of difficulty on this score.

* Fig. 1 illustrates a first-order standing wave for $n = 1$ and also represents an instantaneous snapshot of the corresponding traveling wave, as the illustrated pattern rotates about the cylinder axis.

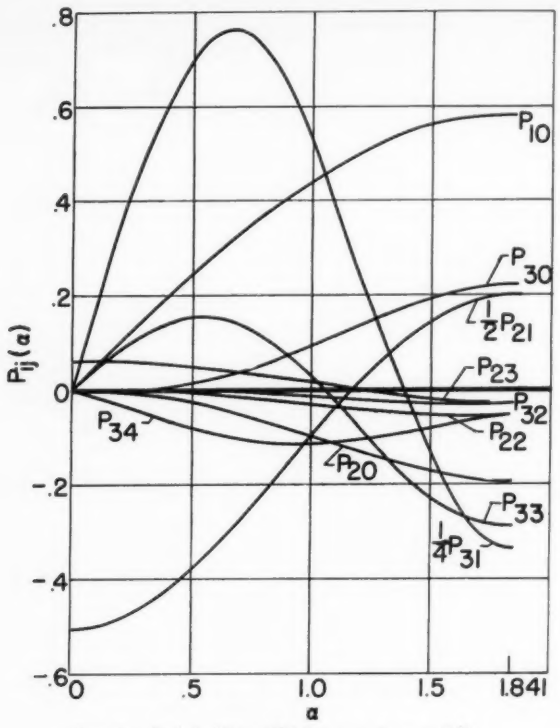

FIG. 3. $P_{ij}(\alpha)$, [Eqs. (7)] for $n = 1$, $\gamma = 7/5$.

EFFECTS OF VISCOSITY

So far as the internal aerodynamics of a jet engine are concerned, the possible permanence of strong isentropic transverse waves is likely to be important in the following sense: if the combustion process is able to provide energy to drive an oscillation in any mode, then large amplitudes will tend to be associated with modes having small inherent damping. Thus perhaps, transverse oscillations may commonly be more severe than longitudinal, the latter being subject to shock losses.

Full consideration of the damping of possible strong wave systems is beyond the scope of this paper. However, certain interesting results may be found by assuming that all viscous stresses are confined to a thin boundary layer near the cylinder wall, and studying the effect of this boundary layer on the wave motion. It is assumed that the through flow Mach Number is small, so that the main stream boundary layer and that of the wave motion can be considered independent.

Boundary-Layer Solutions

To find the solutions for a strong wave in the presence of a thin boundary layer, the equations of motion [see Eq. (1)] can be expanded in powers of the amplitude. Thus, if

$$\left.\begin{aligned} T &= 1 + \epsilon T^{(1)} + \epsilon^2 T^{(2)} + \dots \\ \underline{u} &= \epsilon \underline{u}^{(1)} + \epsilon^2 \underline{u}^{(2)} + \dots, \text{ etc.} \end{aligned}\right\} \tag{8}$$

sets of linear inhomogeneous differential equations defining the successive approximations are readily found. The equations can be simplified by making the usual boundary-layer approximations. The boundary conditions are that the velocity and the temperature fluctuation vanish at the wall. To illustrate the kind of solutions that arise, the first-order expressions for a traveling transverse wave may be given. These consist of the potential solution already found plus viscous boundary-layer terms. These solutions, valid throughout the chamber, are, for constant wall temperature,

$$\begin{aligned}
P^{(1)} &= -\gamma \cos(t + n\theta)\, J_n(\alpha) \\
\rho^{(1)} &= -\cos(t + n\theta)\, J_n(\alpha) - (\gamma - 1)\, J_n(\beta) e^{-\eta\sqrt{\sigma}} \cos(t + n\theta - \eta\sqrt{\sigma}) \\
T^{(1)} &= -(\gamma - 1)\cos(t + n\theta)\, J_n(\alpha) + (\gamma - 1)\, J_n(\beta) e^{-\eta\sqrt{\sigma}} \cos(t + n\theta - \eta\sqrt{\sigma}) \\
w^{(1)} &= n\cos(t + n\theta)\frac{J_n(\alpha)}{\alpha} - \frac{nJ_n(\beta)}{\beta} e^{-\eta}\cos(t + n\theta - \eta) \\
v^{(1)} &= \sin(t + n\theta)\, J_n'(\alpha) - \frac{\delta J_n(\beta)}{2} \left\{ \begin{aligned} &\frac{(\gamma - 1)}{\sqrt{\sigma}}\left[e^{-\eta\sqrt{\sigma}} \cos\left(t + n\theta - \eta\sqrt{\sigma} + \frac{\pi}{4}\right) - \cos\left(t + n\theta + \frac{\pi}{4}\right)\right] \\ &+ \frac{n^2}{\beta^2}\left[e^{-\eta}\cos\left(t + n\theta - \eta + \frac{\pi}{4}\right) - \cos\left(t + n\theta + \frac{\pi}{4}\right)\right] \end{aligned} \right\}
\end{aligned} \tag{9}$$

where $\eta = (\beta - \alpha)/\delta$

For a longitudinal wave, the same expressions hold, provided one sets $J_n(\alpha) = J_n(\beta) = (n/\alpha) = (n/\beta) = 1$, $J_n'(\alpha) = 0$, $n\theta = x$, and $w^{(1)} = u^{(1)}$.

In the calculation of the relative losses in longitudinal and transverse modes, some second- and third-order longitudinal properties are needed. Having the first-order solution in this mode [see Eq. (9)], the second-order axial velocity is readily found. The result, valid throughout the chamber, is

$$\begin{aligned}
u^{(2)} = {} & \frac{\gamma + 1}{4}\, t \left\{ \sin 2(t + x) - e^{-\eta\sqrt{2}} \sin(2t + \right. \\
& \left. 2x - \eta\sqrt{2}) \right\} + \frac{1}{2}\left\{ \frac{1}{2} + \frac{\gamma - 1}{1 + \sigma}(1/\sigma - \sigma\mu_T) \right\} \times \\
& \left\{ e^{-\eta} - \frac{2}{\sqrt{\pi}} \int_{\eta/\sqrt{2t}}^{\infty} e^{-\xi^2} d\xi \right\} \\
& + \text{terms harmonic in } (t + x) \text{ and vanishing at } \eta = 0, \infty \\
& + \text{terms independent of } t \text{ and } x \text{ and vanishing at } \\
& \eta = 0, \infty
\end{aligned} \tag{10}$$

The integral term is a solution of the homogeneous boundary-layer equations found by the Laplace transform method on the assumption that, at a certain time $t = 0$, the viscosity is, so to speak, suddenly turned on. This term will be discussed further in a later section.

Finally, a partial third-order solution is

$$u^{(3)} = -\frac{(\gamma+1)^2 t^2}{32} \times \left\{ \begin{array}{l} 3\cos 3(t+x) - 3e^{-\eta\sqrt{3}}\cos(3t+3x-\eta\sqrt{3}) \\ +\cos(t+x) - e^{-\eta}\cos(t+x-\eta) \\ +\text{terms of lower order in } t \end{array} \right\} \quad (11)$$

These expressions enable one to find the leading terms in the dissipation. The analogous expressions for a transverse wave can also be found. They differ, for the present purpose, from those for a longitudinal wave in that they do not vary as strongly with time.

Viscous Dissipation

The rate at which mechanical energy is dissipated in a fluid element is $\mu_0\omega^2\,[\mu(w_\alpha^2 + u_\alpha^2)]$. Averaged over a full cycle, the rate of energy dissipation, D, in the chamber is

$$D = \frac{V}{(2\pi)^2}\rho_0 a_0^2 \frac{\delta\omega}{\beta}\int_{2\pi N}^{2\pi(N+1)} dt \int_0^{2\pi} d\theta \times \int_0^1 d\left(\frac{x}{(\omega L/a_0)}\right)\int_0^\infty \mu(w_\eta^2 + u_\eta^2)\,d\eta \quad (12)$$

where V is the chamber volume, and where the integration is over only the boundary layer; the remaining dissipation being negligible, as it is proportional to δ^2—i.e., μ_0.

The energy dissipated is conveniently expressed as a function of the energy of the potential wave, which is constant and, to first order, twice the average of the initial kinetic energy of the wave. Thus, the energy is

$$E = \frac{2V}{(2\pi)^2}\rho_0 a_0^2 \int_0^{2\pi} dt \int_0^1 d\left(\frac{x}{(\omega L/a_0)}\right) \times \int_0^{2\pi} d\theta \int_0^1 \rho\frac{\alpha}{\beta}\,[w^2 + u^2 + v^2]\,d\left(\frac{\alpha}{\beta}\right) \quad (13)$$

If Eqs. (9), (10), and (11) are put into Eqs. (12) and (13), it follows that the fraction of original wave energy dissipated per unit time in a longitudinal mode is

$$\frac{D}{E} = \frac{\delta a_0}{R}\left\{1 + \epsilon^2\left[\frac{(\gamma+1)^2}{16}(\sqrt{2}-1)t^2 + 0(t)\right] + \ldots\right\} \quad (14a)$$

In a similar manner, the analogous result for a transverse wave, either standing or traveling, is found to be

$$D/E = (\delta a_0/R)\left\{[n^2/(\beta^2 - n^2)] + 0(\epsilon^2)\right\} \quad (14b)$$

where the ϵ^2 term does not grow with time as it does in Eq. (14a).

For the higher transverse modes, the greater is n, the greater the dissipation, as indicated in Fig. 4. For a purely radial mode ($n = 0$), the dissipation is zero to this order (in δ) as there is no wave boundary layer.

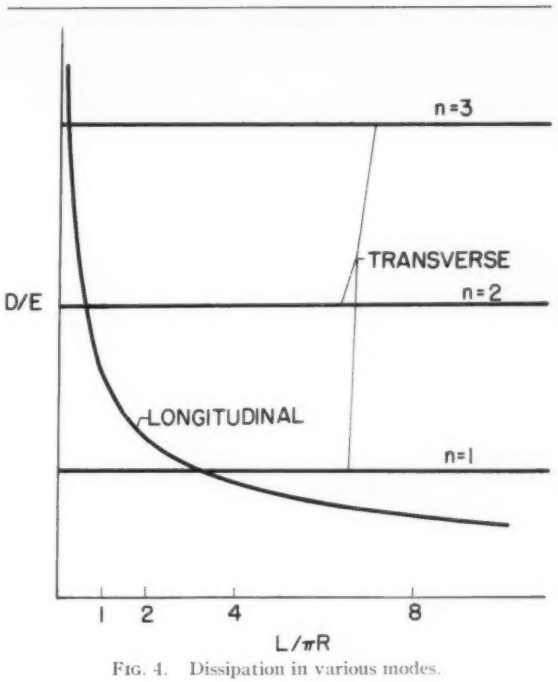

FIG. 4. Dissipation in various modes.

However, based on the analysis of reference 3, it is not expected that this mode would be driven to large amplitude in most current engines, because of the configuration of the burning. Amplification of a radial mode requires the burning to be concentrated at the cylinder axis.

On the assumption that the length of cylinder L is equal to the half wave length of the longitudinal wave, the leading term of Eq. (14) is shown in Fig. 4 as a function of L for fixed R. It appears that viscous dissipation favors predominance of longitudinal resonance over the transverse kind for large L/R while the converse is true for small L/R. If the wave amplitude is large, Fig. 4 must be modified to favor the appearance of transverse resonance, because the longitudinal dissipation increases faster (as $\epsilon^2 t^2$) with time than does the transverse [see Eq. (14)].

Thus one may conclude that if, in a cylindrical chamber, there is a mechanism for providing energy at a certain rate to drive an acoustic oscillation, the transverse mode can be driven to a larger amplitude than can a longitudinal mode. The degree to which this is the case in practice depends in part on other considerations such as hardware, burner configuration, and the like. Of course, this result might have been anticipated if the large losses due to shocks in the plane case, as opposed to the transverse one, had been considered directly.

Streaming

In addition to viscous dissipation of energy, the boundary layer of a strong wave causes a second-order change in the mean fluid motion. This is illustrated for a plane mode in Eq. (10). The first term, $[(\gamma+1) \div 4]t \sin 2(t+x)$, is the potential term and the remainder

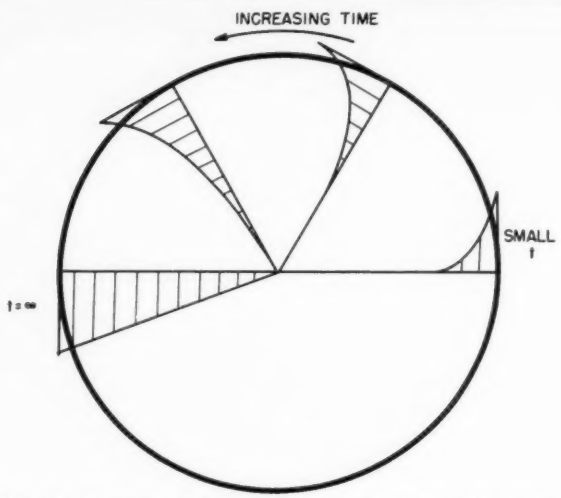

FIG. 5. Development of streaming velocity profile in traveling mode.

are viscous. Of the viscous terms, all except the integral term correspond to a very thin periodic boundary layer which has no unusual properties. In particular, its thickness does not increase with time. The remaining term is

$$\frac{2}{\sqrt{\pi}}\int_{\eta/\sqrt{2t}}^{\infty} e^{-\zeta^2}\, d\zeta \equiv \operatorname{erfc}(\eta/\sqrt{2t}) \qquad (15)$$

This has a quite different character. It vanishes as $n \to \infty$, and goes to unity at the wall, $\eta = 0$, as required by the wall boundary conditions. It has a rather arbitrary character in that it implies that, at $t = 0$, viscosity suddenly appears. The term is not periodic but rather, as time progresses, its effect penetrates farther and farther from the wall. This growth represents the diffusion of vorticity into the chamber and is analogous in this respect to the spacewise growth of a steady boundary layer.

For oscillations in a chamber such as is encountered in rockets and jet engines where there is a net through flow, one might expect that the time involved in Eq. (15) would be that required for a particle to be swept through the zone containing the oscillation. This time is of the order of the chamber length divided by the mean through velocity. Thus, the boundary layer represented by this term is, crudely, of the same thickness as that associated with the through flow (for a rocket) and grows at the same rate. The remainder of the wave boundary layer [see Eqs. (9) and (10)] is much thinner and is periodic. On the other hand, if there is no through flow, the time involved can be considered essentially infinite and the boundary layer represented by the integral term fills the chamber. Thus, if t is large enough, $\eta/\sqrt{2t} \to 0$ for all finite η and Eq. (10) becomes, for large η,

$$u^{(2)} = \frac{\gamma + 1}{4}\, t \sin 2(t + x) - \frac{1}{2}\left[\frac{1}{2} + \frac{\gamma - 1}{1 + \sigma} \times \left(\frac{1}{\sigma} - \sigma\mu_T\right)\right] \qquad (16)$$

This expression violates the assumed boundary condition that the velocity approach the potential value (the first term of this equation). Therefore, in this case, for the wave motion to be permanent, the solution, valid as $t \to \infty$, must include a steady (second order in ϵ) outer flow, not necessarily irrotational, which goes, at the wall, to the same value as does $u^{(2)}$ in Eq. (10). This added external flow replaces the error function term in Eq. (10), and is the limiting flow toward which that term was developing. This development is somewhat analogous to the growth of the steady boundary layer at the entrance to a pipe into a fully developed Poiseuille flow.

In the present instance, that of a longitudinal traveling wave, the additional flow is clearly a solution of the homogeneous counterpart of the second-order equations for steady flow. It reduces to simply $\nabla^2 u^{(2)} = 0$. The required solution is then a uniform "streaming" flow replacing the integral term in Eq. (10) and leading to the conclusion that Eq. (16) is correct outside the boundary layer. The motion is in the same direction as the wave.

The final time independence of this flow is perhaps rather surprising in view of its generation by an oscillatory flow. Another unusual result is that, although this motion is found by consideration of the wave boundary layer, the final shape and amplitude are explicitly independent of viscosity.

This fully developed flow is a classical phenomenon known as "acoustic streaming." It can, in general, be determined without examining the initial motion. This approach has been followed by a number of authors[5-9] who were primarily concerned with the streaming induced by plane waves. The first such analysis was given by Rayleigh toward the end of the last century.[5]

In the case of a transverse wave the streaming motion is somewhat more complex, although near the wall the solution is similar to the one just given. This transverse wave solution will be described and the third-order solution will also be determined.

The motion is readily found without computing the entire boundary-layer flow. Streaming only arises as a nonharmonic part of the second-order flow. Thus, the first-order solution [Eq. (9)] can be put into the second-order equations and the harmonic terms deleted. Particular integrals of the resulting expressions are readily found and are of boundary-layer type—i.e., decaying exponentially with $\eta = (\beta - \alpha)/\delta$. Complementary solutions are then required to cancel these and any potential flow terms at the wall.

For small time, the solutions are error functions. In the limit as $t \to \infty$, the complementary solutions can be found by defining a stream function $\psi^{(2)}$ such that $\psi_\alpha{}^{(2)} = -w^{(2)}$ and $\psi_\theta{}^{(2)} = \alpha v^{(2)}$. The function $\psi^{(2)}$ is biharmonic and $T^{(2)}$ is harmonic. The resulting solutions follow easily and are

$$\left.\begin{aligned} v^{(2)} &= P^{(2)} = 0 && \to 0 \\ w^{(2)} &= C_9 \operatorname{erfc}(\eta/\sqrt{2t}) && \to (\alpha/\beta)C_9 \\ T^{(2)} &= -\rho^{(2)} = C_{10} \operatorname{erfc}(\eta\sqrt{\sigma/2t}) && \to C_{10} \end{aligned}\right\} \quad (17)$$

where the first expressions apply for small t and the last as $t \to \infty$. C_9 and C_{10} are given in Appendix B. These expressions, together with the potential result [Eq. (16)], form the complete solution to second order for a traveling transverse wave; the purely harmonic boundary-layer terms being omitted.

To this order, the solution is permanent, or, more correctly, approaches a permanent form. The primary effect of streaming is to generate a steady wheel flow (see Fig. 5) whose direction of rotation depends on the sign of C_9. For low-order modes C_9 is positive, indicating that the steady flow is in a direction opposite to that of the wave. For high-order modes $n/\beta \to 1$ and C_9 is negative, so that the steady flow is in the same direction as the wave motion. If one takes the limit as $n, \beta \to \infty$, then $n/\beta = 1$ and the solution reduces to that for the plane wave case [the steady part of Eq. (16)].

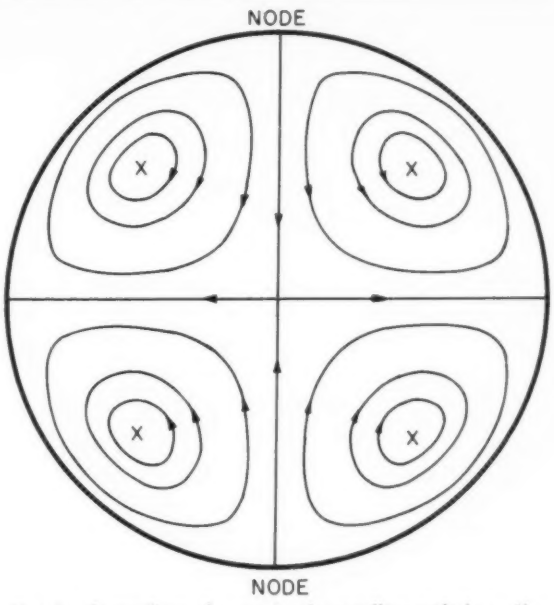

FIG. 6. Streamlines of streaming in standing mode ($n = 1$).

The streaming corrections to the potential solution for a standing transverse wave can be shown, in a similar manner, to be

$$\left.\begin{aligned} v^{(2)} &= 0 && \to nC_6 \cos 2n\theta \left(\frac{\alpha}{\beta}\right)^{2n-1}\left[\left(\frac{\alpha}{\beta}\right)^2 - 1\right] \\ w^{(2)} &= -C_6 \sin 2n\theta \operatorname{erfc}\left(\frac{\eta}{\sqrt{2t}}\right) && \to nC_6 \sin 2n\theta \left(\frac{\alpha}{\beta}\right)^{2n-1}\left[1 - \frac{n+1}{n}\left(\frac{\alpha}{\beta}\right)^2\right] \\ T^{(2)} &= -\rho^{(2)} = -(C_7 + C_8 \cos 2n\theta) \operatorname{erfc}\left(\eta\sqrt{\frac{\sigma}{2t}}\right) && \to -C_7 - C_8\left(\frac{\alpha}{\beta}\right)^{2n} \cos 2n\theta \\ P^{(2)} &= 0 && \to 0 \end{aligned}\right\} \quad (18)$$

where, again, the error functions terms apply for small time and the other expressions as $t \to \infty$. C_6, C_7, and C_8 are given in Appendix B.

For small time, there tends to be a drift of the flow immediately adjacent to the wall toward the nodes. In the limit of large time, the main effect of streaming is to introduce a set of $4n$ vortices symmetrically placed with respect to the nodal lines of the first-order wave and whose sense of rotation is inward toward the cylinder axis along the nodal lines (Fig. 6). This result is very similar to that described by Rayleigh[5] and Schlichting[6] for plane flow. In passing, it might be noted that the present analysis is valid for high Reynolds Numbers. In the low Reynolds Number regime,[10] a qualitatively similar result, but with the rotation in the opposite sense, is to be expected.

Next the third-order solution can be found. Unless the boundary-layer solutions are desired, only the first-order potential flow [Eq. (9)] and the second-order streaming [Eqs. (17) and (18)] need be considered. In this case the third-order equations are readily integrated in closed form. For large t and a traveling wave the resulting pressure is [in addition to the potential contribution of Eq. (7)]

$$P^{(3)} = -\gamma[(n/\beta)C_9 + (1/2)C_{10}] \cos(t + n\theta)\alpha J_n'(\alpha) \quad (19)$$

To satisfy the boundary condition (only that of vanishing normal velocity at the wall, as the boundary-layer solution is not considered), a second frequency perturbation, $\tilde{\zeta}_2$, is required. Thus, the frequency can be written now as

$$\omega = \omega_1 [1 + \epsilon^2(\zeta_2 + \tilde{\zeta}_2) + \dots] \quad (20)$$

where ω_1 and ζ_2 take their potential flow values [Eq. (6b)], and $\tilde{\zeta}_2$ is given in Appendix B.

For a standing wave, there is found

$$P^{(3)} = -\frac{\gamma}{2}C_7 \cos t \cos n\theta\, \alpha J_n'(\alpha) - \frac{\gamma C_8}{4(2n+1)} \cos t \left(\frac{\alpha}{\beta}\right)^{2n} \{\cos n\theta\, [\alpha J_n'(\alpha) +$$

$$(n+1)J_n(\alpha)] + \cos 3n\theta\, [\alpha J_n'(\alpha) + (3n+1)J_n(\alpha)]\} - n\gamma C_6 \left(\frac{\alpha}{\beta}\right)^{2n} \sin t \times$$

$$\left\{\cos n\theta \left[\frac{1}{2}\left(\frac{\alpha}{\beta} - \frac{\beta}{\alpha}\right)J_n'(\alpha) + \left\{-\frac{\alpha^2}{4(n+1)\beta} + \frac{\beta}{4n} - \frac{n^2-n-1}{2n\beta} - \frac{n\beta}{2\alpha^2}\right\}J_n(\alpha)\right]\right.$$

$$\left.+ \cos 3n\theta \left[\frac{1}{2}\left(\frac{n-1}{n+1}\frac{\alpha}{\beta} - \frac{\beta}{\alpha}\right) J_n'(\alpha) + \left\{\frac{-\alpha^2}{4(n+1)\beta} + \frac{\beta}{4n} - \frac{n^3+6n^2+4n+1}{2n(n+1)\beta} + \frac{n\beta}{2\alpha^2}\right\}J_n(\alpha)\right]\right\} +$$

$$\frac{\gamma C_8}{4(2n+1)} \cos t \cos 3n\theta \left[-\beta + \frac{n(7n+2)}{\beta}\right] J_n(\beta)\, \frac{J_{3n}(\alpha)}{J_{3n}'(\beta)} + n\gamma C_6 \sin t \cos 3n\theta \times$$

$$\left[\frac{1}{n+1}\left(1 - \frac{7n^3+5n+1}{\beta}\right)\right] J_n(\beta)\, \frac{J_{3n}(\alpha)}{J_{3n}'(\beta)} + \frac{n\gamma C_6}{\beta(\beta^2-n^2)}\, [t \cos t\, J_n(\alpha) + \alpha J_n'(\alpha) \sin t] \cos n\theta \quad (21)$$

with a similar frequency fluctuation, ξ_2, given in Appendix B. The term linear in t (in the last bracket) represents an attenuation of the fundamental of the oscillation [Eq. (7) or (9)] for it has the same shape but the opposite sign.

If consideration is limited to the case of $t \to \infty$, it can be shown, in general (the proof follows readily by induction), that the traveling transverse wave is permanent to all orders of solution even when a boundary layer and streaming are assumed to be present. No such statement can be made for a standing mode. Indeed, Eq. (21) shows that this is not true and that the wave attenuates. On this basis, a traveling transverse wave can perhaps be driven to larger amplitude than can a standing one.

The streaming contributions probably do not affect the flow pattern importantly except in the case of very strong waves, for, as can be seen from the small values of C_6 to C_{10} (Appendix B), the magnitude of the streaming is negligible unless ϵ is large. It is possible that, in a rocket having a very low mean through velocity and large length to diameter ratio, the streaming boundary layer could significantly influence the flow if there was an extremely strong transverse oscillation present.

Concluding Remarks

The general results obtained are really three in number—the primary one dealing with potential flow, and the others with viscous dissipation and with acoustic streaming. It has been shown that a permanent potential wave motion of finite amplitude is quite possible in cylindrical mode for an internal flow, as contrasted with the nonexistence of such a motion in a plane mode. Thus, the cylindrical mode cannot be regarded as a train of distinct pulses, but is rather an interference pattern in which the scattering effect of the wall overcomes any tendency for components to steepen into shocks such as occur in a plane mode of oscillation. Extrapolating from these results, it seems likely that such a strong permanent wave can be found for almost any nonplanar mode of oscillation in a chamber. In practice, the degree to which this statement would hold would be dependent on the degree to which the walls are nonplanar. Considering the problem in terms of a series expansion such as is used in the present study, the criterion seems merely to be that the frequencies of the normal modes of oscillation in the system cannot be integral multiples of each other. This is certainly a necessary condition.

The amplitude variation of the finite potential wave is, for a cylindrical mode, symmetric in both time and angle. The frequency is a function of wave amplitude, although, for waves of moderate strength, this frequency is near that of the corresponding acoustic mode. For example, if the maximum peak-to-peak pressure amplitude in the first (lowest frequency) transverse mode is one-third the chamber pressure—i.e., about 176 decibels—the frequency of the strong wave is reduced from that of the associated sonic mode by less than 2 per cent.

The detailed form of the first three approximations to a purely cylindrical mode is given in Eqs. (6) and (7) and a number of pressure profiles for the first standing transverse mode are sketched in Fig. 7. Fig. 7(a) shows the pressure profiles around the wall for several values of time. The profiles differ from sine waves primarily in showing a typical second harmonic distortion. On the other hand, the time histories at several points on the wall [see Fig. 7(b)] appear to be approaching a square pattern. It should be remembered that the small irregularities in the profiles are probably due to the order of the solution rather than being indicative of the final wave shape. If the wall pressure in the first traveling transverse mode were plotted against $(\omega t + \theta)$, the resulting plot would be quite similar to that in Fig. 7(a) for $t = 0$.

An estimate of the viscous dissipation in longitudinal and transverse modes indicates that, for large (small) length to diameter ratios longitudinal (transverse) waves are damped the least, but that the dissipation of longitudinal waves increases faster with time than does that of a transverse mode [Eq. (14)]. Hence it appears that transverse waves can be driven to higher amplitude than can longitudinal ones. This result could have been expected on the basis of the presence of shocks and their accompanying losses in the latter case and their absence in a transverse mode. Of course, in a real situation, these conclusions could be modified by the particular geometry, hardware, inlet and exit conditions, and driving force.

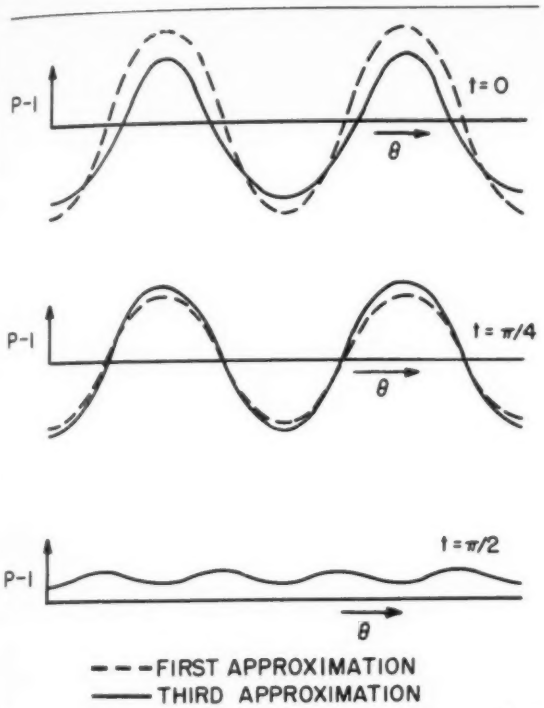

FIG. 7(a). Angular variation of wall pressure profiles, standing mode ($n = 1$).

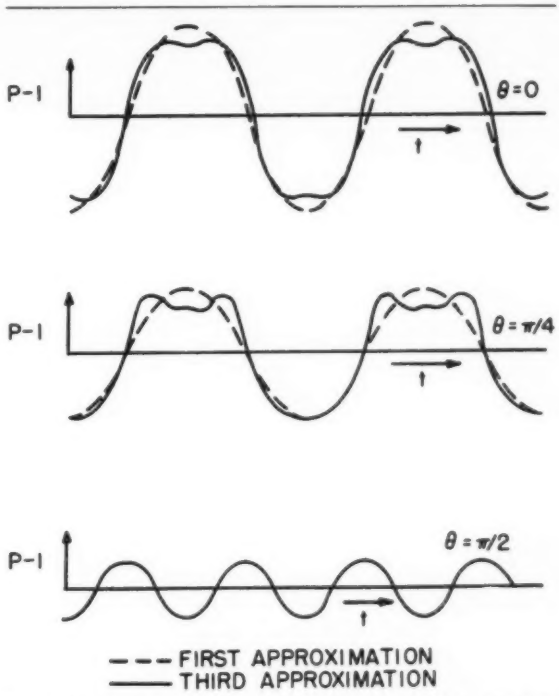

FIG. 7(b). Time variation of wall pressure profiles, standing mode ($n = 1$).

As a corollary of the boundary-layer calculations for determining the dissipation, there are found the acoustic streaming terms. For moderate or small times—such as the time for a particle to traverse a rocket combustion chamber—the streaming appears as a boundary-layer term [that is, proportional to $\operatorname{erfc}(\eta \div \sqrt{2t})$], growing with time, and much thicker than the periodic portion of the layer. If sufficient time elapses, as would happen if there were no through flow, this growing boundary layer will fill the chamber in much the same manner that the steady boundary-layer flow near the entrance of a pipe develops into the Poiseuille flow. In the present problem, that of transverse waves, several interesting features arise in the end state of fully developed streaming. For a traveling—i.e., spinning—wave, the second-order streaming exhibits a steady temperature perturbation and a steady wheel flow [Eq. (17)], but no pressure perturbation. The flow direction for practical modes is opposite to that of wave propagation, differing in this respect from the corresponding result for plane flow [Eq. (16)]. For the standing wave, there is a steady temperature perturbation as well as a steady vortex motion [Eq. (18)]. The cellular flow associated with the standing wave is similar to that found in the analogous flat plate problem.[5, 6] The existence of such a structure has been verified experimentally.[6, 11]

In the third-order streaming solution, the traveling wave is still periodic [Eq. (19)]. Indeed, it can be shown that, to all orders, the fully developed streaming flow in a traveling transverse mode is permanent. On the other hand, the standing mode is not permanent [Eq. (21)]. The third-order solution indicates an attenuation of the fundamental, the decrement being proportional to the square of the wave amplitude. On the basis of this attenuation, it may be expected that a traveling wave is more likely to occur than a standing one or, at least, can be driven to larger amplitude.

In summary then, on the basis of the present admittedly idealized analysis the following picture might be expected when strong oscillations occur in a cylindrical chamber, such as is used in many modern engines.

Assuming that the bare appearance of all modes of oscillation is equally probable, it would be expected that a longitudinal mode could be dominant only for moderate wave amplitudes, with this dominance more likely in a long chamber. If there is sufficient energy available, as from burning, to drive an oscillation to very large amplitude, then it is to be expected that the dominant mode will be a transverse one. This lateral mode will probably be the fundamental (lowest frequency) mode. Its profile will be symmetric in angle and time and should involve no shocks. The frequency of the mode will be near to that of the corresponding acoustic wave. Unless the geometry dictates otherwise, the mode will probably be a traveling, or "spinning," one rather than a standing, or "sloshing" one. The spinning mode will be accompanied by a quasi-steady flow in a direction opposite to that of wave propagation, which tends to develop into a steady wheel flow propagation. If the mode is standing the tendency will be toward a set of steady vortices (four for the first mode) symmetrically placed with respect to the nodal lines. The degree of development of these steady

patterns will depend on the magnitude of the through velocity and the length of the chamber.

Finally, then, strong resonant potential oscillations in a mode transverse to the axis of a circular cylinder are possible. To a good degree of approximation, their shape, and particularly their frequency, can be described by linear acoustic theory.

Appendix A

Functions Appearing in Eqs. (6)

The functions $f(\alpha)$, $g(\alpha)$, and $F_i(\alpha)$ are solutions of inhomogeneous Bessel equations. They satisfy

$$f'' + (f'/\alpha) + 4[1 - (n^2/\alpha^2)]f = J_n^2(\alpha)$$

$$g'' + (g'/\alpha) + 4g = J_n^2(\alpha)$$

where

$$f(0) = f'(\beta) = g(0) = g'(\beta) = 0$$

and

$$L_i\left\{F_i - \frac{\gamma+1}{4} J_n(m_{i1}f + m_{i2}g)\right\} = \frac{(\gamma+1)}{2}\left\{m_{i3}J_n f + m_{i4}J_n g + m_{i5}\frac{J_n^3}{2}\right\} + \frac{(\gamma+1)}{4}\left\{m_{i6}\frac{J_n J_n'^2}{2} + h_{i1}J_n^3\right\} + \frac{1}{4}\left\{m_{i7}\frac{J_n'^3}{\alpha} + h_{i2}J_n J_n'^2 + m_{i8}\frac{n^2 J_n^2 J_n'}{\alpha^3} + h_{i3}J_n^3\right\}$$

where

$$F_1'(\beta) = F_2'(\beta) = F_3'(\beta) = F_4'(0) = F_5'(0) = 0$$

and the solutions are nonsingular.

The L_i, m_{ij} and h_{ij} are defined by the matrices,

$$L_i = \begin{bmatrix} \frac{d^2}{d\alpha^2} + \frac{1}{\alpha}\frac{d}{d\alpha} + 9 - \frac{9n^2}{\alpha^2} \\ \frac{d^2}{d\alpha^2} + \frac{1}{\alpha}\frac{d}{d\alpha} + 9 - \frac{n^2}{\alpha^2} \\ \frac{d^2}{d\alpha^2} + \frac{1}{\alpha}\frac{d}{d\alpha} + 1 - \frac{9n^2}{\alpha} \\ \frac{d^2}{d\alpha^2} + \frac{1}{\alpha}\frac{d}{d\alpha} + 1 - \frac{n^2}{\alpha^2} \\ \frac{d^2}{d\alpha^2} + \frac{1}{\alpha}\frac{d}{d\alpha} + 1 - \frac{n^2}{\alpha^2} \end{bmatrix}$$

$$h_{ij}(\alpha) = \begin{bmatrix} \left(1 - \frac{5n^2}{2\alpha^2}\right)\left(8 + \frac{n^2}{\alpha^2}\right)\left(8 - \frac{7n^2}{\alpha^2} - \frac{n^4}{\alpha^4}\right) \\ \left(3 + \frac{5n^2}{2\alpha^2}\right)\left(24 - \frac{5n^2}{\alpha^2}\right)\left(24 + \frac{7n^2}{\alpha^2} + \frac{n^4}{\alpha^4}\right) \\ \left(1 - \frac{n^2}{2\alpha^2}\right)\left(-8 - \frac{3n^2}{\alpha^2}\right)\left(\frac{5n^2}{\alpha^2} + \frac{3n^4}{\alpha^4}\right) \\ \left(3 + \frac{n^2}{2\alpha^2}\right)\left(-24 + \frac{15n^2}{\alpha^2}\right)\left(-\frac{5n^2}{\alpha^2} - \frac{3n^4}{\alpha^4}\right) \\ \left(1 - \frac{5n^2}{2\alpha^2}\right)\left(-8 + \frac{5n^2}{\alpha^2}\right)\left(\frac{n^2}{\alpha^2} - \frac{n^4}{\alpha^4}\right) \end{bmatrix}$$

$$m_{ij} = \begin{bmatrix} -3 & 0 & 3 & 0 & -1 & 5 & 1 & -1 \\ -3 & -6 & 3 & 6 & -3 & 15 & 3 & 1 \\ 1 & 0 & 1 & 0 & -1 & 1 & -3 & 3 \\ 1 & 2 & 1 & 2 & -3 & 3 & -9 & -3 \\ 1 & 0 & 1 & 0 & -1 & 1 & -3 & -1 \end{bmatrix}$$

Appendix B

Constants Appearing in Eqs. (6b) and (17) to (21)

Standing wave

$$C_6 = \frac{nJ_n^2(\beta)}{2\beta}\left[\frac{3n^2}{4\beta^2} + \frac{(\gamma-1)\sqrt{\sigma}}{2(1+\sigma)}(1-\mu_T)\right] = 0.0204^*$$

$$C_7 = -\frac{\gamma-1}{4}J_n^2(\beta)\left[\frac{\gamma-1}{2}(1-\mu_T) - 1 + \frac{n^2}{2\beta^2}\left(\frac{\sigma^2+2\sigma+3}{1+\sigma}\right)\right] = 0.0388$$

$$C_8 = C_7 + \frac{\gamma-1}{4}\frac{n^2}{\beta^2}J_n^2(\beta)\left[\frac{\sigma^3+2\sigma^2-5\sigma-2}{(1+\sigma)^2}\right] = 0.0318$$

$$\xi_2 = [\text{Eq. (6c)}] = -0.281$$

$$\bar{\xi}_2 = -\frac{C_7}{2} - \frac{C_8}{4(2n+1)}\left[\frac{\beta^2 - n(3n+2)}{\beta^2 - n^2}\right] = -0.0110$$

Traveling wave

$$C_9 = \frac{nJ_n^2(\beta)}{2\beta}\left[1 - \frac{3n^2}{2\beta^2} - \frac{\gamma-1}{\sigma(1+\sigma)} + \frac{(\gamma-1)\sigma}{1+\sigma}\mu_T\right] = 0.377^*$$

$$C_{10} = 2C_7 = 0.0776$$

$$\bar{\xi}_2\ [\text{Eq. (6c)}] = -0.084$$

$$\check{\xi}_2 = -[(n/\beta)C_9 + (1/2)C_{10}] = -0.0593$$

* These values are for $n = 1$, $\gamma = 7/5$, $\sigma = 0.73$, $\mu_T = 1$, and β given by the smallest zero of $J_1'(\beta)$—i.e., $\beta = 1.841$.

Appendix C

P_{ij}, Functions of (α) [Eqs. (7)]

$$P_{10} = J_n$$

$$P_{20} = \frac{1}{2}\left[J_n^2 - (\gamma + 1)f - (J_n'^2/4) - (J_n^2/4)(1 - n^2/\alpha^2)\right]$$

$$P_{21} = \frac{1}{2}\left[J_n^2 - (\gamma + 1)g - (J_n'^2/4) - (J_n'^2/4)(1 + n^2/\alpha^2)\right]$$

$$P_{22} = \frac{1}{2}\left[\quad + (J_n'^2/4) - (J_n^2/4)(1 + n^2/\alpha^2)\right]$$

$$P_{23} = \frac{1}{2}\left[\quad + (J_n'^2/4) - (J_n^2/4)(1 - n^2/\alpha^2)\right]$$

$$P_{30} = \frac{1}{4}\left[3F_1 + \frac{\gamma+1}{4}J_n'f' + \frac{\gamma+1}{2}J_n\left\{(1 - n^2/\alpha^2)f\right\} + \frac{J_n}{8}\left\{-3J'^2 + 3\frac{n^2J_n^2}{\alpha^2} - \frac{\gamma+10}{3}J_n^2\right\}\right]$$

$$P_{31} = \frac{1}{4}\left[3F_2 + \frac{\gamma+1}{4}J_n'(f' + 2g') + \frac{\gamma+1}{2}J_n\left\{(1 + n^2/\alpha^2)f + 2g\right\} + \frac{J_n}{8}\left\{-9J_n' - 3\times \frac{n^2J_n^2}{\alpha^2} - (\gamma + 10)J_n^2\right\}\right]$$

$$P_{32} = \frac{1}{4}\left[F_3 - \frac{\gamma+1}{4}J_n'f' + \frac{\gamma+1}{2}J_n\left\{(1 + n^2/\alpha^2)f\right\} + \frac{J_n}{8}\left\{+3J_n'^2 - 3\frac{n^2J_n^2}{\alpha^2} - (\gamma+2)J_n^2\right\}\right]$$

$$P_{33} = \frac{1}{4}\left[F_4 - \frac{\gamma+1}{4}J_n'(f' + 2g') + \frac{\gamma+1}{2}J_n\left\{(1 - n^2/\alpha^2)f + 2g\right\} + \frac{J_n}{8}\left\{+9J'^2 + 3\frac{n^2J_n^2}{\alpha^2} - 3(\gamma+2)J_n^2\right\}\right] + \alpha\zeta_2 J_n'$$

$$P_{34} = \left[F_5 - \frac{\gamma+1}{4}J_n'f' + \frac{\gamma+1}{2}J_n\left\{(1 - n^2/\alpha^2)f\right\} + \frac{J_n}{8}\left\{+3J_n'^2 + n^2J_n^2/\alpha^2 - (\gamma+2)J_n^2\right\}\right] + \alpha\zeta_2 J_n'$$

All the f, g, F_i, and J_n are functions of α. If the acoustic frequency is used in calculations, include the terms involving ζ_2 (standing value in P_{33}, traveling value in P_{34}). Otherwise omit these terms.

References

[1] Crocco, Luigi, and Cheng, Sin-I., *High Frequency Combustion Instability in Rocket Motor with Concentrated Combustion*, Jour. Am. Rocket Soc., Vol. 23, No. 5, pp. 301–313, September–October, 1953.

[2] Grad, Harold, *Resonance Burning in Rocket Motors*, Communications on Pure and Appl. Math., Vol. 2, No. 1, pp. 79–102, March, 1949.

[3] Moore, Franklin K., and Maslen, Stephen H., *Transverse Oscillations in a Cylindrical Combustion Chamber*, NACA TN 3152, 1954.

[4] Rayleigh, *The Theory of Sound*, Vol. II, p. 480, Dover Publications, New York, 1945.

[5] Rayleigh, *On the Circulation of Air Observed in Kundt's Tubes and on Some Allied Acoustical Problems*, Royal Soc. (London), Phil. Trans., Vol. 175, Pt. 1, pp. 1–21, 1884.

[6] Schlichting, H., *Berechnung Ebener Periodischer Grenzschichtströmungen*, Phys. Zeit., Vol. 33, pp. 327–335, 1932.

[7] Nyborg, W. L., *Acoustic Streaming due to Attenuated Plane Waves*, Jour. Acoust. Soc. Am., Vol. 25, No. 1, pp. 68–75, 1953.

[8] Westervelt, Peter J., *The Theory of Steady Rotational Flow Generated by a Sound Field*, Jour. Acoust. Soc. Am., Vol. 25, No. 1, pp. 60–67, 1953.

[9] Andres, J. Milton, and Ingard, Uno, *Acoustic Streaming at High Reynolds Numbers*, Jour. Acoust. Soc. Am., Vol. 25, No. 5, pp. 928–932, 1953.

[10] Andres, J. Milton, and Ingard, Uno, *Acoustic Streaming at Low Reynolds Numbers*, Jour. Acoust. Soc. Am., Vol. 25, No. 5, pp. 932–938, 1953.

[11] Andrade, E. N. da C., *On the Circulations Caused by the Vibration of Air in a Tube*, Proc. Roy. Soc. (London), Series A, Vol. 134, pp. 445–470, 1931.

Influence of the Leading-Edge Shock Wave on the Laminar Boundary Layer at Hypersonic Speeds†

LESTER LEES‡

California Institute of Technology

SUMMARY

In order to bring out the importance of the leading-edge region at hypersonic speeds, the influence of the leading-edge shock wave on the laminar boundary layer is investigated in two simple cases of steady flow over a semi-infinite, insulated flat plate: (1) sharp leading edge; (2) blunt leading edge, as approximated by a normal shock wave. The streamlines that enter the boundary layer over a large region of the plate surface has previously crossed the shock wave very near the leading-edge, where the shock is strong and highly curved. Consequently, the temperature at the outer edge of the boundary layer is appreciably higher than free-stream temperature, and the vorticity there is not zero. The effects of this shock-wave "heating" and vorticity on the boundary layer are shown to be much larger than the usual "errors" made in the boundary-layer theory, and an estimate of these effects can therefore be obtained within the framework of that theory. The numerical magnitude of the shock-wave influence is found to be appreciable. For the case of the blunt leading edge the slope of the curve of induced pressures plotted against the hypersonic interaction parameter closely approaches the experimental data of Hammitt and Bogdonoff obtained in helium at large values of this parameter. These approximate results show that the influence of the leading-edge region at hypersonic speeds requires careful theoretical and experimental study.

SYMBOLS

a^* = sound speed, $\sqrt{\gamma RT^*}$
C_p, C_v = specific heat at constant pressure and constant volume, respectively
C = constant in viscosity-temperature relation, $\mu^* = CT^*$ where $C = \mu_w^*/T_w^*$
F = constant obtained from Falkner-Skan solution
h^* = distance from shock wave to plate surface
M = Mach Number, u^*/a^*
p^* = pressure
R = gas constant, per unit mass
Re = Reynolds Number, $(\mu_\infty^* t^*)/\nu_\infty^*$
Re_{x^*} = Reynolds Number, $(u_\infty^* x^*)/\nu_\infty^*$
S^* = entropy, per unit mass
t^* = time
T^* = absolute temperature
u^*, v^* = components of velocity parallel and normal to plate surface, respectively
x^*, y^* = coordinates parallel and normal to plate surface respectively, with origin at leading edge
z = η_i/η_{i_δ}
β = parameter in Falkner-Skan solution, $(\gamma - 1)/\gamma$
γ = ratio of specific heats
δ = boundary-layer thickness
δ^*, δ^{**} = displacement and momentum thickness, respectively
ψ^* = stream function
μ^* = ordinary coefficient of viscosity
ν^* = μ^*/ρ^*
ρ^* = density
$\bar{\chi}$ = hypersonic boundary-layer interaction parameter, $(M_\infty^3\sqrt{C})/\sqrt{Re_x^*}$
η = nondimensional "distance" normal to plate surface, $y^*\sqrt{u_\infty^*/\nu_\infty^* x^* C}$
η_i = corresponding η in equivalent incompressible flow
p = p^*/p_∞^*
ρ = ρ^*/ρ_∞^*, etc.

Subscripts

∞ = free-stream quantities
δ = quantities evaluated at the outer edge of the boundary layer
w = plate surface
1 = location along the plate surface
2 = quantities just behind the leading-edge shock wave

(1) INTRODUCTION

AT HYPERSONIC SPEEDS the kinetic energy of gas motion is large compared to the ambient thermal energy, and the deceleration of the gas as it penetrates the viscous layer at the surface of a body generates high temperatures in this region. As a result the hypersonic laminar boundary layer is from 10 to 100 times thicker than at low speeds at the same Reynolds Number, and the outward streamline deflection induced by this thick boundary layer as it grows along the surface amounts to a significant change in the "effective shape" of the body. Large induced pressure changes are transmitted into the "external" flow field, and these pressures in turn feed back into the viscous layer and affect its rate of growth. Previous investigations of this interaction phenomenon have dealt with the problem completely within the framework of the Prandtl boundary-layer theory, in which the flow is divided into distinct viscous and inviscid regions and the influence of the nose or leading edge is ignored. But the change in effective shape of the body surface brought about by the growth of the boundary layer also alters the shape of the leading-

Received February 3, 1955.

† This work was supported by the U.S. Army Ordnance and U.S. Air Force under Contract No. DA-04-495-Ord-19. The author would like to express his appreciation to Dr. Antonio Ferri, Polytechnic Institute of Brooklyn, for his stimulating arguments on the importance of the leading-edge region at hypersonic speeds, and to Dr. Keith Stewartson, Bristol University, for many discussions on hypersonic boundary-layer problems. Dr. Ting-Yi Li read the manuscript and contributed several valuable suggestions, and he and Dr. H. Yang checked the formulas and numerical calculations.

‡ Professor of Aeronautics, Guggenheim Aeronautical Laboratory.

edge or nose shock wave, and the resultant changes in entropy are transported downstream along the streamlines. At hypersonic speeds the mass flux in the boundary layer is very small, so that the stream lines that enter the layer have previously crossed the shock wave far upstream near the leading edge, where the shock is strong and highly curved (see Fig. 1). In other words, the local value of the entropy S_δ^*, or the temperature T_δ^*, may be considerably higher than its free-stream value and may depend upon conditions in the immediate leading-edge region. Also the vorticity at the outer edge of the viscous layer is certainly not zero, as assumed in the usual boundary-layer theory. Ferri and Libby[1] recently pointed out that the boundary conditions for the viscous flow at the outer edge of the boundary layer must be modified accordingly in such cases. In one special example they show that these modifications have a significant influence on the skin friction. Dr. Ferri also suggested to the present author that shock-wave "heating" and vorticity at hypersonic speeds will tend to reduce the mass flux in the boundary layer and may thereby increase the boundary-layer thickness and induced pressures.

In the closely related problem of the outward-moving shock wave generated by the impulsive motion of an infinite plate in its own plane, Stewartson[2] has shown that the increment in plate temperature caused by the shock-wave "heating" of the inviscid "external" flow is of order $[\nu_\infty^*/(a_\infty^*)^2 t^*]^{(1/2)-(1/3\gamma)}$ in the strong interaction regime, or of order $(M_\infty/\sqrt{Re})^{1-(2/3\gamma)}$ where $Re = (u_\infty^{*2} t^*/\nu_\infty^*)$. Stewartson states that this effect is negligible when $(\nu_\infty^*/a_\infty^{*2} t^*) \ll 1$. We may add that for any fixed value of the interaction parameter $(M_\infty^3/\sqrt{Re})$, an "error" of this order approaches zero as $M_\infty \to \infty$, and the solutions found by him, and by the present author and R. Probstein[3-5] in the related steady flow problem, are the correct limiting forms. But for any *finite* Mach Number this heating effect is much larger for all real gases $(1 \leq \gamma \leq 5/3)$ than the usual errors made in the boundary-layer theory, which are of order $M_\infty/\sqrt{Re}$ in the strong interaction region, and the numerical magnitude of the heating effect may not be negligibly small.

The purpose of this paper is to investigate the influence of shock-wave heating and vorticity on the hypersonic laminar boundary-layer thickness and induced pressures in a simple example, in order to bring out the importance of the leading-edge region. Two cases of steady flow over a semi-infinite, insulated flat plate are considered: (1) flat plate with a sharp leading edge; (2) blunt leading edge as approximated by a normal shock wave. For the present the treatment is restricted to the strong interaction region where the effects are largest. Since the order of magnitude of the shock-wave heating effect is expected to be much larger than $M_\infty/\sqrt{Re}$ in these cases, the calculation is carried out within the framework of the

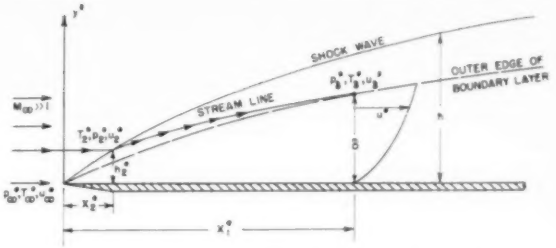

FIG. 1. Hypersonic viscous flow over a flat plate.

Prandtl boundary-layer theory, with the proper modifications in the boundary conditions at the "outer edge." However, the conditions under which the somewhat arbitrary division of the flow into distinct viscous and inviscid regions is still justified must be reexamined in these cases (see Appendix).

(2) Temperature, Velocity, and Vorticity at Outer Edge of Boundary Layer

Flat Plate with Sharp Leading Edge

The temperature, velocity, and vorticity at the outer edge of the boundary layer at station x_1^* depend on the local pressure p_δ and on the shock-wave slope and curvature at the point (x_2^*, h_2^*) previously crossed by the streamline that enters the boundary layer at x_1^* (see Fig. 1). The point (x_2^*, h_2^*) is identified later by recognizing that the mass flux across the boundary layer must be equal to the entering mass flux, or $\rho_\infty^* \psi_\delta^* = \rho_\infty^* \psi_2^* = \rho_\infty^* u_\infty^* h_2^*$. Since the flow is isentropic along the streamline downstream of the shock, the temperature T_δ^* is given by the expression

$$T_\delta = T_2 (p_\delta^{(\gamma-1)/\gamma} / p_2^{(\gamma-1)/\gamma}) \tag{1}$$

But the shock wave is "strong" in the region of interest, so that

$$p_2 \cong [2\gamma/(\gamma+1)]\, M_\infty^2 (dh^*/dx^*)_2^2$$

$$T_2 \cong [2\gamma(\gamma-1)/(\gamma+1)^2] M_\infty^2 (dh^*/dx^*)_2^2 \dagger$$

Therefore

$$T_\delta \cong \frac{2\gamma(\gamma-1)}{(\gamma+1)^2} \left(\frac{\gamma+1}{2\gamma}\right)^{(\gamma-1)/\gamma} \times p_\delta^{(\gamma-1)/\gamma} \left[M_\infty^2 \left(\frac{dh^*}{dx^*}\right)_2^2 \right]^{1/\gamma} \tag{2}$$

$$u_\delta^2 \cong 1 + \frac{2}{\gamma-1}\frac{1}{M_\infty^2} - \frac{2}{\gamma-1}\frac{T_\delta}{M_\infty^2} \cong 1 - \frac{2}{\gamma-1}\frac{T_\delta}{M_\infty^2} \tag{3}$$

† An error of order $M_\infty \sqrt{C}/\sqrt{Re_{x_2^*}}$ is introduced here when the shock wave angle is supposed to be small enough so that $\sin\theta_s \cong \tan\theta_s$. Terms of order $1/\bar{\chi}$ are neglected when the "strong shock" formulas are employed. Neither of these errors enters into a first-order calculation of the influence of the entropy wake on the boundary layer.

By Crocco's theorem the vorticity at the outer edge of the boundary layer, which is very nearly $-(\partial u^*/\partial y^*)$, is equal to

$$(p_\delta^*/R)[(1/\rho_\infty^*)(dS^*/d\psi^*)]_\delta$$

Since S^* is a function of ψ^* alone, $dS^*/d\psi^*$ has the same value all along a given streamline and is most conveniently evaluated at the shock wave. For strong shocks

$$(dS_2^*/d\psi_2^*) \cong (C_v/p_2^*)(dp_2^*/d\psi_2^*)\dagger$$

and the vorticity in nondimensional form is

$$\left(\frac{\delta}{u_\infty^*}\frac{\partial u^*}{\partial y^*}\right)_\delta = -\frac{1}{\gamma - 1}\frac{\delta p_\delta^*}{u_\infty^*}\left(\frac{1}{p_2^*}\frac{dp_2^*}{\rho_\infty^* d\psi_2^*}\right) \quad (4)$$

Since the "similar solution" for the boundary-layer flow in the strong interaction region satisfies the boundary conditions $u^* \to u_\infty^*$ (or $\{T/[(\gamma - 1)/2] \times M_\infty^2\} \ll 1$) and $(\partial u^*/\partial y^*) \to 0$ as $\eta \to \infty$, it furnishes the proper starting point for the calculation of the first-order approximations to T_δ, u_δ, and $(\partial u^*/\partial y^*)_\delta$ from Eqs. (2)–(4). According to the results of reference 4:

(i) $\delta = \delta_0 C^{1/4}[\sqrt{M_\infty} x^*/(Re_{x^*})^{1/4}]$ and $p_\delta^{(0)} = p_0\tilde{\chi}$ for $\tilde{\chi} \gg 1$.

(ii) For an insulated surface and a Prandtl Number of unity, the velocity u is the same function of a nondimensional stream function, ζ, as in the well-known Falkner-Skan solution for the low-speed boundary layer, with the Falkner-Skan parameter β equal to $(\gamma - 1)/\gamma$. Here

$$\zeta = (\psi^*/\sqrt{2p_\delta^{(0)}})(1/\sqrt{\nu_\infty^* u_\infty^* C x^*})$$

(iii) The constant p_0 is given by the relation

$$p_0 = (9/32)\gamma(\gamma + 1)\delta_0^2 = (3/8)[\gamma(\gamma + 1)]^{1/2}(\gamma - 1)F$$

where

$$F = (\delta^*\sqrt{u_\infty^*/\nu_\infty^* x^*} + \delta^{**}\sqrt{u_\infty^*/\nu_\infty^* x^*})_{\beta=(\gamma-1)/\gamma}$$

—i.e., F is the sum of the nondimensionalized displacement and momentum thickness in the Falkner-Skan solution.

Our calculation is greatly simplified by utilizing Stewartson's result[6] that a similar solution for the inviscid rotational flow between boundary layer and shock wave also exists in the strong interaction region. His work shows that the ratio of the distance of the shock wave from the plate surface to the boundary-layer thickness is a constant—i.e.,

$$\text{(iv)} \quad h_2^* = \frac{h_0}{\delta_0}\delta = h_0 C^{1/4}\frac{\sqrt{M_\infty}}{(Re_{x_2^*})^{1/4}} x_2^*$$

where h_0/δ_0 is a function of γ alone.

According to (iv) the shock-wave angle dh^*/dx^* is simply related to h^* itself, and therefore to $\psi^* = u_\infty^* h^*$. In fact

$$\left(\frac{dh^*}{dx^*}\right)_2 = \frac{(3/4)h_0^{4/3}C^{1/3}M_\infty^{2/3}}{(u_\infty^*/\nu_\infty^*)^{1/3}(\psi_2^*/u_\infty^*)^{1/3}} \quad (5)$$

By definition $\psi_2^* = \psi_\delta^* = \sqrt{2p_\delta^{(0)}}\sqrt{\nu_\infty^* u_\infty^* x_1^* C}\,\zeta_\delta$ where $p_\delta^{(0)}$ is given by (i) with $x^* = x_1^*$, so that

$$\left(\frac{dh^*}{dx^*}\right)_2 = 1.56\frac{(h_0/\delta_0)^{4/3}}{\zeta_\delta^{1/3}[\gamma(\gamma + 1)]^{2/3}} p_0^{1/2}\left(\frac{M_\infty\sqrt{C}}{\sqrt{Re_{x_1^*}}}\right)^{1/6} \quad (6)$$

By substituting this last result into Eq. (2) and again utilizing the relation (i) for $p_\delta^{(0)}$ and also (iii), one obtains

$$\frac{T_\delta^{(1)}}{[(\gamma - 1)/2]M_\infty^2} = 1 - u_\delta^{(1)^2} = \frac{3}{4}\theta_1(\gamma)\left(\frac{M_\infty\sqrt{C}}{\sqrt{Re_{x_1^*}}}\right)^{1-(2/3\gamma)} \quad (7)$$

where

$$\theta_1(\gamma) = \frac{(4.86)^{1/\gamma}\gamma^{(1/2)-(1/3\gamma)}}{(\gamma + 1)^{(1/2)+(7/3\gamma)}}\frac{(\gamma - 1)(h_0/\delta_0)^{8/3\gamma}F}{(\zeta_\delta)^{2/3\gamma}}$$

As anticipated, the same parameter $(M_\infty\sqrt{C} \div \sqrt{Re_{x^*}})^{1-(2/3\gamma)}$ appears here as in Stewartson's expression for the increment in plate temperature in the related nonsteady flow problem.

Now $p_2^* \sim (dh^*/dx^*)_2^2 \sim 1/\psi_2^{*2/3}$

so that $\dfrac{1}{p_2^*}\dfrac{dp_2^*}{d\psi_2^*} = -\dfrac{2}{3}\dfrac{1}{\psi_2^*} = -\dfrac{2}{3}\dfrac{1}{\psi_\delta^*}$

According to Eq. (4) the vorticity at the outer edge of the boundary layer is given by the following expression:

$$\left(\frac{\delta}{u_\infty^*}\frac{\partial u^*}{\partial y^*}\right)_\delta = \frac{2}{3}\frac{1}{\gamma - 1}\frac{\delta p_\delta^*}{\psi_\delta^* u_\infty^* \rho_\infty^*} = \frac{1}{3}\frac{F}{\gamma\zeta_\delta} \quad (8)$$

a constant independent of x_1^*.

The extent to which the entropy jump generated at the shock wave is transported downstream in the inviscid flow is illustrated by the relation between $Re_{x_2^*}$ and $Re_{x_1^*}$. By equating the expression for the shock-wave angle in Eq. (6) with the result obtained by differentiating (iv), one finds

$$\frac{Re_{x_2^*}}{Re_{x_1^*}} = 0.680\left\{[\gamma(\gamma + 1)]^{1/2}\frac{\zeta_\delta}{h_0/\delta_0}\right\}^{4/3}\left(\frac{M_\infty\sqrt{C}}{\sqrt{Re_{x_1^*}}}\right)^{4/3} \quad (9)$$

in the strong interaction region, or $Re_{x_1^*} \sim (Re_{x_2^*})^2$ at a given Mach Number. In other words, over a large portion of the plate surface the streamlines that enter the boundary layer have previously crossed the shock wave very near the leading edge.

For helium $\gamma = 5/3$, $\beta = 0.40$, $F = 1.74$, $\zeta_\delta = 4.09$,‡ and $(h_0/\delta_0) = 2.08$ according to reference 6. Therefore,

$$[(\delta/u_\infty^*)(\partial u^*/\partial y^*)]_\delta = 0.085$$

† See previous footnote.

‡ The value of ζ_δ is taken to correspond to a velocity ratio $u_0 = 0.9990$ in the zeroth-order solution.

$$\frac{T_\delta^{(1)}}{[(\gamma-1)/2]M_\infty{}^2} = 1 - u_\delta^{(1)2} = 0.785\left(\frac{M_\infty\sqrt{C}}{\sqrt{Re_{x_1}*}}\right)^{0.60}$$

Also $Re_{x_2}*/Re_{x_1}* = 4.50(M_\infty\sqrt{C}/\sqrt{Re_{x_1}*})^{4/3}$

Hammitt and Bogdonoff[7] have measured induced pressures on an insulated flat surface in the Princeton helium-operated tunnel at $M_\infty = 12$ and Reynolds Numbers as low as 4×10^4. For these conditions ($C = 0.25$),

$$\{T_\delta^{(1)}/[(\gamma-1)/2]M_\infty{}^2\} \cong 0.0950$$
$$u_\delta^{(1)} \cong 0.95$$
$$Re_{x_2}* \cong 1670$$

(It should be noted that even for $Re_{x_1}* = 10^6$ the value of $Re_{x_2}*$ is only 4850.)

For air $\gamma = 1.40$, $\beta = 0.286$, $F = 1.88$, $\zeta_\delta = 3.99$, and, according to reference 6, $(h_0/\delta_0) = 1.69$. Therefore

$$[(\delta/u_\infty{}^*)(\partial u^*/\partial y^*)]_\delta = 0.112$$

$$\frac{T_\delta^{(1)}}{[(\gamma-1)/2]M_\infty{}^2} = 1 - u_\delta^{(1)2} = 0.402\left(\frac{M_\infty\sqrt{C}}{\sqrt{Re_{x^*}}}\right)^{0.524}$$

while $Re_{x_2}* = 4.77(M_\infty\sqrt{C})^{4/3}(Re_{x_1}*)^{1/3}$.

For $M_\infty = 12$ and $Re_{x_1}* = 4 \times 10^4$, $C \cong 0.446$ for an insulated surface, and $\{T_\delta^{(1)}/[(\gamma-1)/2]M_\infty{}^2\} \cong 0.075$, while $u_\delta^{(1)} \cong 0.96$. In this case $Re_{x_2}* \cong 2{,}600$.

While these calculated effects on temperature and velocity are small, they are sufficient to cause appreciable changes in boundary-layer thickness and induced pressure [Section (3)], and they represent the *minimum* possible influence of the leading-edge shock wave on the boundary layer.

Flat Plate with Blunt Leading Edge

In real life the leading-edge radius is always small but finite, and in many flows of technical interest the radius (or appropriate dimension normal to the flow) is much larger than the mean free path in the gas. In such cases a considerable portion of the mass that later enters the boundary layer crosses a near-normal detached shock wave at the leading edge.† An estimate of the maximum effect of a finite leading-edge radius on the boundary-layer flow is obtained by calculating the temperature (and velocity) at the outer edge of the boundary layer on the assumption that the flow has previously traversed a normal shock at the free-stream Mach Number and then undergone an isentropic expansion to the local pressure p_δ.‡

In this case, the expression for T_δ is given by Eq. (2) with dh^*/dx^* replaced by unity, or,

$$\frac{T_\delta}{[(\gamma-1)/2]M_\infty{}^2} = \frac{2(2\gamma)^{1/\gamma}}{(\gamma+1)^{1+(1/\gamma)}}\frac{1}{M_\infty{}^{2[1-(1/\gamma)]}}p_\delta{}^{(\gamma-1)/\gamma} \tag{10}$$

When p_δ is approximated by $p_0\bar{\chi}$, the first-order T_δ is expressed as

$$\frac{T_\delta^{(1)}}{[(\gamma-1)/2]M_\infty{}^2} = 1 - u_\delta^{(1)2} \cong \frac{3}{4}\theta_2(\gamma)\left(\frac{M_\infty\sqrt{C}}{\sqrt{Re_{x^*}}}\right)^{1-(1/\gamma)} \tag{11}$$

or
$$u_\delta^{(1)} \cong 1 - \frac{3}{8}\theta_2(\gamma)\left(\frac{M_\infty\sqrt{C}}{\sqrt{Re_{x^*}}}\right)^{1-(1/\gamma)} \tag{11a}$$

where $\theta_2(\gamma) = (5.33)^{1/\gamma}\dfrac{\gamma^{1/2[1+(1/\gamma)]}}{(\gamma+1)^{(1/2)+(3/2\gamma)}} \times [(\gamma-1)F]^{1-(1/\gamma)}$

For helium $\theta_2(\gamma) = 1.102$ and $\{T_\delta^{(1)}/[(\gamma-1)/2] \times M_\infty{}^2\} \cong 0.826(M_\infty\sqrt{C}/\sqrt{Re_{x^*}})^{0.40}$; for air $\theta_2(\gamma) = 1.03$ and $\{T_\delta^{(1)}/[(\gamma-1)/2]M_\infty{}^2\} \cong 0.770(M_\infty\sqrt{C} \div \sqrt{Re_{x^*}})^{0.286}$. In helium at $M_\infty = 12$ and $Re_{x^*} = 4 \times 10^4$ (for example), $\{T_\delta^{(1)}/[(\gamma-1)/2]M_\infty{}^2\} \cong 0.20$ and $u_\delta^{(1)} \cong 0.89$. As expected, these effects are much larger than for the sharp leading edge.

(3) Effect of Temperature, Velocity, and Vorticity at Outer Edge of Boundary Layer on Induced Pressure

As suggested by Eq. (7), or Eqs. (11) and (11a), the axial velocity and temperature in the boundary layer can be expressed as asymptotic series in the parameter $(M_\infty\sqrt{C}/\sqrt{Re_{x^*}})^k$, and the coefficients of these series expansions are functions only of the nondimensional stream function ζ.†† To obtain the first-order shock-wave effect on the boundary-layer thickness and induced pressure, in general one must solve two simultaneous ordinary differential equations for the velocity and stagnation enthalpy perturbations and apply the boundary conditions specified by Eq. (7), or Eqs. (8) and (11a). However, it is desirable to have an estimate first of the *maximum* possible first-order effect. The fact that $[(\delta/u_\infty{}^*)(\partial u^*/\partial y^*)]_\delta > 0$ while $u_\delta < 1$ means that the mass flux across the boundary layer is reduced and the boundary-layer thickness and induced pressure are increased, as compared with the original solution in which the entropy wake behind the shock wave is ignored. But this increase in induced pressure in turn tends to thin out the boundary layer. An estimate of the maximum first-order influence of the shock wave on the boundary layer is obtained by considering only the modifications in the boundary conditions at the outer edge of the boundary layer and ignoring the effect of the *change*

† Slip-flow effects are expected to appear when the leading edge radius is *small* compared with the mean free path in the gas. The viscous layer thickness and effective body shape for a flat plate probably grow linearly with distance from the leading edge at first, as described approximately by Schaaf. In this case the plate leading edge is "effectively sharp" so far as the boundary-layer flow far downstream is concerned.

‡ Here we are interested primarily in the effect of the shock wave on the boundary layer and not in the inviscid pressure distribution along the surface produced by the blunt leading edge. In the weak interaction region particularly, this last effect may also be quite important (see reference 8).

†† $k = 1 - 2/3\gamma$ for the sharp leading edge and $k = 1 - 1/\gamma$ for the blunt leading edge.

in induced pressure. In calculating the new boundary-layer thickness the velocity profile is approximated by a fourth-degree polynomial in proper coordinates, which is known to be a highly accurate representation for the case of negative pressure gradient. The induced pressure on the plate surface is then obtained from the new boundary-layer thickness by means of the tangent-wedge approximation connecting the pressure and the flow deflection $\theta_\delta = (d\delta^*/dx^*) \cong (d\delta/dx^*)$.

From the definition of ζ it follows that $(d\zeta/d\eta) = [1/\sqrt{2p_\delta^{(0)}}]\rho u$, where $\eta = y^*\sqrt{u_\infty^*/\nu_\infty^* x^* C}$. The normal distance parameter η_i in the equivalent low-speed flow is defined by the relation $(d\zeta/d\eta_i) = u$, so that $\eta = \dfrac{1}{\sqrt{p_\delta^{(0)}}/\sqrt{2}}\displaystyle\int_0^{\eta_i} T d\eta_i$. When the effect of the *change* in induced pressure on the boundary-layer thickness is ignored, the expression for this thickness is of the same form as in reference 4, with the Prandtl Number equal to unity, namely

$$\frac{\delta}{x^*}\frac{(Re_{x^*})^{1/4}}{C^{1/4}\sqrt{M_\infty}} = \frac{1}{\delta_0}\frac{(4/3)(\gamma-1)}{\sqrt{\gamma(\gamma+1)}}\int_0^{\eta_{i\delta}}(1-u^2)d\eta_i \tag{12}$$

[see Eqs. (8) and (8a) of reference 4]. Suppose that δ and the integral I for the average temperature across the boundary layer appearing in Eq. (12) are expressed as asymptotic series of the following form:

$$\frac{\delta}{x^*} = \delta_0 C^{1/4}\frac{\sqrt{M_\infty}}{(Re_{x^*})^{1/4}}\left[1 + \delta_1\left(\frac{M_\infty\sqrt{C}}{\sqrt{Re_{x^*}}}\right)^k + \dots\right] \tag{13a}$$

$$I = \int_0^{\eta_{i\delta}}(1-u^2)d\eta_i = I_0\left[1 + I_1\left(\frac{M_\infty\sqrt{C}}{\sqrt{Re_{x^*}}}\right)^k + \dots\right] \tag{13b}$$

where δ_0, δ_1, ..., and I_0, I_1, ..., are constants. Then

$$\delta_0 = (2/\sqrt{3})\{\sqrt{\gamma-1}/[\gamma(\gamma+1)]^{1/4}\}\sqrt{I_0}$$

where $I_0 \equiv F$, and $\delta_1 = I_1$ where I_1 is proportional to the coefficient of the first-order correction to u_δ given by Eq. (7) or Eq. (11a).

From the oblique shock relations

$$p_\delta = (\gamma/2)(\gamma+1)M_\infty^2(d\delta^*/dx^*)^2 + \dots$$

for strong shocks. Therefore

$$p_\delta = p_0\bar{x}[1 + p_1(M_\infty\sqrt{C}/\sqrt{Re_{x^*}})^k + \dots] \tag{14}$$

where $$p_0 = (3/8)[\gamma(\gamma+1)]^{1/2}(\gamma-1)F \tag{14a}$$

as before, and

$$p_1 = 2[1 - (2/3)k]\delta_1 = 2[1-(2/3)k]I_1 \tag{14b}$$

For the flat plate with a sharp leading edge, $p_1 = (2/3)[1 + (4/3\gamma)]I_1$, and for the blunt leading edge, $p_1 = (2/3)[1 + (2/\gamma)]I_1$.

In order to compute the integral I appearing in Eq. (13b) the velocity profile in the equivalent low-speed flow is represented as a fourth-degree polynomial in $z = (\eta_i/\eta_{i_\delta})$, where η_{i_δ} is the value of η_i corresponding to the outer edge of the boundary layer. This polynomial satisfies the following boundary conditions:

At the plate surface ($z = 0$), $u = 0$. Also the curvature of the velocity profile at the surface is the same as in the original "similar solution" when the effect of the *change* in induced pressure is ignored—i.e., $(d^2u/d\eta_i^2)_0 = -(\beta/2) = -(1/2)[(\gamma-1)/\gamma]$ [Eq. (7), reference 4]. Let

$$(d^2u/dz^2)_0 = \eta_{i_\delta}^2(d^2u/d\eta_i^2)_0 = 2a_2$$

then $$a_2 = -\eta_{i_\delta}^2[(\gamma-1)/4\gamma]$$

At the outer edge of the boundary layer ($z = 1$), $u = 1 - \alpha_1$, where

$$\alpha_1 = (3/8)\theta_1(\gamma)(M_\infty\sqrt{C}/\sqrt{Re_{x^*}})^{1-(2/3\gamma)}$$

or $$= 3/8\theta_2(\gamma)(M_\infty\sqrt{C}/\sqrt{Re_{x^*}})^{1-(1/\gamma)}$$

for the sharp leading edge [Eq. (7)] and for the blunt leading edge [Eq. (11a)], respectively. In both cases we take $[(\delta/u_\infty^*)(\partial u^*/\partial y^*)]_\delta = (1/3)(F/\gamma\zeta_\delta)$ and $(d^2u/dz^2)_{z=1} = 0$.† But

$$\left(\delta\frac{\partial u}{\partial y^*}\right)_\delta = \frac{\displaystyle\int_0^{\eta_{i_\delta}} T d\eta_i}{T_\delta\eta_{i_\delta}}\left(\frac{du}{dz}\right)_{z=1} = \frac{\displaystyle\int_0^{\eta_{i_\delta}}(1-u^2)d\eta_i}{\eta_{i_\delta}\dfrac{T_\delta}{[(\gamma-1)/2]M_\infty^2}}\left(\frac{du}{dz}\right)_{z=1}$$

so that $$(du/dz)_{z=1} = (2/3\gamma)(\eta_{i_\delta}/\zeta_\delta)\alpha_1 = \alpha_2$$

to the first-order.

A quartic satisfying these conditions is

$$u = \{[2 - \alpha_2 - (a_2/3)] - 2\alpha_1\}z + a_2z^2 + [(2\alpha_2 - 2 - a_2) + 2\alpha_1]z^3 + \{[1 + (a_2/3) - \alpha_2] - \alpha_1\}z^4$$

and for this profile

$$I_0 \equiv F = \eta_{i_\delta}\{0.418 - 0.019[(\gamma-1)/4\gamma]\eta_{i_\delta}^2\} \tag{15a}‡$$

which determines the value of η_{i_δ}, and

$$I_1 = \frac{3}{8}\times \left[\frac{(1.165 - 0.019a_2) + (2/3\gamma)(\eta_{i_\delta}/\zeta_\delta)(0.298 - 0.008a_2)}{0.418 + 0.019a_2}\right] \times \theta_1(\gamma) \text{ or } \theta_2(\gamma) \tag{15b}$$

† Actually $(d^2u/dz^2)_{z=1} \neq 0$, but the contribution made by the nonvanishing vorticity gradient to the integral I is even smaller than the contribution of the vorticity, which is itself small compared with the effect of the reduction in velocity u_δ [see Eq. (15b) below].

‡ The term containing a_2^2 is negligibly small and is therefore dropped.

Finally, the induced pressure distribution on the plate surface is determined from Eqs. (14) to (15b).

For helium, $\gamma = 5/3$, $F = 1.74$, $\zeta_\delta = 4.09$, $\eta_{i\delta} = 4.63$, $a_2 = -2.15$; $p_0 = 0.92$; $p_1 = 1.68$ for the sharp leading edge, and $p_1 = 2.17$ for the blunt leading edge. Therefore

$$p_\delta = 0.92\bar{\chi}[1 + 1.7(M_\infty\sqrt{C}/\sqrt{Re_{x^*}})^{0.60} + \ldots] \quad (16)$$

for the sharp leading edge, and

$$p_\delta = 0.92\bar{\chi}[1 + 2.2(M_\infty\sqrt{C}/\sqrt{Re_{x^*}})^{0.40} + \ldots] \quad (17)$$

for the blunt leading edge. In Fig. 2 the original result $p_\delta = 0.92\bar{\chi}$ and the values of p_δ given by Eqs. (16) and (17) for an insulated flat plate in helium are plotted against $\bar{\chi}$ for $M_\infty = 12$ and $M_\infty = 14.5$. The experimental values of induced pressure obtained by Hammitt[7] on an insulated flat surface in the Princeton helium tunnel are also shown in Fig. 2. The numerical magnitude of the shock-wave effect is appreciable for large $\bar{\chi}$, and the results of the present approximate calculations encourage us to undertake a more careful theoretical and experimental study of the influence of the leading-edge region at hypersonic speeds.

(4) Conclusions

(1) At hypersonic speeds the streamlines that enter the boundary layer at a station x_1^* have previously crossed the shock wave at a location x_2^* very near the leading edge, where the shock is strong and highly curved. For example, in the strong interaction region on a flat surface with a sharp leading edge $(Re_{x_2^*} \div Re_{x_1^*}) \sim (M_\infty\sqrt{C}/\sqrt{Re_{x_1^*}})^{4/3}$, or $Re_{x_1^*} \sim (Re_{x_2^*})^3$ at a given Mach Number.

(2) Because of (1), the temperature at the outer edge of the boundary layer is appreciably higher than the free-stream temperature, and the vorticity there is not zero. The ratio $\{T_\delta/[(\gamma - 1)/2]M_\infty^2\}$ is found to be of order $(M_\infty\sqrt{C}/\sqrt{Re_{x^*}})^k$, where $k = 1 - (2/3\gamma)$ for a sharp leading edge, and $k = 1 - (1/\gamma)$ for a blunt leading edge, as approximated locally by a normal shock wave. For all real gases $(1 \leq \gamma \leq 5/3)$ this effect is much larger than the errors made in the usual boundary-layer theory.

For the case of a sharp leading edge the (nondimensional) vorticity $[(\delta/u_\infty^*)(\partial u^*/\partial y^*)]_\delta$ at the outer edge of the boundary layer is a constant, independent of x_1^*.

(3) An approximate calculation of the effects of shock-wave "heating" and vorticity on the laminar boundary-layer thickness and induced pressures in the strong interaction region shows that these effects are also of order $(M_\infty\sqrt{C}/\sqrt{Re_{x^*}})^k$ and that their numerical magnitude is appreciable at large $\bar{\chi}$.

(4) The results of the present approximate calculation show that a careful theoretical and experimental study of the influence of the leading-edge region at hypersonic speeds is required.

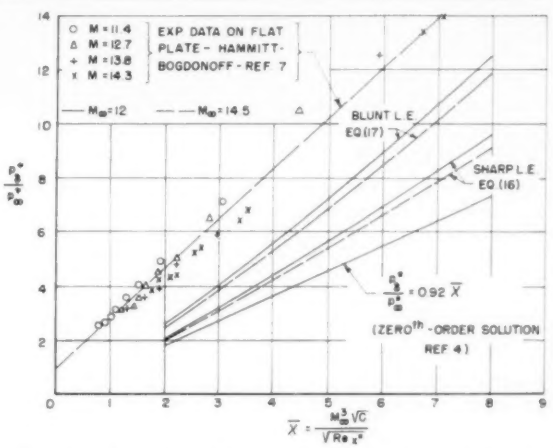

FIG. 2. First-order effect of temperature rise and vorticity generated by leading-edge shock wave on induced pressures over insulated flat plate in helium.

References

[1] Ferri, A., and Libby, P. A., *Note on an Interaction Between the Boundary Layer and the Inviscid Flow*, Readers' Forum, Journal of the Aeronautical Sciences, Vol. 21, No. 2, p. 130, February, 1954.

[2] Stewartson, K., *On the Motion of a Flat Plate at High Speed in a Viscous Compressible Fluid—I. Impulsive Motion.* (To be published by Proc. Cambr. Phil. Soc.)

[3] Lees, L., and Probstein, R. F., *Hypersonic Viscous Flow over a Flat Plate*, Princeton Univ. Aero. Engrg. Lab. Report No. 195, April 20, 1952.

[4] Lees, L., *On the Boundary-Layer Equations in Hypersonic Flow and Their Approximate Solutions*, Readers' Forum, Journal of the Aeronautical Sciences, Vol. 20, No. 2, pp. 143–145, February, 1953.

[5] Lees, L., *Hypersonic Viscous Flow over an Inclined Wedge*, Readers' Forum, Journal of the Aeronautical Sciences, Vol. 20, No. 11, pp. 794–795, November, 1953.

[6] Stewartson, K., *On the Motion of a Flat Plate at High Speeds in a Viscous Compressible Fluid—II. Steady Motion*, Journal of the Aeronautical Sciences, Vol. 22, No. 5, p. 303, May, 1955.

[7] Hammitt, A. G., and Bogdonoff, S. M., *A Study of the Flow About Simple Bodies at Mach Numbers from 11 to 15*, WADC ARDC TR 54-257, October, 1954.

[8] Bertram, M. H., *Viscous and Leading-Edge Thickness Effects on the Pressures on the Surface of a Flat Plate in Hypersonic Flow*, Readers' Forum, Journal of the Aeronautical Sciences, Vol. 21, No. 6, pp. 430–431, June, 1954.

Appendix

Existence of Distinct Viscous and Inviscid Flow Regions

At hypersonic speeds the shock wave is strong and highly curved near the leading edge, and large temperature gradients are produced across the flow behind the shock. In such cases it is important to define the precise conditions under which the effects of viscosity and heat conductivity actually are confined to the "boundary layer" and the interior of the shock wave itself, as assumed in the usual extension of Prandtl's concept to high-speed flows. A convenient measure of these effects is the ratio of the rate at which heat is transported across streamlines by conduction to the rate at which enthalpy is carried along

streamlines. As an illustration, the order of magnitude of this ratio is calculated for the simple case of a semi-infinite flat plate with a sharp leading edge in two regions of the supposedly inviscid, rotational flow: (1) just downstream of the shock wave; (2) near the outer edge of the boundary layer proper.

(1) Along the shock wave $T_2 \sim \psi^{*-(2/3)}$ in the strong interaction region [Eq. (5)], and

$$\frac{1}{T_2}\frac{\partial T_2}{\partial y^*} = \frac{1}{T_2}\frac{\partial T_2}{\partial \psi^*}\rho u^* = -\frac{2}{3}\frac{1}{\psi^*}\rho u^*$$

therefore $(\partial T_2/\partial y^*) \cong -(2/3)(p_2 u_\infty^*/\psi^*)$, and the rate of heat conduction across streamlines (per unit volume) is

$$\dot{q}_y = -k^*\frac{\partial^2 T^*}{\partial y^{*2}} \sim k_\infty^* T_\infty^* u_\infty^{*2}\frac{p_2^2}{\psi^{*2}} \sim k_\infty^* T_\infty^* M_\infty^4 \frac{(h^*)^2}{(x_2^*)^4}$$

The rate at which enthalpy is carried along a streamline is the sum of

$$\rho^* u^* C_p(\partial T^*/\partial x^*) \quad \text{and} \quad \rho^* v^* C_p(\partial T^*/\partial y^*)$$

which is proportional o $C_p T_\infty^* \rho_\infty^* u_\infty^* M_\infty^2[(h^*)^2 \div (x_2^*)^3]$ at the shock wave. Therefore the ratio $\{\dot{q}_y/[\rho^* C_p(dT^*/dt^*)]\}$ is proportional to $(1/Pr)\times(M_\infty^2/Re_{x_2^*})$. According to Eq. (9), $Re_{x_2^*} \sim Re_{x_1^*} \times (M_\infty\sqrt{C}/\sqrt{Re_{x_1^*}})^{4/3}$, so that

$$\frac{M_\infty^2}{Re_{x_2^*}} \sim \frac{M_\infty^2}{Re_{x_1^*}(M_\infty\sqrt{C}/\sqrt{Re_{x_1}})^{4/3}} = \left(\frac{M_\infty\sqrt{C}}{\sqrt{Re_{x_1^*}}}\right)^{2/3}$$

Now K. Stewartson, R. F. Probstein, the present author, and others, have already shown that the rate of heat conduction in the flow direction, $\dot{q}_{x^*}$, is of order $(h^*/x_2^*)^2 \sim (M_\infty\sqrt{C}/\sqrt{Re_{x_1^*}})$ compared to the rate of heat conduction across streamlines. It follows that

$$\frac{\dot{q}_x}{\rho^* C_p(dT^*/dt^*)} \sim \frac{M_\infty\sqrt{C}}{\sqrt{Re_{x_1^*}}}$$

and we conclude that the rotational flow just behind the shock wave is actually inviscid *up to, but not including, terms of order* $(M_\infty\sqrt{C}/\sqrt{Re_{x_1^*}})^{2/3}$. But the first-order effect of shock-wave heating and vorticity on the boundary layer is of order $(M_\infty\sqrt{C} \div \sqrt{Re_{x_1^*}})^{1-(2/3\gamma)}$ for the sharp leading edge [Eq. (7)], which is larger than $(M_\infty\sqrt{C}/\sqrt{Re_{x_1^*}})^{2/3}$ for all real gases $(1 \le \gamma \le 5/3)$. To the first-order, then, it is legitimate to disregard the effects of viscosity and conductivity in the rotational flow just behind the shock wave when computing the effect of the shock wave on the boundary layer. However a second-order calculation of the influence of the shock wave on the boundary layer would bring in terms of order $(M_\infty\sqrt{C}/\sqrt{Re_{x_1^*}})^{2[1-(2/3\gamma)]}$, which are *smaller* in order of magnitude than $(M_\infty\sqrt{C}/\sqrt{Re_{x_1^*}})^{2/3}$. Viscous "corrections" to the external rotational flow must be considered in such a calculation, and the division of the flow into distinct inviscid and viscous regions loses its meaning.

(2) In the zero-order treatment of the strong interaction region in reference 4 there is a sharp division between the boundary layer and the external inviscid flow. The first-order calculation of the present paper shows that $T_\delta \sim M_\infty^2(M_\infty\sqrt{C}/\sqrt{Re_{x_1^*}})^{1-(2/3\gamma)}$, and

$$\left(\frac{\delta}{T_\infty^*}\frac{\partial T^*}{\partial y^*}\right)_\delta = -(\gamma-1)M_\infty^2\left(\frac{\delta}{u_\infty^*}\frac{\partial u^*}{\partial y^*}\right)_\delta = \text{const.} \times M_\infty^2$$

[Eqs. (7) and (8)]. These results imply that a "superlayer," or "entropy layer," exists at the outer edge of the boundary layer, within which the temperature drops rapidly and the order of magnitude of the thickness δ' of this superlayer is given by $(\delta'/\delta) \sim (M_\infty\sqrt{C}/\sqrt{Re_{x_1^*}})^{1-(2/3\gamma)}$. It is interesting to calculate the ratio $\{\dot{q}_y/[\rho^* C_p(dT^*/dt^*)]\}$ in this layer. At the outer edge of the boundary layer

$$\frac{1}{T_\infty^*}\frac{\partial T^*}{\partial y^*} \cong -\frac{2}{3\gamma}\frac{u_\infty^* p_\delta}{\psi_\delta^*}$$

Since the pressure variation across the streamlines is negligible there, one finds that

$$\frac{1}{T_\infty^*}\frac{\partial^2 T^2}{\partial y^{*2}} \cong \frac{2}{3\gamma}\frac{u_\infty^{*2} p_\delta \rho_\delta}{(\psi_\delta^*)^2}$$

$$\dot{q}_y = -(2/3\gamma)Ck_\infty^* T_\infty^*(u_\infty^*)^2[p_\delta^2/(\psi_\delta^*)^2]$$

The order of magnitude of $\rho^* C_p(dT^*/dt)$ is given by

$$-T_\infty^*\rho_\infty^* u_\infty^* C_p(\rho_\delta T_\delta/x_1^*)[1-(2/3\gamma)]$$

By utilizing the relation

$$\psi_\delta^{*2} = (p_\delta/2)(u_\infty^* \nu_\infty^* x^* C)\zeta_\delta^2$$

one obtains the result that

$$\frac{\dot{q}_y}{\rho^* C_p(dT^*/dt^*)} = \left(\frac{4}{3\gamma-2}\right)\frac{1}{Pr}\frac{1}{\zeta_\delta^2}$$

For helium gas $\gamma = 5/3$ and $\zeta_\delta = 4.09$, and this ratio is about 0.10. In other words, the rate of heat conduction across streamlines is of the *same order* as the rate at which enthalpy is carried along streamlines, but much smaller numerically. Of course this ratio decreases very rapidly with distance from the surface, because the value of ζ (i.e., mass flux between plate surface and y-location) about doubles its value in going across the "superlayer."

In the approximate calculation of the present paper the boundary-layer flow and the external rotational flow are "joined" by requiring that the velocity (or temperature) and velocity gradient should be continuous at the outer edge and equal to their "inviscid flow" values. This calculation must overestimate the effects of shock-wave heating and vorticity, but the small value of the ratio $[\dot{q}_y/\rho^* C_p(dT^*/dt^*)]$ at the outer edge of the boundary layer obtained above suggests that the errors from this source are small.

(*Continued on page 612*)

Readers' Forum

BRIEF REPORTS of investigations in the aeronautical sciences and discussions of papers published in the JOURNAL are presented in this special department. Entries must be restricted to a maximum of 1,300 words or the equivalent of one JOURNAL page including formulas and illustrations. Publication is completed as soon as possible after receipt of the material. The Editorial Committee does not hold itself responsible for the opinions expressed by the correspondents.

Contents

Bending of Rectangular Plate with Clamped Edges ..... CHING-SHENG WU 601

Comments on "Computation of Vibration Modes and Frequencies" ..... DAVID FEIGN 603

Approximate Analysis of the Reduction in Torsional Rigidity and of the Torsional Buckling of Solid Wings Under Thermal Stresses ..... N. J. HOFF 603

Boundary-Layer Effect on Local Mach Number Measurements on a Circular Arc Half Profile ..... JAMES B. CARROLL AND GORDON F. ANDERSON 604

Rotational Vibration Response of Inertial Instruments ..... BERNARD H. WALLACH 605

Energy Dissipation in Turbulent Boundary Layers ..... ITIRO TANI 606

Effect of Radioactivity and Corona Discharge on Flame Stabilization ..... MORTON MITCHNER AND ROBERT A. GROSS 607

Column Instability of Pressurized Tubes ..... FELIX E. NAGEL 608

On the Flutter of Panels at High Mach Numbers ..... JOHN M. HEDGEPETH 609

Creep Buckling of Plates at Elevated Temperatures ..... WILLIAM ZUK 610

Comments on "Supersonic Diffuser Instability" ..... ROBERT L. TRIMPI 611

Low-Wave-Drag Bodies of Revolution as Determined by Linearized Theory ..... G. C. GROGAN 612

Bending of Rectangular Plate with Clamped Edges

Ching-Sheng Wu

Graduate Student, Department of Aeronautical Engineering, James Forrestal Research Center, Princeton University

December 15, 1955

THE PROBLEM OF clamped-edged rectangular plate was one of the most famous classical problems in the theory of elasticity. Even now no simple exact solution has appeared. In general, the simplest way to treat a rectangular plate problem is to use the Fourier series. However, it is helpful only in the case of a simply supported plate because the boundary conditions of a clamped-edge plate will not allow the Fourier series to express the deflection function directly.

The following solution is found based on the similar idea of superposition. The method of solution is, however, very simple. From the known solution of a simply supported rectangular plate given by Navier, in which the deflection function w is

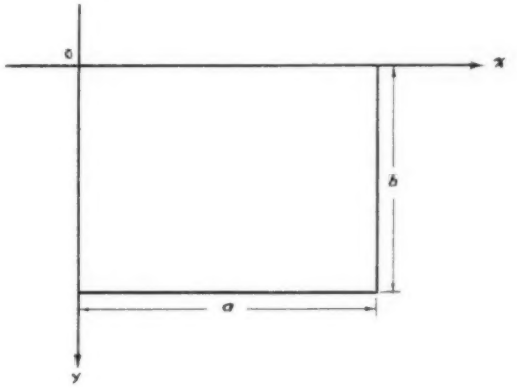

$$w = \frac{16qa^4}{\pi^6 D} \sum_m^\infty \sum_n^\infty \frac{\sin(m\pi x/a)\sin(n\pi y/b)}{(m^2 + \lambda^2 n^2)^2 mn}$$

D = flexural rigidity

mn = 1, 3, 5 . . .

$q(x, y)$ = load per unit area

λ = a/b

a new deflection function w can be constructed in such a way that an algebraic binomial function is added to each term of the sine series. Thus, the final form is

$$w = \frac{1}{D} \sum_m^\infty \sum_n^\infty A_{mn} \left[\frac{a^2}{m\pi} \sin \frac{m\pi x}{a} + (x^2 - ax) \right] \times \left[\frac{b^2}{n\pi} \sin \frac{n\pi y}{b} + (y^2 - by) \right] \quad (1)$$

$$\lambda = a/b \qquad m, n = 1, 3, 5 \ldots$$

Obviously, the deflection w will satisfy the following boundary conditions:

$$w(0, y) = 0 \qquad w(a, y) = 0$$
$$(\partial w/\partial x)_{\substack{x=0\\x=a}} = 0 \qquad (\partial w/\partial y)_{\substack{y=0\\y=b}} = 0$$

The deflection function must also satisfy the governing equation

$$\frac{\partial^4 w}{\partial x^4} + 2\frac{\partial^4 w}{\partial x^2 \partial y^2} + \frac{\partial^4 w}{\partial y^4} = \frac{q(x, y)}{D} \tag{2}$$

Substituting Eq. (1) into (2)

$$\frac{\pi^3}{Da^2}\sum_m^\infty\sum_n^\infty A_{mn}\, m^3 \sin\frac{m\pi x}{a}\left[\frac{b^2}{n\pi}\sin\frac{n\pi y}{b} + (y^2 - by)\right] + \frac{2}{D}\sum_m^\infty\sum_n^\infty A_{mn}\left(-m\pi\sin\frac{m\pi x}{a} + 2\right)\times$$
$$\left(-n\pi\sin\frac{n\pi y}{b} + 2\right) + \frac{\pi^3}{Db^2}\sum_m^\infty\sum_n^\infty A_{mn}\left[\frac{a^2}{m\pi}\sin\frac{m\pi x}{a} + (x^2 - ax)\right] n^3 \sin\frac{n\pi y}{b} = \frac{q(x, y)}{D} \tag{3}$$

The algebraic terms can be expanded into sine series.

$$\frac{\pi^2}{Da^2}\sum_m^\infty\sum_n^\infty A_{mn} m^3 \sin\frac{m\pi x}{a}\left[\frac{b^2}{n\pi}\sin\frac{n\pi y}{b} + (y'^2 - by)\right] = \frac{\pi^2}{D\lambda^2}\sum_m^\infty\sum_n^\infty A_{mn}\frac{m^3}{n}\sin\frac{m\pi x}{a}\sin\frac{n\pi y}{b} -$$
$$\frac{8}{\lambda^2 D}\sum_m^\infty\sum_n^\infty\sum_s^\infty A_{ms}\frac{m^3}{n^3}\sin\frac{m\pi x}{a}\sin\frac{n\pi y}{b} \tag{4}$$

$$\frac{2}{D}\sum_m^\infty\sum_n^\infty A_{mn}\left(-m\pi\sin\frac{m\pi x}{a} + 2\right)\left(-n\pi\sin\frac{n\pi y}{b} + 2\right) = \frac{2\pi^2}{D}\sum_m^\infty\sum_n^\infty A_{mn}\, mn\sin\frac{m\pi x}{a}\sin\frac{n\pi y}{b} -$$
$$\frac{16}{D}\sum_m^\infty\sum_n^\infty\sum_s^\infty A_{ms}\frac{m}{n}\sin\frac{m\pi x}{a}\sin\frac{n\pi y}{b} - \frac{16}{D}\sum_m^\infty\sum_n^\infty\sum_T^\infty A_{Tn}\frac{n}{m}\sin\frac{m\pi x}{a}\sin\frac{n\pi y}{b} + \frac{128}{\pi^2 D}\sum_m^\infty\sum_n^\infty\sum_s^\infty\sum_T^\infty A_{TS}\frac{1}{mn}\sin\frac{m\pi x}{a}\sin\frac{n\pi y}{b} \tag{5}$$

$$\frac{\pi^3}{b^2 D}\sum_m^\infty\sum_n^\infty A_{mn}\left[\frac{a^2}{m\pi}\sin\frac{m\pi x}{a} + (x^2 - ax)\right] n^3 \sin\frac{n\pi y}{b} = \frac{\pi^2\lambda^2}{D}\sum_m^\infty\sum_n^\infty A_{mn}\frac{n^3}{m}\sin\frac{m\pi x}{a}\sin\frac{n\pi x}{a}\sin\frac{n\pi y}{b} -$$
$$\frac{8\lambda^2}{D}\sum_m^\infty\sum_n^\infty\sum_T^\infty A_{Tn}\frac{n^3}{m^3}\sin\frac{m\pi x}{a}\sin\frac{n\pi y}{b} \tag{6}$$

$$\frac{q(x, y)}{D} = \frac{1}{D}\sum_m^\infty\sum_n^\infty B_{mn}\sin\frac{m\pi x}{a}\sin\frac{n\pi y}{b} \tag{7}$$

If $q(x, y)$ is given, B_{mn} can be determined immediately. Substituting Eqs. (4), (5), (6), and (7) into (3), we find a relation between the coefficients A_{mn}

$$\frac{\pi^2}{\lambda^2}A_{mn}\left(\frac{m^3}{n} + 2\lambda^2 mn + \frac{n^3}{m}\lambda^4\right) - \frac{8}{\lambda^2}\left(\frac{m^3}{n^3} + \frac{2m\lambda^2}{n}\right)\sum_s^\infty A_{ms} - 8\lambda^2\left(\frac{n^3}{m^3} + \frac{2n}{m\lambda^2}\right)\sum_T^\infty A_{Tn} + \frac{128}{\pi^2}\sum_T^\infty\sum_S^\infty A_{TS}\frac{1}{mn} = B_{mn} \tag{8}$$

Eq. (8) can be simplified by multiplying both sides $mn\,\lambda^2/\pi^2$

$$A_{mn}(m^2 + \lambda^2 n^2)^2 - \frac{8}{\pi^2}\left(\frac{m^4}{n^2} + 2\lambda^2 m^2\right)\sum_s^\infty A_{ms} - \frac{8}{\pi^2}\lambda^4\left(\frac{n^4}{m^2} + \frac{2n^2}{\lambda^2}\right)\sum_T^\infty A_{Tn} + \frac{128\lambda^2}{4}\sum_T^\infty\sum_S^\infty A_{TS} = mn\frac{\lambda^2}{\pi^2}B_{mn} \tag{9}$$

From Eq. (9) we can solve for A_{mn}. The number of terms of the series we want to consider depends upon how accurate a solution we desire. After A_{mn} has been determined, the deflection at any point on the plate can be found from Eq. (1). The bending moments can be calculated from the following relations.

$$M_x = -D\left(\frac{\partial^2 w}{\partial x^2} + \nu\frac{\partial^2 w}{\partial y^2}\right)$$
$$= -\sum_m^\infty\sum_n^\infty A_{mn}\left\{\left[-m\pi\sin\frac{m\pi x}{a} + 2\right]\left[\frac{b^2}{n\pi}\sin\frac{n\pi y}{b} + (y'^2 - by)\right] + \nu\left[\frac{a^2}{m\pi}\sin\frac{m\pi x}{a} + (x^2 - ax)\right]\left[-n\pi\sin\frac{n\pi y}{b} + 2\right]\right\}$$

$$M_y = -D\left[\frac{\partial^2 w}{\partial y^2} + \nu\frac{\partial^2 w}{\partial x^2}\right]$$
$$= -\sum_m^\infty\sum_n^\infty A_{mn}\left\{\left[\frac{a^2}{m\pi}\sin\frac{m\pi x}{a} + (x^2 - ax)\right]\left[-n\pi\sin\frac{n\pi y}{b} + 2\right] + \nu\left[-m\pi\sin\frac{m\pi x}{a} + 2\right]\left[\frac{b^2}{n\pi}\sin\frac{n\pi y}{b} + (y^2 - by)\right]\right\}$$

ν is Poisson's ratio.

Comments on "Computation of Vibration Modes and Frequencies"

David Feign
Head—Machine Computing Section, Cornell Aeronautical Laboratory, Inc., Buffalo, N.Y.
December 23, 1955

IN THE DECEMBER 1955 issue of the JOURNAL OF THE AERONAUTICAL SCIENCES, W. F. Cahill and S. Levy describe a method for computing vibration modes and frequencies and show an example of some results. However, I believe they omitted one of the most important parts of any article on digital computing methods. There was no discussion of the errors involved in the results and of the means used to minimize these errors. Too many people have fallen into the trap of using, blindly, computing methods they have seen published and believing the results printed out by some automatic computing machine. These automatic computing devices are nowhere near being "Giant Brains," or any kind of brains, and will not interpret their answers except when such interpretation is specifically programmed into them.

In performing matrix calculations of the kinds involved in the subject article, round-off errors pile up quite rapidly, and unless a large number of figures is carried in the arithmetic, the final results may end up with two, one, or even no significant figures. Using ten decimal digit arithmetic in performing similar calculations to determine vibration modes and frequencies for propellers, we have had difficulty in going beyond the third, or sometimes even beyond the second, mode without resorting to special computational tricks.

I would like to have the authors' comments on the arithmetic they used, the errors involved, any special means they used to reduce the errors, how they kept track of their errors so they'd know how many significant figures were involved in their results, and how the method they proposed compares computationally with other methods that might be used.

The presentation of a method for doing something without an accompanying warning as to its limitations can be very misleading. Similarly, the presentation of tabulated results without a statement of the accuracy to be expected implies that all the figures printed are significant, which I am certain is not the case in Table 1 of this paper.

Authors' Reply

Although the paper does point out at several places the use of check columns to indicate computation errors of the machine, Mr. Feign may be correct in indicating that this is not sufficiently emphasized. The methods, of course, are the results of long experience in machine computation and are in general use by computation laboratories.

With regard to Table 1, the iteration method used first converges to the lowest frequency mode, mode 1, which is the mode corresponding to the highest characteristic root of the matrix. The method makes use of orthogonality relationships to obtain convergence to modes 2, 3, etc. The iteration cycle in each case continued until there was no change in the least significant figure.

The results for higher modes are therefore accurate except for the possible build-up of rounding off errors of lower modes in a single cycle of iteration. Since the convergence varies inversely as the frequency squared, one might expect the number of significant figures in mode 6 of Table 1 to be 2 less [$(399.850/41.971)^2 \sim 100$] than for mode 1.

It is evident that this method would give poor accuracy for very high frequency modes. Since these are not ordinarily of structural significance, it is not a serious drawback to use of the method. In some instances, mode computations have been based on stiffness influence coefficients rather than the flexibility influence coefficients indicated in the paper. Where this is done, the situation is reversed, and the high-frequency modes are found with accuracy while the low-frequency modes are of poorer accuracy.

Approximate Analysis of the Reduction in Torsional Rigidity and of the Torsional Buckling of Solid Wings Under Thermal Stresses

N. J. Hoff
Head, Department of Aeronautical Engineering and Applied Mechanics, Polytechnic Institute of Brooklyn, Brooklyn, N.Y.
January 2, 1956

IF THE SOLID WING of rectangular plan form shown in Fig. 1 is heated uniformly with x, uniformly through the thickness, but nonuniformly with y, the thermal stresses developing in it can be calculated by elementary methods[1] if the aspect ratio a/b is large. These thermal stresses σ_x of the wing of infinite aspect ratio are modified near the free edges $x = \pm a$ because there σ_x must vanish, but the region in which these modifications are important is small when the aspect ratio is large. In the present approximate analysis, this edge effect will be disregarded, and the σ_x distribution will be assumed the same in every cross section of the wing. This implies that fictitious edge loads $h\sigma_x$ have to be assumed to act on the edges $x = \pm a$. The thermal stresses $\sigma_x = Rf(y)$ are shown in the figure; all other thermal stress components are assumed to be zero.

The displacements w perpendicular to the plane of the wing will be assumed as

$$w = kxy \tag{1}$$

when the wing buckles under the thermal stresses. This is a simple torsional deformation with an angle of twist

$$\varphi = kx \tag{2}$$

If the torsional rigidity of the wing section is GC, the strain energy U stored in the wing is

$$U = (1/2)\,GC\,(d\varphi/dx)^2\,(2a) = k^2a\,GC \tag{3}$$

The second-order small shortening of the distance between the end points $x = -a$ and $x = a$ of any fiber is

$$\Delta a = k^2a\,y^2 \tag{4}$$

and thus the work done by the fictitious edge forces during buckling is

$$W = \int_{-b}^{b} h\,\sigma_x\,\Delta a\,dy = k^2Ra\,I \tag{5}$$

where I is the second moment of the area of the edge force $h\,\sigma_x/R$,

$$I = \int_{-b}^{b} hy^2f(y)dy \tag{6}$$

Here the stress σ_x is considered positive if compressive.

The effective torsional rigidity of the wing is

$$GC_{eff} = (U - W)/k^2a = GC - RI \tag{7}$$

and the wing buckles when GC_{eff} vanishes. Hence, the critical value of the coefficient R in the expression for the thermal stress of the wing of infinite aspect ratio is

$$R_{cr.} = GC/I \tag{8}$$

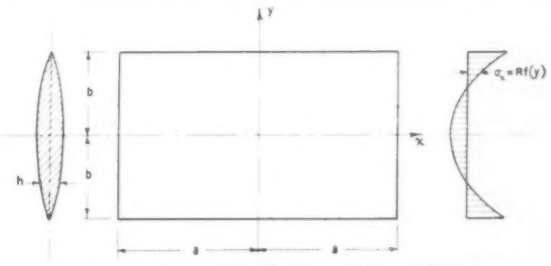

FIG. 1 SOLID WING AND THERMAL STRESS DISTRIBUTION IN ITS MIDSECTION

In particular, when the wing section is a solid rectangle with a small constant depth h, the torsional rigidity is

$$GC_{rect.} = (2/3)h^3bG \tag{9}$$

and the critical value of R becomes

$$R_{cr.\ rect.} = (2/3)h^2bG \Big/ \int_{-b}^{b} y^2 f(y)dy \tag{10}$$

When the wing is rigidly fixed at $x = 0$, additional constraints are present which increase the critical value of R. This effect, just as the effect of the free edges, should be small when the aspect ratio is large.

Addendum

After this Readers' Forum item was accepted for publication, the author became aware that Bernard Budiansky and J. Mayers had derived, with the aid of a different method of analysis, a formula essentially the same as the one given here as Eq. 7. The formula is contained in the excellent paper *Influence of Aerodynamic Heating on the Effective Torsional Stiffness of Thin Wings*, preprinted for the Twenty-Fourth Annual Meeting of the IAS, January 23–25, 1956, as Sherman M. Fairchild Publication Fund Preprint No. 579. The same formula is also presented, but without proof, by John Duberg in *High Temperature Structural Research at the National Advisory Committee for Aeronautics* on p. 230 in "Proceedings of the Conference on High-Speed Aeronautics," Polytechnic Institute of Brooklyn, 1955.

Reference

[1] Timoshenko, S., and Goodier, J. N., *Theory of Elasticity*, 2nd Ed., p. 399; McGraw-Hill Book Co., New York, 1951.

Boundary-Layer Effect on Local Mach Number Measurements on a Circular Arc Half Profile*

James B. Carroll† and Gordon F. Anderson‡
Division of Engineering, Brown University, Providence, R.I.
October 31, 1955

If one desires to calculate the Mach Number at a point on a body suspended in the free stream of a wind tunnel, the usual procedure is to neglect pressure gradients through the boundary layer. Then, by measuring the free-stream stagnation pressure and the static pressure at the point on the surface of the body, one can calculate the Mach Number at the point. This procedure is valid only if the boundary layer is thin, which is the case if the body is suspended in the free stream. One must realize that the Mach Number one calculates is not the actual Mach Number on the surface of the body which is, of course, zero, but is the Mach Number at a point outside of the boundary layer above the actual point on the body. For thin boundary layers this difference is small and is neglected, but where the layer is thick the error can be large.

If one now considers the case of the body mounted on the wall of the tunnel, one sees at once that the boundary layer, starting its growth upstream of the model, is of appreciable thickness by the time it passes over the model. The assumption of a thin boundary layer obviously cannot be made, and pressure gradients must be accounted for in the calculation of the local Mach Number.

An experimental study performed at Brown University's Aerodynamics Research Laboratory is presented here to illustrate some of the points in the above discussion. Fig. 1 shows a scale drawing of the model below the abscissa and the plot of the apparent Mach Number distributions over the profile for several free-stream Mach Numbers ranging from 0.80 to 0.90. These local Mach Numbers were calculated from surface static pressures and the free-stream stagnation pressure. It is to be noted that for free-stream Mach Numbers of 0.83 and above, there seems to exist a supersonic region about the point of maximum thickness of the profile. The data also show no indication of a shock wave up to a free-stream Mach Number of 0.86. This indicates that there apparently exists an isentropic or symmetrical supersonic region such as described in reference 1.

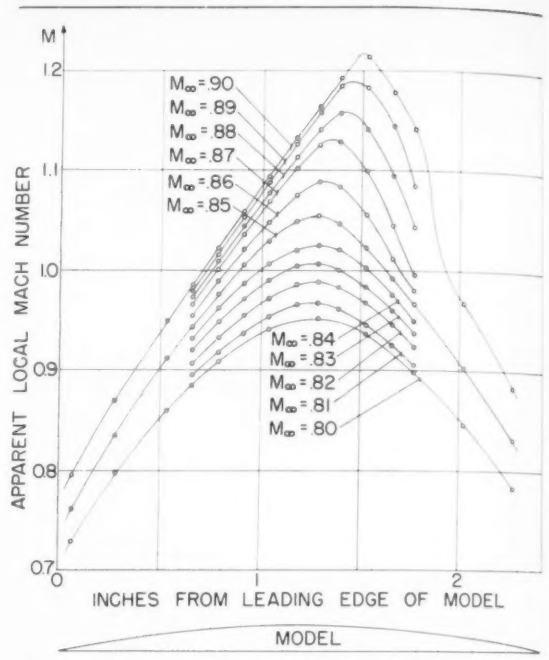

Fig. 1. Apparent local Mach Number calculated by neglecting pressure gradients through the boundary layer over a circular arc half profile. Span = 9 in., chord = 2.5 in., thickness ratio = 10 per cent.

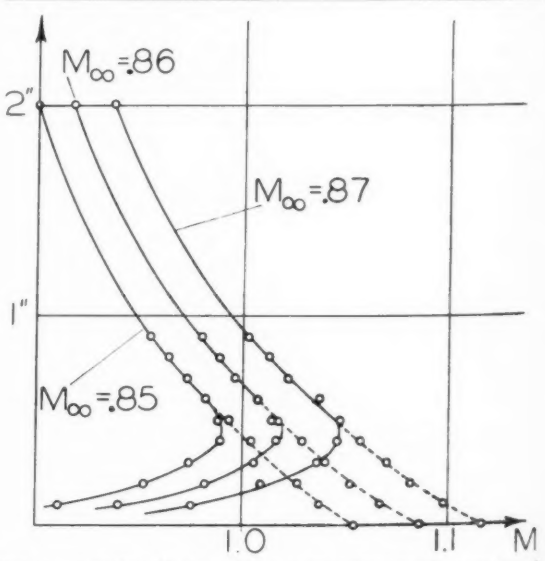

Fig. 2. Vertical Mach Number distributions at the location of the maximum thickness of the profile.

* This work was sponsored by the Office of Scientific Research of the Air Research and Development Command and performed under Contract AF 18(600)-664.

† Now, Research Dept., United Aircraft Corp., East Hartford, Conn.

‡ Research Associate.

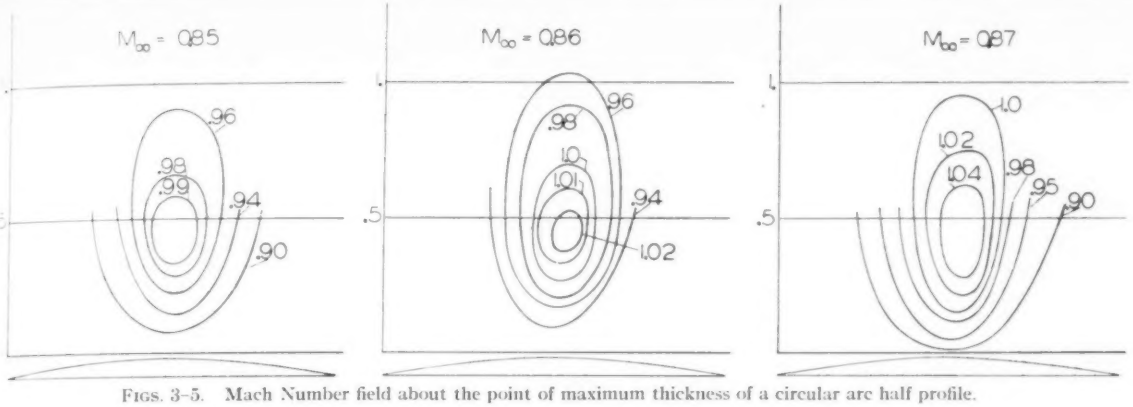

FIGS. 3–5. Mach Number field about the point of maximum thickness of a circular arc half profile.

The results of static- and stagnation-pressure measurements taken in a vertical plane at the maximum thickness of the profile are shown in Fig. 2. These were made at free-stream Mach Numbers of 0.85, 0.86, and 0.87, since in this range the shock wave first appears. One observes at once that at a free-stream Mach Number of 0.85 the flow is still subsonic, in contradiction to the indications of Fig. 1. The dashed curves represent the Mach Number variation if one neglects the stagnation-pressure gradient. The point on the axis is the Mach Number as calculated from the surface pressure and the free-stream stagnation pressure. One sees that at a free-stream Mach Number of 0.85 an error of 6 per cent is made in the calculation of the maximum Mach Number, if one neglects the pressure gradients.

Figs. 3, 4, and 5 are plots of the Mach Number field in the neighborhood of the maximum thickness for Mach Numbers of 0.85, 0.86, and 0.87. These figures show the progressive nonsymmetrical nature of the supersonic region. Since the local Mach Number is so close to 1, shock waves would be too difficult to detect by the measurement of pressure differences. However, the nonsymmetrical form of the constant Mach Number lines does indicate their presence.

REFERENCE

[1] Michel, R., Marchand, F., and Le Gallo, J., *Etude Des Ecoulements Transsoniques Autour Des Profiles Lenticulaires A Incidence Nulle*, Office National d'Etudes et de Researches Aeronautiques, Pub. No. 65, 1953.

Rotational Vibration Response of Inertial Instruments

Bernard H. Wallach
*Staff Engineer, Kearfott Co., Inc., Clifton, N.J.**
January 5, 1956

IN INSTRUMENTS employing rotational inertial elements—such as linear and angular accelerometers—and single degree of freedom gyros, rotational vibration of the supporting frame may induce steady torque about the output axis. Such torque corresponds to spurious input and results in steady error.

Referring to Fig. 1, the inertial element is capable of rotation with respect to the supporting frame about the output (y) axis of a set (x, y, z) attached to the inertial element. Considering rotational vibration of the supporting frame only, the classical equation for torque about the y axis contains the following angular velocity product terms:[1]

$$T_y = (A - C)\omega_x\omega_z + E(\omega_x^2 - \omega_z^2) \qquad (1)$$

where

A = moment of inertia about x
C = moment of inertia about z
E = product of inertia with respect to xz
ω_x, ω_z = angular velocity components along x and z

and T_y may be considered an error torque since it involves no functional input.

Consider a rotational oscillation of the supporting frame with amplitude θ_0 and frequency ω, about the axis a, shown in Fig. 1. Then

$$\omega_z = \omega\theta_0 \cos \omega t \cos \alpha \qquad (2)$$

$$\omega_x = \omega\theta_0 \cos \omega t \sin \alpha \qquad (3)$$

Substituting Eqs. 2 and 3 into Eq. 1 and retaining only the steady component of T_y

$$T_y = [(A - C)/4]\omega^2\theta_0^2 \sin 2\alpha - (E/2)\,\omega^2\theta_0^2 \cos 2\alpha \qquad (4)$$

If either yz or yx is a plane of symmetry, E vanishes.

When a gyro rotor is added to the inertial element, spinning about an axis parallel to z, A includes the inertia of the rotor about axis x, but C should not include the inertia of the rotor about the spin axis.[2] A conventional floated gyro would then

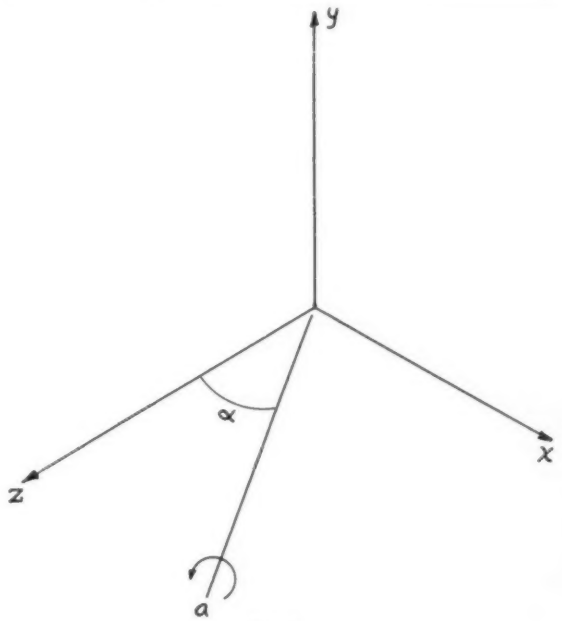

FIG. 1

* Now, Head of Analysis, United States Time Corp., 500 Fifth Ave., New York.

have an A-C approximating the moment of inertia of the rotor about an axis through its c.g. normal to the spin axis.

REFERENCES

[1] Page, Leigh, *Introduction to Theoretical Physics*, 2nd Ed., p. 120; Van Nostrand, 1935.

[2] See above, p. 123.

Energy Dissipation in Turbulent Boundary Layers

Itiro Tani

Institute of Science and Technology, University of Tokyo, Komaba, Meguroku, Tokyo, Japan

January 9, 1956

MOST OF THE EXISTING methods of calculating two-dimensional incompressible turbulent boundary layers are based on the use of two integral forms of the boundary-layer equations. These are the momentum equation

$$(d/dx)\,(U^2\theta) + \delta^* U(dU/dx) = \tau_0/\rho \tag{1}$$

and the energy equation

$$\frac{d}{dx}\,(U^3\theta^*) = 2\int_0^\delta \frac{\tau}{\rho}\frac{\partial u}{\partial y}\,dy \tag{2}$$

respectively, where x is the distance parallel to the wall, y the distance normal to the wall, u the velocity component in the direction of x, U the velocity outside the boundary layer, ρ the density, τ the shearing stress, τ_0 the shearing stress at the wall, δ the thickness of the boundary layer, and δ^*, θ, and θ^* are the displacement thickness, momentum thickness, and energy thickness of the boundary layer, respectively. Solution of Eqs. (1) and (2) requires the assumption of a single-parameter family of velocity profiles and the knowledge of the nondimensional coefficients of wall shearing stress $\tau_0/\rho U^2$ and energy dissipation

$$e = \int_0^\delta \frac{\tau}{\rho U^2}\frac{\partial}{\partial y}\left(\frac{u}{U}\right)dy \tag{3}$$

In most of the recent papers,[1-3] there is a general agreement on the use of the ratio $H = \delta^*/\theta$ for the profile parameter and the Ludwieg-Tillmann formula[4]

$$\tau_0/\rho U^2 = 0.123 \times 10^{-0.678H} \times R_\theta^{-0.268} \tag{4}$$

for the wall shearing stress, where $R_\theta = U\theta/\nu$ is the local Reynolds Number. However, less common agreement has been found on the coefficient of energy dissipation e. By assuming e to depend only on H and R_θ and by adjusting the result to fit the measurement of Schubauer and Klebanoff,[5] Rotta[6] has determined e for a range of values of H and R_θ, the effect of H being found to be rather small. Some doubts arise, however, because the evaluation is based on a single experiment and, moreover, the wall shearing stress as found in this experiment is known to be too high.

Elimination of $d\theta/dx$ between Eqs. (1) and (2) gives

$$\theta\frac{dH}{dx} = \left(2e - G\frac{\tau_0}{\rho U^2}\right)\frac{dH}{dG} + (H-1)\,G\,\frac{dH}{dG}\frac{\theta}{U}\frac{dU}{dx} \tag{5}$$

where $G = \theta^*/\theta$ and is considered as a function of H according to the single-parameter representation of velocity profiles with H as the parameter. Schuh[2] assumed $e/(\tau_0/\rho U^2)$ to depend on H and $(\theta/U)\,(dU/dx)R_\theta^{0.268}$ and brought the equation for dH/dx into a form which allows the coefficients in the equation to be determined directly from available experiments—not necessarily the experiments in which the distribution of shearing stress was measured. As a matter of fact, a similar procedure had already been made by Rubert and Persh,[7] who evaluated e by solution of Eq. (5) for experimental values of H, θ, R_θ, and dU/dx. The correlation thus obtained can be expressed in the form

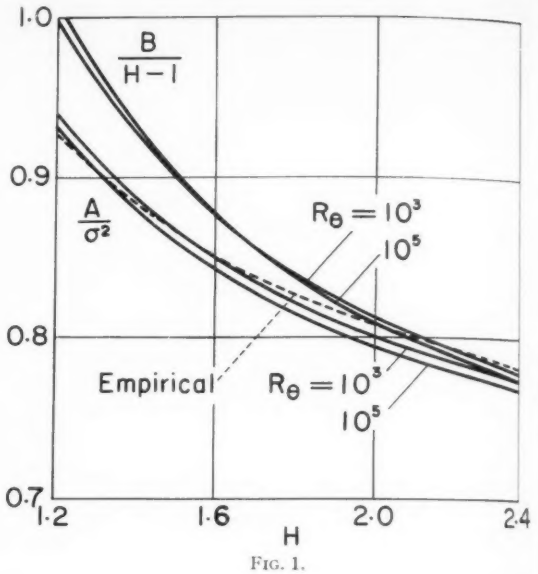

FIG. 1.

$$c = A - B(\theta/U)\,(dU/dx) \tag{6}$$

for values of $(\theta/U)\,(dU/dx)$ between 0 and -0.004, where

$$A = (\tau_0/\rho U^2)\,[6H(H-0.3) - 0.2]/(3H-1)^2 \tag{7}$$

$$B = A\,[1360(H-1.25)^{0.535} - 270] \tag{8}$$

for values of H between 1.28 and 2. The result seems to support the assumption made by Schuh. It must be admitted, however, that the experimental material is too scanty to justify the assumption.

The purpose of this note is to present a new method of evaluating e from a different point of view.

It is well-known that the effect of Reynolds Number on the velocity profile is almost unnoticeable if $(U-u)/\sqrt{\tau_0/\rho}$ is plotted against y/δ. The so-called "velocity-defect law," first announced in this form by von Kármán for pipe flows, has been demonstrated by Schultz-Grunow[8] to hold for the boundary layers with zero pressure gradient and later by Rotta[6] for the more general case of boundary layers with arbitrary pressure gradient. It has also been shown by Rotta that, for certain pressure distributions, the boundary-layer equations have "similar solutions" in which the velocity profiles at each section are identical when $(U-u)/\sqrt{\tau_0/\rho}$ is plotted against y/δ. Quite recently, the prediction was verified by a remarkable experiment of Clauser,[9] who called the similar profile an "equilibrium profile."

The area under the curve of the ordinate $(U-u)/\sqrt{\tau_0/\rho}$ is equal to unity, if $\sigma y/\delta^*$ is taken as abscissa instead of y/δ, where $\sigma = \sqrt{\tau_0/\rho U^2}$. The parameter characterizing the velocity profile is then defined by

$$I_1 = \int_0^\infty \left(\frac{U-u}{\sigma U}\right)^2 d\left(\frac{\sigma y}{\delta^*}\right) \tag{9}$$

which is independent of Reynolds Number, depending only on the pressure distribution. For example, I_1 has the value 6.1 for the boundary layer with zero pressure gradient.[9] The customary parameters are given by

$$\left.\begin{aligned} H &= 1/(1-I_1\sigma) \\ G &= (2 - 3I_1\sigma + I_2\sigma^2)/(1-I_1\sigma) \end{aligned}\right\} \tag{10}$$

where

$$I_2 = \int_0^\infty \left(\frac{U-u}{\sigma U}\right)^3 d\left(\frac{\sigma y}{\delta^*}\right) \tag{11}$$

and is a function of I_1 only, as shown in Fig. 3 of reference 6.

Consider now the boundary layer in which the velocity profile

remains similar—that is, the parameter I_1 preserves a constant value along the wall. Substitution of Eqs. (4) and (10) into Eqs. (1) and (2) then gives c the expression of the form (6), where the coefficients A and B are

$$A = \frac{2 - 3I_1\sigma + I_2\sigma^2}{2(1 - I_1\sigma)}\sigma^2 + \frac{I_1 - 2I_2\sigma + I_1I_2\sigma^2}{2(1 - I_1\sigma)^2}\omega\sigma^2 \quad (12)$$

$$B = \frac{2 - 3I_1\sigma + I_2\sigma^2}{2(1 - I_1\sigma)^2}I_1\sigma + \frac{(2 - I_1\sigma)(I_1 - 2I_2\sigma + I_1I_2\sigma^2)}{2(1 - I_1\sigma)^3}\omega \quad (13)$$

with $\omega = 0.134\ \sigma/[1 + 0.781I_1\sigma/(1 - I_1\sigma)^2]$; or, in terms of the customary parameters

$$A = \sigma^2\left[\frac{G}{2} + 0.067\,\frac{H + 3 - G(H + 1)}{1 + 0.781H(H - 1)}\right] \quad (14)$$

$$B = (H - 1)\left[\frac{G}{2} + 0.067\,\frac{H + 1\ H + 3 - G(H + 1)}{H - 1\ 1 + 0.781H(H - 1)}\right] \quad (15)$$

As shown in Fig. 1, where A/σ^2 and $B/(H - 1)$ are presented as functions of H, the explicit effect of R_θ is very small. This is due to the very slight effect of R_θ on the relation between H and G. The approximate formulas which, for values of H between 1.2 and 2.4 and R_θ between 10^3 and 10^5, yield values differing less than 0.4 per cent from those given by Eqs. (14) and (15) are

$$A = \sigma^2\left[1.476 - 0.465\,H + 0.504\,\frac{(H - 1)^2}{H}\right] \quad (16)$$

$$B = (H - 1)\left[1.790 - 0.675H + 0.742\,\frac{(H - 1)^2}{H}\right] \quad (17)$$

In Figs. 1 and 2, moreover, the empirical values given by Eqs. (7) and (8) are shown by dotted lines for comparison with the calculated results. The agreement is excellent for A; it is not so good for B but tolerable.

The result of this calculation seems to be noteworthy on three points. First, it supports Schuh's assumption for energy dissipation. Second, it demonstrates the usefulness of the similarity assumption in that the calculated values of energy dissipation are in fair agreement with those deduced from experiments having no such similarity. Third, the single-parameter representation of velocity profiles of the form of "velocity-defect law" dispenses with the knowledge of the coefficient of energy dissipation, for which a separate assumption has so far been required.

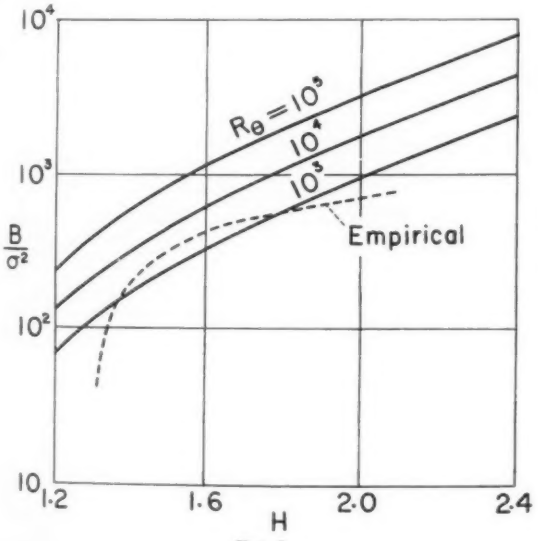

FIG. 2.

REFERENCES

[1] Truckenbrodt, E., *Ein Quadraturverfahren zur Berechnung der laminaren und turbulenten Reibungsschicht bei ebener und rotationssymmetrischer Strömung*, Ing. Arch., Vol. 20, p. 211, 1952.

[2] Schuh, H., *On Calculating Incompressible Turbulent Boundary Layers with Arbitrary Pressure Distribution*, Kungl Tekniska Högskolan, AERO TN 41, 1954.

[3] Wieghardt, K., *Über Reibungsschichten bei Druckanstieg; Eine Übersicht über Berechnungsmethoden*, Forschungshefte für Schiffstechnik, Schiffbau, Schiffsmachinenbau, 1955.

[4] Ludwieg, H., and Tillmann, W., *Untersuchungen über die Wandschubspannung in turbulenten Reibungsschichten*, Ing. Arch., Vol. 17, p. 288, 1949; also available as NACA TM 1285, 1950.

[5] Schubauer, G. B., and Klebanoff, P. S., *Investigation of Separation of the Turbulent Boundary Layer*, NACA TN 2133, 1950; superseded by NACA TR 1030, 1951.

[6] Rotta, J., *Über die Theorie der turbulenten Grenzschichten*, Mitteilungen aus dem Max-Planck Institut für Strömungsforschung, Göttingen, No. 1, 1950; also available as NACA TM 1344, 1953.

[7] Rubert, K. F., and Persh, J., *A Procedure for Calculating the Development of Turbulent Boundary Layers under the Influence of Adverse Pressure Gradients*, NACA TN 2478, 1951.

[8] Schultz-Grunow, F., *Neues Reibungswiderstandsgesetz für glatte Platten*, Luftfahrtforschung, Vol. 17, p. 236, 1940.

[9] Clauser, F. H., *Turbulent Boundary Layers in Adverse Pressure Gradients*, Journal of the Aeronautical Sciences, Vol. 21, No. 2, p. 91, February, 1954.

Effect of Radioactivity and Corona Discharge on Flame Stabilization

Morton Mitchner and Robert A. Gross

Arthur D. Little, Inc., Cambridge, Mass., and Fairchild Engine Division, Deer Park, L. I., N.Y., Respectively

January 14, 1956

THIS NOTE SUMMARIZES some previously unreported and perhaps unique experimental results obtained in exploratory studies carried out at the Harvard Combustion Laboratory during the summer of 1952. Flame stabilization mechanisms have been the thesis of many recent investigations in the field of combustion aerodynamics. The work by Zukowski[1] at the Jet Propulsion Laboratory recently shed some light on the mechanism of bluff body flame stabilization while the work of one of the present authors[2] attempted to gain some insight into the interaction of a flame front with a laminar boundary layer. What would happen if a flat plate flame holder emitted cold electrons and radioactive particles into a premixed combustible mixture? Would this significantly affect the initial chemical chain reactions and manifest itself by a change in the blowoff characteristics of such a flat plate flame holder? In an attempt to obtain a qualitative answer to this question, the authors placed a thin flat plate in the Harvard Combustion Tunnel and carefully obtained its blowoff characteristic. The plate was aligned in the direction of the flow and the flame was stabilized in the laminar boundary layer. Fig. 1 indicates the general arrangement. The blowoff curve for a thin (0.020 in. thick) steel plate is a function of air-fuel ratio, and a typical such curve is shown in Fig. 2. All tests were carried out using propane-air mixtures as the reactants.

The plate was made radioactive by bombardment in the Harvard cyclotron. For one set of experiments, the beam was concentrated on the plate leading edge while another set of experiments had the trailing edge (where the flame entered the boundary layer) radioactive. A crude measure of the intensity of radiation was made just prior to the "hot" plate being installed in the combustion tunnel, and another measurement made after the blowoff data were obtained. Typical radiation data are as follows: Before test (9:30 a.m.), 20 milliroentgen per hour, 7 ft. from plate; after test (10:30 a.m.), 20 milliroentgen per hour, 3 ft. from plate. This amount of radiation is equivalent to about 2×10^6 disintegrations per min., but this includes, of course, particles being emitted into the plate as well as out into the boundary layer.

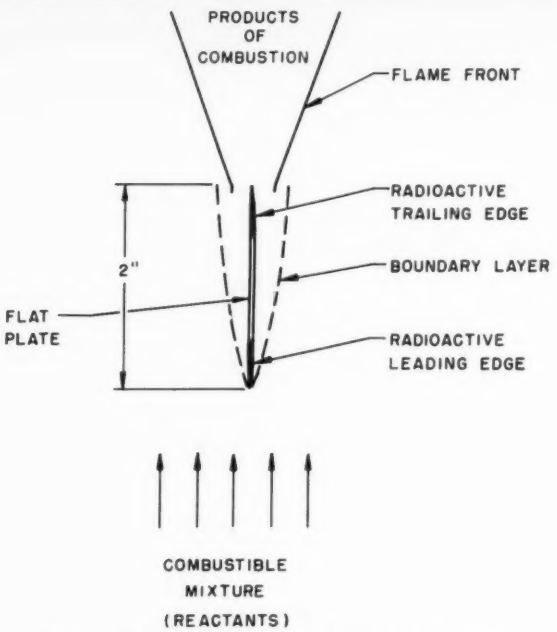

FIG. 1. Radioactive plate flame holder arrangement.

The results of these radioactive flat plate blowoff tests forced the authors to conclude that at this level of radiation, at least, there were no significant macroscopic effects noted.

While brooding over this rather disappointing negative result, the authors were led to another approach suggested by Professor W. Batteau of Harvard. Why not really affect the combustion wave with different particles and molecules and more energy by having an electric corona discharge from the plate trailing edge? Out of curiosity more than carefully calculated scientific approach, a Tesla coil was wound and placed in series with a commercial diathermy machine. This produced a terminal voltage of about 25,000 volts at about 1 kc. A thin flat plate was electrically insulated from the combustion tunnel walls and placed at this voltage. Corona discharge occurred at several places along the trailing edge of the plate when only air was flowing by the plate. The air corona distribution was a result of local voltage gradients caused by very small local roughness elements along the trailing edge. As soon as a combustible mixture flowed by the plate, the corona usually caused ignition and the flame stabilized itself all along the trailing edge of the plate.

The corona distribution changed once combustion had started and now formed quite evenly spaced (along trailing edge) discharges into the products of combustion. It is suspected that the ions in the combustion zone had a marked influence upon this remarkable even spacing of the corona.

The corona discharge had a significant effect on the blowoff characteristics of a flat plate. Typical data at 800 watts are shown in Fig. 2. The voltage was determined by the sphere-gap sparkover method. The results were sometimes rather erratic, depending upon the voltage and power being supplied to the plate. The corona act somewhat as point-type continuous pilots for the flame. In some blowoff experiments, the many corona along the plate trailing edge would, one by one, loose their flame until finally the flame would be "hanging on" to the plate, anchored by one large central corona. It was impossible to blow the flame off the plate under this condition within the velocity range capacity of the tunnel (about 150 ft./sec. maximum) and this with a plate whose normal blowoff maximum was of the order of 50 ft./sec. In Fig. 2, only the "clean" blowoff data are presented, and the occasional large single corona results previously mentioned have been omitted.

Although these experiments did not yield any further insight into fundamental combustion aerodynamics, they did point out some interesting phenomena which may one day find application and eventual understanding.

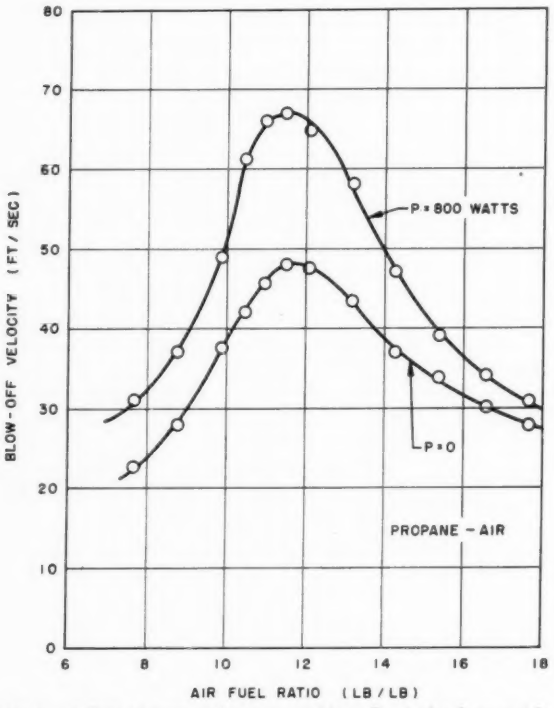

FIG. 2. Effect of corona discharge on blowoff velocity from a thin flat plate.

REFERENCES

[1] Zukowski, E. E., and Marble, F. E., *The Role of Wake Transition in the Process of Flame Stabilization in Bluff Bodies*, AGARDOGRAPH 9, Combustion Researches and Reviews, p. 167, 1955.

[2] Gross, R. A., *Boundary Layer Flame Stabilization*, Jet Propulsion, p. 288, June, 1955.

Column Instability of Pressurized Tubes

Felix E. Nagel
Douglas Aircraft Company, Inc., Tulsa, Okla.
January 16, 1956

THE INSTABILITY of a pressurized tube may be visualized by an analogy to a tube filled with balls as shown in Fig. 1. The allowable compressive load depends on the bending stiffness of the tube to stabilize the column formed by the balls. The tube has no axial load. Fig. 2 shows a tube simply supported at intervals L in the buckled-out state. We also consider a single bay of length L (Fig. 3).

Let p and A denote pressure and area of the fluid column inside of the tube, respectively. We obtain

$$\text{Shear load}_{x=0} = p\,A\left(\frac{dy}{dx}\right)_{x=0} = p\,A\left(\frac{dy}{dx}\right)_0$$

For an element of tube length Δx, the fluid pressure causes a load

$$w\,\Delta x = -p\,A\,\Delta\frac{dy}{dx} = -p\,A\,\frac{d^2y}{dx^2}\,\Delta x; \quad w = -p\,A\,\frac{d^2y}{dx^2} \quad (1)$$

The external load acting to the left of a cross section gives a moment

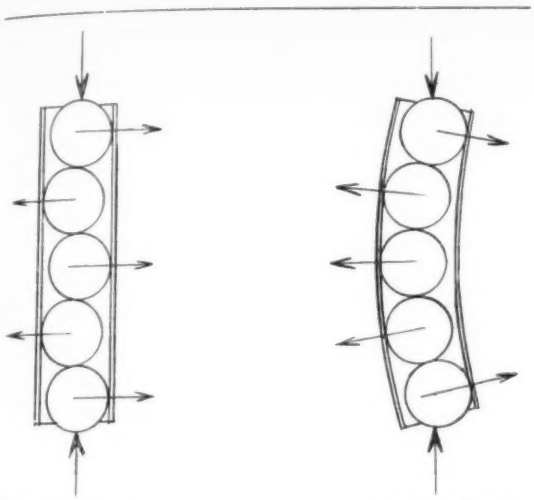

FIG. 1. Column of spherical balls stabilized by tube.

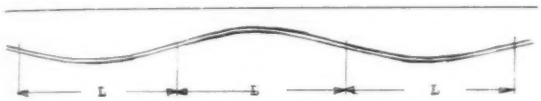

FIG. 2. Continuous tube over supports.

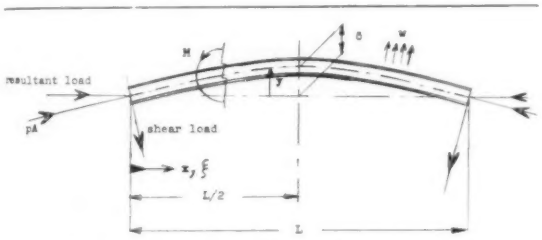

FIG. 3. Force balance on pressurized open tube.

$$M = pA\left(\frac{dy}{dx}\right)_0 \cdot x - \int_0^{\xi} w\,(\xi - x)\,dx$$

The moment parameter becomes

$$\frac{M}{pAL} = \left(\frac{dy}{dx}\right)_0 \frac{x}{L} - \frac{x}{L}\int \frac{w}{pA}\,dx + \int \frac{w}{pA}\,\frac{x}{L}\,dx$$

Substituting Eq. 1

$$\frac{M}{pAL} = \left(\frac{dy}{dx}\right)_0 \frac{x}{L} + \frac{x}{L}\int_0^x \frac{d^2y}{dx^2}\,dx - \int_0^x \frac{d^2y}{dx^2}\,\frac{x}{L}\,dx = \frac{x}{L}\frac{dy}{dx} - \int L\,\frac{d^2y}{dx^2}\,\frac{x}{L}\,d\,\frac{x}{L} \quad (2)$$

By partial integration

$$\int L\,\frac{d^2y}{dx^2}\,\frac{x}{L}\,d\,\frac{x}{L} = \frac{dy}{dx}\,\frac{x}{L} - \int \frac{dy}{dx}\,d\,\frac{x}{L} = \frac{dy}{dx}\,\frac{x}{L} - \frac{y}{L}$$

Substituting in Eq. 2 and using sign conventions of Fig. 3,

$$M/(pAL) = y/L = -[EI/(pAL^2)]\cdot L\,d^2y/dx^2$$

A solution of this equation satisfying boundary conditions is

$$y/L = (\delta/L)\sin(\pi x/L)$$

yielding $pAL^2/(EI) = \pi^2$

This equation is identical with the Euler formula for $F = pA$.

On the Flutter of Panels at High Mach Numbers

John M. Hedgepeth
Head—Dynamics and Aeroelasticity Section, Langley Aeronautical Laboratory, NACA, Langley Field, Va.
January 16, 1956

INTRODUCTION

THERE HAVE RECENTLY arisen some questions[1, 2] as to the possibility of panel flutter at high dynamic pressures and Mach Numbers. In addition, some doubts have been raised about the convergence of the Galerkin method when applied to such problems. This note is intended to shed light on these matters.

ANALYSIS

Consider a two-dimensional simply supported panel of length l and thickness h with air flowing above at supersonic Mach Number M in the positive x-direction. The differential equation of motion is

$$\left.\begin{aligned} &D\frac{\partial^4 w}{\partial x^4} + P\frac{\partial^2 w}{\partial x^2} + m\frac{\partial^2 w}{\partial t^2} = p_a(x,t) \\ &w(0,t) = \frac{\partial^2 w}{\partial x^2}(0,t) = w(l,t) = \frac{\partial^2 w}{\partial x^2}(l,t) = 0 \end{aligned}\right\} \quad (1)$$

In Eq. 1, D is the plate stiffness $Eh^3/12(1-\mu^2)$, P is an applied compressive load per unit width, m is the mass per unit area of the panel, and p_a is the aerodynamic pressure. The exact expression for p_a within the framework of linearized supersonic flow theory has been derived by Miles[3] for oscillating motion; however, his expression is too complicated for our purposes here. Experience has shown that for Mach Numbers greater than about 1.6 and for normal air and material densities, the reduced frequencies at flutter are so low that the "static" approximation of Hayes[4] yields answers that agree well with the predictions of more refined expressions. Therefore, we let

$$p_a(x,t) = -(2q/\beta)\,(\partial w/\partial x) \quad (2)$$

where q is the dynamic pressure and $\beta = \sqrt{M^2 - 1}$. Eq. 1 then becomes

$$D\frac{\partial^4 w}{\partial x^4} + P\frac{\partial^2 w}{\partial x^2} + \frac{2q}{\beta}\frac{\partial w}{\partial x} + m\frac{\partial^2 w}{\partial t^2} = 0 \quad (3)$$

If the substitutions

$$w = Re\{\bar{w}e^{i\omega t}\}$$
$$x = lx_1$$

are made, we get

$$\left.\begin{aligned} &\bar{w}^{IV} + R\bar{w}^{II} + \lambda w^{I} - k^2\bar{w} = 0 \\ &\bar{w}(0) = \bar{w}^{II}(0) = \bar{w}(1) = \bar{w}^{II}(1) = 0 \end{aligned}\right\} \quad (4)$$

where

$$R = Pl^2/D = \pi^2(P/P_{Eu})$$
$$\lambda = 2ql^3/\beta D$$
$$k = \omega/\sqrt{D/ml^4}$$

The parameter R is equal to π^2 when P equals the Euler load P_{Eu}, and the frequency coefficient k is equal to $(n\pi)^2$ ($n = 1, 2, 3, \ldots$) at the in-vacuo natural frequencies of the simply supported plate. Note that the dynamic pressure parameter λ contains all the aerodynamic effects; the mass ratio is absent by virtue of the approximation to the air forces (Eq. 2).

The characteristic equation for Eq. 4 is

$$r^4 + Rr^2 + \lambda r - k^2 = 0 \quad (5)$$

Examination of the behavior of Eq. 5 shows that there are two real roots—one positive and one negative—and a pair of complex roots. We can, therefore, write the roots in the form

$$r = -\gamma \pm \epsilon,\ \gamma \pm i\delta \quad (6)$$

In order to avoid having to solve the quartic directly for r in terms of R, λ, and k, we solve for δ, ϵ, and k in terms of R, λ, and γ. This can be done by equating the coefficients of the quartic to the

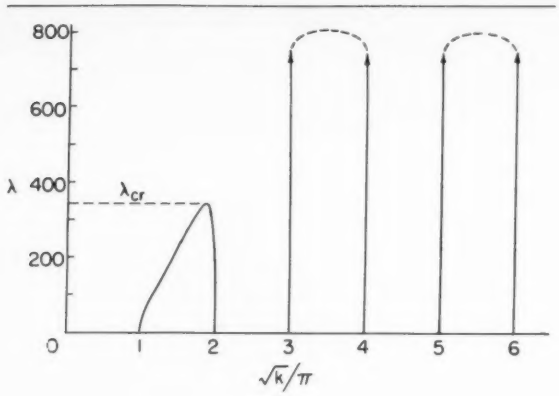

FIG. 1.

proper combinations of the roots. The process yields

$$\left.\begin{aligned} \delta &= \sqrt{\frac{\lambda}{4\gamma} + \gamma^2 + \frac{R}{2}} \\ \epsilon &= \sqrt{\frac{\lambda}{4\gamma} - \gamma^2 - \frac{R}{2}} \\ k &= \sqrt{\frac{\lambda^2}{16\gamma^2} - 4\left(\gamma^2 + \frac{R}{4}\right)^2} \end{aligned}\right\} \tag{7}$$

The solution to Eq. (4) can now be written

$$\bar{w}(x_1) = A[e^{\gamma(1-x_1)} \sin\delta \sinh\epsilon x_1 - e^{-\gamma(1-x_1)} \sinh\epsilon \sin\delta x_1] + B[e^{-\gamma x_1} \sin\delta \sinh\epsilon(1-x_1) - e^{\gamma x_1} \sinh\epsilon \sin\delta(1-x_1)] \tag{8}$$

Note that the boundary conditions $\bar{w}(0) = \bar{w}(1) = 0$ have been satisfied; satisfaction of the other two boundary conditions leads to the frequency equation

$$[(\epsilon^2 + \delta^2)^2 + 4\gamma^2(\delta^2 - \epsilon^2)] \sin\delta \sinh\epsilon = 8\gamma^2\epsilon\delta(\cosh\epsilon \cos\delta - \cosh 2\gamma) \tag{9}$$

If values of λ and R are assumed, a trial-and-error solution of Eq. (9) yields the corresponding values of γ and, hence, k. A plot of the solution for $R = 0$ is shown in Fig. 1. The ordinate is λ; the abcissa is $\sqrt{k}/\pi$. Note that for $\lambda = 0$ we have the in-vacuo natural frequencies. As λ increases, the natural frequencies change smoothly until a critical value of λ is reached where the first two natural frequencies coalesce and disappear. For values of λ less than λ_{cr}, the system is stable; for values of λ greater than λ_{cr}, the system is unstable since the first two natural frequencies have become complex. [Speaking precisely, we say that the solution for k^2 becomes complex and that one of the two square roots of k^2 must have a negative (unstable) imaginary part.] Presumably, as λ is increased further, the third and fourth frequencies, then the fifth and sixth, etc., would coalesce and disappear and the number of unstable modes would be consequently increased. These very high secondary maxima, however, are not germane to the present problem of determining the primary stability boundary.

The closed solution just discussed yields the critical value of λ as

$$\lambda_{cr} = 343.2 \tag{10}$$

A Galerkin solution of Eq. (4) with the natural modes as expansion functions yields the following results: If the first two modes are included, $\lambda_{cr}^{(2)} = 274$. If the first three modes are included, $\lambda_{cr}^{(3)} = 352$. Thus, we can see that convergence is being achieved.

Conclusion

The foregoing analysis indicates that linearized theory does indeed predict flutter of plate panels at high supersonic Mach Numbers. Furthermore, the analysis shows that the Galerkin method can be applied successfully. It is interesting to note that such would not be the case if the panel were a membrane instead of a plate; analysis of a two-dimensional membrane by the aerodynamic theory used herein indicates that no flutter can exist if the differential equation is solved exactly and that the Galerkin method gives erroneous flutter boundaries. The work of Goland and Luke[1] and an unpublished study by Miles agree with this result for membranes. The qualitatively dissimilar behavior of plates and membranes has probably been responsible for the controversy about the nature of panel flutter at high Mach Numbers.

References

[1] Goland, M., and Luke, Y. L., *An Exact Solution for Two-Dimensional Linear Panel Flutter at Supersonic Speeds*, Journal of the Aeronautical Sciences, Vol. 21, No. 4, pp. 275–276, April, 1954.

[2] Shen, S. F., *Remarks on "An Exact Solution for Two-Dimensional Linear Panel Flutter at Supersonic Speeds,"* Journal of the Aeronautical Sciences, Vol. 22, No. 9, pp. 656–657, September, 1955.

[3] Miles, J. W., *The Aerodynamic Forces on an Oscillating Air Foil at Supersonic Speeds*, Journal of the Aeronautical Sciences, Vol. 14, No. 6, pp. 351–358, June, 1947.

[4] Hayes, W. D., *A Buckled Plate in a Supersonic Stream*, North American Aviation Report, AL-1029, 1950.

Creep Buckling of Plates at Elevated Temperatures

William Zuk*
Associate Professor of Civil Engineering, University of Virginia, Charlottesville, Va.
January 18, 1956

THE METHOD OF ANALYSIS presented is a numerical method based on finite difference equations modified to account for creep strains and temperature softening of the material. The solution is an iterative one predicting deformation of the plate with time, load, and temperature history.

Although this numerical procedure is tedious unless assisted by digital computers, it is a very general approach where any temperature distribution, any forces—including thermal and residual ones—any boundary conditions, any creep law, any time, any initial crookedness, and any material property change may be introduced.

The general equation for flat plates with loads perpendicular to and in the plane of the plate is as follows. It is presented in an orthotropic form because creep and temperature softening effects are different in the x and y directions.

$$D_x\left(\frac{\partial^4 w}{\partial x^4}\right) + 2(D_1 + 2D_{xy})\left(\frac{\partial^4 w}{\partial x^2 \partial y^2}\right) + D_y\left(\frac{\partial^4 w}{\partial y^4}\right) = q + N_x\left(\frac{\partial^2 w}{\partial x^2} + \frac{\partial^2 w_i}{\partial x^2}\right) + N_y\left(\frac{\partial^2 w}{\partial y^2} + \frac{\partial^2 w_i}{\partial y^2}\right) + 2N_{xy}\left(\frac{\partial^2 w}{\partial x \partial y} + \frac{\partial^2 w_i}{\partial x \partial y}\right)$$

where

$$D_x = \frac{(E_c)_x h^3}{12(1-\mu^2)}$$

$$D_y = \frac{(E_c)_y h^3}{12(1-\mu^2)}$$

$$D_1 = \frac{\mu E_1 h^3}{12(1-\mu^2)}$$

$$D_{xy} = \frac{(G_c) h^3}{12}$$

μ (Poisson's ratio) is assumed uneffected by creep; E_1 is the modulus of elasticity associated with the particular time and temper-

* Formerly Senior Engineer, The Glenn L. Martin Co., Baltimore, Md.

ature of the material; and $(E_c)_x$, $(E_c)_y$, and (G_c) are the effective moduli as modified by creep, time, and temperature.

E_c (the effective bending modulus) may be computed by the following expression where bending stresses are more dominant than direct stresses:

$$E_c = \frac{ME_1}{M + E_1 \int_{-h/2}^{h/2} \epsilon_c z \, dA}$$

where "M" is the bending moment; ϵ_c is the unrestricted creep strain of a cross-sectional fiber dependent on the stress, time, and temperature history; and z is the distance from the centroidal axis of the plate perpendicular to the surface of the plate.

G_c (the effective twisting modulus) may be computed by the following expression:

$$G_c = \frac{M_{xy} G_1}{M_{xy} + 2G_1 \int_{-h/2}^{h/2} \gamma_c z \, dA}$$

where M_{xy} is the twisting moment and γ_c is the unrestrained twisting shear strain due to creep.

By use of the well-known finite difference approximations of the derivatives in the general plate equation, a set of finite difference equations may be set up at the finite difference grid points on the plate. At each point, the particular temperature, stress, etc., is to be used.

The main difficulty of this method lies in the determination of the effective moduli E_c and G_c. These must be determined by first assuming a reasonable set of deflection values. From these, compute the approximate stresses at the grid points and then evaluate E_c and G_c accordingly for a particular time and temperature history. (Exact stresses may be computed, but it is difficult to do so because creep causes a redistribution of bending and twisting stresses within the plate.)

Once these effective moduli are computed, the finite difference equations may be set up and solved for the deflections. The computed values of the deflections are then compared to the assumed values of the deflections. Thus, by successive correction, the correct value of the deflections may be obtained for a specific time and temperature history.

By taking successive times and repeating the method outlined, the complete deflection history may be obtained until the material becomes plastic. When the material becomes plastic, the expressions for E_c and G_c are no longer valid although they still may be determined by a semigraphical method.

As can be seen, the method is very tedious and is therefore not intended as a design method, but it is presented as one possible general way of predicting plate behavior under elevated temperatures where digital computers are available.

Comments on "Supersonic Diffuser Instability"

Robert L. Trimpi
Aeronautical Research Scientist, Langley Aeronautical Laboratory, NACA, Langley Field, Va.
January 19, 1956

IN THE INTRODUCTION to the article[1] by Dailey, "Supersonic Diffuser Instability," the impression is given that a very important aerodynamic problem has been recognized but remained virtually unattacked for the past 10 years except for the work reported therein. This impression is far from correct since a number of theoretical and experimental papers on inlet instability, as well as on the amplitude and frequency of the oscillation once initiated, have been published in the last 5 years by the NACA. Listed in references 2–6 are a few of several NACA papers which have been declassified since early in 1955. Ferri and Nucci[2] proposed the instability criterion of a vortex sheet, arising from a three-shock intersection, impinging on the cowling lip, and thereby "choking" the entering flow to initiate buzz. The writer[3, 4] used a quasi one-dimensional unsteady-wave analysis to investigate the phenomena in detail and was able to formulate a general theory for instability and buzzing amplitude. The Helmholtz resonator approximation was employed by Sterbentz and Evvard[5] to arrive at stability and frequency criteria and by Sterbentz and Davids[6] to predict amplitude.

The experiments and conclusions of Dailey, although of a more limited scope, are in many cases surprisingly parallel to those published earlier by the writer. A few of the more important points of reinforcement or conflict between references 3, 4, and 1 will be discussed herein to roughly fill out the picture of instability.

The writer was able to get excellent agreement between pressure-time curves for various positions in the ram-jet obtained experimentally and theoretically using the aforementioned quasi one-dimensional flow characteristics analysis. Boundary conditions employed in computing wave reflections were a quasi steady state at the inlet and a "choked" exit nozzle. Waves are always reflected with the same sign at the exit nozzle under this assumption.

A typical buzz cycle was found to follow this basic pattern: The shock moves outward decreasing the inlet mass flow and sending an expansion wave downstream which is reflected at the exit nozzle. This second expansion wave travels upstream until it overtakes the shock, causing the latter to retreat into the cowling. This rearward motion of the shock generates a downstream compression (which is often followed by a smaller expansion arising from the shock "overshooting" during its rearward motion and then returning to the position it would have reached without "overshoot"). This compression (or compression-expansion couplet) is in turn reflected always as a compression (or couplet) of continually diminishing strength both at the exit nozzle and at the shock, each upstream reflection forcing the shock further forward up the diffuser until the shock reaches its initial unstable position and the cycle is repeated. Thus, rather than a relaxation type, the plenum pressure-time curve is more nearly a series of steps. (See Fig. 10 of reference 1.)

Now the relative magnitude of the wave reflected at the exit nozzle to the incident wave varies as $\{1 - [(\gamma - 1)/2] M_d\} \div \{1 + [(\gamma - 1)/2] M_d\}$, where M_d is the Mach Number in the combustion chamber just before the choked nozzle. Consequently as the nozzle area is reduced with subsequent lower average mass flow, M_d decreases and the magnitude of the reflected wave increases for the same incident wave. The explanation found for the increase in oscillation frequency with decrease in mass flow is as follows: Until the buzz becomes particularly violent at mass flows far removed from that of the minimum stable mass flow, the cycle was always initiated at about the same shock position. Consequently, since the nozzle reflections were increased with decreasing average mass flows, fewer traversals up and down the ram-jet of the compression wave are required to move the shock from its most supercritical position to the unstable position, and, hence, there is a decrease in cyclic time or an increased frequency. This explanation has been verified experimentally.

The writer advanced the theory that the stability of the flow was dependent upon the *instantaneous* values of mass flow and total pressure recovery of the supersonic diffuser and immediate neighboring subsonic diffuser. (Ferri and Nucci demonstrated experimentally that the initial rate of subsonic diffusion could be important to stability.) The prevalent factors are the relative values of the *rate* of increase of entropy and of boundary-layer growth (separation is a special case of rapid boundary-layer growth) compared to the *rate* of decrease of mass flow through spillage around the cowl lip. These factors cause generation of waves moving both upstream and downstream, and the relative magnitudes of these waves will determine whether an inlet perturbed by a random disturbance is stable or unstable.

It is to be noted, contrary to reference 1, that it is definitely not necessary in general to "block" or even to "choke" (in the sense that an instantaneous value of $M = 1$ is obtained locally)

the inlet, although the waves generated become stronger as $M \rightarrow 1.0$.

A fact overlooked by Dailey is that a *growing* separation generates upstream traveling compression waves as well as downstream expansion waves. Consideration of this in his wave travel times discussion and pressure behavior discussion on pages 745–746 would introduce additional possibilities to be explained. Another application of this fact, coupled with the knowledge that the outward shock motion with resultant increased spillage generates downstream expansions, results in a plausible explanation for the droop in plenum chamber pressure noted by Dailey before the inlet pressure fall-off begins. For example, at a station between the growing separation and the cowling entrance, the static pressure can be either rising (upstream compressions > downstream expansions), steady, or falling; while simultaneously at a station aft of the separation, the pressure is falling due to the downstream expansions.

References

[1] Dailey, C. L., *Supersonic Diffuser Instability*, Journal of the Aeronautical Sciences, Vol. 22, No. 11, pp. 733–749, November, 1955.

[2] Ferri, A., and Nucci, L., *The Origin of Aerodynamic Instability of Supersonic Inlets at Subcritical Conditions*, NACA RM L50K30, January, 1951.

[3] Trimpi, R. L., *An Analysis of Buzzing in Supersonic Ram Jets by a Modified One-Dimensional Nonstationary Wave Theory*, NACA RM L52A18, March, 1952.

[4] Trimpi, R. L., *A Theory for Stability and Buzz Pulsation Amplitude in Ram Jets and an Experimental Investigation Including Scale Effects*, NACA RM L53G28, October, 1953.

[5] Sterbentz, W. H., and Evvard, J. C., *Criterions for Prediction and Control of Ram Jet Flow Pulsations*, NACA RM E51C27, August, 1951.

[6] Sterbentz, W. H., and Davids, J., *Amplitude of Supersonic Diffuser Flow Pulsations*, NACA RM E52I24, December, 1952.

Low-Wave-Drag Bodies of Revolution as Determined by Linearized Theory

G. C. Grogan*

Convair, A Division of General Dynamics Corporation, Ft. Worth, Tex.

February 3, 1956

H. M. Parker[1] has presented a linearized method of determining minimum-wave-drag ducted bodies of revolution. This note is submitted to demonstrate how Parker's method of satisfying the boundary conditions may be extended to include a larger class of body shapes with arbitrary body radius control points.

Referring to Fig. 1 and assuming unit free-stream velocity and density, Parker pointed out that the annulus of undisturbed air passing between the concentric cylinders having radii of $R(0)$ and $R(x_1)$ must pass through a control surface of radius $R(x_1)$

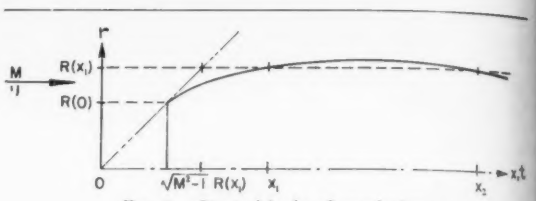

Fig. 1. Ducted body of revolution.

lying between the stations $\sqrt{M^2 - 1}\, R(x_1)$ and x_1. This relation may be expressed as

$$\pi[R^2(x_1) - R^2(0)] = \int_{\sqrt{M^2-1}\,R(x_1)}^{x_1} 2\pi R(x_1)\varphi[x, R(x_1)]dx \quad (1)$$

or, by introduction of the source potential, radial differentiation, and longitudinal integration, the expression becomes

$$\pi[R^2(x_1) - R^2(0)] = \int_0^{x_1 - \sqrt{M^2-1}\,R(x_1)} \frac{(x_1 - t)\, f(t)\, dt}{\sqrt{(x_1 - t)^2 - (M^2 - 1)R(x_1)}} \quad (2)$$

which relates the unknown source strength $f(t)$ to the body radius distributions $R(x_1)$. Note that if the body is slender in the sense that $\sqrt{M^2 - 1}\, R(x_1)$ is quite small, then the source strength is simply the longitudinal gradient of the cross-sectional area as discovered by von Kármán.[2]

If now the radius point under consideration is at station x_2, Eq. (2) is still valid (with x_2 substituted for x_1). This is so because the mass transport through that segment of the $R(x_1) = R(x_2)$ control cylinder lying between stations x_1 and x_2 is zero since that segment is bounded by the body, a stream surface.

The general design problem of passing a low-drag meridian curve through a selected number of control points may now be solved by a method similar to that previously published in the Journal.[3] The source strength $f(t)$ is assumed to be a polynomial in t; it is introduced into Parker's drag expression,[1] and the resultant series is minimized by the variational calculus compatible with the imposed constraints defined by the expanded forms of Eq. (2).

A general procedure for this approach is currently being coded for an electronic digital computer at Convair. It is hoped to publish a more detailed analysis along with computational results in the near future.

References

[1] Parker, H. M., *Minimum-Drag Ducted and Pointed Bodies of Revolution Based on Linearized Supersonic Theory*, NACA TN 3189, March, 1954.

[2] von Kármán, Th., *The Problem of Resistance in Compressible Fluids*, Atti del Convegno della Fondazione Alessandro Volta 1935, pp. 210–220, 1936.

[3] Haskell, R. N., and Grogan, G. C., *Slender Bodies of Low Wave Drag*, Readers' Forum, Journal of the Aeronautical Sciences, Vol. 22, No. 2, pp. 138–139, February, 1955.

* Aerodynamics Group Engineer.

Influence of the Leading-Edge Shock Wave . . .

(*Continued from page 600*)

In a more precise calculation the axial velocity would be expressed as

$$u(x, y) = u_0(\zeta) + (M_\infty \sqrt{C}/\sqrt{Re_{x^*}})^{1-(2/3\gamma)}\, u_1(\zeta) + \ldots$$

and it is required that $u_0(0)$ and $u_1(0)$ vanish and that $u_0(\zeta) \rightarrow 1$ and $u_1(\zeta) \rightarrow (\text{const.}/\zeta^{2/3\gamma})$ as $\zeta \rightarrow \infty$ [see Eq. (7)]. In other words, the solution of the boundary-layer equations is required to reproduce the continuous transition from the boundary-layer type of behavior near the surface to the behavior of the inviscid rotational flow "far" from the surface.

$\frac{1}{x_2} \cdots \rightarrow x_1 t$

This rela-

$)]dx$ (1)

entiation,

$\overline{\overline{\quad}}$ (2)
$R(x_1)$

dy radius
the sense
rength is
l area as

tation x_1,
is so be-
$R(x_1) =$
x_2 is zero
urface.
meridian
y now be
ed in the
e a poly-
ion,[1] and
ulus com-
expanded

ng coded
hoped to
al results

Revolution
1954.
ble Fluids,
. 210–220,

Vave Drag,
No. 2, pp.

∞ [see
undary-
tinuous
ehavior
id rota-